UNIVERSITÉ DE STRASBOURG

UNIVERSITÉ DE STRASBOURG

École doctorale
Physique, chimie-physique
ED 182
Université de Strasbourg

ÉCOLE DOCTORALE Physique et Chimie-Physique (ED 182)

Institut de Physique et de Chimie des Matériaux de Strasbourg

UMR 7504

THÈSE présentée par :

Maryna HRYTSAIENKO

soutenue le : **03 Octobre 2023**

pour obtenir le grade de : **Docteur de l'université de Strasbourg**

Discipline/ Spécialité : Physique de la matière condensée

Dynamique de relaxation dans des boîtes quantiques GaN/AlN: étude par photoluminescence et transmission différentielle pompe-sonde résolues en temps

THÈSE dirigée par :

M. Mathieu GALLART	Maître de conférences, Université de Strasbourg, Institut de physique et chimie des matériaux de Strasbourg

RAPPORTEURS :

M. Andrea BALOCCHI	Professeur INSA, Université de Toulouse, Laboratoire de physique et chimie des nano-objets
M. Bernard GIL	Directeur de recherche CNRS, Laboratoire Charles Coulomb, Université de Montpellier

AUTRES MEMBRES DU JURY :

Mme. Iryna GOZHYK	Ingénieure de recherche, Saint-Gobain, CNRS
M. Thierry CHARITAT	Professeur, Université de Strasbourg, Institut Charles Sadron CNRS

Acknowledgements

This project would not have been possible without the support of many people.

My sincere thanks to my supervisor, Dr. Mathieu Gallart, for your guidance, and support. I have benefited greatly from your wealth of knowledge and meticulous editing. I am extremely grateful that you took me on as a student and give me liberty during my study, it allowed me to grow as a person and a scientist.

I am fortunate to have been a part of the NanoFemto group.

Thank you, Mark Ziegler, for your support and help with any questions concerning work in the laboratory. Thanks for all our friendly conversation and jokes that helped me stay in the benevolent and supportive atmosphere in the lab.

I am grateful to Olivier Crégut for your technical expertise, lucid explanations during experimental alignment, and ensuring we always found the optimal solutions. Your guidance has enriched my learning with numerous experimental insights.

I extend my gratitude to Dr. Pierre Gilliot for keeping me motivated, showing consistent interest in my work's progression, and providing invaluable feedback during our group meetings throughout my PhD.

A special acknowledgment to the team from Lausanne University who produced the state-of-the-art samples that were instrumental to our research. Dr. Sebastian Tamariz, Dr. Nicolas Grandjean and especially Dr. Raphaël Butté, your commitment, expertise, and continuous discussions have been invaluable throughout my PhD journey.

Lastly, my family deserves endless gratitude. My accomplishments and success are because they believed in me.

Thank you to my parents for your constant love and endless support. You have always stood behind me, and this was no exception.

Deepest thanks to my brother, who reminds me of what is important in life, and is always supportive of my adventures.

The birth of my beautiful son during this PhD journey has been a source of immense joy and inspiration. I want to thank him for being the light of my life and for all the strength he has unknowingly provided me.

Finally, to my husband, words cannot encapsulate the depth of my gratitude for your unwavering love and support, not just during this thesis but every single day.

Contents

List of Figures

List of Tables

List of Abbreviations

s/c	Semiconductor
AlN	Aluminium nitride
GaN	Gallium nitride
InN	Indium nitride
AlGaN	Aluminium gallium nitride
InGaN	Indium gallium nitride
AlInN	Aluminium indium nitride
1D	One dimensional
2D	Two dimensional
3D	Three dimensional
QD	Quantum dot
RT	Room temperature
WZ	Wurtzite
ZB	Zincblende
Eg	Band gap
CB	Conduction band
VB	Valance band
NH3	Ammonia
MBE	Molecular beam epitaxy
MOCVD	Metal organic chemical vapor deposition
HVPE	Hydride vapor phase epitaxy
ML	Monolayer
DT	Deposition temperature
SA	Self-assemble
SK	Stranski-Krastanov
RHEED	Reflection high-energy electron diffraction
UHV	Ultra high vacuum
STEM	Scanning transmission electron microscopy (STEM)
LED	Light emitting diode
PD	Photodetectors
UV	Ultraviolet
DUV	Deep ultraviolet
IR	Infrared
NIR	Near infrared
CW PL	Continuous-wave photoluminescence
LBO	Lithium Triborate doubling crystal
BBO	Beta Barium Borate crystal
SHG	Second garmonic generator
OPA	Optical parametric amplifier
PP	Pump-probe
4WM	Four wave-mixing

Chapter 1

State of the art

Semiconductor heterostructures have been an active area of research for several decades. The first publication on quantum dots (QDs) is generally attributed to Alexei Ekimov and colleagues, who reported on the synthesis of semiconductor nanocrystals in 1981. This work represented a significant breakthrough in the field of nanotechnology. It demonstrated that it was possible to synthesize nanometer-scale semiconductor crystals of copper chloride (CuCl) [1] with well-defined sizes and shapes. From the first optical characterizations in the 80s [2, 3, 4, 5], QD dots have been presenting a huge interest because of their unique size-dependent optical [6, 7, 8, 9], electronic properties [10]. Nanoparticles made of metal or semiconductor materials found their place in a lot of fields including chemistry, physics, and biomedical sciences. As a result, QDs have been successfully integrated into our daily life as a part of available application, such as:

- Display technology, including TVs, monitors, and smartphones [11]
- Medical imaging and diagnostics [12, 13, 14]
- Lighting and energy-efficient light-emitting diode (LED) bulbs [15, 16]
- Solar cells and photovoltaics [17, 18]
- Biological imaging and sensing [19, 20]
- Security tagging and anti-counterfeiting measures [21, 22]
- Quantum computing and information processing [23, 24, 25]

The latter technologies use the principles of quantum mechanics to perform computational and informational tasks. On the contrary to the classical computers that use binary digits or bits to represent information and perform calculations, quantum computers use quantum bits or qubits, which can exist in multiple states simultaneously.

After the development of quantum mechanics, which provided a fundamental understanding of the behavior of matter and energy at the atomic and subatomic level in the early 20th century, the second quantum revolution [26] developed the practical applications based on the principles of quantum mechanics. At this stage, QDs occupied an important place due to their potential use in quantum technologies.

So their synthesis, characterization and application are still a very active area of research. Beyond fundamental aspects, the ongoing interest in semiconductor QDs is motivated by their potential for a wide range of applications.

Here are some examples of how QDs are being used in quantum devices:

- Qubit Devices: QDs are being used as potential qubits in quantum computing and communication devices. By controlling the electronic states of the QDs, researchers can create a system of qubits that can be used to perform quantum operations [27, 28].
- Single-Photon Emitters: QDs can also be used as single-photon emitters, which are essential components in quantum communication systems. By exciting a QD with a laser, researchers can generate single photons, which can be used to transmit information in a secure manner [29, 30, 31].

- Quantum Sensors: QDs are being used as highly sensitive detectors in quantum sensors. By monitoring the electronic states of the QDs, researchers can detect changes in physical quantities, such as magnetic fields or temperature, with high precision [32, 33].
- Quantum Memory: QDs are being explored as potential quantum memory devices. By using the electronic states of QDs to store quantum information, researchers hope to create a stable and efficient quantum memory device [34].
- Quantum Cryptography: QDs are being used in the development of quantum cryptography systems. By using the unique electronic properties of QDs, researchers hope to create secure communication channels that are impossible to hack or intercept [35, 36].

For a review see for instance [37, 38].

There are several popular categories of semiconductor QDs that are currently being researched and developed for quantum technologies, each with their own unique properties and advantages. The first category is colloidal QDs. They are typically made from materials such as cadmium selenide, lead sulfide, or indium arsenide. Colloidal QDs are more suitable for applications that require high efficiency, tunability, and a wide range of sizes and shapes. The second sort is self-assembled QDs, which are formed through self-assembly during the epitaxial growth process. Among them, the best mastered and most studied system consists in QDs of indium arsenide in a matrix of gallium arsenide (InAs/GaAs). Self-assembled QDs are known for their high optical quality, meaning they can emit high purity and coherence photons. This is the requirement for potential building blocks of quantum devices (to produce only one photon per demand, since multi-photon emission can compromise the security of quantum cryptography and reduce the performance of quantum computers).

Semiconductor QDs of the arsenide family, such as In(Ga)As/(Al)GaAs, have been widely studied as single-photon emitters (SPE) [39, 40]. The main disadvantage of arsenide based systems is its cryogenic operating temperature, which complicates its integration into real devices. On the other hand, among the wide range of available QD systems, GaN/Al(Ga)N QDs offer attractive features because of the large band offsets at the AlN/GaN interface, enabling three-dimensional confinement of electron-hole (e-h) pairs up to room temperature [41]. Another difference between arsenides and nitrides is the operating spectral range. The first ones have a relatively small bandgap, which means they can absorb and emit photons in the near-infrared and visible regions of the spectrum. Nitrides have a relatively large bandgap, which means they can absorb and emit photons in the ultraviolet and visible regions of the spectrum. However, the emission range of nitrides could be adjusted depending on the composition of the material.

In contrast to arsenides, progress in the synthesis methods of nitride QDs is slow-moving due to poor crystallinity. The first growths of GaN/AlN QDs were achieved in the late 1990's [42, 43]. Since then, the growth of III-nitride crystals has been one of the main problems for the development of III-nitride devices. Isamu Akasaki, Hiroshi Amano, and Shuji Nakamura have contributed a lot to the developement of the growth methods of gallium nitride materials and as a result, the first high-efficiency blue LED was presented in 1994. Further work of these scientists has been awarded with a Nobel Prize in Physics by Royal Swedish Academy of Sciences in 2014 for the invention of efficient blue light-emitting diodes which have enabled bright and energy-saving white light sources. So relatively recently, III-nitrides have proven to be the second most important semiconductors after silicon. This was mainly due to improved material quality. Using III-nitrides QDs in operating quantum devices requires a high-quality crystalline structure and the absence of structural defects such as dislocations. It means that the field of III-nitride substrate fabrication and the development of growth methods remains one of the main research area.

Advantages of increased crystalline quality and reduced impurities in gallium nitride nanostructures were taken to achieve single UV-photon emission at 300 K [44, 45] and even above [46]. Long-lived optical orientation was also experimentally observed [47]. Such experimental accomplishments go hand in hand with strong efforts regarding the growth of self-assembled nitride QDs in order to control their structural parameters, especially their size and surface density [48, 49].

Among the wide range of III-V nanostructures, the structural and thus, optical properties of III-nitrides aroused a great interest. In wurtzite crystalline form these materials exhibit a spontaneous polarization without the presence of an external electric field [50]. Early theoretical studies of spontaneous polarization and piezoelectric constants of III-V nitrides (AlN, GaN and InN) [51] highlighted that piezoelectric constants are up to ten times larger than in conventional III-V and II-VI semiconductor compounds and comparable to ZnO compounds. Growing wurtzite GaN QDs encapsulated in an AlN matrix, the difference in both spontaneous and piezoelectric polarizations between the two materials causes the presence of a strong built-in electric field along the $[000\bar{1}]$ direction. Theoretical study by Williams et al. [52] reported the simulations of nitride QDs as significantly different than those of GaAs-based QDs. The combination of an intrinsic electric field with a quantum-confinement in QDs give rise to the quantum confined Stark effect (QCSE). The latter has been responsible for strongly redshifted optical emission in large QDs reported in [53, 54]. The intrinsic electric field can reach values up to 10 MV/cm [55].

The electric field decreases the oscillator strength by inducing a spatial separation of electron and hole wave-functions (formation of a dipole), hence leading to a strong dependence of the radiative lifetime on the dot height [56, 57, 54] that spans several orders of magnitude from the picosecond to the microsecond range. The consequences are dramatic for the largest QDs. First, as their probability of radiative recombination is decreased, other dephasing mechanisms become dominant and the radiative lifetime of those QDs will exceed the most optimistic values of the dephasing time that could be expected for this type of system. Furthermore, their weak oscillator strength will hinder any resonant excitation and the control of coherent phenomena. Finally, the possible transient screening of the electric field is responsible for a complex recombination dynamics, which is non exponential and strongly depends on the number of injected e-h pairs [54]. These are major drawbacks if one considers for instance the possibility of generating and manipulating entangled states. This is what motivates the present work on small GaN/AlN QDs whose emission energy lies above the strained bulk GaN bandgap and for which a significant value of the oscillator strength is preserved. Because of their short radiative lifetime –in the nanosecond range– these QDs are also expected to be less sensitive to any possible screening of the built-in electric field, be it due to the carrier injection regime (low to high) or to surrounding charges.

Key conditions to use QDs for nanophotonic applications rely on the full understanding and, if possible, the control of the different dynamics associated with electronic excitations, namely population, spin- and phase relaxation. For example, generating indistinguishable photons from single QDs requires the radiative lifetime of the exciton T_1 to be shorter than its coherence time T_2, which is favored in the Purcell regime [58, 59].

While there have been many studies on carrier relaxation in GaN QDs, a complete understanding of the full mechanism has not yet been achieved. Some studies have focused on the role of carrier-phonon interactions in the relaxation processing [60], where the energy of the carriers is transferred to lattice vibrations. Other studies have investigated the influence of surface states and surface recombination processes on carrier relaxation [61]. Additionally, the influence of quantum confinement effects on carrier dynamics in GaN QDs has been extensively studied. Despite these studies, a complete understanding of the full mechanism of carrier relaxation in GaN QDs is still lacking. After excitation carriers non-radiatively relax to the radiative state within ps range. Therefore, this requires ultra-fast optical spectroscopy methods operating in the deep UV spectral range. These demands make the investigation quite challenging. As well there are challenges of modeling these complex systems theoretically.

In this work, we are interested in the relaxation dynamics of e-h pairs in gallium nitride QDs encapsulated in an aluminum nitride (GaN/AlN) matrix by means of ultra-fast optical spectroscopy techniques. We will take advantage of the joint use of time-resolved photoluminescence and differential transmission experiments to follow the relaxation dynamics of e-h pairs from their injection into the wetting layer or into the excited states of QDs until their trapping and recombination in dots. We will extract the characteristic times at each relaxation stage and try to shed light on the physical processes at work during the carrier thermalization.

Chapter 2

Introduction to GaN/AlN wurtzite quantum dots

In this general chapter, we introduce the necessary notions so that the non-specialist reader can serenely understand the physics of AlN/GaN quantum dots.

In the section 2.1, we will present in a concise way the nitride semiconductors, their crystalline structure responsible for the internal polarization fields encountered in the nanostructures, their band structure as well as a quick overview of their optical properties.

Section 2.2 will introduce the basic concepts of semiconductor quantum dots regardless of the material from which they are made. We will review the effects of confinement on electronic states, their fine structure and excitonic complexes.

Finally, we will expose in the section 2.2 the specificities of GaN/AlN quantum dots: we will detail the consequences of the internal polarization field on their electronic states and their optical properties.

2.1 III-nitrides semiconductors

2.1.1 Crystalline structure

The group of III-nitride semiconductors refers to compounds combining an element from column III of the periodic table, such as aluminum, gallium or indium, with nitrogen (column V). III-nitrides are direct bandgap semiconductors. The energies of the forbidden bands, at low temperature, cover values ranging from 0.78 eV for indium nitride (InN) to 6.25 eV for aluminum nitride (AlN) passing through the value of 3.51 eV in the case of gallium nitride (GaN) (Tab. 2.1). Consequently, the whole visible spectrum can be covered by synthesizing ternary alloys such as $In_xGa_{1-x}N$, $InAlN$ and $AlGaN$. The group-III nitrides AIN, GaN can crystallize in the zinc-blende (cubic system), wurtzite (hexagonal system) and rocksalt structure. The wurtzite is thermodynamically stable under ambient conditions [62]. The schematic views of wurtzite and zinc-blende crystalline structures are shown on Fig. 2.1. In both cases, the group III element is surrounded by four atoms of the group V element, which are arranged at the vertices of a tetrahedron.

Among the wide range of available QD systems, GaN/AlN QDs offer attractive features because of the large band offsets at the AlN/GaN interface, enabling three-dimensional confinement of e-h pairs up to room temperature [41].

2.1.2 Spontaneous and piezoelectric polarization

III-nitrides structures in wurtzite form exhibit a spontaneous polarisation [50]. Wurtzite lies among the highly symmetrical crystalline structures. The crystal point group correspond to C_{6v} in the Schönflies notation ($6mm$ in Hermann–Mauguin notation). This point group includes a six-fold rotation axis and six mirror planes. Wurtzite symmetry implies that the spontaneous polarization should be parallel to the $\boldsymbol{c}$-axis, $\mathbf{P}^{sp} = P_3^{sp}\mathbf{u}_z$ [64]. In an

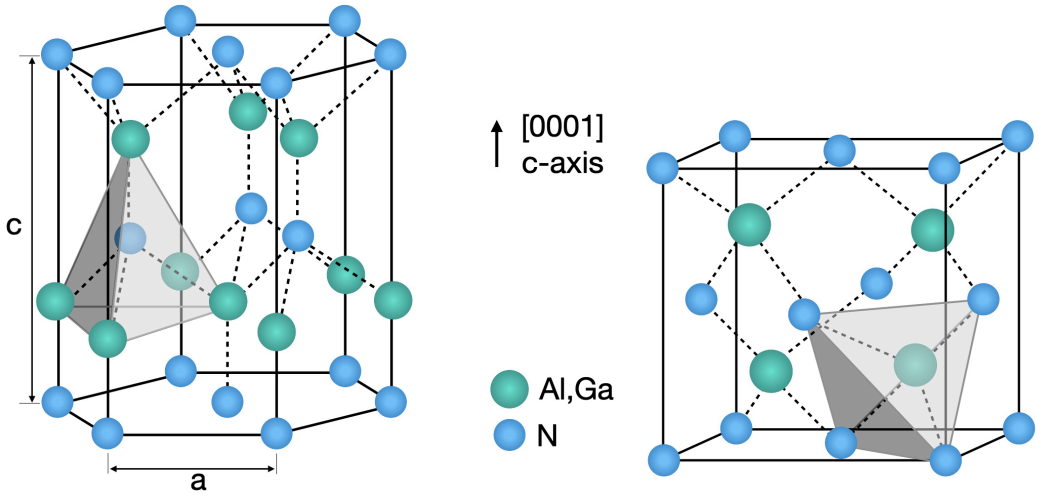

(a) (b)

FIGURE 2.1: Wurtzite(a) and zinc-blende (b) crystal structures.

TABLE 2.1: Lattice parameters and bandgaps of nitride semiconductors in the wurtzite crystal structure [63].

	InN	**GaN**	**AlN**
a (Å) at $T = 300$ K	3.545	3.189	3.112
c (Å) at $T = 300$ K	5.703	5.185	4.982
c / a	1.61	1.63	1.60
Eg (eV)	0.78	3.51	6.25

ideal tetrahedron the condition ($\frac{c}{a} = \sqrt{\frac{8}{3}}$) must be satisfied. The GaN and AlN are polar materials: the difference in electronegativities between nitrogen, the most electronegative element of the V-group, and the metal lead to the highest bond ionicity among all III–V compounds. This leads to a strong ionic character of the bonds, resulting in a significant spontaneous polarization. The $\frac{c}{a}$ is slightly smaller than 1.633 (see Tab. 2.1). In this case the electron cloud along III-N binding is shifted towards the N atom.

A relative displacement between the center of mass of the cations and anions along the [0001] direction creates an inherent dipole moment. This is caused by the structure deformation where the bond along the ***c***-axis is longer than other bonds and the bond angles deviate from their ideal values. Therefore an intrinsic spontaneous polarization occurs as shown in Fig. 2.2. This intrinsic or spontaneous polarization, however, does not make much of a difference in bulk materials. The reason is that in bulk, spontaneous polarization is effectively screened by mobile charges at the surface of the sample or in its volume. But when we move to the realm of low-dimensional heterostructures, like quantum wells (QWs) and QDs, the scenario changes dramatically. Unlike bulk, these structures are finite, so the polarization is not perfectly screened or cancelled out. In these finite structures, especially when the ***c***-axis is perpendicular to the interfaces, the internal spontaneous polarization can lead to the formation of a static electric field within the structure.

The piezoelectric polarization appears when a stress is applied to a non-centrosymmetric material [65]: the additional deformation undergone by the primitive tetrahedral cell, inherent to the wurtzite structure, shifts the relative location of cations and anions within the unit cell altering the electric polarization of the material (see Fig. 2.4).

The induced piezoelectric polarization is a vector the direction of which is not necessarily along the direction of the applied stress. This implies that an applied stress in a particular

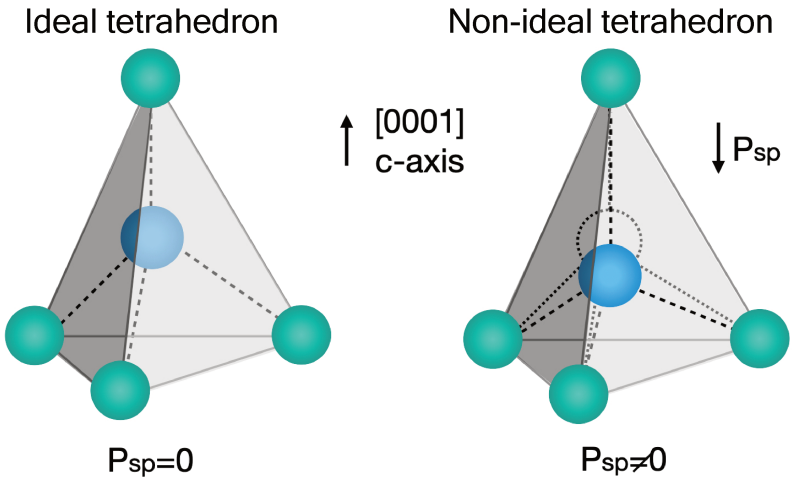

FIGURE 2.2: Illustration of spontaneous polarization from a non-ideal c/a ratio of GaN tetrahedron.

TABLE 2.2: Calculated values of the spontaneous polarization in nitride compounds [51].

	InN	**GaN**	**AlN**
P_{sp} (Cm^{-2})	-0.032	-0.029	-0.081

direction could generate a piezoelectric polarization in a different direction, depending on the specific crystal symmetry and orientation. The component P_i $(i = x, y, z)$ of a stressed material could be represented mathematically using the piezoelectric stress coefficients (d_{ij}) as follows:

$$P_i = \sum_{j=1}^{3} \sum_{k=1}^{3} d_{ijk} \sigma_{jk}. \tag{2.1}$$

where d, σ_{ij} are the piezoelectric tensor of rank 3 and stress tensor, respectively. The coefficient d_{ijk} are called the piezoelectric moduli. The previous equation could be represented in matrix form since, with respect of tensor symmetries, jk coefficient in σ_{ij} and d_{ijk} could be replaced by only one [64]. In the new notation it will be:

$$P_i = \sum_{j=1}^{3} d_{ij} \sigma_j. \tag{2.2}$$

or in the matrix form:

$$\begin{pmatrix} P_x \\ P_y \\ P_z \end{pmatrix} = \begin{pmatrix} d_{11} & d_{12} & d_{13} & d_{14} & d_{15} & d_{16} \\ d_{21} & d_{22} & d_{23} & d_{24} & d_{25} & d_{26} \\ d_{31} & d_{32} & d_{33} & d_{34} & d_{35} & d_{36} \end{pmatrix} \begin{pmatrix} \sigma_{xx} \\ \sigma_{yy} \\ \sigma_{zz} \\ \sigma_{xy} \\ \sigma_{yz} \\ \sigma_{zx} \end{pmatrix} \tag{2.3}$$

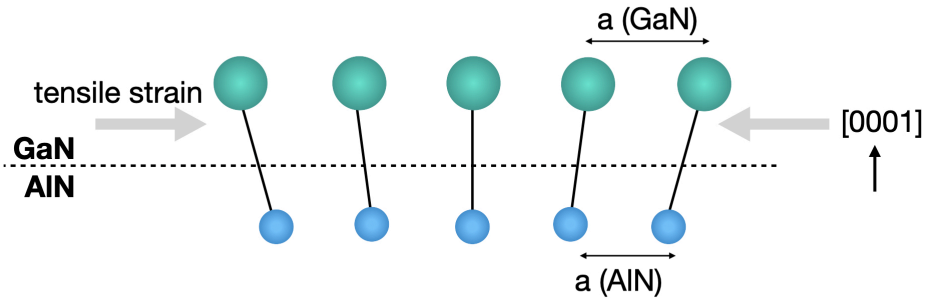

FIGURE 2.3: The mismatch in the lattice parameters is responsible for the existence of a strain at the GaN/AlN interface.

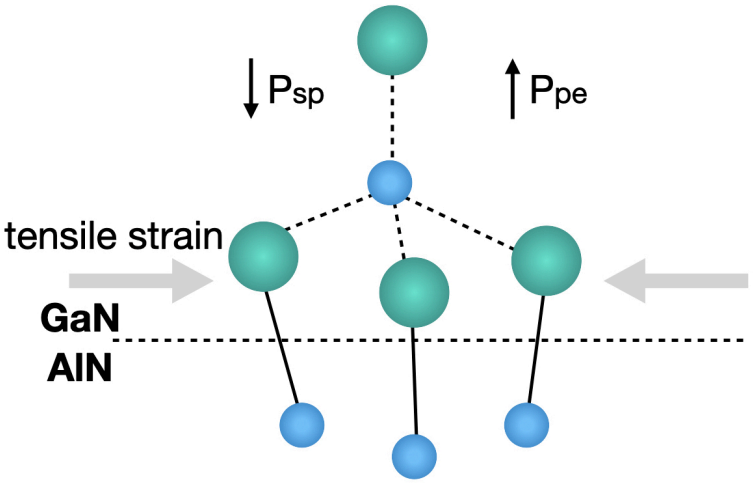

FIGURE 2.4: Schematic diagram showing the origin of the piezoelectric polarization at the GaN/AlN interface.

For a crystal with hexagonal symmetry $6mm$, the piezoelectric tensor can be reduced to the following non-zero elements: d_{31}, d_{33}, and d_{15} [64]. The piezoelectric tensor becomes:

$$\begin{pmatrix} 0 & 0 & 0 & 0 & d_{15} & 0 \\ 0 & 0 & 0 & d_{15} & 0 & 0 \\ d_{31} & d_{31} & d_{33} & 0 & 0 & 0 \end{pmatrix} \tag{2.4}$$

In the case of elastic deformation the stress tensor is related to the applied strain in the material by the Hooke's law:

$$\sigma_{ij} = c_{ijkl}\varepsilon_{kl}, \tag{2.5}$$

where ε_{kl} is the strain tensor, c_{ijkl} is the stiffness tensor which represents the elastic properties of the material. In anisotropic crystals, the stiffness tensor is fourth-rank and contains up to 81 elements, but due to symmetry and the properties of stress and strain, only 21 elements are

independent in the most general case. In a material with higher symmetry, like the wurtzite structure of III-nitrides, there are even fewer independent elements.

Using the symmetries of the tensor as well as the wurtzite crystal structure, we can simplify the stiffness tensor and write Hooke's law in matrix notation. For the case of the wurtzite structure, the stiffness tensor becomes a 6x6 matrix, and the stress and strain become 6-component vectors. The simplified relation takes the following form:

$$\begin{pmatrix} \sigma_{xx} \\ \sigma_{yy} \\ \sigma_{zz} \\ \sigma_{xy} \\ \sigma_{yz} \\ \sigma_{zx} \end{pmatrix} = \begin{pmatrix} c_{11} & c_{12} & c_{13} & 0 & 0 & 0 \\ c_{12} & c_{11} & c_{13} & 0 & 0 & 0 \\ c_{13} & c_{13} & c_{33} & 0 & 0 & 0 \\ 0 & 0 & 0 & c_{44} & 0 & 0 \\ 0 & 0 & 0 & 0 & c_{44} & 0 \\ 0 & 0 & 0 & 0 & 0 & \frac{1}{2}(c_{11} - c_{12}) \end{pmatrix} \begin{pmatrix} \varepsilon_{xx} \\ \varepsilon_{yy} \\ \varepsilon_{zz} \\ \varepsilon_{xy} \\ \varepsilon_{yz} \\ \varepsilon_{zx} \end{pmatrix} \tag{2.6}$$

where σ_{xx}, σ_{yy}, and σ_{zz} are normal stresses, σ_{xy}, σ_{yz}, and σ_{zx} are shear stresses, ε_{xx}, ε_{yy}, and ε_{zz} are normal strains, ε_{xy}, ε_{yz}, and ε_{zx} are shear strains.

Equations (2.3) and (2.6) give the relationship between the piezoelectric polarization and the strain. During the epitaxial growth, the deposited material undergoes a biaxial strain in the plane perpendicular to the growth axis. The shear strain is therefore zero and

$$\begin{aligned} \varepsilon_{xx} &= \varepsilon_{yy} = \frac{a - a_0}{a_0} \\ \varepsilon_{zz} &= -2\frac{c_{13}}{c_{33}}\varepsilon_{xx} \end{aligned} \tag{2.7}$$

a_0 being the in-plane lattice parameter at zero strain.

The only non-zero term of the polarization tensor is the component along the ***c***-axis [0001] ($\mathbf{P}^{pz} = P_3^{pz}\mathbf{u}_z$), so:

$$P_3^{pz} = 2d_{31}\varepsilon_{xx}(c_{11} + c_{12} - 2\frac{c_{13}^2}{c_{33}}). \tag{2.8}$$

Values of the elastic coefficients for wurtzite III-nitride materials have been reported in Ref. [66]. The contribution of the piezoelectric polarization will be opposite to the one of spontaneous polarization. The effect of polarization causes a separation of positive and negative charges at the interfaces between different materials. These separated charges form what are known as "polarization charges" or "charge sheets", leading to a built-in electric field across the interfaces. This electric field is of particular interest as it can greatly impact the optical and electronic properties of the GaN/AlN QD system.

2.1.3 Electronic properties

Band structure

Having established a clear understanding of the principal crystallographic properties of III-nitrides, we now shift our attention to the consequential electronic properties that arise. The electronic properties, which include but are not limited to transport and optical characteristics, are fundamentally dictated by the band structure, that is, the set of allowed electronic states. The electronic structure of solid-state crystals is a generalization of the molecular orbital theory to a large number of atoms. The coupling between N identical discrete states leads to the formation of continuous bands of allowed energies split by forbidden bandgaps. In a semiconductor, at 0 K the highest occupied energy band is full of electrons and is called the valence band (VB). The first allowed band located at an energy immediately above the VB is completely unoccupied and is called the conduction band (CB). These bands are split by the bandgap that is usually denoted by E_g. At the thermal equilibrium, the Fermi level lies in the middle of the bandgap (see Fig. 2.5). As the arrangement of atoms within the

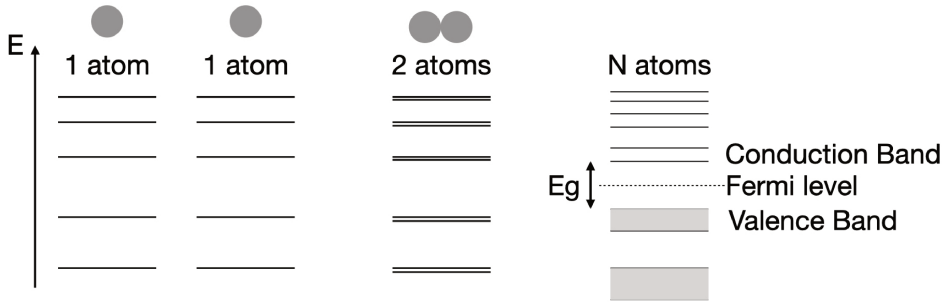

FIGURE 2.5: Schematic illustration of the energy band formation around the Fermi energy level at $T = 0$ K. In grey is represented the presence of electrons.

crystal is periodical, the Coulomb potential seen by electrons is periodical as well. It results that the electronic wavefunction has to be the product of the function having the translational symmetry of the lattice by a plane wave with wavevector $\boldsymbol{k}$. This constitutes the well known Bloch theorem. The energies of the different bands in the reciprocal space strongly depend on the quasi momentum $\boldsymbol{k}$.

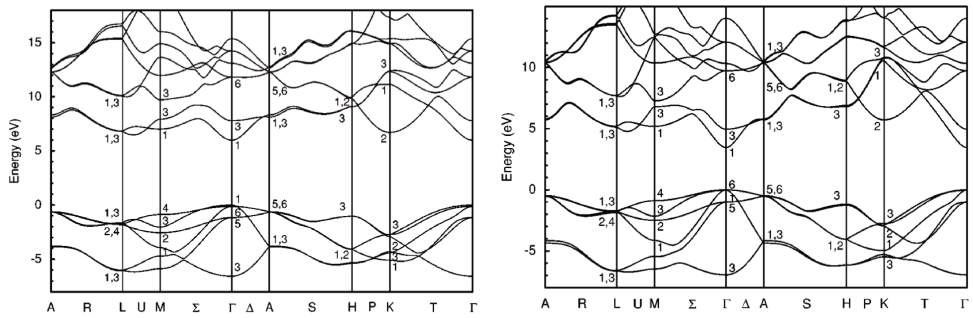

(a) (b)

FIGURE 2.6: Band structure of wurtzite (a) AlN and (b) GaN along high-symmetry lines in the Brillouin zone. Reprinted Ref.[67].

The complex band structures of wurtzite GaN and AlN were studied by several groups using different methods of theoretical calculation based on the local density approximation [68, 69], *ab initio* approach [70], ionic potentials model [67]. The resulting band structures of wurtzite AlN and GaN given by Ref. [67] are presented in Fig. 2.6. For the sake of completeness, first Brillouin zones of both zinc blende and wurtzite structure are sketched in Fig. 2.7.

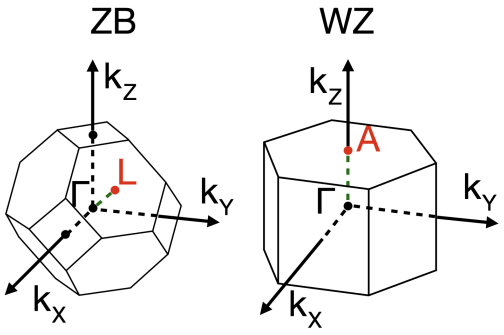

FIGURE 2.7: Diagrams of the Brillouin zones for the zinc blende (ZB) and wurtzite (WZ) crystal phase structures.

As has already been said, GaN and AlN are direct bandgap semiconductors. The maximum of the VB and the minimum of the CB are both located at the Γ point of the first Brillouin zone, where $\vec{k}$=(0,0,0). The valence and conduction bands are separated by an energy gap and are of opposite curvature.

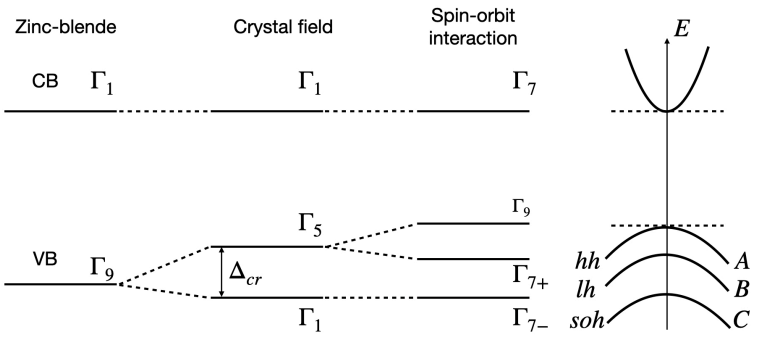

FIGURE 2.8: Simplified model of band structure near the Γ point of GaN without and with spin-orbit interaction.

In a spinless description, the triplet at the top of the VB is split into a doublet with symmetry Γ_5 and a singlet with symmetry Γ_1(using the Kostar's notation) by the crystal field. Thaking into account the spin-orbit interaction, the VB energy splits in three subbands with different effective masses: the heavy-hole (subband A at Γ_9), light-hole (subband B at Γ_{7+}), and spin-orbit (subband C at Γ_{7-}) [68, 71]. The final symplified schematic band structure of the conduction and the VBs see right Fig. 2.8.

The detailed VB structures of GaN and AlN at the Γ point are represented in Fig. 2.9 reprinted from Ref. [72]. Because the crystal-field splittings have opposite signs in GaN and AlN the hierarchy between the singlet Γ_1 and the doublet Γ_5 is reversed from one material to the other. It results that the top of VB is Γ_9 in GaN while it is Γ_7 in AlN. However, this analysis does not take into account the possible effect of strain that can reverse the order Γ_9 and Γ_7 bands in GaN.

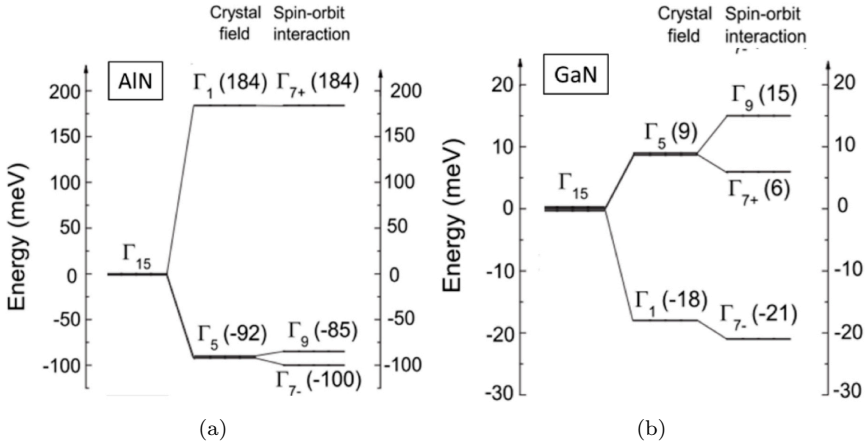

FIGURE 2.9: Characteristic splittings and energy shifts due to the crystal-field splitting and the spin-orbit interaction in the VB structure of AlN and GaN. The threefold degenerate $\Gamma_{1,5}$ level is used as energy zero. In parenthesis are presented the absolute energy values in meV (Reprinted from Ref. [72]).

Effect of temperature

The bandgap energy of semiconductors is known to decrease as the temperature increases. This phenomenon is attributed to the thermal expansion of the material, leading to changes in the lattice parameters. This relationship between the bandgap energy and the temperature of the crystal can be described by the empirical Varshni equation [73]:

$$E_g(T) = E_g(0) - \frac{\alpha T^2}{T + \beta}. \tag{2.9}$$

where α and β are two constants characteristic of the material presented in Tab. 2.3.

TABLE 2.3: Bandgap energies of GaN and AlN at T = 0 K and Varshni parameters [63].

	GaN	**AlN**
$E_g(T = 0K)$ (eV)	3.507	6.23
α (meV/K)	0.909	1.999
β (K)	830	1429

The Varshni equation essentially states that as the temperature increases, the lattice expands, resulting in a decrease in the bandgap energy. This implies significant implications for the electronic and optical properties of the semiconductor. The energies of optical transitions, that is to say the absorption and emission spectra, shift as a function of temperature due to the changing bandgap.Note that the concentration of free carriers also change with temperature, which affect the electrical conductivity of the material.

Effect of strain

Piezoelectricity is not the only phenomenon resulting from the displacement of atoms from their ideal positions within the crystal. During the heteroepitaxy of nitrides, the substrate imposes its lattice parameter on the deposited layer which then presents a residual stress. For example, GaN deposited on sapphire always exhibits a biaxial compression in the plane perpendicular to the growth axis. The resulting deformation causes a displacement of the band extrema at the center of the first Brillouin zone and, consequently, a variation of the bandgap and of the energies of optical transition. Without going into the details of the

calculations, the energy shift of the band extrema of GaN are given by the expressions [74]

$$\begin{aligned} \Delta E_{CB}(\Gamma_7) &= a_{cz}\varepsilon_{zz} + a_{ct}\varepsilon_{\perp} \\ \Delta E_{VB}(\Gamma_{9/7+}) &= (D_1 + D_3)\varepsilon_{zz} + (D_2 + D_4)\varepsilon_{\perp} \\ \Delta E_{VB}(\Gamma_{7-}) &= D_1\varepsilon_{zz} + D_2\varepsilon_{\perp} \end{aligned} \tag{2.10}$$

where a_{cz} and a_{ct} are the deformation potentials of the CB and the D_i are the deformation potentials of the VB.

These strain induced energy displacements influence the value of the band discontinuities between the different materials present during the heteroepitaxy of nanostructures and, consequently, the depth of the confinement potentials.

2.1.4 Optical properties

Excitons

During the absorption of a photon the energy of which is larger than the bandgap, an electron from one of the VBs is promoted into the CB. The Coulomb interaction of the conduction electron (effective mass m_e^*, wavevector $\boldsymbol{k}_e$) with the hole in the VB (effective mass m_h^*, wavevector $\boldsymbol{k}_h$) gives rise to the creation of a quasi-particle called an exciton. An exciton is the first excited state of a crystal. It is therefore a hydrogenoid system, characterized by an effective Bohr radius a_B^* and an effective Rydberg R_y^*, whose center of mass is free to propagate in the crystal with a quasimomentum $\boldsymbol{K}$. For energies lower than the bandgap E_g, the excitonic spectrum, made up of bound states, presents a discrete n^{-2} series like the hydrogen atom:

$$E_X(n, \boldsymbol{K}) = E_g - \frac{R_y^*}{n^2} + \frac{\hbar \boldsymbol{K}^2}{2M} \tag{2.11}$$

with $\boldsymbol{K} = \boldsymbol{k}_e + \boldsymbol{k}_h$ and $M = m_e^* + m_h^*$

For energies greater than E_g, the exciton is ionized and the spectrum is a continuum associated with the diffusion states of the decorrelated e-h pair

$$E_X(\boldsymbol{K}) = E_g + \frac{\hbar \boldsymbol{K}^2}{2M} \tag{2.12}$$

The binding energy of the exciton R_y^* is obtained by the minimization of the total energy. It varies from a few meV to a few tens of meV in inorganic semiconductors but may be enhanced in confined systems.

Excitons are generally observed at low temperature, thermal energy tending to ionize them if their bond energy is low. The presence of excitons is characteristic of semiconductors of high crystalline quality. They give rise to marked structures on the reflectance spectrum and to intense and sharp emission lines in the PL spectrum. In nitrides, from the Γ_7 conduction band, and the Γ_9, Γ_{7+}, Γ_{7-} valence subbands, 3 excitons are build, labelled X_A, X_B and X_C, respectively. The binding energy of the $A-$exciton is estimated between 23 and 28 meV [63].

The displacement of the band extrema at the point Γ of the Brillouin zone (paragraph 2.1.3) causes a variation of the energies of the excitons X_A, X_B and X_C according to the deformation of the deposited layer. Thus, the differences in energy between the 3 excitons is characteristic of the strain state and varies according to the substrate used. A way to represent the corresponding energies as a function of that of the exciton X_A (Fig. 2.10).

Optical spectra

Fig.2.11 shows the PL and reflectance (RF) spectra for a high-crystalline layer of homoepitaxial GaN. Note on the RF spectrum the ground state ($n = 1$) and the first excited state ($n = 2$) of the 3 excitons X_A, X_B and X_C. At low temperature, the PL spectrum is dominated by the recombination of excitons bound to donor (D^0, X_A) and acceptor (A^0, X_A) impurities. The PL of free excitons X_A and X_B is also visible although an order of magnitude lower in intensity. When the temperature is increased, bound excitons are gradually untrapped to the

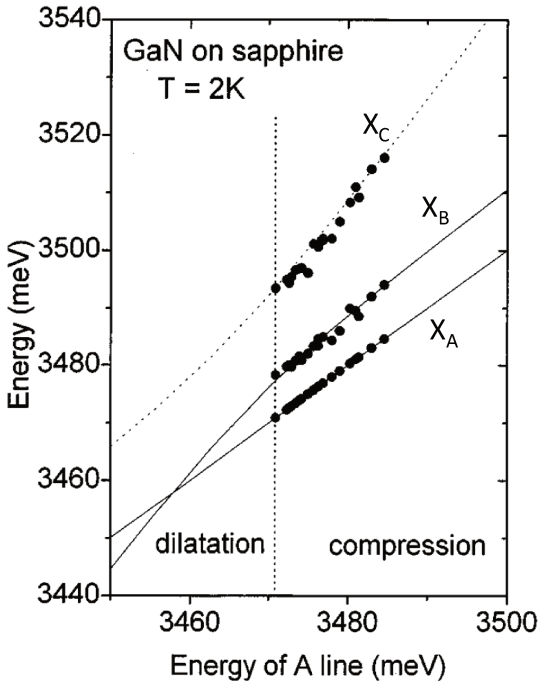

FIGURE 2.10: Energy evolution of the A, B and C excitons as a function of the X_A energy. Reprinted fom Ref.[71].

benefit of the free excitons. However, being free to propagate throughout the volume of the crystal, these are much more subject to de scattered on non-radiative defects (threading dislocations). The recombination dynamics is then dominated by non-radiative recombinations. Note that, in the case of a layer in dilation, the order of the excitons A and B is reversed.

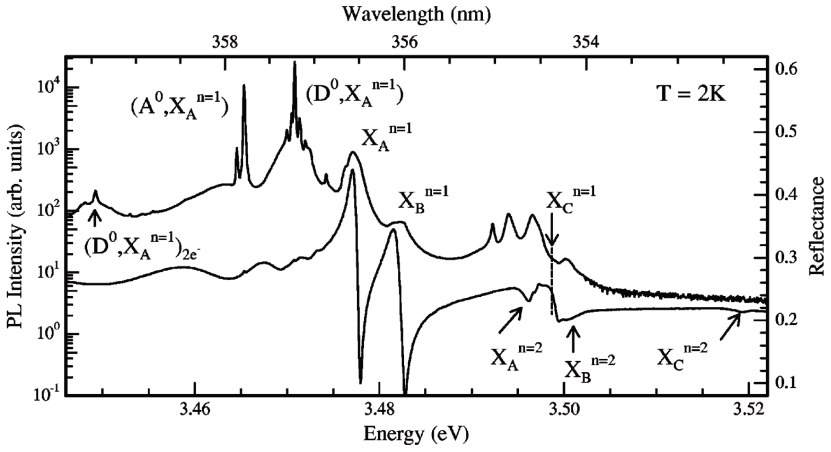

FIGURE 2.11: Low-temperature PL and reflectance spectra of a high quality homoepitaxial GaN layer. Reprinted from Ref.[75].

2.2 General information on semiconductor nanostructures

2.2.1 Confinement

A semiconductor nanostructure is an artificial edifice which consists of the assembly of several materials of different bandgap energies. The simplest system is the one-dimensional QW: a nanometric slice of semiconductor A with bandgap E_g is sandwiched between two layers of a semiconductor B with a bandgap larger than E_g. If the thickness of the layer A becomes comparable to the de Broglie wavelength of electrons, the difference between the bandgaps is seen as a potential barrier by electons and holes. The motion is restricted to the plane of the layer A and the carrier energies become quantized in the perpendicular direction. The top of the VB and the bottom of the CB are shifted to higher energies by the confinement effect and the density of electronic states is profoundly modified. Such a system is said to be bidimensional (2D). Semiconductor QDs are said to be zero-dimensional (0D) systems because they confine electron and holes along the 3 directions of space. It results in a total discretization of energy levels. Fig. 2.12 shows the comparison between the density of states of bulk, QWs, quantum wires, and QDs.

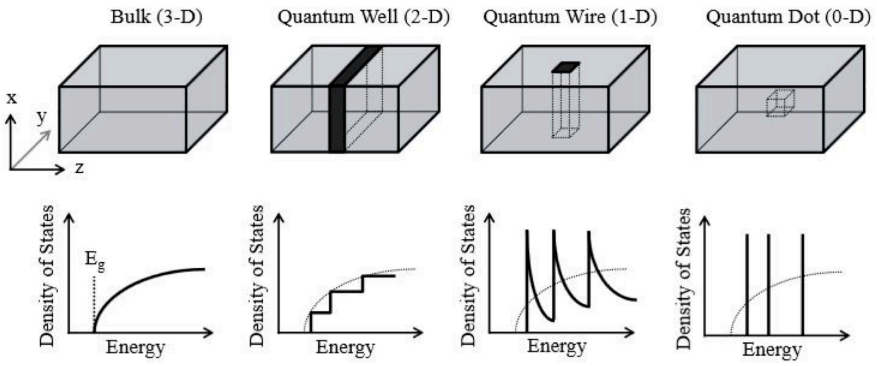

FIGURE 2.12: Electronic density of states for particles with three (bulk), two (QW), one (quantum wire), and zero (QD) spatial degrees of freedom.

In order to demonstrate the basic effects of three-dimensional quantum confinement, let consider a simple model, where QDs have a prism-like geometry with infinite barrier heights. Such an approximation dramatically reduces the complexity of real structures and enables to analytically express the electronic states of a QD.

A QD with infinite barriers is modeled with a potential $V(x,y,z) = 0$ for $z \in [0, h_{QD}]$ and $x, y \in [0, L_{QD}]$ and $V(x,y,z) \to \infty$ elsewhere. In the effective mass (m^*) approximation, the expressions of the eigenfunctions and eigenenergies when solving the envelope-function equation can be written as:

$$\Psi_{n,l,m}(\vec{r}) = \sqrt{\frac{8}{h_{QD} L_{QD} L_{QD}}} \sin\left(\frac{n\pi}{h_{QD}} z\right) \sin\left(\frac{l\pi}{L_{QD}} x\right) \sin\left(\frac{m\pi}{L_{QD}} y\right). \tag{2.13}$$

$$E(n,l,m) = \frac{\hbar^2\pi^2 n^2}{2m^*_\perp h^2_{QD}} + \frac{\hbar^2\pi^2 l^2}{2m^*_\parallel L^2_{QD}} + \frac{\hbar^2\pi^2 m^2}{2m^*_\parallel L^2_{QD}}. \tag{2.14}$$

where $n,l,m \in N$ are the quantization numbers along the three axes z, x, y, respectively. We can simplify equation (2.14) in the case of QD with a square base as follows:

$$E(n,l,m) = \frac{\hbar^2\pi^2 n^2}{2m^*_\perp h^2_{QD}} + \frac{\hbar^2\pi^2(l^2+m^2)}{2m^*_\parallel L^2_{QD}}. \tag{2.15}$$

In QD structures, symmetry leads to degenerate excited levels for $l \neq m$ where to a given eigenenergy will correspond two eigenfunctions. From a practical point of view, the degeneracy is usually lifted by small imperfections in the QD shape and results in transition doublets with a small splitting. Due to the confinement effect, the band-edge is shifted (see Fig. 2.13). As follows, for smaller QD there is a blue-shift of transition energy (Eq. 2.16).

$$E_{e_1h_1} = E_g + e_1 + h_1, \tag{2.16}$$

where E_g is the bandgap energy, and e_1 and h_1 are the confinement energies of the electron and hole, respectively. The term $E_{e_1h_1}$ in this equation represents the energy of the e-h pair in the QD.

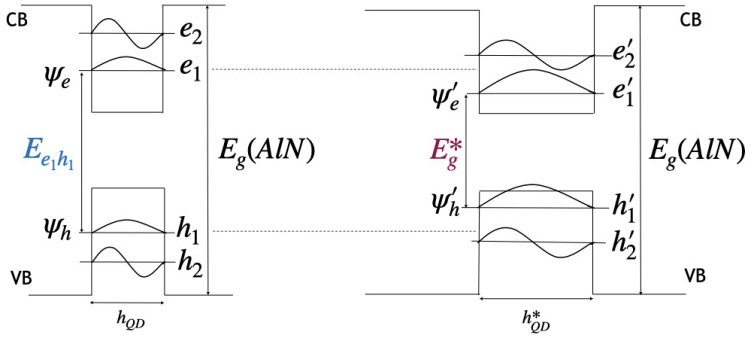

FIGURE 2.13: Dependence of the bandgap on the confinement size in AlN/GaN QDs as a function of the dot height h_{QD}.

2.2.2 Fine structure and excitonic complexes

Exciton in QDs

The existence, in a QD, of an exciton in the strict sense of the term, i.e. a state of two particles bound by Coulomb interaction, depends on the relative extensions of the confinement potential and the bulk Bohr radius. Two limiting cases arise. In the *weak confinement* situation, the dimensions of the QD are larger than the Bohr radius of the exciton in the bulk material. There is then only confinement of the center of mass and the notion of exciton retains its primary meaning. But otherwise, the system is said to be in a *strong confinement* regime and the e-h distance is imposed by the geometry of the dot itself. Strictly speaking, it becomes improper to speak of an exciton in a QD in the strong confinement regime. Nevertheless, the term exciton has been gradually generalized in the spectroscopy of semiconductor QDs for the last 20 years. The concept of exciton is convenient to manipulate when considering the total angular momentum of the e-h pair inside the QD or the fine level structure that results from considering Coulomb interactions. It also makes it possible to manipulate the notion of excitonic complexes when the dot contains more than two charge carriers (charged excitons, biexcitons). In the rest of this thesis, we will favor the term e-h pair but we will occasionally use the excitonic image, especially when we compare our results with published works that use it or when we evoke the electronic fine structure as in the following paragraph.

Fine structure

In QDs, from an electron of spin $|s, s_z\rangle = \left|\frac{1}{2}, \pm\frac{1}{2}\right\rangle$ and a heavy hole of total angular momentum $|j, j_z\rangle = \left|\frac{3}{2}, \pm\frac{3}{2}\right\rangle$, we can form four combinations with the projections of the angular

momentum on the quatification axis : $|-2\rangle$, $|-1\rangle$, $|+1\rangle$ and $|+2\rangle$. The $|\pm1\rangle$ states are optically active (*bright states*) while the $|\pm2\rangle$ states do not couple with the electromagnetic field (*dark states*). At this stage, the four states are degenerate. In the excitonic representation, the e-h exchange interaction (neglected up to now) completely lifts the degeneracy between these four excitons. Since only the result interests us, we will not go into the details of the theory, which is beyond the scope of this thesis. We refer the reader to the Ref.[76] which presents a very didactic approach to this physics, in the context of the study of InAs/GaAs QDs, and from which we have taken Fig.2.14. The lowest lying excitonic state in a QD is a dark state. Even if it does not couple with light, it has been shown that it can still play an important role in the recombination dynamics as evidenced in numerous QDs system (see for instance [77]).

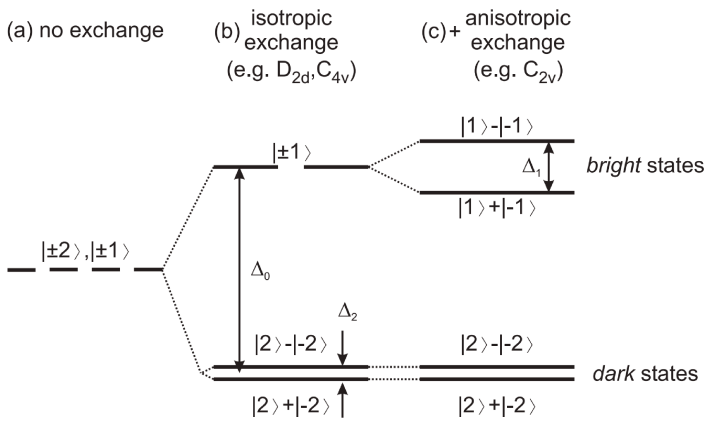

FIGURE 2.14: Fine structure for the lowest energy heavy hole exciton states in QDs: (a) without exchange interaction, (b) with exchange interaction for, e.g., D2d or C4v symmetry, (c) with exchange interaction for, e.g., C2v symmetry. Reprinted from [76].

Excitonic complexes

The 3D confinement in QDs enables to observe complexes of 3 particles ($2e$+$1h$, $1e$+$2h$) or four particles ($2e$+$2h$), or even more, that would not necessarily be observable in the 3D material. On the one hand, because such complexes would have been unstable in absence of the confinement potentiel, on the other hand because the enhanced Coulomb interactions leads to a clear separation of the energies of these different configurations in spectroscopy. Depending on excitation conditions, different excitonic complexes such as biexcitons $|XX\rangle$, charged excitons or excitons $|X\rangle$ can be excited in QDs [78].

3-particle complexes exist in doped samples, the QDs of which permanently host a single charge (electron or hole) in the absence of any optical excitation. The photo injection of an e-h pair into the dot will lead to the formation of a charged exciton $\left|X^{\pm}\right\rangle$.

A bound state of two electron–hole pairs is called a *biexciton*. In the same way that an exciton is analogous to a hydrogen atom, the biexciton is analogous to a dihydrogen molecule H_2. The biexciton energy $E_{XX}$is expressed as

$$E_{XX} = 2E_X - E^b_{XX} \tag{2.17}$$

where E_X and E^b_{XX} are the exciton and the biexciton binding energy, respectively.

The experimental observation of a biexciton requires that the energies E_X and E_{XX} be well separated relative to the resolution of the measurement system. That is to say that the

binding energy E_b is large. This condition is usually met in QDs and the first theoretical and experimental evidences of biexciton states in semiconductor QDs have been observed in 1990s in CuCl [7],CdS and CdSe QDs [79].

We call *QD conventional biexciton*, and denote it $|XX\rangle$, a pair of excitons the ground state of which consists of two electrons and two holes with opposite spin configuration, resulting in a total momentum $M = 0$. This boson can decay into the one of two bright exciton state $|X_B\rangle$ with $M = \pm 1$ by emitting a photon. Thus, the recombination of biexcitons will include a decay cascade of XX $\rightarrow X_B \rightarrow$ empty QDs.

In general, the stable configuration of the biexciton corresponds to a situation where the attractive Coulomb interaction between charges of opposite signs is greater than the repulsion between charges of the same sign. However, this condition is not necessarily fulfilled in a QD since the 4 charges within the structure are forced to "see each other" by the effect of the confinement. This leads to the observation in QDs of biexcitons with positive binding energy (*bonding biexciton*) but also with negative binding energy (*antibonding biexciton*).

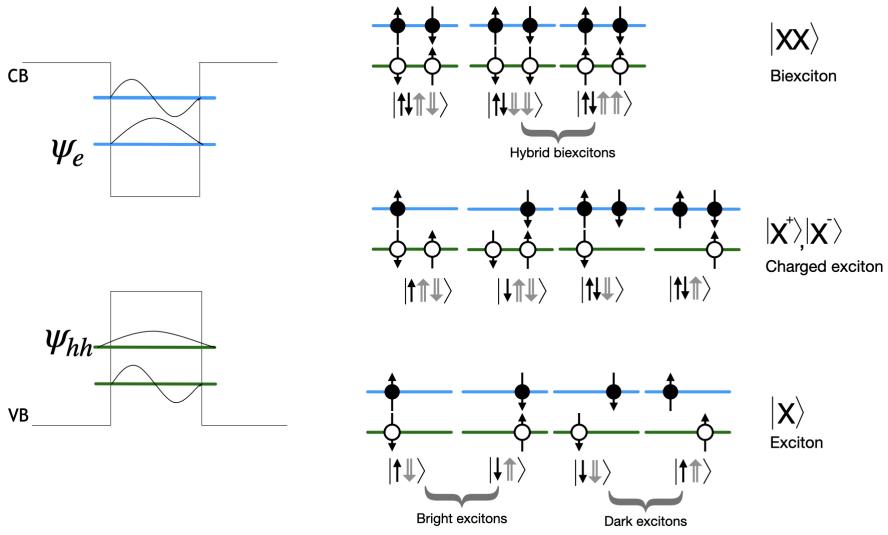

FIGURE 2.15: On the left illustrated the lowest discrete energy levels in the QD for electrons and the holes; on the right there presented possible configuration of s-shell energy level. Filled and empty circles represents electrons and holes respectively and the arrows represents the spin state.

In Fig. 2.15 are summarized the different charge configurations. Similarly, a triexciton consists of three excitons. Higher-order complexes can also exist, but they are typically less stable and more difficult to produce and study.

2.2.3 Auger effect

The Auger recombination is a non-radiative process that has been shown to be very effective in QDs. It is a multi-particle process in which a charge carrier relaxes by giving up its energy to one or more other carriers which then become scattered to higher energy states. It involves the conservation of the total energy of the carriers involved in the process. Auger-like recombination in nanocrystals was first evidenced in the late 1980s in semiconductor-doped glasses [80]. Afterwards, it has been observed in many different nanocrystal systems (see for instance [81]). Fig. 2.16 presents a schematic representation of Auger recombinations involving together 2 (exciton), 3 (trion) and 4 particles (biexciton) in a QD. Top and bottom bands represent the potential wells for electrons and holes, respectively, their discrete energy levels being denoted by horizontal lines. Energy conservation is preserved in each process, as depicted by the correspondence of arrow lengths with energy differences.

Fig. 2.16a provides an illustration of an electron thermalisation process in an Auger recombination of an exciton, showcasing the progression of an electron and a hole as they transition

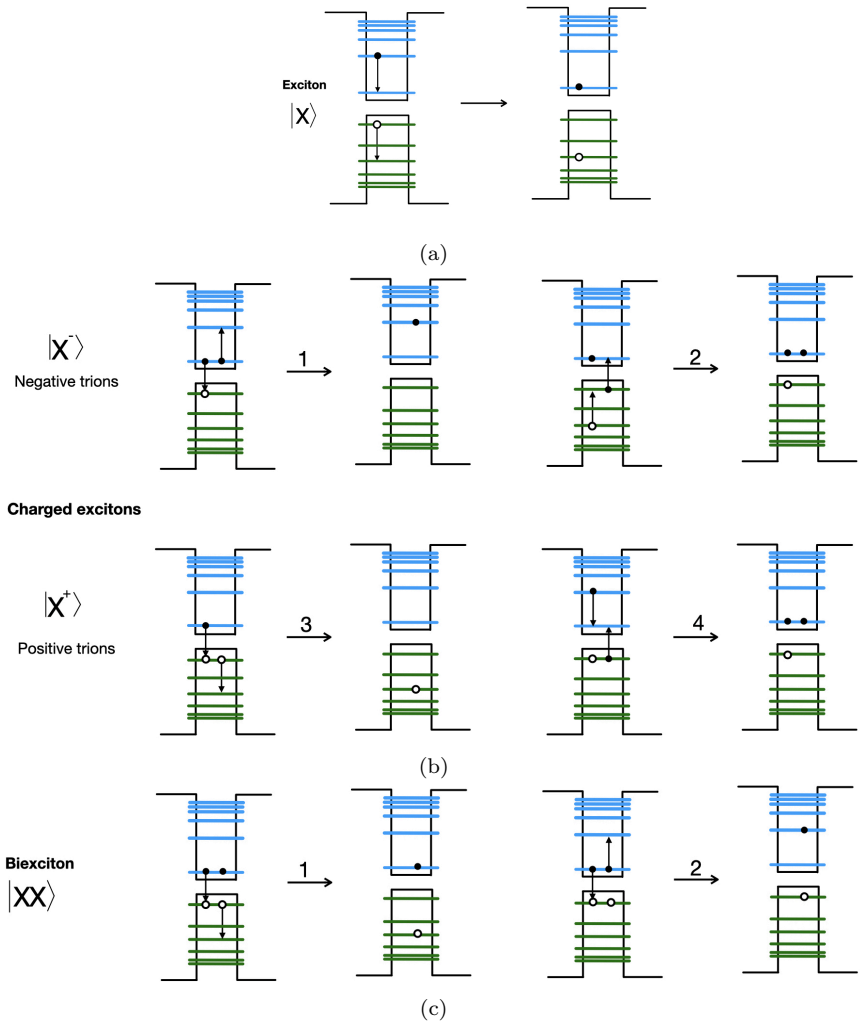

FIGURE 2.16: Illustration of different type of Auger process in QDs for (a) exciton, (b) trions and (c) biexcitons multiexcitonic complexes.

through different energy states. Fig. 2.16b includes illustration for negative (1) and positive (3) trion recombination, where an electron from a high energy state in the CB drops to fill a hole in the VB, transferring its energy to another hole (electron) respectively. In an Auger process within a QD, photon absorption can lead to a dual sequence of events, collectively known as electron-initiated and hole-initiated ionization (see Fig. 2.16b (2) and (4) respectively), also called carrier multiplication. This was attributed to the generation of multiple excitations upon absorption of a single photon and the subsequent Auger recombination of these excitations [82]. In the hole-initiated process (2), the hole in the VB is moving from an excited to the fundamental energy state transfering the released energy to an electron within the CB. Concurrently, in the electron-initiated process (4), an electron in the CB descends from a higher energy state to lower energy state. The energy released from this transition similarly propels another electron within the CB to a higher energy state or ejects it from the QD entirely. Both processes, although initiated differently, end up generating high-energy electrons within the CB. The key thing to remember here is that whether the Auger process is initiated by an electron or a hole, the end result involves the generation of high-energy electrons within the QD.

In the context of a biexciton within a QD, the Auger process also involves two sequential events, namely the hole-initiated and the electron-initiated ionizations (Fig. 2.16c (1) and (2) respectively). These two processes, although initiated differently, end up accelerating the remaining e-h pairs within the QD. It is important to note that in the context of a biexciton, whether the Auger process is initiated by an electron or a hole, the net result is the rapid

recombination of one exciton, and the ejection or excitation of an electron or hole from the remaining exciton, thereby transforming the biexciton into an exciton, or possibly to a high-energy free carrier. Typically these processes are fast compared to the radiative recombination in the QDs. It lies in a ps time scale [82].

In GaN/AlN QDs, non-radiative recombination is expected to be significantly suppressed. This is because the wider bandgap of the AlN barrier helps to confine carriers within the GaN QDs, reducing the probability that they will interact with defects or impurities in the barrier or substrate, which are common pathways for non-radiative recombination. In addition, the large energy difference between the QD and barrier states makes Auger processes where the carrier is expelled less likely.

2.3 GaN/AlN QDs

2.3.1 Morphology of GaN/AlN QDs

GaN/AlN QDs are part of what are called *self-assembled QDs*. Starting from the 2D growth of GaN on AlN, the large mismatch in lattice parameters between the two materials leads, after some critical thickness (typically 2 atomic monolayers), to a transition towards a 3D growth (Stranski-Krastanov growth). It results in the formation of nano-islands, the dots, on a 2D layer,the wetting layer (WL). More detail on this growth technique and the geometry of QDs will be given in 4 which is devoted to the presentation of the samples. Previous studies have shown that GaN/AlN QDs present a shape truncated hexagonal pyramid [83] as evidenced by the HREM picture in Fig.2.17 and schematically shown in Fig. 2.18.

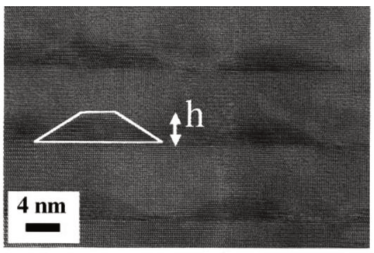

FIGURE 2.17: HREM picture showing a cross section of stacked layers of GaN/AlN QDs. Reprinted from [83].

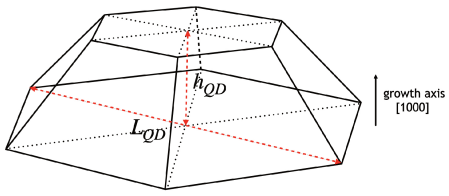

FIGURE 2.18: Schematic view of GaN hexagonal island.

2.3.2 Quantum confined Stark effect (QCSE)

Actually, Fig.2.13 is not correct because it lacks a fundamental and intrinsic feature of wurtzite GaN/AlN quantum nanostructures: the presence of a strong built-in electric field along the $[000\bar{1}]$ direction. This electric field is caused by the difference in both spontaneous and piezoelectric polarizations between the GaN and AlN materials [51]. Although it is not always easy to distinguish between the two components, it has been proven that the fields involved can reach very high values, of the order of several MV/cm [83, 55, 54]. The presence of such a static electric field gives rise to the quantum confined Stark effect (QCSE) [84]. The

band profiles become tilted (see Fig. 2.19)which has a significant impact on the energies of the carriers as well as on their envelope functions. Considering the expression of the transition

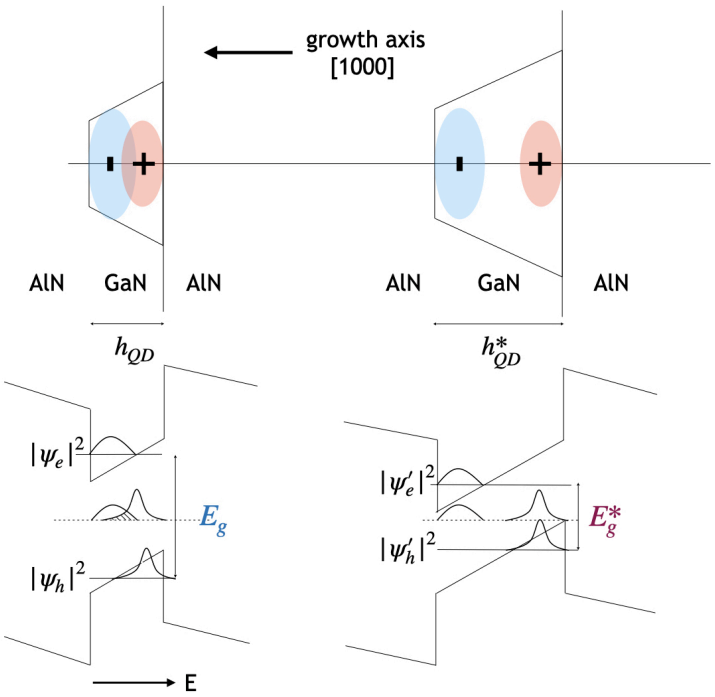

FIGURE 2.19: Illustration of the presence of the electric field in the band profile of a GaN QD, with the electron(hole) probability density distribution $|\psi_e|^2(|\psi_h|^2)$ and overlap the wave functions of the electron and the hole in QDs.

energy of an e-h pair in the fundamental state of a triangular QW as depicted in Fig. 2.19, takes the following form:

$$E_{PL}^{QD} = E_g + e_1 + h_1 - eFh_{QD} \tag{2.18}$$

where e_1 and h_1 are the electron and hole confinement energies, e i the electronic charge, h_{QD} is the QD height and F is the value of the built-in electric field. Compared to the equation 2.16, the transition energy is reduced by the quantity eFh_{QD}. As both e_1 and h_1 vary as h_{QD}^{-2} (see equation 2.15), it exists two limiting situations depending on the QD height:

- for small height QDs, eFh_{QD} is negligible compared to the confinement energies e_1 et h_1, $E_g < E_{e_1h_1}$ and the optical properties remain close to the properties of a square potential well.
- on the contrary, for large height QDs, eFh_{QD} becomes comparable or even larger than the confinement energies e_1 et h_1, $E_{e_1h_1}$ evolves linearly with h_{QD} and ,as a consequence, E_{PL}^{QD} can be smaller than the GaN bandgap.

As far as the wave functions are concerned, the electric field spatially separates the carriers of opposite charges along the axis z, the electron begin pushed at the apex of the pyramid while the hole becomes located at its base [85, 86]. It strongly reduces the overlap integral between their respective envelope functions. This results in a decrease in the recombination probability and therefore an increase of the radiative lifetime when the dot height is increased.

We will see later how the QCSE dramatically influences the optical properties of GaN/AlN QDs.

So far, we have only discussed the intrinsic electronic states of GaN/AlN QDs inherited from the band structure of the perfect crystal and conditioned by the size and shape of the dots

as well as their stress state. It is also necessary to take into account extrinsic states whose existence is due to any deviation from the ideal structure and which are generally undesirable. These defect states are due to a variety of factors such as impurities, dislocations, vacancies (missing atoms), or interstitials (extra atoms) and are essentially localized within the bandgap of the material.

They are generally difficult to identify because they indirectly alter the intrinsic optical properties of the systems studied. They can act as non-radiative recombination centers leading to decreased efficiency in light-emitting applications. Alternatively, they can also act as radiative recombination centers whose optical signature is superimposed on the intrinsic spectrum. Free charges, localized on defects in the vicinity of QDs influence by Coulomb interaction the electronic properties of these (spectral diffusion) [87].

2.3.3 Optical properties

Introduction

GaN-based nanostructures have been studied and used in industry mainly for their near-UV light emission properties. The mastery of the various ternary alloys based on GaN, InN and AlN associated with the presence of the QCSE ensures these systems a high tunability in wavelength, which allows them, in theory, to cover the entire spectrum from IR up to UV. The main disadvantage of these compounds is their poor crystalline quality which results from the absence of a cheap, lattice-matched parameter substrate. The synthesized materials present high densities of threading dislocations which are non-radiative defects and deteriorate the optical properties. Thus, in large GaN QWs for instance, the extension of the radiative lifetime by the QCSE makes the carriers vulnerable to non-radiative processes as soon as the samples are no longer at cryogenic temperature.

However, these disadvantages are circumvented in GaN/AlN QDs. Indeed, the confinement of carriers in the three directions of space prevents them from being captured on dislocations. Moreover, the band discontinuities between GaN and AlN generate very high potential wells which keep the carriers trapped in the dots up to room temperature. These systems have radiative efficiencies close to 1.

Continuous wave spectroscopy

GaN/AlN QDs are usually investigated by PL spectroscopy, possibly with time resolution. Carriers are photoinjected non-resonantly in the the WL or in the dot excited states. Carrier injection in the AlN barrier at 6.2 eV should require a source with a wavelength around 200 nm. To our knowledge, there is currently no published work about time-resolved pump-probe experiments on GaN/AlN QDs. Studying QD ensemble (typical density 10^{10} cm^{-2}) with standard PL set-up (spot size 100 µm in diameter) result in the photoexcitation of 10^6 dots. Fluctuations in size and shape from one dot to another lead to a dispersion of the transition energies. Thus, PL spectra are broad bands, with a significant inhomogeneous broadening of several hundreds of meV. The presence of the internal electric field leading to a redshift of the optical transitions energies, dots can emit below the GaN bandgap and the PL covers the visible and near UV spectrum depending on their height [41, 42, 57, 83] as seen in Fig.2.20.

Micro-PL experiments, on the contrary, make it possible to observe the emission of single dots whose emission lines are a few meV broad (Fig.2.21). The position and broadening of these lines are affected by spectral diffusion caused by charge trapping in the vicinity of the dots [87]. Studying single GaN/AlN QD enabled to evidence the fine structure of excitons and the role of dark states in the intra-dot relaxation [88, 45], the size dependence of the biexciton binding energy [89, 90], single photon emission [44, 46, 45].

Even if it has a particular interest because it is the one from which the photon emission takes place, the electronic states are not limited to the ground state of the e-h pair in the dot. At higher energies, a number of excited states are accessible to electrons and holes depending on the dot size. They extend to the two-dimensional density of state of the wetting layer. Fig.2.22 shows the structure of the electronic states of a single QD measured by excitation of

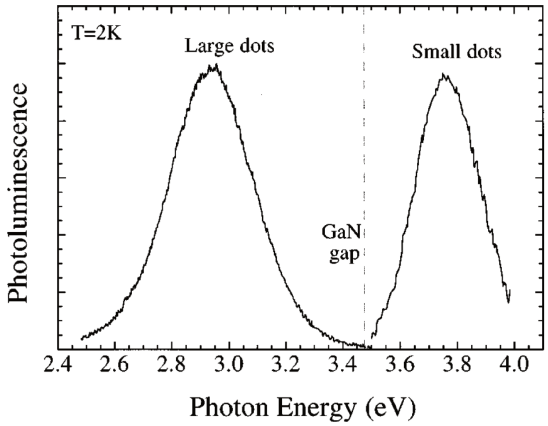

FIGURE 2.20: PL spectra of GaN/AlN QDs at $T = 2$ K for different dot heights. Reprinted from Ref.[83].

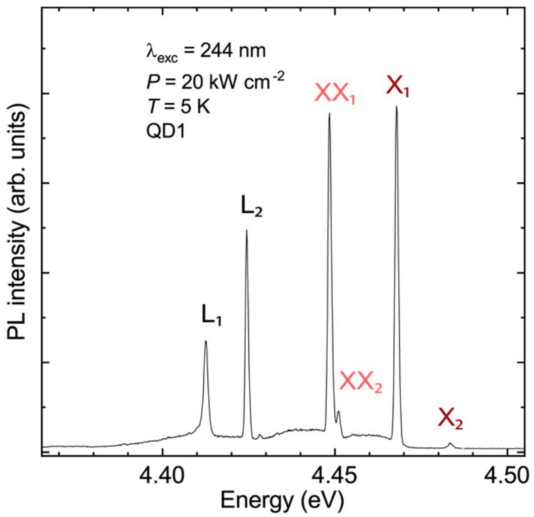

FIGURE 2.21: Micro-PL spectrum of a high-quality single GaN/AlN QD at at $T = 5$ K. Reprinted from Ref.[45].

photoluminescence (PLE) by Holmes et al. Series of discrete lines, starting ~ 50 meV above the energy of the fundamental state, correspond to the excited states of the QD. We can also see a background increasing monotonically with energy usually identified as a transition from the 0D states of the QDs to the 2D states of the WL.

Earlier investigations into biexcitons in GaN/AlN QDs have demonstrated that the sign of their binding energy, E^b_{XX}, which originates from the exchange interaction, varies based on the QD height and lateral extension [89, 92, 90]. For a given dot height, the spatial separation between electrons and holes by the QCSE along the growth axis remains constant and so does the attractive interaction within the exciton. Decreasing the lateral extension reinforces the repulsive electron-electron and hole-hole interactions, which has the effect of decreasing the biexciton binding energy and the confinement energy as well. It results in a negative slope of E^b_{XX} versus the exciton energy (part b) of figure 6.26. On the contrary, E^b_{XX} decreases with the dot height: the repulsive interaction between carriers of the same sign remains now approximately constant, however, increasing the dot height reduces the overlap of the envelope functions of electrons and holes along the polar axis, thus decreasing the attractive Coulomb interaction between carriers of opposite charges in favor of the repulsive component. As a consequence, the evolution of E^b_{XX} with the exciton energy displays a positive slope (see part a) of figure 6.26).

Moreover, an exceptional feature of GaN/AlN QDs, that has been theoretically predicted and

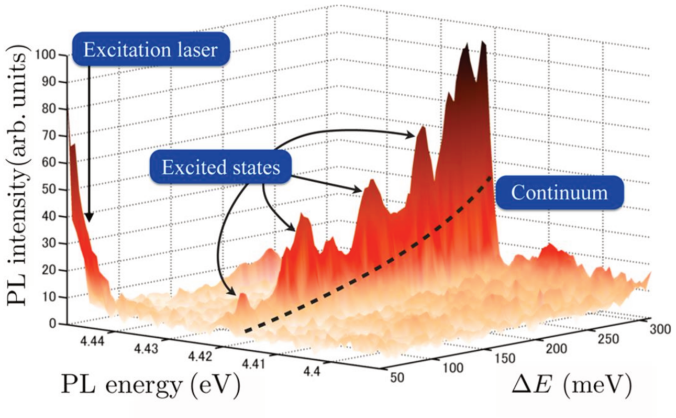

FIGURE 2.22: PLE spectrum of a single GaN/AlN QD emitting at 4.42 eV. It exhibits several well resolved lines associated with excited state. the dotted line is the continuum of states associated to the 0D-2D transition (reprinted from Ref.[91]).

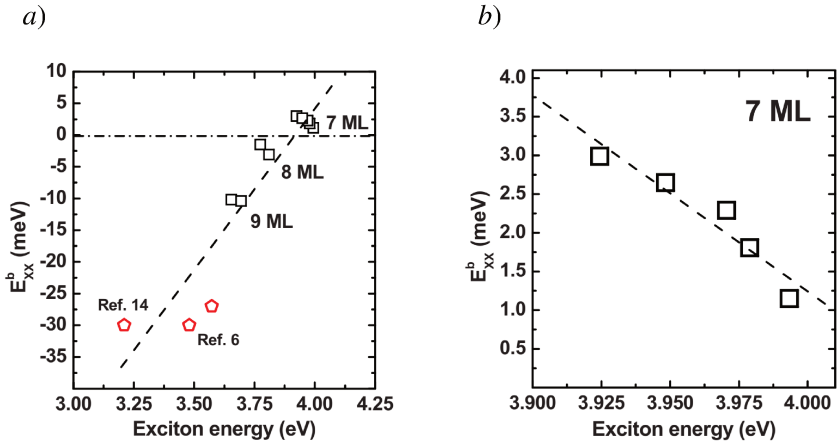

FIGURE 2.23: *a*) Dependence of E^b_{XX} on the exciton emission energy for the QDs of different vertical sizes. *b*) Dependence of E^b_{XX} on the exciton emission energy for the QDs with the same vertical size (7 ML). From Ref.[89].

experimentally observed [90], is the presence of hybrid biexcitons. A biexciton configuration where two electrons with opposite spins and pair of holes with parallel spins give rise to a total angular momentum of $M = \pm 3$. With regard to the selection rules ($\Delta M = 1$), the possible recombination of hybrid biexcitons is possible to the dark exciton state (with $s = \pm 2$). The phonon induced spin-flip from the dark to the bright exciton state is involved into the futher recombination of the carriers to empty the QDs population. In this case the non-classical decay cascade of hybrid (unconventional) biexcitons is present: XX $\rightarrow X_D \rightarrow X_B \rightarrow$ empty QDs. The $X_D \rightarrow X_B$ transition is a phonon-assisted spin-flip process [93].

Dynamics

The QCSE also influences the recombination dynamics of e-h pairs in GaN/AlN QDs. By spatially separating the electron and the hole along the growth axis, it decreases the overlap of their wave functions (see 2.19) and, consecutively, their probability to recombine radiatively. This results in a huge variation in radiative lifetime that spans several orders of magnitude

from the picosecond to the microsecond range depending with dot height [85, 56, 57, 54]. The strong impact of the QCSE on the recombination dynamics has been studied by several authors by means of time-resolved photoluminescence (TRPL) [94, 54].The variation of carrier lifetime with emission energy qualitatively follows a universal law whose main parameter is the amplitude of the internal electric field. However, from a quantitative point of view, the experimental values are scattered as compared to this law which turns out to be only an average. This is because many parameters in the structure of the studied samples influence the dynamics in a way that is not yet well understood.

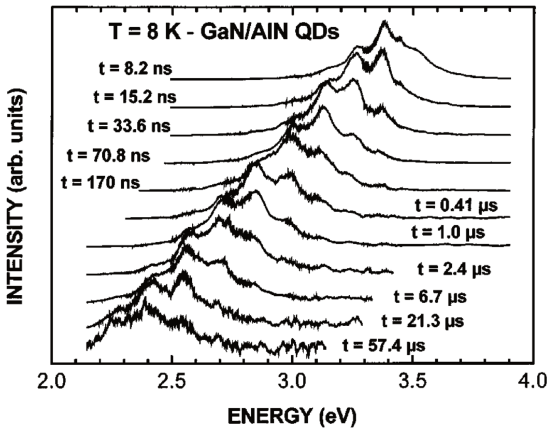

FIGURE 2.24: Evolution of the PL spectrum of GaN/AlN QDs at $T = 8$ K for different delays following the excitation pulse.. Reprinted from Ref.[95].

Another striking feature originates from the possibility of screening the internal electric field in large height dots : the dynamics strongly depends on the number of photocreated carriers and, under strong optical injection, the transition energies as well as the lifetimes can be violently modified resulting in a time-dependent redshift (Fig.2.24) a complex non-exponential dynamics [54, 95]. However, a recent work has shown that even in the low excitation regime, the PL dynamics could be biexponential [96]. A possible explanation would involve the fine structure of excitons. Anyway, these results are proof that the e-h pairs dynamics in nitride quantum dots is still not totally understood and its study remains a topic of interest.

Chapter 3

GaN/AlN QDs samples

In this chapter, we focus on the growth and structural characterization of GaN/AlN QDs samples.

In section 3.1, we discuss the growth of GaN/AlN QDs through self-assembly, which is a common technique used to form QDs. We also discuss the control parameters used to optimize the growth of QDs, including the substrate temperature, the growth rate, and the composition of the material.

In section 3.2 we present the details of the studied samples. Specifically, we investigate two different samples: 1-plane GaN/AlN QDs and 10-plane GaN/AlN QDs. These samples have different QD size distributions and number of stacked layers, which have significant effects on their electronic and optical properties.

3.1 Growth

Progress in synthesis methods of nitride QDs has been relatively slow compared to other materials due to the complexity of the growth process and the properties of the materials.

III-Nitrides are most commonly grown by metal–organic vapour phase epitaxy (MOVPE) [97]. It involves a complex set of growth parameters that must be carefully controlled to achieve the desired QD properties. Additionally, nitrides are grown by heteroepitaxy on typical substrates like sapphire (Al_2O_3), SiC or Si, all of them exhibiting a lattice mismatch resulting in issues with crystal quality.

Despite these challenges, significant progress has been made in recent years in the synthesis of nitride QDs. [98, 99, 31]. For example, researchers have developed new protocols to improve growth techniques such as molecular beam epitaxy (MBE) and hydride vapor phase epitaxy (HVPE), which offer a high control over the growth process and the properties of the resulting QDs. Additionally, advances in nanofabrication techniques have enabled the integration of nitride QDs into devices for applications in optoelectronics and quantum computing.

3.1.1 Self-assembled QDs

Self-assembled quantum dots (QDs) are a type of semiconductor nanostructure that forms spontaneously during epitaxial growth when the material undergoes a lattice mismatch or strain. The self-assembled growth of GaN QDs in the Stranski-Krastanov (SK) growth mode, see Fig. 3.1, is considered to be the most adaptable method of fabrication due to its simplicity, scalability, and the precise control it offers over the size and shape of the QDs, which is critical for their performance in optoelectronic applications.

Atoms of QD material (GaN) are deposited layer by layer on a two-dimensional wetting layer (WL) on a thick buffer layer of AlN. Due to the mismatch in lattice parameters between GaN and AlN, the compressive strain increases with the thickness of the deposited GaN layer.

Material deposited onto the WL naturally arranges itself into a three-dimensional pattern, driven by the minimization of strain and surface energy. The most favorable process to achieve is a 2D-3D transition that results in formation of islands (QDs) [48]. The shape and

size of the QDs are determined by the interplay between the strain induced by the the lattice mismatch between the film and the substrate and the surface energy of the material.

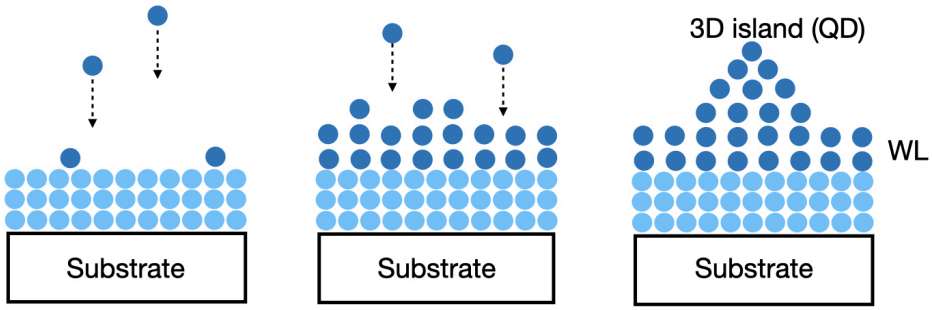

FIGURE 3.1: Stranski-Krastanov growth mode of self-assemble quantum dots.

3.1.2 Control parameters

The self-assembled growth of GaN QDs allows for the precise control of their size and shape, which can be tuned to achieve specific optical and electronic properties. For example, the size of the QDs can be adjusted to achieve a specific emission wavelength or to optimize their performance as single-photon emitters or quantum dot lasers.

At the beginning of my PhD, I had a one-month internship in the Ecole Polytechnique Federale de Lausanne in the laboratory that has expertise in the growth of III-Nitride nanomaterials. As an intern, I was able to follow the growth process of nitride QDs. This experience gave me the advantage of a deeper understanding of the structural properties which turn out to be valuable during my further experimental work on the samples. I have observed different control techniques for the growth process and challenges that appear during this process.

Since there are different requests for a wide range of applications described in the previous chapter, it is required to control the size, density, and uniformity of the QDs during the growth process. A lot of studies have been made to determine the best control parameters of the self-assembled growth process in SK growth mode. Some of the most important control parameters include substrate temperature (T_{sub}), growth rate (V_g), precursor flux ratio, surface treatment, and growth time (t_g).

The substrate temperature during growth is a critical parameter that affects the surface diffusion and desorption rates of the deposited atoms. A higher substrate temperature promotes faster diffusion and desorption, which can lead to larger and more uniform QDs [100]. The growth rate affects their size and density. A higher V_g can result in smaller and more densely packed QDs, while a lower V_g can lead to larger QDs with smaller density [101]. The precursor flux ratio, such as the nitrogen to gallium flux ratio can affect the growth rate and thus the size and shape of the QDs. Surface treatment is another important parameter that affects the nucleation and growth of the QDs [102]. Surface treatments such as annealing can promote a smooth and uniform surface for QD growth [103]. The growth time can affect the final size and density of the QDs. Longer t_g can produce larger QDs with higher density, while a shorter t_g can lead to smaller, more widely spaced QDs.

With careful optimization of these parameters, it is possible to fabricate QDs with specific electronic and optical properties that are well-suited for a wide range of optoelectronic applications. The growth process of GaN/AlN QDs is not the main subject of my thesis but as a short summary, I would like to provide the following "recipe" for the sample fabrication. It can be divided into the following stages (see Fig. 3.2):

1. On top of an AlN buffer layer grown by MOVPE, a thick AlN layer is deposited by MBE using amonia as nitrogen source.

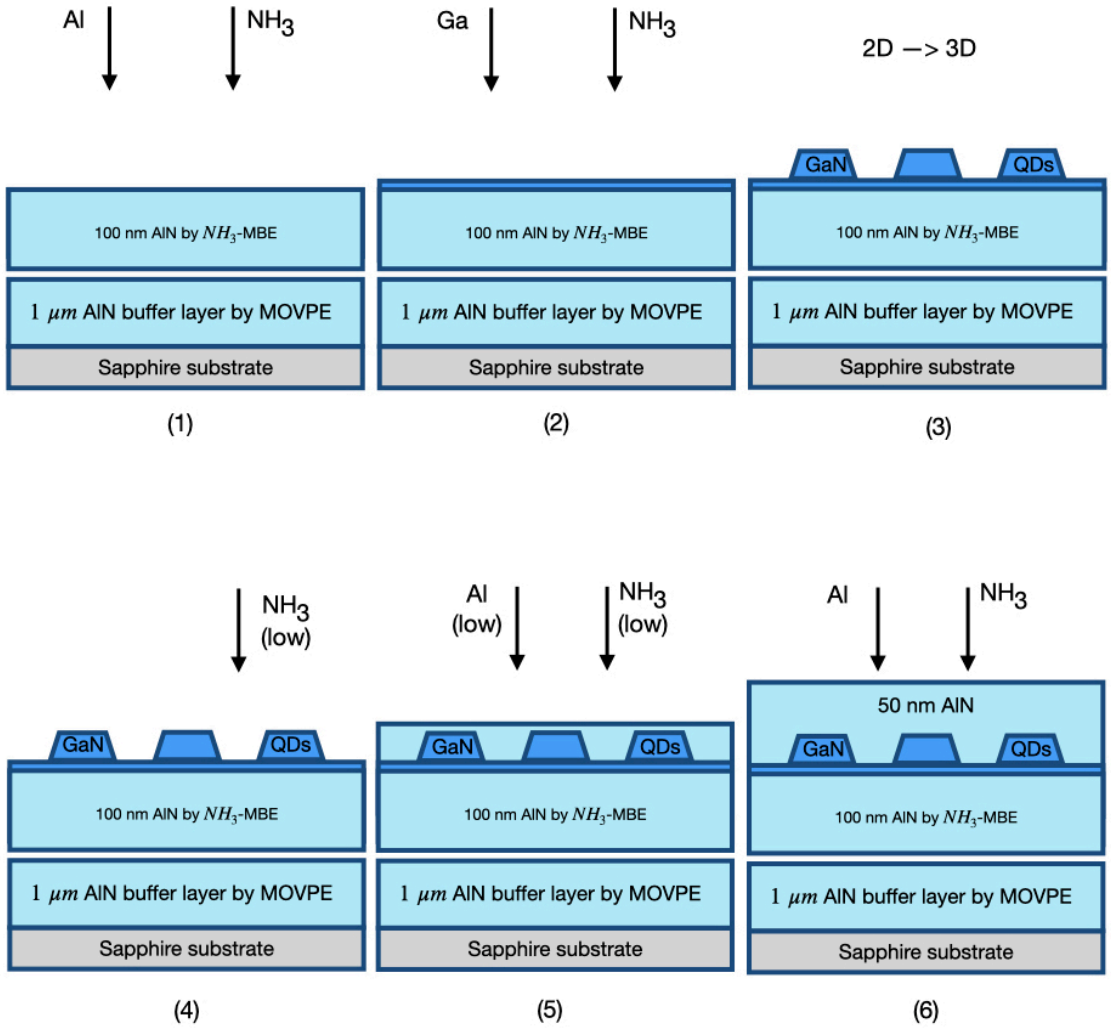

FIGURE 3.2: Growth procedure used for the formation of GaN QDs on AlN (sapphire substrate). The numbers correspond to different steps mentioned in the text.

2. After forming a relaxed AlN layer, T_{sub} is decreased and a GaN layer is applied on the top.
3. After reaching the critical thickness of GaN [104] to allow the formation of QDs in Stranski-Krastanow growth mode, the deposition is interrupted and 2D-3D transition occurs. It means the interruption of the amonia flux. The real time formation of quantum dots is monitored by reflection high-energy electron diffraction (RHEED) technique.
4. In order to not destroy the QDs, the ammonia flux is reduced and under such conditions, GaN QDs ripen (controlling the evaporating T_{sub} can modify the islands size and density).
5. A low flux of Al is added to the chamber and the cap layer of AlN starts growing.
6. When the QDs are fully covered with the AlN layer the further deposition of cap layer can be done under high flow regime.

During the MBE growth of GaN/AlN QDs, the main control parameters were the growth temperature, the V/III flux ratio and the ammonia flow [105] that controls the QDs size, density. Additionally, evaporation process has been added. It is often employed as a post-growth process. However, during the reconstruction of the surface, defects can be induced in the QD structure. This is because the high temperatures required for the evaporation process can cause the surface of the substrate to undergo a reconstruction, resulting in the formation of atomic steps and terraces. These steps and terraces can act as preferential sites for the nucleation of new material, which can lead to the formation of defects such as threading dislocations and stacking faults. In addition, the presence of these defects can also affect the morphology and optical properties of the quantum dots, which can have negative impacts on their performance in optoelectronic devices.

3.2 Studied samples

Our samples were made by Dr. Sebastian Tamariz in a team-leading by Prof. Nicolas Grandjean at the Federal Institute of Technology in Lausanne. It is worth noticing that the NH_3-MBE growth method was developed more recently than the MOVPE growth of nitride QDs and it is a different approach. In order to carry out optical transmission measurements, the two samples were deposited on a sapphire substrate polished on both sides.

3.2.1 1 plane GaN/AlN QDs

The sample consists of a single plane of GaN/AlN QDs (see Fig. 3.4) deposited on a *c*-plane sapphire substrate by ammonia-source MBE in the SK growth mode. The template is composed of a commercial 1 μm thick AlN buffer layer (DOWA Electronics) grown by MOVPE and a 100 nm thick AlN layer deposited by MBE. The GaN QDs were grown under constant low ammonia flux (NH_3 beam equivalent pressure of $3 \cdot 10^{-7}$ Torr) at 750°C and 4.5 monolayer (ML) GaN nominal coverage. After forming the QDs the Ga flux was stopped and the dots were capped with a 55 nm thick AlN barrier.

To understand the tendency of the GaN/AlN QD morphology, atomic force microscopy (AFM) scans of similar nitride self-assembled QDs has been performed (see Fig. 3.5). This magnification of a dot and dislocation has been taken for the layer a GaN QDs without capping layer. The growth method used here is the same as described above. Most of the QDs are aligned on the top of terraces related to the substrate. The dot density under such growth conditions is in the 10^{10}-10^{11} cm^{-2} range [49].

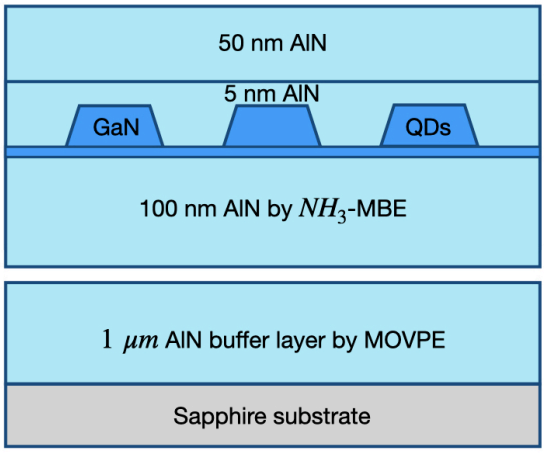

FIGURE 3.4: Schematic transverse view of 1 plane GaN/AlN QDs sample.

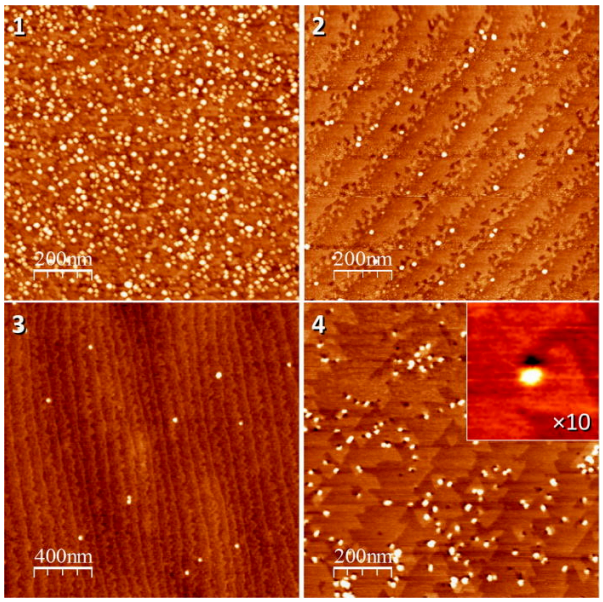

FIGURE 3.5: AFM images 1 to 3 originate from QD growth on AlN single crystal substrates, whereas image 4 originates from growth on an AlN/sapphire template, reprinted from Ref.[49].

3.2.2 10 planes GaN/AlN QDs

Fig. 3.6 presents a schematic view of the 10-planes GaN/AlN QD sample. The growth conditions of each layer are the same as described in the previous section except for the deposition temperature (DT). The main feature of this sample is the gradient of QDs size within the sample. The temperature is one of the main control parameter during the growth process. A temperature gradient, from 750°C to 770°C, was maintained from one side of the sample to the other one. Under such conditions 10 planes of GaN/AlN QDs were deposited. It leads to the formation a gradient of QDs size distribution.

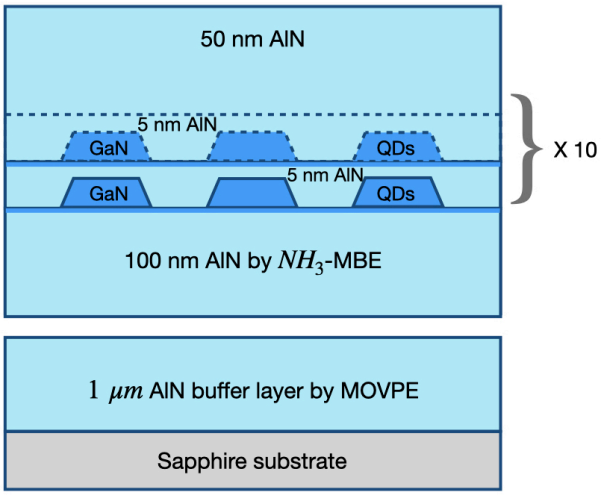

FIGURE 3.6: Schematic view of 10 planes GaN/AlN QDs sample.

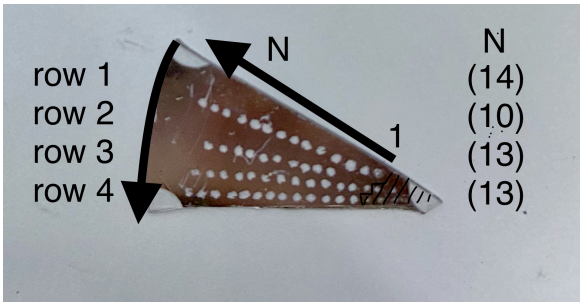

FIGURE 3.7: Photography of the 10-planes GaN/AlN QDs sample with a metallic mask deposited on top it.

To be consistent in our measurements and to control the position during the experiment, a metallic mask was deposited on the top of the sample surface (see Fig. 3.7). We only worked with the first row of points, because it has the widest range of PL emission energy and thus covers a large variation of QDs size from one side of the sample to another one. Each position has its own mark ri_n, where i - number of the row and n - the number of the aperture on the mask.

Chapter 4

Experimental set-ups

Chapter 4 offers a comprehensive presentation of the experimental techniques used in this research work to explore the optical properties of MBE grown GaN/AlN QDs.

First, section 4.1 presents the continuous-wave photoluminescence, a basic bu powerful method to investigate both intrinsic and extrinsic electronic states in semiconductors.

The principle and experimental set-up of time-resolved photoluminescence (TRPL) is exhibited in section 4.2. This technique, with a resolution of the order of a few picoseconds, probes the lifetime of e-h pairs after their thermalization and capture in QDs. Cryogenic techniques are also introduced in this section.

Moving forward, section 4.3 outlines the non-degenerate and degenerate pump-probe experiment set-up, which were used for the investigation of carrier dynamics within the GaN/AlN QDs. A significant part of the discussion is dedicated to the description of the excitation laser source, including the Ti:sapphire oscillator and regenerative amplifier. The probe generation technique, which used an optical parametric amplifier (OPA) and second harmonic generation, is also discussed. Additionally, the pump generation technique is described.

Finally, section 4.4 revisits photoluminescence in a broader context, providing additional insights into how this powerful tool can be used to control the study of quantum dots.

Overall, this chapter presents a detailed description of the experimental setup used for investigating the optical properties of GaN/ALN QDs. The techniques and equipment described in this chapter were critical to the successful completion of this study.

4.1 Continuous-wave photoluminescence (CW PL)

An easy but very powerful way to get information about electronic states in condensed matter systems is to perform continuous-wave photoluminescence (PL) [106]. This kind of experiment provides valuable information about the band structure and electronic properties of materials, including their defect structures and impurity states. In particular, excitation spectra of the PL (PLE) can reveal information about the density of states (DOS) of a material, which is a critical parameter that determines its electronic and optical properties. In PL experiment the studied sample is excited by a light source whose photon energy is larger than the bandgap energy. Photon absorption gives rise to the creation of a population of electron-hole pairs. The created carriers will relax by emitting phonons, in a time short compared to the radiative recombination time (the characteristic time for electron-phonon interaction is typically 100 femtoseconds while recombination times are rather on the nanosecond scale). It results that the electron-hole population reaches a thermodynamic quasi-equilibrium before recombining and that the photoluminescence observed experimentally comes statistically from the deepest available energy levels. The experimental setup is shown in Fig.4.1.

In addition to the basic PL experiment described above *photoluminescence excitation* (PLE) experiments can also be performed. It involve monitoring the resulting PL emission while varying continuously the excitation energy of the light source. It requires a tunable light source that consists in the resent case, in the emission from a broad-band lamp going through a monochromator. It is well suited to study the absorption and density of state (DOS) of a

material as a function of excitation energy [107]. PLE can be performed in either transmission or reflection geometry, and the latter has the advantage of being able to study thin films and surfaces. In the setup we used, the collected light is dispersed in a spectrometer and detected by a cooled charge transfer device (CCD) camera.

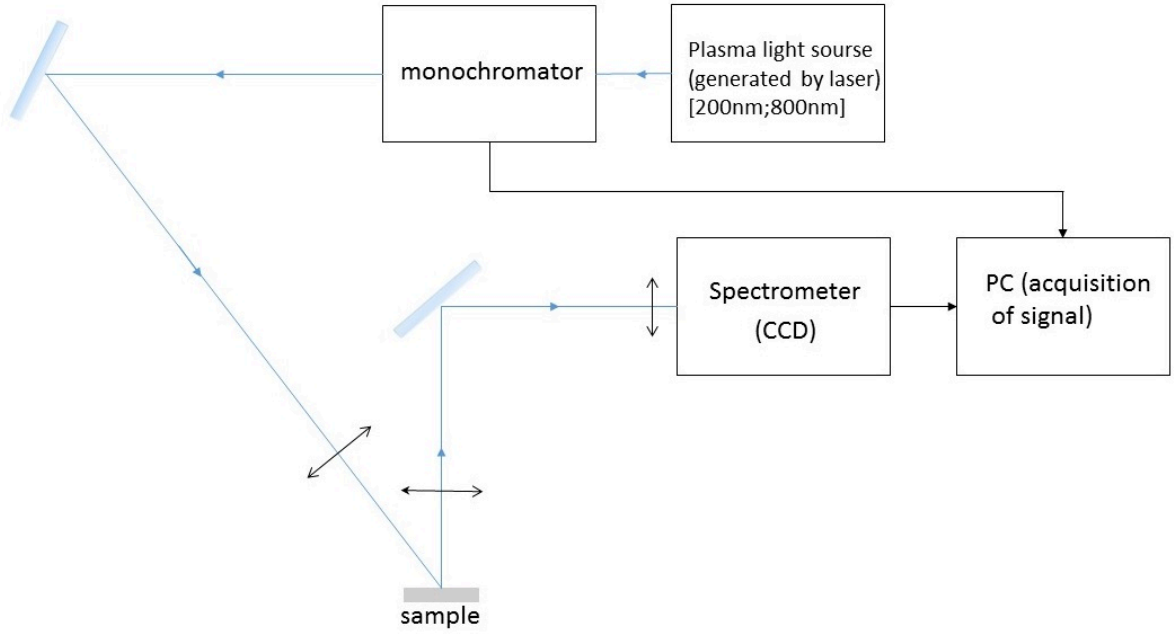

FIGURE 4.1: Optical scheme of CW PL experiment.

4.2 Time-resolved photoluminescence

To obtain information on the recombination dynamics in QD ensembles, time-resolved photoluminescence (TRPL) spectroscopy is required. TRPL spectroscopy is a pulsed excitation technique that allows us to study the transient population of e-h pairs on a radiative state by measuring the temporal evolution of the spontaneous emission. Any fluctuations in the time resolution can affect the accuracy of the measurements. Additionally, the technique is sensitive to environmental factors such as temperature and ambient light, which need to be carefully controlled during the experiment.

The experimental effective lifetime of the PL signal τ_{PL} depends on both the radiative and non-radiative lifetime, τ_R and τ_{NR} respectively, according to the following expression:

$$\frac{1}{\tau_{PL}} = \frac{1}{\tau_R} + \frac{1}{\tau_{NR}}. \tag{4.1}$$

Non-radiative processes are often thermally enhanced and can depopulate the excited state without emitting photons. These processes can arise from interactions with extrinsic defects.

The optical scheme of the TRPL experimental setup is presented in Fig. 4.2. We use the TRPL set up with two different laser sources. Both are Ytterbium Fiber lasers produced by AMPLITUDE company. We used a TANGERINE laser for the 1-plane GaN/AlN QDs sample and a SATSUMA HP for the 10 planes sample. These sources share the same following parameters: 1030 nm wavelength, 40 MHz repetition rate, 270 fs pulse duration. The only difference is the average power of emitted light that is 20 W for TANGERINE laser while it is limited to 10 W for SATSUMA HP.

Two beta baryum borate (BBO) crystals provide a fourth (257 nm) harmonic output of the fundamental (1030 nm) wavelength. The collected luminescence is dispersed by a spectrometer with a 25 cm-focal length and a 150 grooves/mm grating before being recorded by a streak camera.

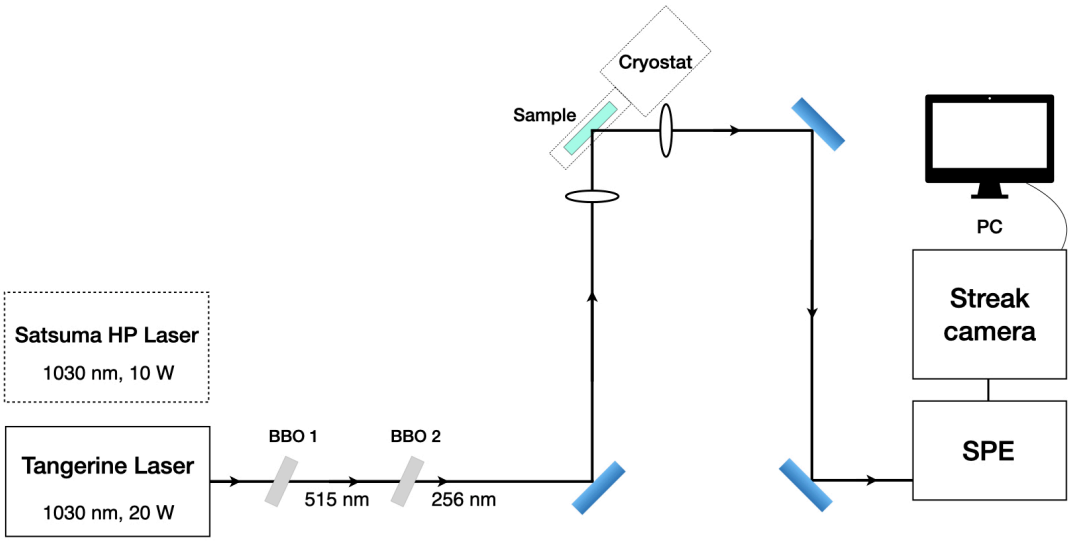

FIGURE 4.2: Optical scheme of the time-resolved photoluminescence experimental setup.

4.2.1 Streak Camera

The carrier recombination in QDs occur in a ps-ns time range. To achieve such temporal resolution, we used an ultrahigh-speed detector: a streak camera HAMAMATSU S 20. The following is a description of the general principle of its operation.

After being dispersed through the spectrometer, the PL signal collected from the sample is focused on the photocathode of the Streak tube (see Fig. 4.3). The photons are converted into electrons, the number of which is proportional to the intensity of the incident light. Then, the carriers pass between two sweep electrodes that apply a transverse electric field that is triggered by the pulsed laser and the intensity of which is proportional to the arrival time of the photons on the photocathode. It results, in a vertical distribution of electrons, from the top to the bottom of the micro-channel plate (MCP), that reflects the time profile of the PL signal. The MCP multiplies electrons before they hit a phosphor screen that convert them back into light. The spectral range of the Streak camera is 200-850 nm with a time resolution of 10 ps on the shortest timescale.

4.2.2 Cryogeny

To distinguish between radiative and non-radiative phenomena, a temperature-dependent TRPL experiment can be performed. By varying the temperature, we can determine the relative contribution of radiative and non-radiative processes to the PL decay. To perform temperature-dependent TRPL experiments, a cryostat is typically used. In this study, a cryostat produced by OXFORD company was utilized. The sample is mounted on a holder made of copper in a vacuum chamber. The holder is in contact with a cold finger that is cooled by the circulation of Helium. The vacuum is achieved by means of a turbomolecular pump, which allows for a clean environment for the sample to be studied. The cryostat also contains

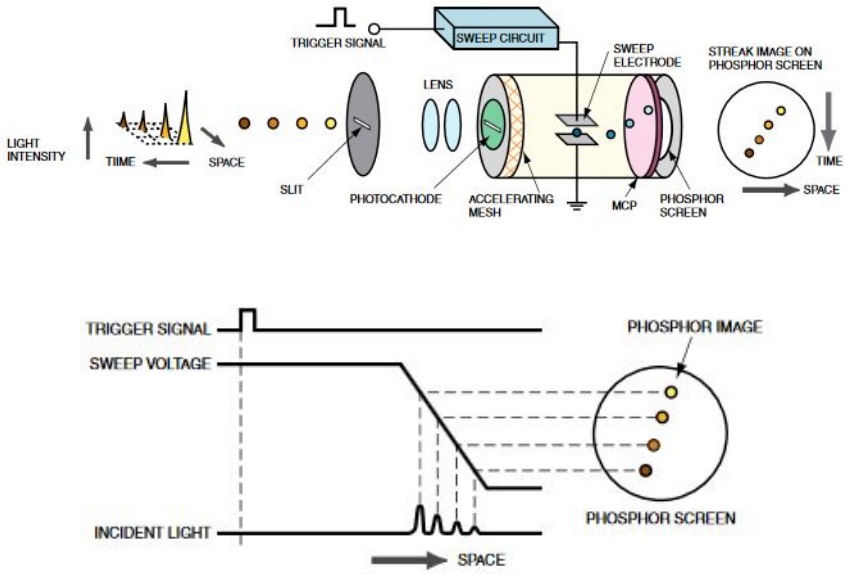

FIGURE 4.3: Operating principle of a Streak Camera.

a heating resistor inside the chamber, which enables the sample temperature to be tuned continuously up to room temperature. By cooling the sample to very low temperatures (down to 5 K), thermal broadening can be avoided and the non-radiative recombination mechanisms can be diminished, allowing for the radiative recombination lifetime to be measured accurately.

4.3 Non-degenerate pump-probe experiment

The mechanism underlying carrier relaxation phenomena in QDs is not yet completely understood. It directly impacts the performance of devices that incorporate these materials. In particular, the efficiency of the relaxation cascade - the process by which carriers lose energy and return before being trapped in QDs - is critical to the performance of QD-based devices. Recent advancements in experimental techniques have provided new insights into the relaxation process. One such technique is the non-degenerate pump-probe experiment, which is a time-resolved spectroscopic method used to investigate the relaxation mechanism of the carriers in QDs.

The non-degenerate pump-probe experiment has been used to investigate the relaxation of carriers in various types of QDs, such as CuCl [8], CdSe [108, 109] and (In,Ga)As/GaAs [110, 111], and has provided valuable insights into the relaxation mechanism. For instance, the experiment has been used to study the relaxation of carriers in InAs QDs, and it has been found that the relaxation time depends on the size and shape of the QDs, as well as the temperature of the sample [112]. Moreover, the experiment has been used to study the dynamics of carrier relaxation in CdSe QDs and has revealed the existence of two relaxation pathways in these materials [113].

This experiment requires two laser pulses: the first one, called the "pump" pulse, excites the sample by promoting electrons from the VB towards the CB. The second pulse, called the "probe" pulse, is passing through the sample, probing its transmission. In other words, it tests the changes, induced by the pump, in the optical properties of the sample. The delay between the probe and pump pulses can be adjusted by means of an optical delay line. Thus, the transmission spectrum of the probe, detected at various pump-probe delays, makes it possible to get an information about the relaxation of the system. In such experiments the temporal resolution is limited by the duration of the light pulses, so extremely short pulses are required.

This section describes the functionality of the elements in the non-degenerate pump-probe experiment setup, its optical scheme is presented in Fig. 4.4.

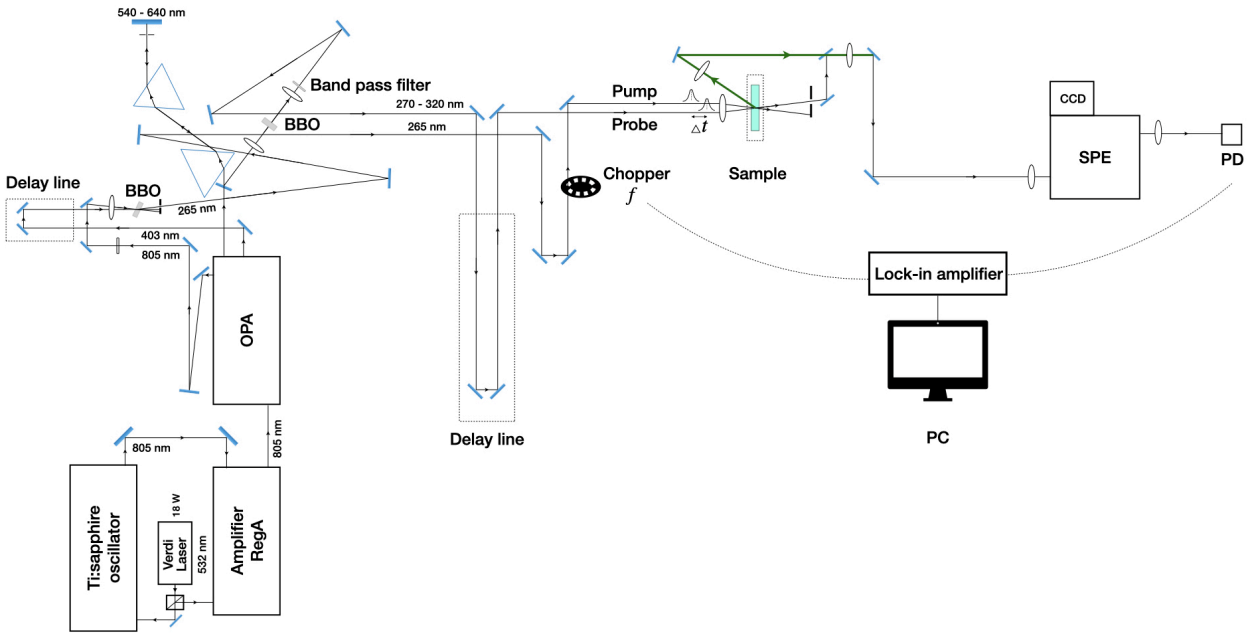

FIGURE 4.4: Optical scheme of a non-degenerate pump-probe experimental setup.

4.3.1 Excitation laser source

To study relaxation phenomena in semiconductor QDs, an ultra-short laser source producing fs pulses is needed. Studying UV GaN/AlN QDs present several challenges associated with excitation laser sources. It includes the limited availability of laser sources, laser power (high laser power levels are necessary to achieve high signal-to-noise ratios in spectroscopy experiments), stability (deep UV lasers can be susceptible to instability due to changes in the laser cavity's temperature or alignment), photodegradation of samples (deep UV range can cause photodegradation of samples, which can affect the observed properties), and sensitivity to ambient conditions (fluctuations of temperature and humidity can affect the laser output power and stability, leading to variations in experimental results). Moreover, many conventional optical materials and detectors are not suitable for use in the deep UV region due to their reduced transparency and sensitivity. Therefore, special optics and detectors designed for UV applications are often required, increasing the complexity and cost of the experiment.

To generate femtosecond pulses with tunable wavelength, we use a chain that consists in four components: an oscillator pumped by a CW laser, that produces ultrashort pulses, a regenerative amplifier that increases the pulse power by several orders of magnitude, an optical parametric amplifier and second harmonic generation (SHG) to adjust the wavelength according to the needs of our study.

Laser source

As a laser source we used a VERDI G solid-state diode-pumped laser produced by the COHERENT company. It generates a monochromatic laser beam at 532 nm with an output power of 18 W. Such a laser is frequently used for pumping Ti:Sapphire lasers and amplifiers. The optical scheme of the laser is shown in Fig. 4.5. The gain medium is a Neodymium Vanadate (Nd:YVO4) crystal placed in an optical cavity. A crystal with a strong absorption at 809 nm wavelength and an emission at 1064 nm is pumped with two laser diodes. Passing through the lithium triborate doubling crystal (LBO) the fundamental wavelength is frequency doubled to 532 nm. This laser is equipped with a series of temperature controllers (on the Vanadate, the power supply diodes, the LBO and the base) that ensure its steady operation. The VERDI

laser generates a full average power of 18 W: 3 W are used to pump the oscillator, while the remaining 15 W are used to pump the amplifier.

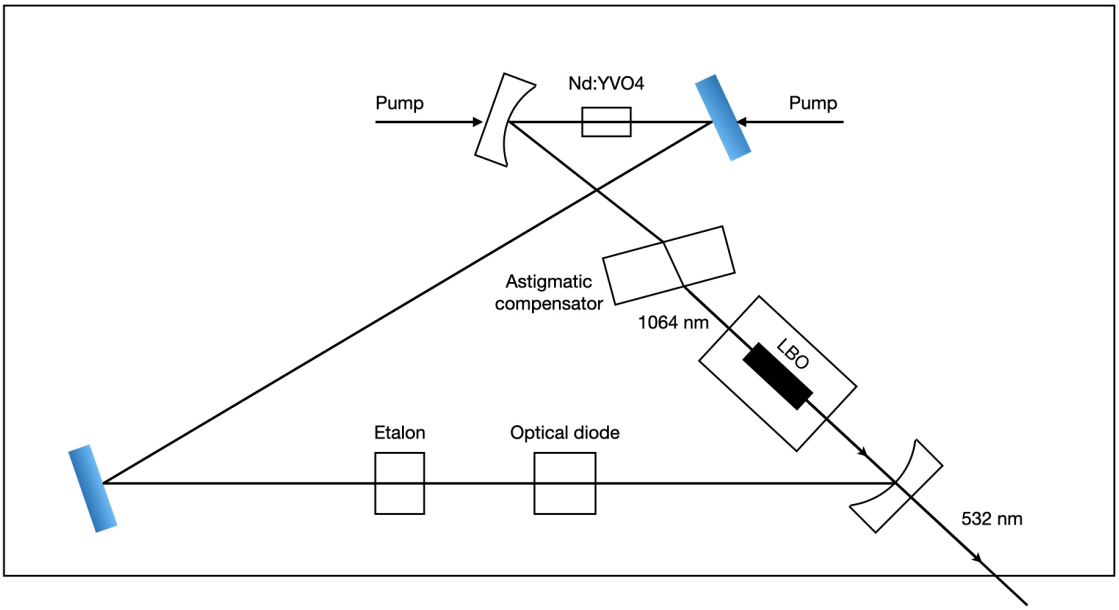

FIGURE 4.5: VERDI laser optical scheme

Ti:sapphire oscillator

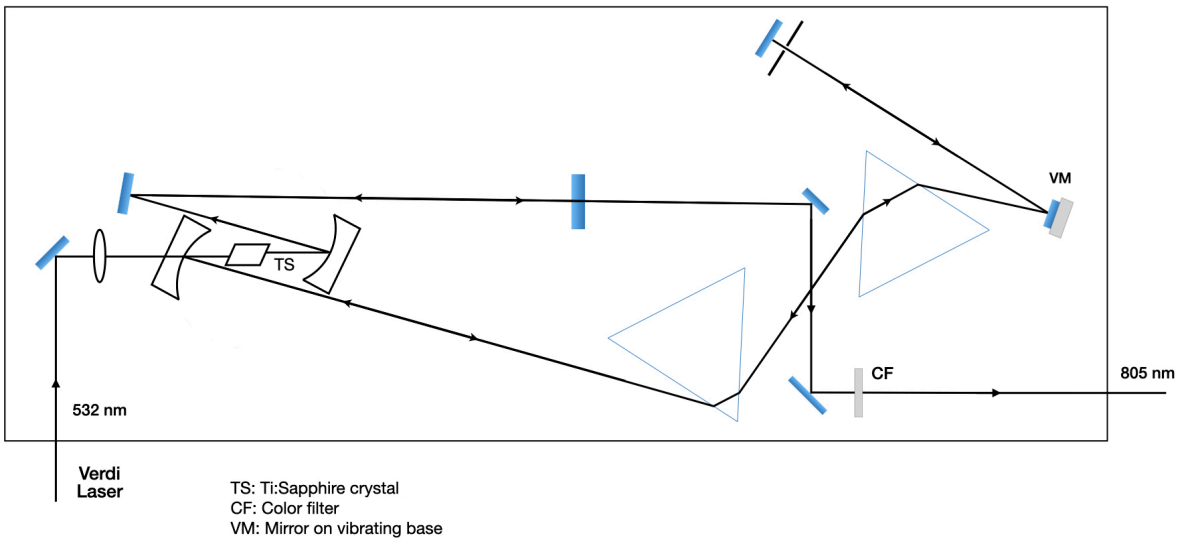

FIGURE 4.6: Optical scheme of Ti:Sapphire oscillator.

To generate ultrashort light pulses in the range from 670 to 1100 nm, Ti:sapphire oscillator are commonly used. The optical scheme of our home made oscillator is schematically presented in Fig. 4.6. It consists of z-like optical resonator and a prism compressor. The gain medium is a sapphire crystal (Al_2O_3) doped with Ti^{3+} ions. It is optically pumped with a frequency-doubled Nd:YVO4 lasers described above. Inside the cavity, the gain medium produces longitudinal modes in wide spectral range (from 750 to 850 nm). These modes are standing waves of the cavity and their wavelength λ satisfy $L = n\frac{\lambda}{2}$, where L is the cavity length and n is an integer. If the individual phases of the different modes present some random fluctuations,

the modes interfere destructively: the output intensity fluctuates randomly around a nearly constant mean value. Fortunately, pulse generation is achieved if each mode maintain a well defined phase relationship with all the other modes. Such a mode-locking condition can be obtained thanks to the optical Kerr-effect inside the gain medium: the refractive index is dependent on the field intensity. The optical losses are larger when the modes are not locked. Hence, the pulsed operation is preferable. However, it requires an external intervention to make the continuous-wave operation unstable in order to switch to the pulsed regime. In our case, we use a mirror on a vibrating base (VM). The time modulation of optical resonator parameters introduces the phase relationship between the longitudinal modes thus giving rise to constructive interference and triggering the transition to pulse regime. A pair of prisms compensates the positive dispersion of the group velocity for all other elements in the cavity. A slit, located inside the compressor, enables us to tune the central wavelength of pulses. The cavity length is 3 m and produces pulses of 200 fs duration with a repetition rate of 80 MHz.

Regenerative amplifier

We use a commercial CW-pumped optical regenerative amplifier REGA 9000 produced from the textsccoherent VERDI G. A General optical layout of it is shown in Fig. 4.7. It is designed to amplify the output pulses of Ti:sapphire oscillator to a power ranging from a few nanojoules up to a few microjoules per pulse. The amplification proceeds in two stages: the generation of "giant" pulses and the synchronization with pulses generated by the Ti:sapphire oscillator described in section 4.3.1.

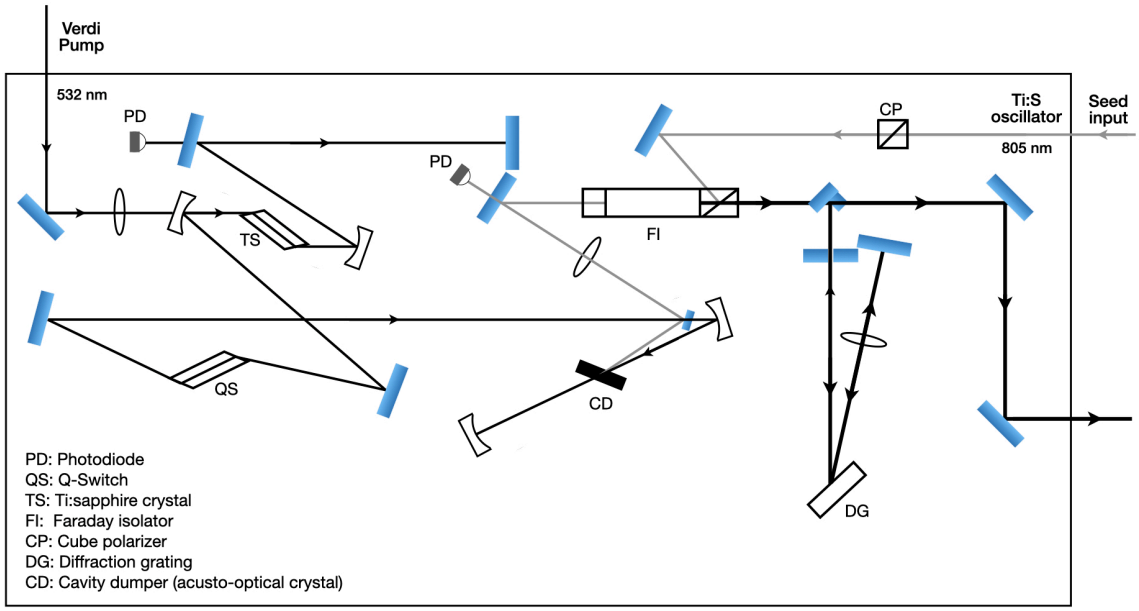

FIGURE 4.7: Optical layout of REGA 9000 amplifier.

Basically, REGA 9000 is the same as the Ti:sapphire oscillator, but inside the optical resonator is placed a Q-switch cell working in two regimes: high and low resonator losses. The gain medium is pumped with the VERDI laser and the Q-switch in the high losses regime prevents the lasing by storing the light until the gain medium is saturated. When the stored energy is maximum an external reference pulse (seed input on Fig. 4.7) from the Ti:sapphire oscillator is injected in the cavity for synchronization. At this point, the Q-switch reduces the losses in the cavity and the high energy pulses we created in the resonator by stimulated emission. The amplified pulses are then ejected from the cavity at a lower repetition rate than the oscillator pulses.

The oscillator works at a repetition rate of 80 MHz, this frequency corresponds to a pulse separation time of 12.5 ns. Pump-probe experiments require a lower repetition rate. It can be

controlled in the amplifier by an acousto-optical switch (fused silica crystal). High-frequency acoustic signal applied to an acousto-optical Bragg cell modulates the material density and thus the refractive index of the medium. It acts like an optical grating on the laser beam, so it allows to eject a single pulse from the pulse train in the resonator by diffraction. The modulation frequency of the acoustic signal defines the repetition rate of the amplifier. As in any optical setup, a dispersion of the group velocity increases the duration of these pulses. At the amplifier output is located a compressor to compensate the pulse elongation. The output of RegA 9000 has the following characteristic: an energy of 5 microjoules per pulse, a duration of less than 200 fs and a repetition rate of 200 kHz.

Probe generation: optical parametric amplifier (OPA)+second harmonic generation

In a non-degenerate pump-probe experiment two color femtosecond pulses are required. We used an optical parametric amplifier OPA 9400 produced by company coherent to adjust the wavelength of the pulses according to the needs of the study. Its optical scheme is presented in Fig. 4.8. The beam from RegA amplifier is split into two parts. The first beam (25%) is focused on a sapphire crystal which generates a white continuum by self-phase modulation. The second one (75%) is focused on a BBO crystal (SHG) and generate 400 nm pulses. The optical parametric amplifier in a second BBO crystal makes the pump beam (400 nm) weaker and amplifies some specific frequency bands inside the continuum spectrum. The signal (highest frequency) the wavelength of which is computed between 9000 and 700 nm.The idler which wavelength is in the 940-1040 nm range.

The pulse is amplified through two successive passes in the crystal. The signal wavelength is controlled by changing the phase-matching angle of the BBO crystal and the delays of the two amplification passes via two corresponding delay lines.

A pair of prisms (Fig. 4.4) compensates the positive dispersion of the group-velocity to bring the pulse duration back to less then 200 fs. Finally, the UV range (270-320 nm) is obtained thanks to a second harmonic generation process in one additional BBO crystal.

The use of OPA can be challenging due to its sensitivity to alignment and phase-matching conditions. Maintaining stable operation requires careful alignment of the optical components and precise control of the temperature and pressure of the nonlinear crystals. Furthermore, the efficiency of OPAs can be quite low, especially at extreme wavelengths, leading to a significant reduction in the available probe power.

Pump generation

In our non-degenerate pump-probe experiment, the pump wavelength remains fixed and it is the third harmonic of the infrared pulses coming from the regenerative amplifier. The pump pulses are generated by performing a sum-frequency process between a fraction of the 800 nm beam from RegA and its second harmonic taken from the OPA. Changing the phase-matching conditions manually for frequency conversion (doubling, tripling) is a tedious and time-consuming process. It also requires precise control over the angle and temperature of the nonlinear crystal. Any fluctuations can result in significant changes in the output power and wavelength. Moreover, frequency conversion processes are typically not very efficient, leading to substantial power losses. To adjust the pump wavelength, we focused the RegA 9000 signal of 403 nm from the OPA and the fundamental beam of 805 nm on the BBO crystal (see Fig. 4.4). The phase-matching conditions were fulfilled and a pump of 266 nm wavelength was generated.

4.3.2 Detection

The resulting signal is very weak and difficult to detect. To remove the diffusion of the pump from the final result, the probe beam is spectrally cleaned up by passing it through a spectrometer after transmission through the sample. Afterwords the transmitted intensity is detected by a photodiode. In the field of experimental physics to improve the signal-to-noise ratio of weak signals lock-in amplification technique is commonly used. It involves modulating

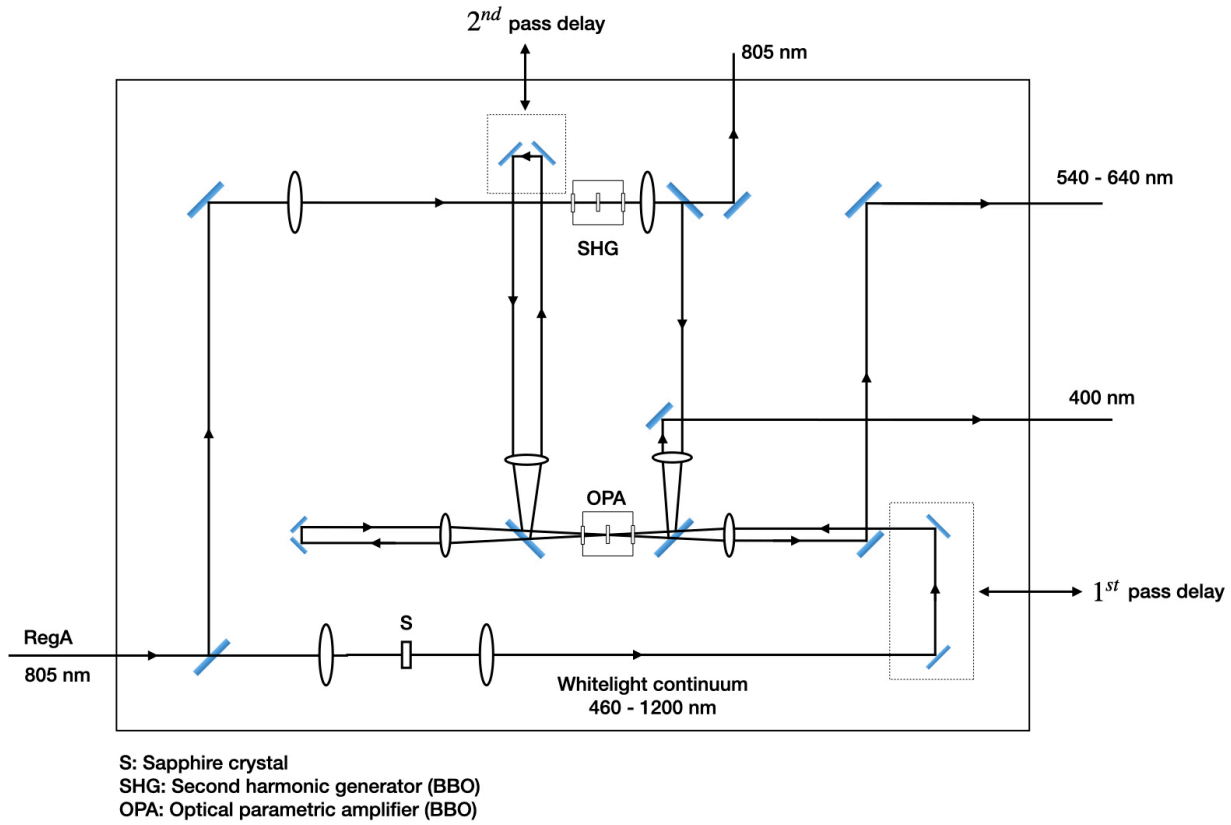

FIGURE 4.8: Optical scheme of optical parametric amplifier.

the amplitude of a signal at a known frequency and then measuring the output signal at the same frequency using a lock-in amplifier. By doing so, the pump beam is modulated at a frequency of 415 Hz using a mechanical chopper. The pump-probe delay is varied using a delay line. The differential transmission signal is measured by taking the ratio of the transmission signals with and without the pump beam, as shown in Equation 4.2.

$$\Delta T(t) = \frac{T_{with\,pump}(t) - T_{without\,pump}}{T_{without\,pump}}. \tag{4.2}$$

This signal is then amplified by the lock-in amplifier at the same frequency as the pump modulation frequency, effectively isolating the signal of interest from any background noise not modulated at this frequency. The result is an improved signal-to-noise ratio, which enables more accurate measurements of the relaxation dynamics of the carriers in the sample.

4.4 Degenerate pump-probe experiment

On the basis of the previous experimental setup, we are also able to perform a degenerate pump-probe experiment. It differs from the non-degenerate one in terms of the combination of colors of the pump and probe pulses used. The latter one requires two colors of pulses: high energy excitation pulse and we followed the carrier relaxation with the tunable lower energy pulse until its radiative recombination state. On the contrary, In a degenerate experiment, the pump and probe pulses have the same energy, which allows for the investigation of the depopulation dynamics of the probed level. Fig. 4.9 displays an optical scheme of the degenerate pump-probe experiment. As an excitation source, we have used the frequency-doubled OPA output. By means of a beam splitter, we separate the pump and the probe lines to insure the required geometry of the excitation/detection in the experiment.

In pump-probe experiments, spatial and temporal overlap of the pump and probe beams are critical for accurate measurements. Achieving perfect overlap is challenging due to the sensitivity of the experiment to alignment. Any misalignment or timing fluctuations can lead to a reduction in the signal-to-noise ratio and potential misinterpretation of the results. Moreover, maintaining stable overlap over long experimental runs is difficult due to drifts in the optical setup.

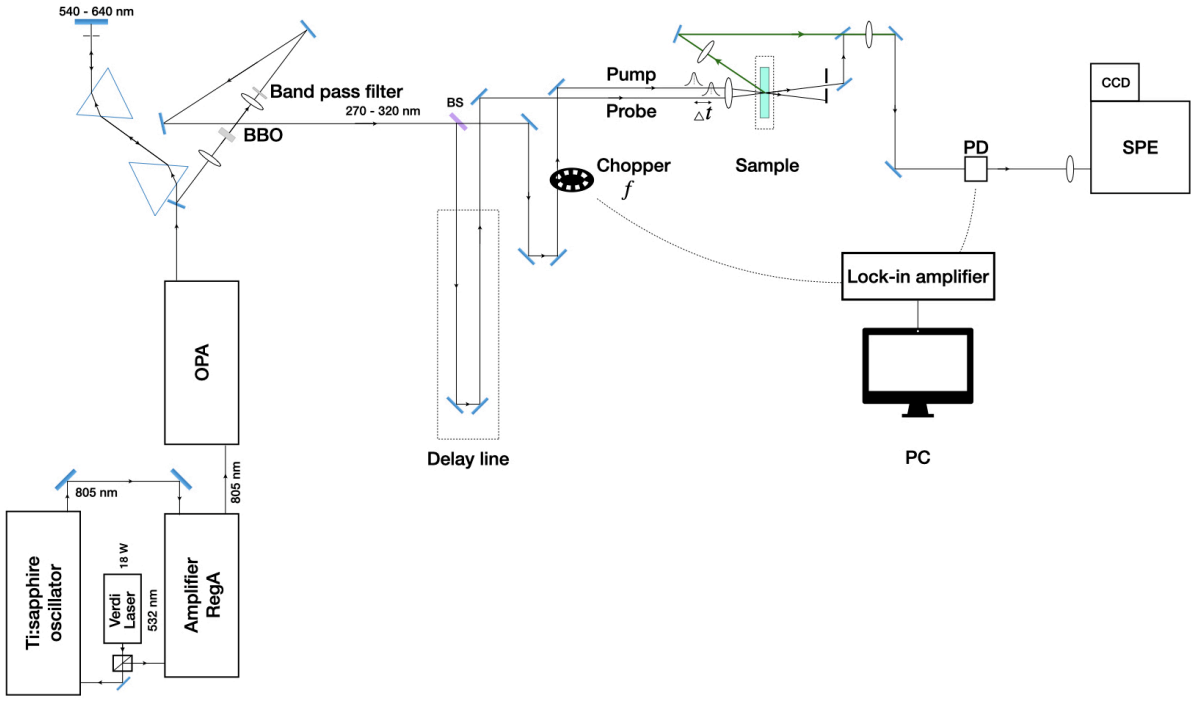

FIGURE 4.9: Optical scheme of degenerate pump-probe experimental setup.

4.5 Photoluminescence

In both degenerate and non-degenerate pump-probe experimental setups, the PL spectrum is systematically measured.. This is a significant advantage since it provides a valuable understanding of the optical properties and spatial distribution of QDs on the sample. It is achieved by using the pump beam as the sole excitation source, and then detecting the emitted radiation using a spectrometer and a cooled CCD camera. The green beam path in Fig. 4.4, 4.9 represents this setup. One critical advantage of photoluminescence spectroscopy in pump-probe experiments is the ability to determine the spatial distribution of QDs on the sample. By measuring the intensity of the emitted PL at various positions on the sample, a "map" of the QD distribution can be constructed. Furthermore, PL spectroscopy provides an indirect method of estimating the size of the QDs. This is because the spectral characteristics of the emitted PL are affected by the QD size distribution. Specifically, larger QDs emit light at longer wavelengths, while smaller QDs emit photons at shorter wavelengths. So, by following the spectral characteristics of the PL, during pump-probe experiments, we can investigate specific QD ensembles.

Chapter 5

Recombination dynamics in ensembles of GaN/AlN QDs :

This chapter is devoted to the study by TRPL of the recombination dynamics of e-h pairs in GaN/AlN QD ensembles which have the particularity of emitting at a photon energy higher than the bandgap of GaN. On the two concerned samples, we make a detailed study of the lifetimes as a function of the emission energy.

Results related to the 1-plane sample are exposed in section 5.1. They are interpreted with both analytical and numerical models. Although the QCSE rules the lifetime vs. energy dependence over a 3 eV range, the deviation from this trend is explained by taking into account the effect of the lateral extension of the dots on the confinement energy.

Then, in section 5.2, the study of the sample with 10-plane of dots, which also presents a gradient of height of the dots, makes it possible to highlight the existence of two different morphologies of QDs which have different average lifetimes for a given photon energy, but which are modulated according to the height of dots by the QCSE.

5.1 Influence of the quantum confined Stark effect and of the lateral confinement on the recombination dynamics

5.1.1 Experimental conditions

The dynamics is studied by TRPL at low temperature ($T = 10$ K), using the experimental setup detailed in Chapter 4. The excitation consists in the fourth harmonic of a pulsed ytterbium laser (Tangerine) emitting at 257 nm (4.82 eV) with a pulse duration of 270 fs and a repetition rate of 50 kHz. The excitation energy is below the AlN bandgap. The sample, described in detail in Chapter 3, has a wetting layer with a thickness between 2 and 3 monolayers (MLs). As observed in a similar sample, the steady-state photoluminescence (PL) of the WL occurs at energies distributed between 4.5 and 5.0 eV. We therefore assume that e-h pairs are mostly created in the wetting layer even if the excited discrete states of the QDs likely play a role in the photogeneration process.

The low repetition rate also ensured that the dots relax to their ground state between two successive excitation pulses. The energy per pulse is 0.2 nJ and the diameter of the excitation spot focused on the sample was about 0.4 mm, giving an incident photon flux of $2 \cdot 10^{11}$ photons $\cdot$ cm^{-2}.

5.1.2 TRPL in low excitation regime at 10 K

Figures 5.1(a) and 5.1(b) present the streak camera image of the QD emission recorded at low temperature ($T = 10$ K) and the corresponding time-integrated PL spectrum, respectively. The PL spectrum consists of a broad band modulated by fringes due to Fabry-Perot

interference occurring within the epilayer stack (see Appendix A). Because of the small size of the GaN QDs, the quantum confinement increases the recombination energy far above the GaN bandgap. A comparison with a sample where the emission of GaN QDs with different heights was investigated [89] indicates that the thickness of those QDs would range between 6 and 8 MLs (1.6 - 2.1 nm, since 1 ML of GaN along the c-axis is equal to ~ 0.26 nm [63]). Figure 5.2 presents normalized PL spectra recorded at different delay times after excitation. The emission, which is centered around 3.8 eV and has a full width at half maximum (FWHM) of ∼500 meV, exhibits a continuous redshift as a function of time.

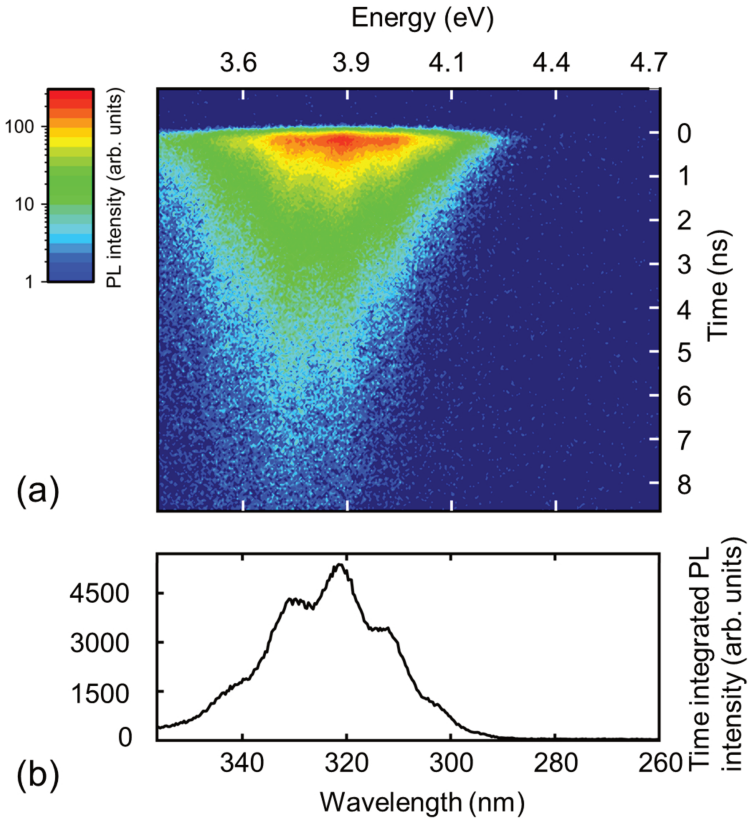

FIGURE 5.1: (a) Streak camera image of GaN/AlN QDs recorded at $T = 10$ K using a 4.82 eV pulsed laser for an incident photon flux of $2 \cdot 10^{11}$ photons $\cdot$ cm^{-2}, (b) corresponding time-integrated PL spectrum.

Mechanisms behind the redshift of the PL spectra

Both the quantum confinement and the QCSE depend on the QD height [56, 114]. Due to the size-dispersion of the dots, PL emission experiences an inhomogeneous broadening that we assumed to be Gaussian. This is justified by the quasi-linear dependence of the PL emission energy with the QD height as we will show in our calculations (cf. Sec. 5.1.2). An energy shift is observed between $t = 0$ and $t = 3.8$ ns (∼90 meV) that is much smaller than the FWHM of the PL band (∼500 meV). Two phenomena can contribute to this shift. First, because of the QCSE, the spectral contributions from dots with different heights will display different dynamics. Thus, at long time delay, the contribution from the low energy side of the PL band is enhanced with respect to the high energy emission that decays faster. The larger QDs, which emit at lower photon energies, show indeed a higher QCSE that increases the e-h spatial separation and, consequently, their radiative lifetime. Another explanation could be a possible screening of the built-in electric field: The initial e-h pair population modifies the QD band profile, inducing a blueshift of the PL emission at short time delay that will disappear with the recombination of this population [115].

Unfortunately, both effects have the same physical origin and are always present and inter-dependent, leading to a complex PL dynamics that is challenging to interpret[95]. However,

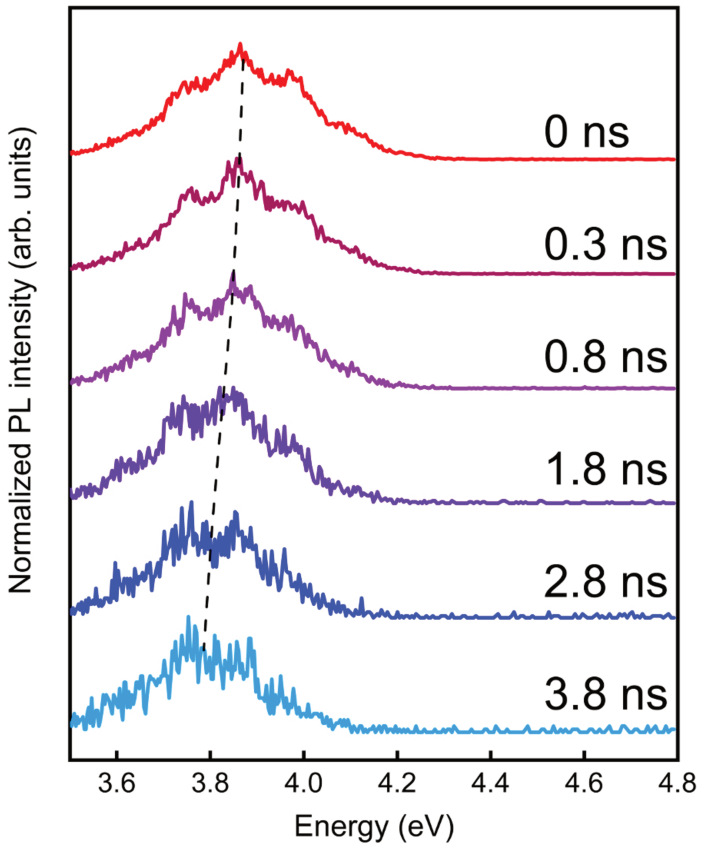

FIGURE 5.2: Low temperature ($T = 10$ K) normalized PL spectra of a GaN/AlN QD ensemble at different delay times after pulsed laser excitation. The dashed line represents the energy position of the PL maximum, $E_{max}(t)$, obtained from Gaussian fits of the spectra.

in the limit of low carrier injection, i.e., for less than one e-h pair per dot, the screening of the electric field becomes negligible. For these reasons, we performed our experiment at low excitation intensity. Taking into account the above-mentioned photon flux and the absorption of the sample ($\simeq$ 3.5 %, measured at room temperature on a commercial UV-Vis-NIR Perkin-Elmer Lambda 950 spectrophotometer), we estimate that, in the limit where each absorbed photon creates one e-h pair, their maximum surface density would be $7 \cdot 10^9$ cm^{-2}. Compared to the surface density of QDs given above of 10^{10}-10^{11} cm^{-2}, it is reasonable to assume that there is no more than one e-h pair per dot knowing that e-h pairs will most likely not all end up in a QD (capture efficiency <100%). Hence, screening effects (and possibly Auger processes) are expected to be negligible in the present set of experiments. This is also supported by modeling of the emission as demonstrated hereafter.

Time evolution of the PL spectra

In order to study the PL dynamics as a function of QD height, we have extracted several series of time-profiles integrated on spectral slices within the emission spectrum. If, as discussed above, there is no screening effect, the PL transients should exhibit an exponential decay for sufficiently narrow spectral slices. Obviously, this is not the case as can be seen in Fig. 5.3 that displays a few typical decay profiles spectrally integrated over 5 nm wide regions together with the corresponding fitting curves. The fitting function is the sum of three contributions: two exponential decays, together with a constant background (see Eq. (5.1)).

$$I(t) = A_s e^{-\frac{t}{\tau_s}} + A_l e^{-\frac{t}{\tau_l}} + y_0. \tag{5.1}$$

where $I(t)$ is PL intensity as a function of time, A_s and A_l are weighting coefficients, in the following, we denote τ_l and τ_s the time constants related to the slow (l: long delays) and fast (s: short delays) components, respectively, y_0 represents a background. The latter represents a very long recombination process that is not resolved in our experiments. It will be discussed later on. For the first two contributions, at each spectral position, the fast component does not depend on the photon energy while the slower one follows the energy dependence expected in the context of the QCSE.

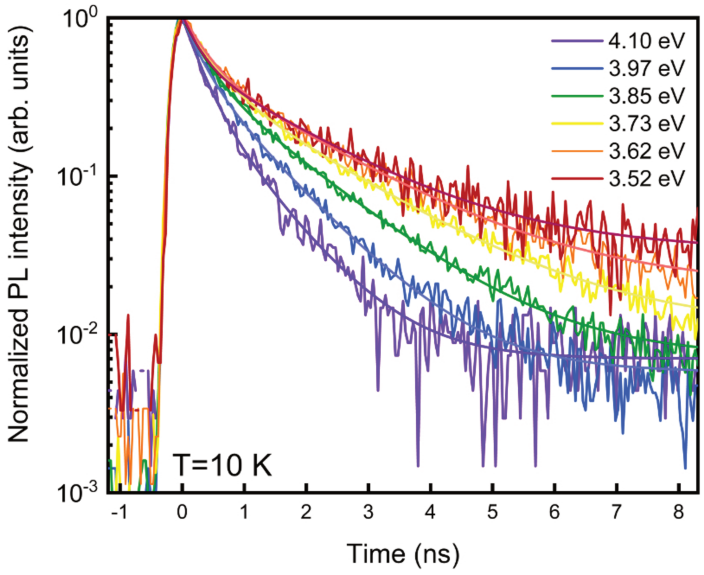

FIGURE 5.3: Low temperature ($T = 10$ K) PL decays of GaN/AlN QDs depending on the emission energy corresponding primarily to different heights of dots.

PL dynamics at short and very long delays

The fact that, before reaching a plateau, the dynamics is bi-exponential indicates that we are dealing with two independent relaxation channels. Concerning τ_s, its value is close to 0.3 ns. Being independent of the photon energy (and therefore of the dot size), it does not contribute to the spectral shift described in the previous paragraph. Since τ_s is not affected by the dot height, it leads us to assume that it is related to a non-radiative process. Unfortunately, our experimental data do not enable us to identify in an unambiguous manner the nature of the electronic states that constitute the ending step of this transfer. However, as this short decay is not usually seen in experiments performed on non-unintentionally doped high quality GaN/AlGaN quantum wells (QWs) (see for exemple [116]), we postulate that these features are specific to QDs. Processes involving the trapping of a single carrier outside the dots, like in colloidal nanocrystals (see for example [117]), are very unlikely, especially when taking into account the large difference in bandgap energy between GaN and AlN. Indeed, it would imply bringing an energy of several hundreds of meV to ionize the QDs, which can be excluded at 10 K. As less than one e-h pair is created within each dot, scattering events between two such pairs giving rise to an ionization are also unlikely. Moreover, such processes where a single carrier remains within the dot are known to favor nonradiative recombination like Auger processes that are not observed here. Instead, we could have either an extrinsic process, that involves for example the trapping of a carrier at a point defect within the QD or at the interface with the barrier material, or an intrinsic process, like the relaxation toward the fundamental state of the QD that would be a dark level with a different spin configuration [45].

We can now focus on the very long component that shows up as a constant background in our experiments. It could be tentatively explained by the reverse process where the e-h pairs that have experienced a relaxation toward a dark state will slowly flip back to their bright radiative state. The schematic representation of the trap defect level in energy level diagram of the QD as well as time constants involved in the radiative recombination mechanism is shown in Fig. 5.4.

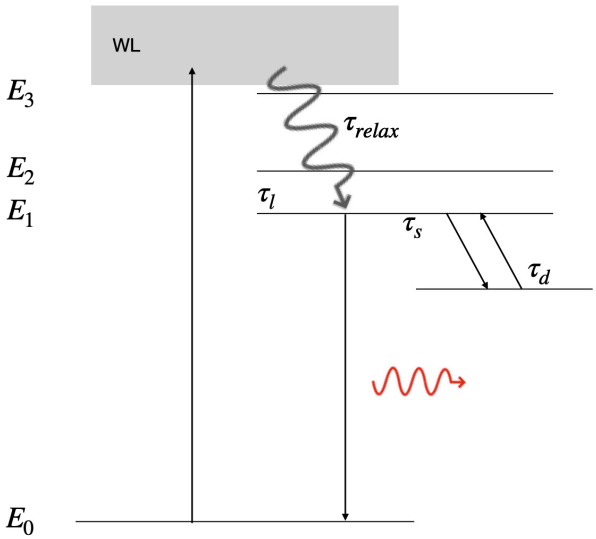

FIGURE 5.4: Schematic representation of the trap defect level in energy level diagram of the QD as well as time constants involved in the radiative recombination mechanism.

PL dynamics at intermediate delays

Unlike the short decay characterized by τ_s, τ_l shows an evolution with the photon energy that is characteristic of a height-induced variation of the radiative lifetime of a QD that undergoes the QCSE. Indeed, the experiments being performed at 10 K, the decay that we measure is purely radiative. In Fig. 5.5, we have plotted the corresponding recombination

rate $\gamma(E) = (\tau_l(E))^{-1}$ as a function of emission energy. Its variation can be written as a Taylor expansion to second order around E_0, the initial position of the PL maximum:

$$\gamma(E) = \gamma_0 + \gamma_1(E - E_0) + \frac{1}{2}\gamma_2(E - E_0)^2, \tag{5.2}$$

with $\gamma_1 = \left.\frac{d\gamma}{dE}\right|_{E_0}$ and $\gamma_2 = \left.\frac{d^2\gamma}{dE^2}\right|_{E_0}$.

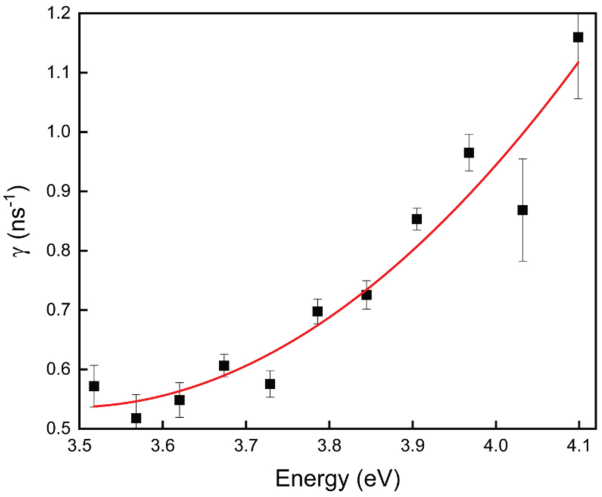

FIGURE 5.5: Evolution of the experimental radiative rate $\gamma(E)$ deduced from the PL decays recorded at $T = 10$ K as a function of QD emission energy (black squares) and its fit using a second order polynomial (red continuous line).

The best agreement is obtained for

$$E_0 = 3.869 \text{ eV}, \tag{5.3}$$
$$\gamma_0 = 0.76 \pm 0.02 \text{ ns}^{-1}, \tag{5.4}$$
$$\gamma_1 = 1.2 \pm 0.1 \text{ ns}^{-1}\text{eV}^{-1}, \tag{5.5}$$
$$\gamma_2 = 3.1 \pm 1.3 \text{ ns}^{-1}\text{eV}^{-2}. \tag{5.6}$$

These values show large uncertainties, mainly because fitting the dynamics at different energies can lead to approximate values of γ in the spectral region where the signal to noise ratio of the PL is poor. We thus used another method that allows a better precision especially on the second derivative: We perform an analysis by fitting the entire spectrum recorded at different delay times (Fig. 5.2) in order to provide a better averaged value of $\gamma(E)$.

Unsurprisingly, the spectra displayed in Fig. 5.2 fit nicely with a Gaussian lineshape after removing the oscillations due to the Fabry-Perot effect (see Appendix A). Indeed, the homogeneous linewidth is negligible with regard to the inhomogeneous broadening that gives rise to the observed linewidth due to the size distribution of the QDs. If screening effects are negligible, the relation between the dot height and the emission energy is expected to be a bijection. The radiative recombination probability is independent of time and the dynamics for one given height of quantum dots is exponential. Then, considering an ensemble of QDs with heights following a normal distribution, the temporal evolution of the corresponding PL intensity spectrum $I_{PL}(E,t)$ can be written:

$$I_{PL}(E,t) \propto e^{-\frac{(E-E_0)^2}{\Gamma_{inh}^2}} \cdot e^{-\gamma(E)t}, \tag{5.7}$$

where Γ_{inh} is the inhomogeneous broadening, E_0 is the energy of the PL maximum at zero delay, and, as above, $\gamma(E) = 1/\tau_l(E)$ is an implicit function describing the energy dependence of the radiative lifetime. As long as $\gamma(E)$ contains only linear and quadratic terms in E, the spectral shape will remain Gaussian at any time, with simply a width and a central value that change together with the maximum intensity.

The first derivative of Eq. (5.7) with respect to energy cancels at the maximum of the Gaussian curve, as detailed in Appendix B:

$$E_{max}(t) = E_0 - \frac{\Gamma_{inh}^2 \gamma_1 \cdot t}{2 + \Gamma_{inh}^2 \gamma_2 \cdot t}. \tag{5.8}$$

To first order, the time evolution of the PL maximum position is thus a linear function of time. The FWHM is given by the second derivative of Eq. (5.7):

$$\Delta E(t) = \frac{2\,\Gamma_{inh}}{\sqrt{2 + \Gamma_{inh}^2 \gamma_2 \cdot t}}. \tag{5.9}$$

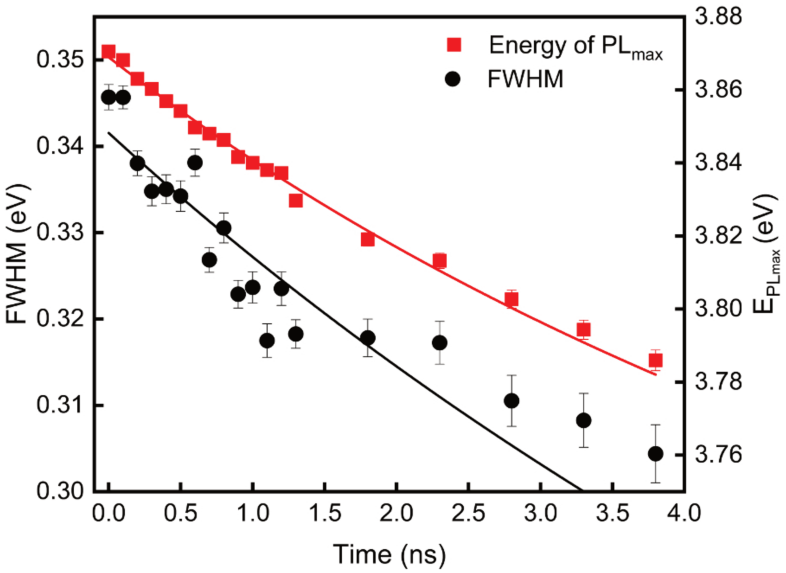

FIGURE 5.6: Time evolution of both the center $E_{max}(t)$ and the FWHM of the Gaussian function $\Delta E(t)$ modeling the low temperature PL spectra of GaN/AlN QDs recorded at different delay times.

The last Gaussian parameter is the intensity:

$$I_{PL}(E_{max},t) \propto \exp\left\{\left(-\gamma_0 \cdot t + \frac{1}{2}\left(\frac{\Gamma_{inh}^2 \gamma_1^2}{2 + \Gamma_{inh}^2 \gamma_2 t}\right) \cdot t^2\right)\right\}. \tag{5.10}$$

Using this analytic approach, the temporal behavior of the PL lineshape provides information about a possible screening of the electric field.

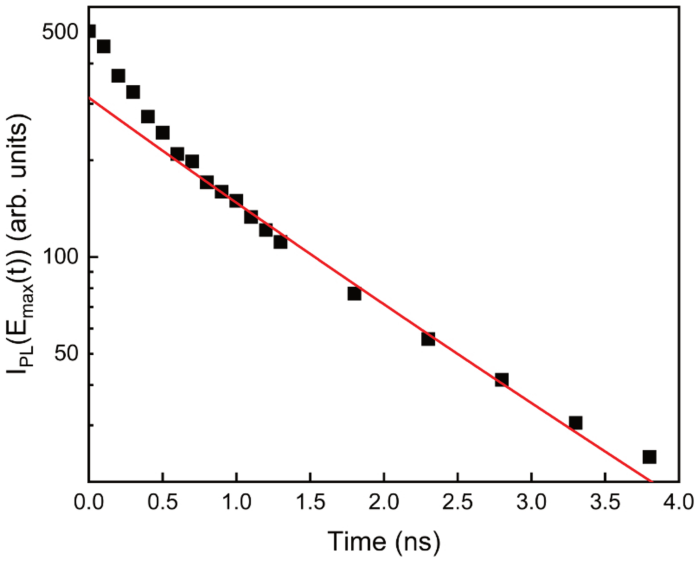

FIGURE 5.7: Time evolution of the PL intensity at $E_{max}(t)$.

The time evolution of the PL lineshape parameters as well as the corresponding fits are plotted in Fig. 5.6, while the intensity time evolution is shown in Fig. 5.7. For the latter, we have to take into account the fast component decay $\tau_s = 0.3$ ns. Therefore, we performed the fit (red curve in Fig. 5.7) for times longer than 0.6 ns. The experimental data are nicely described by the above-mentioned expression demonstrating that the temporal evolution of the PL line is mainly due to the variation in the radiative lifetime within the QD distribution. The fitting procedure gives:

$$\Gamma_{inh} = 0.242 \pm 0.001 \text{ eV}, \tag{5.11}$$

$$\gamma_0 = 0.77 \pm 0.02 \text{ ns}^{-1}, \tag{5.12}$$

$$\gamma_1 = 1.05 \pm 0.02 \text{ ns}^{-1}\text{eV}^{-1}, \tag{5.13}$$

$$\gamma_2 = 3.08 \pm 0.36 \text{ ns}^{-1}\text{eV}^{-2}. \tag{5.14}$$

As expected, this method leads to an improved precision regarding the numerical coefficients considered in the Taylor expansion of $\gamma(E)$.

At this stage, let us note that the very good agreement observed between experimental data and our fitting procedure strongly supports the idea that neighboring QDs exhibit a marginal interaction between them even though our sample is characterized by a dot density ranging between 100 and 1000 per squared micron. This can be understood on the basis of the strong confinement at play in GaN/AlN QDs and the reduced size of the exciton Bohr radius in those zero-dimensional nanostructures. As a reminder, the large effective masses in the GaN/AlN system are such that the amplitude of the carrier wave functions in the barriers becomes vanishingly small after a penetration depth of 1 nm.

Dependence of the radiative lifetime on the dot height

The coefficient γ_1 in the Taylor expansion of $\gamma(E)$ is positive, which reflects the increase in the recombination probability when decreasing the dot height due to the smaller weight of the QCSE. Hence, $\Delta E(t)$ is a monotonous decreasing function of time. The longer the delay time, the narrower the distribution of populated QDs because the larger radiative recombination

rate of small QDs is such that only the larger dots emitting at lower photon energies will contribute to the PL spectra, thus leading to the observed decrease in the FWHM.

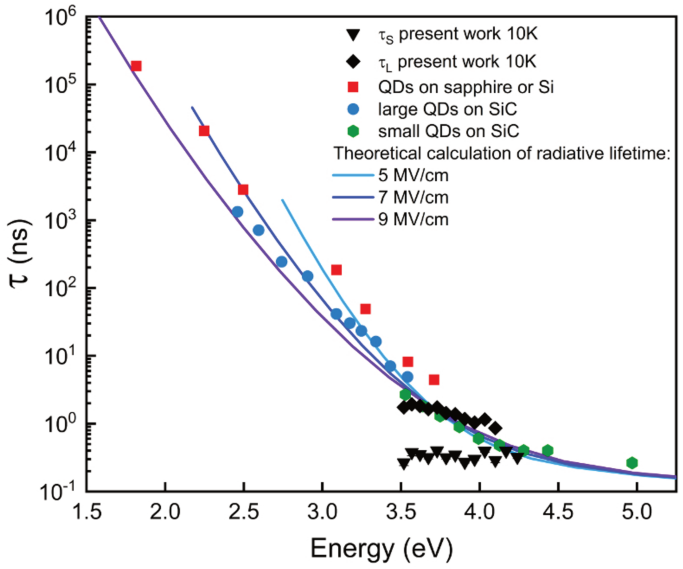

FIGURE 5.8: Radiative lifetime τ_l of GaN/AlN QDs as a function of emission energy: black diamonds (present work), red squares (Ref. [54]), blue circles and green hexagons (Ref. [57]). Black down triangles correspond to the fast time constant τ_s (present work) ascribed to a nonradiative relaxation process. The continuous lines are results of calculations of τ_{rad} based on a 2D envelope-function modeling for different values of the built-in electric field.

The time constants extracted by means of the fitting procedure are summarized in Fig. 8.1 together with literature data related to samples containing different heights of GaN/AlN QDs. Our experimental data complete nicely the set of data from references [54, 57]. In order to estimate the emission energy and the radiative lifetime of e-h pairs in GaN/AlN QDs, the envelope-function equation was solved numerically for both electrons and holes, using a finite difference method by means of a home-made SCILAB code. The confinement within the layer plane, i.e., perpendicular to the growth direction is, in a first step, neglected as the built-in electric field has the most important impact on the optical properties of III-nitride based nanostructures grown along the *c*-axis. Thus, the QDs are first modeled as two-dimensional (2D) QWs subjected to a static electric field along the growth direction, the carriers being free to propagate in the well plane. We took into account the blueshift of the GaN bandgap to 3.71 eV at low temperature ($T = 10$ K) due to the strain originating from pseudomorphic growth on the AlN layer. The radiative lifetime τ_{rad} is then given by the expression: $A \cdot (\hbar\omega)^{-3} |J_{eh}|^{-2}$ [118] where $\hbar\omega$ is the photon energy, J_{eh} is the overlap integral of electron and hole envelope-functions and A is an adjustable parameter. The resulting function $\tau_{rad}(\hbar\omega)$ is plotted as a continuous line in Fig. 8.1 for different values of the electric field F and $A = 20$ ns·eV^{-1}. Such a simple calculation provides curves that qualitatively reproduce the experimental variation in the radiative lifetime over six orders of magnitude for values of the electric field ranging between $F = 5$ MV/cm and $F = 9$ MV/cm, the best agreement being obtained for a mean built-in electric field value $F = 7$ MV/cm. The mean value of our experimental data agrees well with compiled data from the literature showing the variation of the radiative lifetime for a large range of dot heights.

In order to be more quantitative, let us note that the QD ensemble in our sample exhibits a large inhomogeneous broadening. To illustrate this aspect, we consider Fig. 8.2, which shows that the variation in the radiative lifetime does not exactly match the curves (continuous lines) that only take into account the variation of the QCSE due to the changes in dot height.

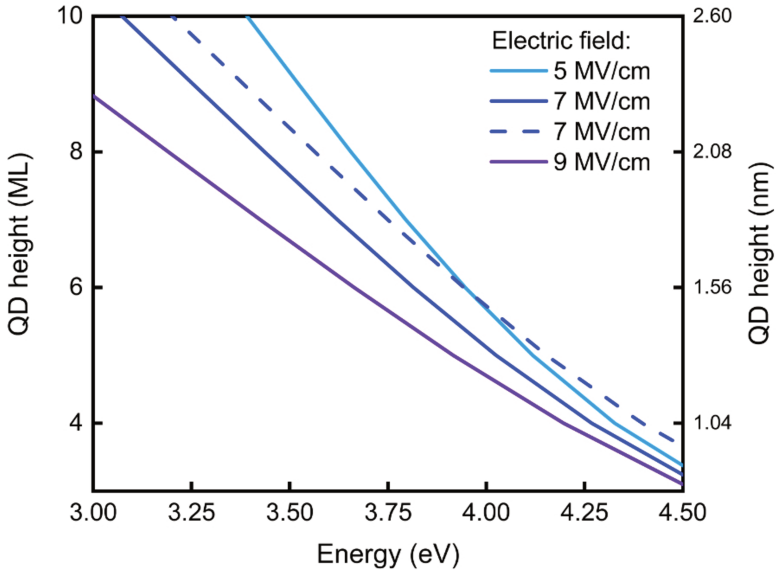

FIGURE 5.9: Radiative lifetime τ_L of GaN/AlN QDs as a function of emission energy. The continuous lines are issued from 2D-QW calculations of τ_{rad} for different values of the built-in electric field assuming a continuous variation in the dot height. The dotted lines show the effect of the QD lateral size with radii ranging between 3 and 20 nm. Each curve corresponds to a different QD height expressed in MLs. The size of the black diamonds is proportional to the PL intensity, which reflects the weight of the corresponding dot height within the QD distribution.

In fact, the fluctuations occurring within the dot ensemble are likely to also originate from the lateral confinement with an increasing weight of the latter when the QD lateral size becomes comparable to the exciton Bohr radius. Indeed, the 2D QW model works better for the largest dots for which variations in the oscillator strength are essentially due to changes in the e-h overlap along the growth axis. For small dots, the in-plane localization of the envelope-functions is no longer negligible. To estimate this effect on the energy and the lifetime of an e-h pair, we performed a simple calculation based on the variational method (see Appendix C): the in-plane confinement potential is supposed to be step-like with a cylindrical symmetry. The in-plane envelope function of the carriers is considered to be a Gaussian centered in the cylindrical dot and for which the spatial extent is the variational parameter. This method is known to give reasonable qualitative results in spite of its simplicity [119]. For a given QD height, a variation in the localization radius has little influence on the lateral overlap while it strongly affects the confinement energy. As a consequence, the variation in the lifetime versus energy becomes less pronounced. This is illustrated in Fig. 8.2 that shows as dashed lines the effect of the variation in the lateral dot size on the transition energy and the radiative lifetime for various dot heights. We thus see that the slope of the dashed lines nicely matches the relatively flat variation in the radiative lifetime as a function of photon emission energy observed experimentally. Obviously, more realistic calculations would consider the different lateral confinement experienced by electrons and holes. First, these carriers have different effective masses and the wave function of the lighter particle, the electron, should leak into the barrier. Second, if the dot shape looks like truncated pyramids, as confirmed by high-resolution transmission electron microscopy measurements [120], the confinement potential would act differently on the two particles which are pushed away to opposite sides, the electron to the top of the pyramid and the hole in the wetting layer. Hence, both effects will change the lateral overlap of the electron and hole wave functions [121]. However, our approach shows that such a detailed description of the QD wave functions is not mandatory. The lateral confinement plays a major role by blueshifting the emission energy without changing the e-h

overlap and thus the radiative lifetime.

Finally, we can interpret these data in the following way: from one dot to the other any variation in the mean radiative lifetime is primarily governed by a change in the dot height that involves the QCSE as already demonstrated in many publications (see, e.g., Fig. 8.1 that displays literature data). However, the present analysis shows that, within a given QD sample, changes in the QD emission energy by several hundreds of meV accompanied with only slight changes in the radiative lifetime can be understood through fluctuations in the lateral dot dimensions within a given QD subset corresponding to a well-defined height. In this respect, we recall that the identification of GaN/AlN QD subsets with a well-defined height within the same sample was already reported for dots exhibiting a variation in the biexciton binding energy that was correlated to the exciton energy and the dot radius within a QD subset with a given height [89]. Let us note that for QDs emitting around 3.5-4.1 eV, as those studied here, the effect of the built-in electric field is less important than in higher dots where the QCSE has more dramatic effects on the emission energy and the oscillator strength and for which only a mean radius has to be considered. Thus, in dots emitting in the UV range, which are of prime interest for single photon emission [44, 45], the weaker weight of the QCSE enables to reveal otherwise hidden effects originating from changes in the e-h lateral confinement, be it what governs variations in the biexciton binding energy [89] or a relative insensitivity of the radiative lifetime while covering a wide spectral range in the QD emission energy (here, up to ∼600 meV).

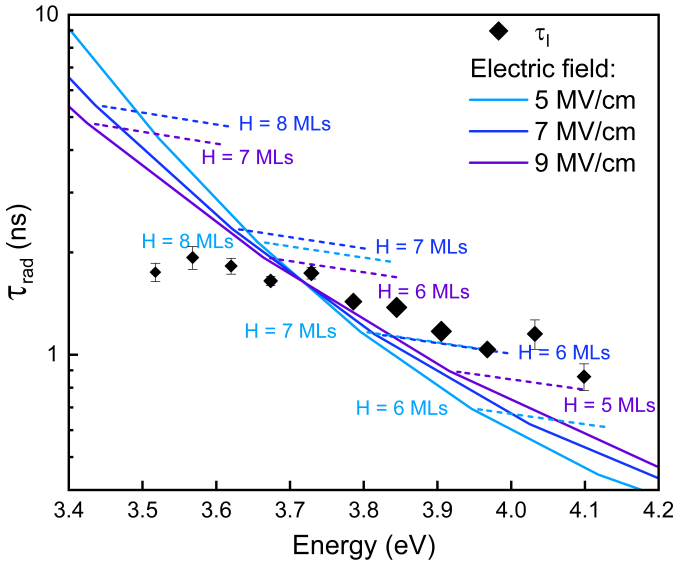

FIGURE 5.10: Correlation between the calculated transition energy and the QD height for different values of the built-in electric field. The straight lines correspond to calculations based on a 2D QW model (no lateral confinement), while the dashed one correspond to calculations based on the variational method for small dots with a lateral radius of 3 nm.

The reported behavior confirms that the main mechanism behind the relaxation of the e-h pair population is the radiative recombination process and that the radiative lifetime follows the expected evolution for QDs subjected to the QCSE. Moreover, our results strengthen the fact that, if care is taken to avoid any screening of the built-in electric field, the relation between the radiative lifetime and the emission energy tends to a universal trend (Fig. 8.1). This can be well understood within a simple model including a mean value of the built-in electric field that is the same for all GaN/AlN QD samples. From a practical point of view, the calculations presented in Fig. 8.3 allow to estimate that the QD height lies between 5 and 8 MLs (1.3 and 2.08 nm).

5.1.3 Temperature dependance of the TRPL

While we have investigated the radiative recombination processes in GaN/AlN quantum dots at low temperatures using time-resolved photoluminescence (TRPL), it's important to note that these dynamics can be significantly influenced by temperature. Non-radiative processes, although typically suppressed at low temperatures, can play a crucial role in carrier recombination dynamics as temperature increases. Regarding the depth of the potential well seen by carriers when they are trapped in a GaN/AlN QD, a non-radiative escape by overcoming the AlN barrier is not expected, even at room temperature. However, thermally induced tunneling from QDs to deep centers located in the surrounding AlN matrix is possible [53] if their energy is close to the carrier energy within the dot (defect levels or centers trap the electron or hole preventing the pair to recombine radiatively). A non-radiative recombination acting a radiative state would have an impact on both the dynamics and the intensity of PL. Non-radiative processes can also occur during the relaxation from the wetting-layer towards the QDs. They do not have any influence on the PL dynamics, because we only measure the emission from carriers once they are thermalized, but can affect the PL intensity by reducing the capture efficiency of electron-hole pairs by quantum dots. They can result from:

- interaction with phonons [122] (transfer of energy to the lattice),
- Auger recombination [123] (the energy is transfered to other free single carriers, exciting them to higher energy states)

The joint studies of the dynamics and the intensity of the PL in a time-resolved experiment give precious information about the occurence and the nature of possible non-radiative processes. Moreover, such information can clarify certain relaxation-recombination mechanisms. This subsection is dedicated to the temperature dependence of the TRPL experiments measured on the 1-plane GaN/AlN QD sample. The TRPL experiments were performed over a temperature range from 10 to 280 K. The low excitation regime is maintained, as in the experiment described in Sec. 5.1.1. At each temperature, we have determined the energy of the PL-maximum, the FWHM of the PL-spectrum, the integrated PL-intensity and the lifetime of photocarriers. The analysis of the PL dynamics shows that the biexponential decay behavior observed at low temperature persists up to ambient temperature as observed by [96], in a low excitation regime, on $c-$plane SA GaN/AlN QD grown on a Si substrate. Because the spectral position of the PL-spectrum slightly shifts with T, we analyzed the time profiles of the maximum of the spectrum, denoted $E_{PL_{max}}(T)$.

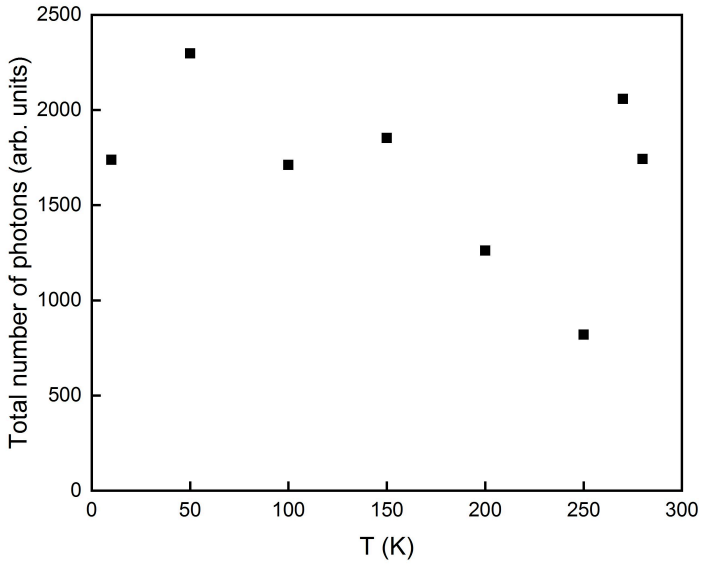

FIGURE 5.11: Total number of photons.

Fig. 5.11 represents the spectrally and temporally integrated PL intensity (equivalent to the total number of photons emitted during the full time range following the arrival of the exciting pulse) while 5.12 displays the temperature dependence of the PL decay fit parameters such as τ_s and τ_l, and A_s and A_l. We do not observe any noticeable variation of the PL dynamics with temperature in accordance with previous observation [124], due to the strong carrier confinement in the QDs.

The slight increase in the total number of emitted photons from 10 to 50 K might be due to the increase in thermal energy that facilitates the carriers' transition into the quantum dots. At 10 K, the carriers may not have enough thermal energy to efficiently transition into the quantum dots, which means some may remain in the wetting layer, leading to a fewer number of photons being emitted. However, as the temperature increases up to 50 K, the carriers gain more thermal energy and the transition into the QDs is facilitated. This efficient transition process results in more electron-hole pairs in the QDs, and since the confinement is strong within the QDs, the radiative recombination is likely to dominate, leading to more photons being emitted. Also, considering the nature of GaN/AlN QDts, the slight increase in temperature might enhance the radiative recombination process without significantly activating non-radiative recombination pathways, as the thermal energy at these temperatures (10-50 K) is not yet enough to considerably increase the phonon population, which could promote non-radiative recombination.

But as we increase the temperature from 50 K to 250 K, we observe a decrease in the total number of photons emitted, even though there's no noticeable change in the PL dynamics due to the strong confinement of our GaN/AlN quantum dots. In GaN/AlN QDs the large difference in bandgaps (over 3.4 eV) makes the thermal escape of carriers from the quantum dots highly unlikely, even at temperatures as high as 250 K. In this case, other mechanisms could be contributing to the observed decrease in photon emission. For example, thermally activated non-radiative recombination processes can become increasingly prominent with temperature. Non-radiative recombination can occur via defects or trap states in the AlN matrix surrounding the QDs or within the QDs themselves. While these states may not be directly involved in the radiative recombination observed in the PL dynamics, they can capture carriers and prevent them from contributing to the radiative process. One more possible explanation for this could involve non-radiative recombination during the diffusion of excitons in the wetting layer before they are captured in the quantum dots. This kind of behavior has been observed in InAs QDs [125].

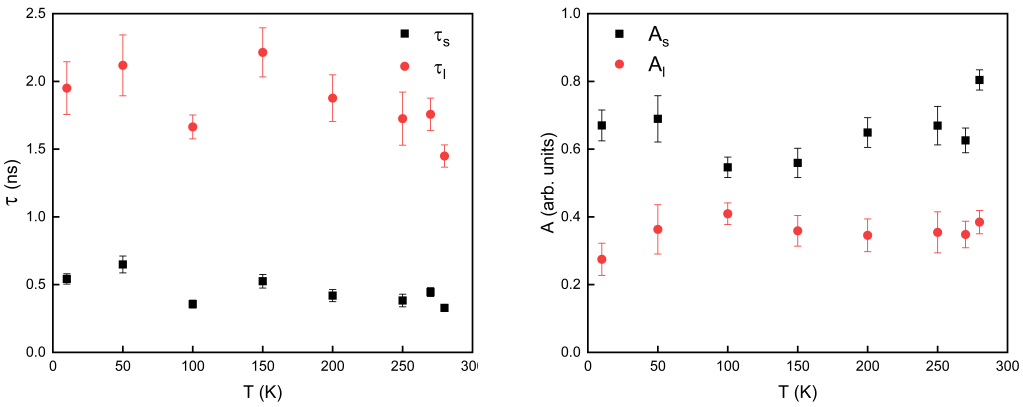

(a) (b)

FIGURE 5.12: Temperature dependence of two-exponential decay fit parameters of normalized PL intensity decay profiles at the $E_{PL_{max}}$; (a) time decay constants and (b) amplitude of these components in the fit; the red and black colours correspond to the short and long component, respectively.

However, the fact that this variation is non-monotonic could be explained by an artifact in the following way: the decrease could be caused by a continuous thermal expansion of

the sample holder that shifts the sample region seen by the collection lens while the sudden increase above 250 K may be induced by manually aligning the experimental setup during measurements. It is a common problem when temperature is continuously varied, where not only intrinsic physical processes are involved but also the effect of the temperature on the experimental set-up itself.

Currently, we focus on the temperature evolution of $E_{PL_{max}}$ and of the FHWM at 0 ns time delay, see Fig. 5.13. The variation of $E_{PL_{max}}$ remains negligible, compared to the FWHM of the PL line plotted on the right side of the figure. It follows more or less the variation of the GaN bandgap, modeled by the Varshni law (Sec. 2.2.1 (2.9)), plotted as a black line in the same figure. The $E_g(0\ K)$ is set to 3.9 eV for the GaN QD.

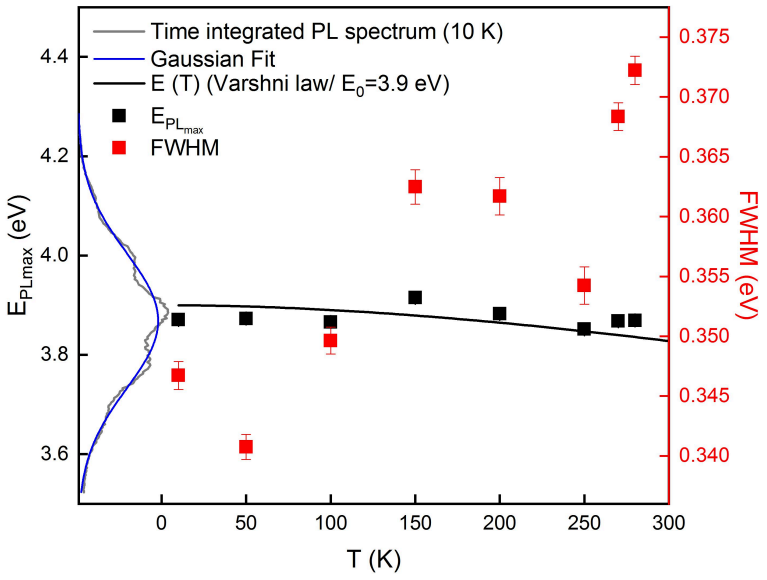

FIGURE 5.13: Temperature evolution of the energy position of the PL peak maximum (E_{PLmax}) (black squares) and spectral linewidth (FWHM) (red squares) at 0 ns delay. The black line corresponds to the bandgap temperature variation due to Varshni law, with $E(0\ K)$ set to 3.9 eV. The grey line represents the PL spectra at 10 K and the corresponding Gaussian fit (blue line).

Simultaneously, the Full Width at Half Maximum (FWHM) of the photoluminescence spectrum was seen to increase as the temperature rose from 10 K to room temperature. This spectral broadening could be primarily attributed to increased carrier-phonon interactions at elevated temperatures. At low temperatures, the thermal vibrations of the lattice are minimal. However, as temperature increases, the number of thermally excited phonons in the system also increases, leading to a higher degree of carrier-phonon interactions. When carriers in the quantum dots interact with these phonons, they can gain or lose energy, leading to a spread in their energy states. This effectively broadens the energy distribution of the carriers, which manifests as spectral broadening in the PL spectrum. Moreover, these interactions do not lead directly to non-radiative recombination; they cause energy spreading of the carriers, but these carriers can still undergo radiative recombination within the QDs.

5.1.4 Conclusion

In conclusion, our time-resolved photoluminescence (TRPL) experiments under low excitation conditions at low temperatures substantiate that the primary relaxation mechanism for the electron-hole (e-h) pair population in GaN/AlN quantum dots (QDs) is the radiative recombination process. Further, the radiative lifetime evolution aligns with expectations for QDs subject to the quantum-confined Stark effect (QCSE).

Our results underscore the relationship between the radiative lifetime and emission energy, adhering to a universal trend (Fig. 8.1), provided that the screening of the built-in electric field is avoided. The intrinsic electric field is estimated to be $F = 7$ MV/cm in our sample. From a practical perspective, the calculations displayed in Fig. 8.3 allow us to estimate that the height of the quantum dot lies between 5 and 8 monolayers (equivalent to 1.3 and 2.08 nm).

Furthermore, our temperature-dependent measurements provide the absence of an observable shift in PL energy with varying temperature and the unchanged recombination dynamics. It demonstrates the absence of a non-radiative recombination channel. This indicates the persistence of deep carrier localization within the quantum dots, even up to room temperature. Therefore, we confidently conclude that GaN/AlN quantum dots exhibit robust quantum confinement and efficient radiative recombination across the studied temperature range.

5.2 Study of a thickness gradient sample: Highlighting of two dot morphologies

Moving forward, we will now delve into the outcomes derived from our analysis of the sample that presents a gradient in QD sizes (for details see Sec. 3.2.2). This intricate sample provides us with an opportunity to discern the effects and influences of QD size variation on our measurements and interpretations.

5.2.1 CW PL & PLE

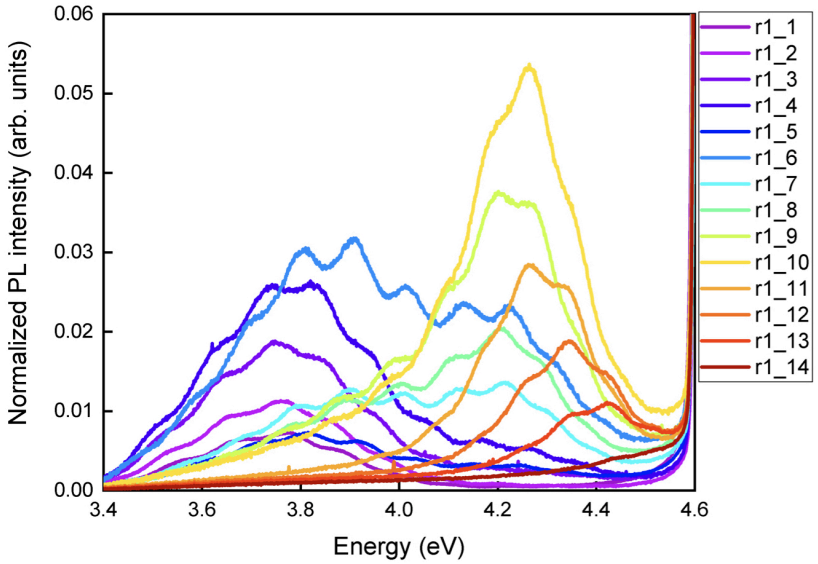

FIGURE 5.14: Normalized room temperature PL spectra of the 10-plane GaN/AlN QDs sample measured at different positions on the sample identified with in the 1^{st} row of apertures of the metallic mask.

Photoluminescence experiment were performed at RT with excitation at 4.66 eV. Experimental setup is described in Sec. 4.5. The PL spectra of the 10-plane sample related to different positions that will be presented in the following are normalized with respect to laser excitation intensity. Spectra are modulated by fringes due to interference caused by multi-reflexion of light in the buffer layer. Fig. 5.14 shows that both shape and position strongly depend on the position on the sample surface. As exposed previously, the QD height is varying continuously from one end of the sample to the other. Consequently, the confinement energy is changing as well, resulting in a shift of the PL energy maximum. There is a transition from large dots, emitting at 3.8 eV, to small dots, emitting at 4.4 eV. In between, the situation is more complex with two local maxima. We attribute it to the intermixing of two ensembles of QDs with different average sizes. The sample growth condition especially substrate temperature is responsible for the island size. The substrate temperature of this sample had a variation from one side of the sample to the other (see Sec. 3.2.2). In the transition from small QDs to large ones, in the intermediate region appear simultaneously two families of QD size. This behavior is in accordance with the bimodal size distribution of QD as reported previously in the literature [126].

In luminescence excitation spectroscopy, the detection spectrometer is set to detect emission on a specific spectral range while the excitation wavelength is varied in the range of interest. In the present case, the detection covers a region from 190 to 490 nm (from 6.5 to 2.5 eV respectively). The excitation wavelength span the range between 260 and 390 nm (4.8 and 3.2 eV) with a 1 nm, step. A PL spectrum is recorded for each excitation wavelength. The corresponding results can be plotted as a 2-dimensional map in which the intensity

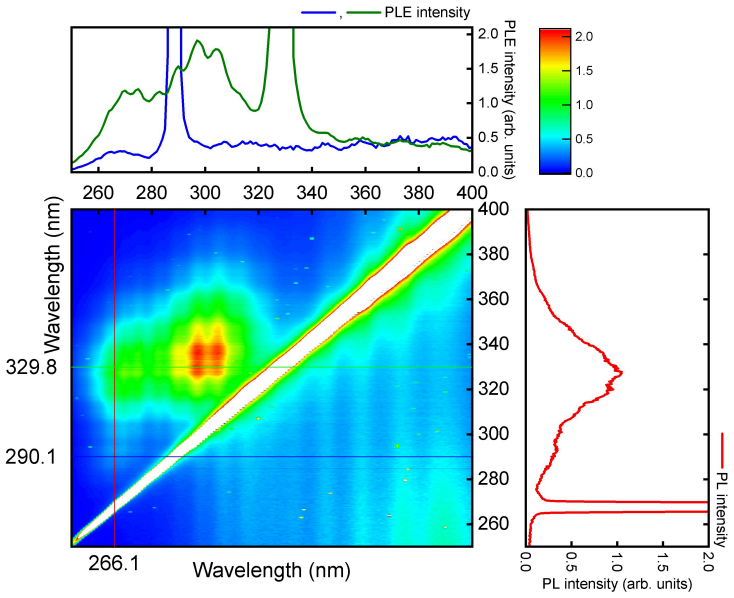

FIGURE 5.15: 2D map of PLE/PL spectrum of 10-plane GaN/AlN QDs measured at RT. The white region correspond to a saturation of the detector due to the Rayleigh scattering excitation line.

is represented by a color scale: in Fig. 5.15, the horizontal scale indicates the excitation wavelength while the vertical scale gives the detection wavelength. Consequently, a vertical profile is a PL-spectrum at a specific excitation wavelength. A horizontal profile, is a PLE spectrum, i.e. the PL intensity at a given emission wavelength as a function of the excitation wavelength. A PLE spectrum is roughly equivalent to an absorption spectrum.

An example of PL spectrum excited at 266 nm (4.66 eV) is plotted as a red line in Fig. 5.16. The PLE spectra related to emissions at 290.1 nm (4.274 eV) and 329.8 nm (3.76 eV) are given by the blue and green lines, respectively. The PL emission of QDs displays two peaks as we have seen before (Fig. 5.20). This corresponds to the situation where mixing between small and large quantum dots occurs. The high emission band is centered around 4.25 eV and the low energy emission band at 3.8 eV. The excitation spectrum for small QDs (blue line in Fig. 5.16) reveals the presence of a strong absorbance at 4.6 eV (269.5 nm) that we attribute to the WL, i.e. the two-dimensional GaN layer on which the QDs form[105, 49]. In the same figure, the green line represents the PLE spectrum of large QDs. It reveals an additional absorption band at 4.15 eV (298.8 nm). Previous studies have shown that some local thickness fluctuations of the WL by 2 or 3 MLs could result in an energy shift of several hundreds of meV, leading to the observation of a high energy satellite in the PL-spectrum[49]. In the same way, a thickening of the WL for large QDs could be responsible for the density of state observed at 4.15 eV in the PLE spectrum. Another possibility is to attribute this resonance to the first excited state of large QDs. The structure would be missing in the PLE spectrum of small dots because the confinement is too large to allow the existence of such an exited state.

5.2.2 TRPL

Experimental conditions

Time-resolved photoluminescence (TRPL) measurements were performed at RT. The excitation consists in the fourth harmonic of a pulsed ytterbium laser (Satsuma HP) emitting at 257 nm (4.82 eV) with a pulse duration of 270 fs and a repetition rate of 40 kHz. For experimental details see Sec. 4.2.

For an excitation power of 0.15 mW, the energy per pulse is 4 nJ and the diameter of the excitation spot focused on the sample was about 0.4 mm, giving an incident photon flux of

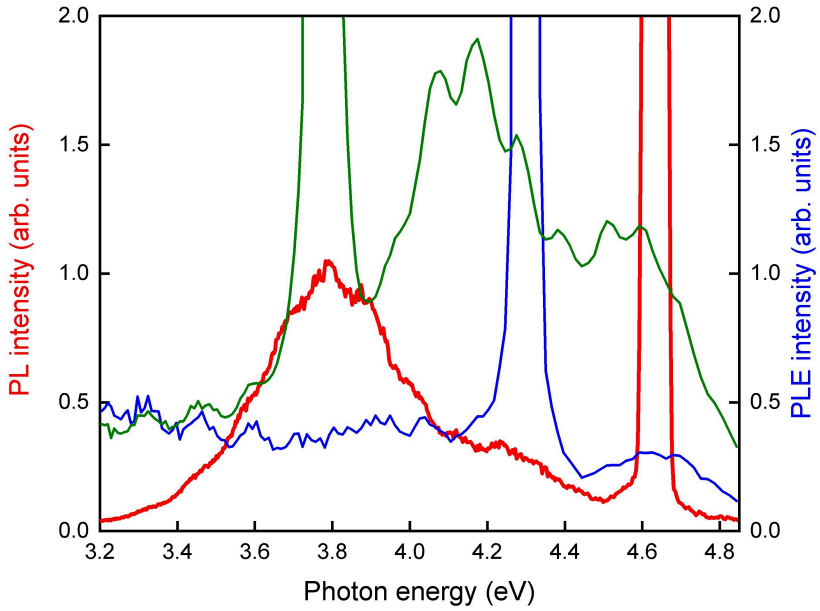

FIGURE 5.16: PLE/PL spectrum of GaN/AlN QDs measured at an arbitrary position on 10 planes sample.

$4 \cdot 10^{11}$ photons $\cdot$ cm^{-2}. Since the sample has 10 layers of QD, the photon flux is, roughly, $4 \cdot 10^{10}$ photons $\cdot$ cm^{-2} per layer of QDs.

5.2.3 10 planes TRPL RT

Fig. 5.17 displays the quasi-continuous wave PL spectra as well as the time-integrated TRPL spectra normalized relatively to the excitation intensity of the laser measured at 3 different positions on the sample. To compare the two sets of results, the time-integrated data were manually multiplied by a constant factor in order to match the amplitude of the quasi-continuous spectra.

We evidence that the PL spectra differs in spectral position and width. We suggest a few effects that could explain these differences:

- The first effect could originate from the sample structure. Our sample consists of 10 layers of GaN QDs separated by AlN spacers of 5 nm. Actually, we do not know if it exists a size-correlation between the QD layers. Such a vertical correlation was found for an AlN spacer thickness of 8 nm, while no correlation was present for a spacer thickness of 20 nm [127]. Another study shows that the formation of the QDs undergoes a drastic change in size from the first to the following layers, becoming more uniform after the deposition of a certain number of layers [128]: As far as one grows successive layers, the formation of large-sized QDs is favoured leading to a drastic reduction of the formation of smaller QDs and a size-uniformization of the QDs.
- The second effect could be due to the experimental geometry. Whether a size-correlation exists or not, one possible source of broadening and shift of the PL spectrum is the tilt of the sample surface. If the propagation direction presents an angle with respect to the normal to the surface (see 5.18), the beam would excite QDs with different average heights in adjacent planes. Moreover, if the 0.3 mm focal spot from the laser is not well centered, from one experiment run to another one, within the 1 mm apertures that identifies the position on the sample surface, it could also explain the discrepancies between the two sets of data.

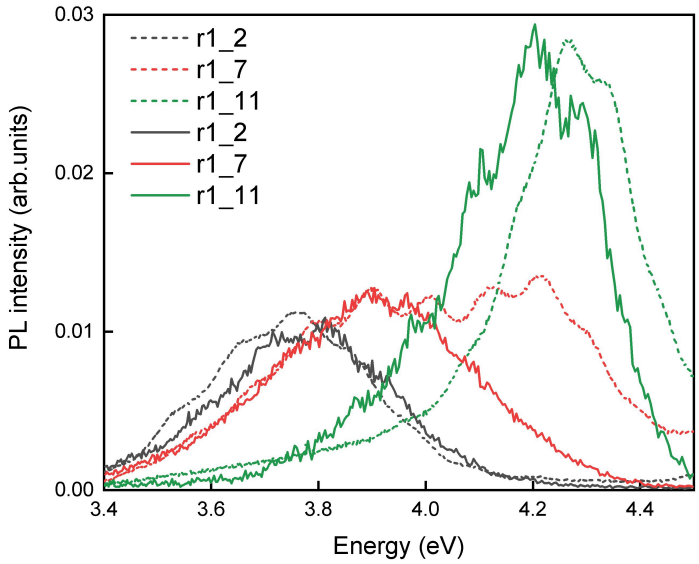

FIGURE 5.17: Comparison of the quasi-continuous PL spectra (dashed line) and time-integrated TRPL spectra (solid line) measured at the same positions on the sample (color of the line). The spectrum amplitudes are normalized relatively to the excitation power.

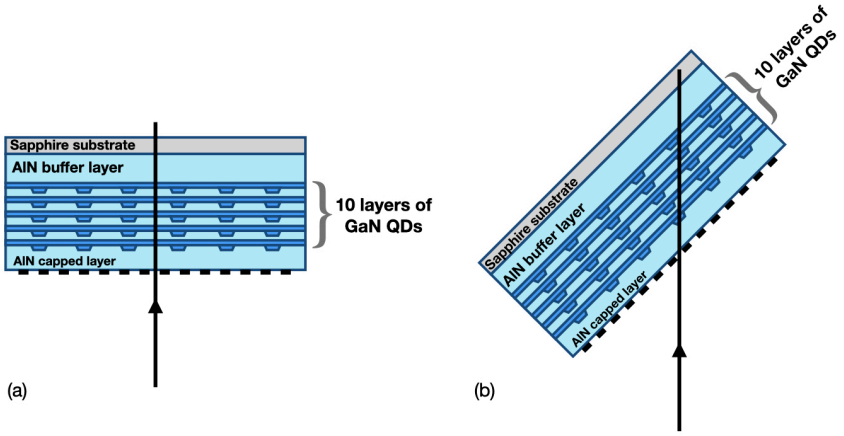

FIGURE 5.18: Schematic representation of different excitation geometry in PL experiment (a) and in TRPL (b). The dashed line on the top of the sample represents the deposited mask to control the position on the sample.

In order to study the PL dynamics as a function of the QD height, we used the same procedure described in Sec. 5.1.2. Fig. 5.19 represents decay profiles spectrally integrated over 5 nm wide regions together with the corresponding fitting curves.

For energies above 4 eV, the PL transients show a monoexponential decay. Below 4 eV, all decay curves are well fitted with a two-exponential function:

$$I(t) = A_{sh} e^{-\frac{t}{\tau_{sh}}} + A_l e^{-\frac{t}{\tau_l}}, \tag{5.15}$$

where $I(t)$ is the PL intensity as a function of time, A_{sh} and A_l are weighting coefficients, and τ_{sh} and τ_l represents the PL decay times related to the short and slow components, respectively. This behavior is common to all tested positions on the sample. Nevertheless, we

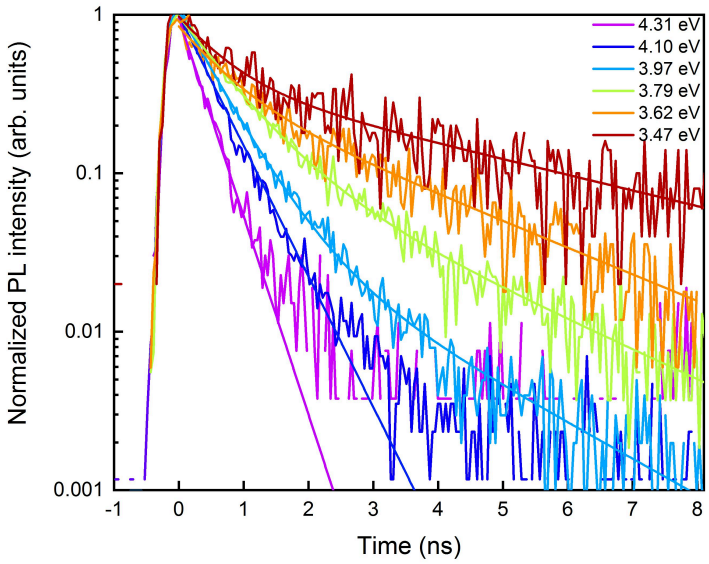

FIGURE 5.19: Normalized PL decays profiles of GaN/AlN QDs depending on the emission energy measured on the 10-planes sample at the position $r1\_7$.

restrained the analysis on data related to 3 positions that we chose because of their emission spectra that span the entire spectral range (Fig. 5.21a). The dependence, with the emission energy, of the extracted fitting parameters is plotted in Fig. 5.21b and 5.21c: for small QDs, the emission energy of which is above 4 eV, the PL dynamics is only ruled by the short time constant. Below this energy, the dynamics presents a short and a long component. When the photon energy is changed, both time constants, τ_{sh} and τ_l, show a comparable evolution: the lower the energy (i.e. the larger the QD), the longer the lifetime. This is in agreement with the evolution of the radiative lifetime under the influence of the QCSE. Moreover, it is very similar to what we observed on the 1-plane sample. Considering the weight of each component (Fig. 5.21c), it appears that the long one dominates at low energy while the short one is predominant at high energy. More precisely, A_l and A_{sh} reach their maxima at 3.6 eV and 4.2 eV, respectively.

From this analysis, we can conclude the following elements concerning the morphology of this sample. As one moves from one end of the sample to the other, there is not a single box morphology whose height varies continuously. In fact, there are two families of dots with different morphologies. We can assume that they do not have the same aspect ratio. They are characterized by their photoluminescence spectra centered at 4.28 and 3.76 eV respectively (identified in figure 5.20). To distinguish them, we will call them in the following "high energy dots" and "low energy dots" for convenience. These two spectral positions correspond to an average value, for each morphology, around which the height varies. PLE experiments also revealed from positions $r1\_1$ up to $r1\_4$, we explore different heights among low energy dots. Then, between positions $r1\_5$ and $r1\_8$, we have a coexistence between the two dot morphologies. Finally, beyond the position $r1\_9$, the dot height decreases within the family of high energy dots. The PLE experiments also revealed that the high-energy dots probably admit only one confined state for electrons and holes and essentially absorb in the wetting layer. On the contrary, low energy dots exhibit an excited state about 400 meV above the PL energy. Each type of dot has an average radiative lifetime, τ_{sh} for small ones and τ_l for large ones, determined by the morphology of the dot which is then modulated by the QCSE when changing the height. The dynamics of photoluminescence is the sum of two independent processes which are the radiative recombinations in each type of dot when they coexist in the same region of the sample. When one of the two families of dots is predominant, its lifetime

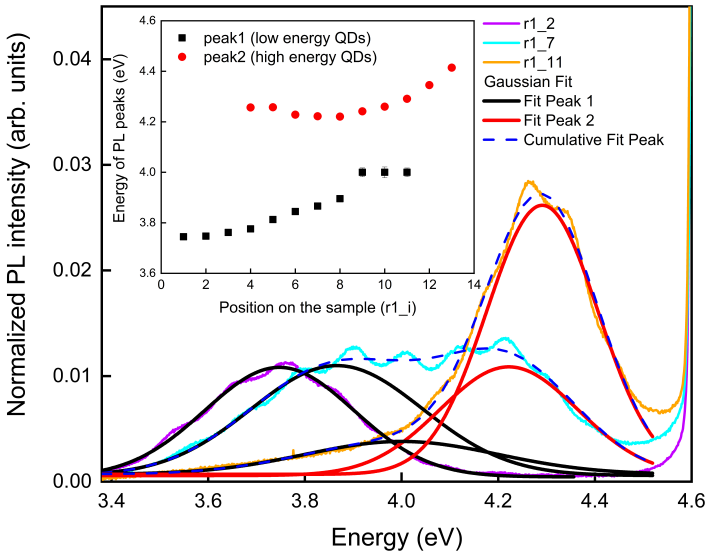

FIGURE 5.20: Normalized room temperature PL spectra of the 10-plane GaN/AlN QDs with the cumulative curves (dashed blue lines) of the Gaussian fit resolved emission peaks (red and black curves). Left top corner graph represents E_{peak} of the PL Gaussian fit with respect to the tested position on the sample.

governs the dynamics of recombination. Thus, the evolution of the weights of each of the components more or less follows the shape of the average spectra associated with each type of dots.

We can offer a more quantitative analysis based on the calculations presented above. From Fig. 8.2 , if we consider an electric field of 7 MV/cm, we see that the two photoluminescence lines centered at 4.2 and 3.8 eV roughly correspond to quantum dots whose heights are distributed around 4 and 6 MLs, respectively. Fig 8.1 shows that if lateral confinement is taken into account, there may be different possible lifetimes for the same emission energy. Our model is very simplified but it makes it possible to understand that if two types of QDs with different morphologies cohabit in the sample, they may give rise to the superposition of two different dynamics for the same emission energy.

We can wonder about the fact that the short component, associated with the time constant τ_{sh}, is present over the entire spectral page studied, down to the lowest energies, while the long component, associated with τ_l, disappears abruptly around 4 eV. Perhaps this is due to the fact that the region around 4.0 eV corresponds to the high energy part of the emission of large dots. We can then imagine that radiative recombination is then in competition with more efficient thermalization processes which would have time constants of the same order of magnitude as τ_{sh}. Conversely, the spectral range around 3.6 eV corresponds to the low energy part of the photoluminescence of small dots. Electron-hole pairs that emit at this energy occupy the deepest states of the dot distribution and have no way out but to recombine radiatively. However, we have no element to conclude if the two box morphologies coexist inside the same plane or if they belong to adjacent planes. Indeed, given the thickness of the structure and the wavelength used, the laser excites all 10 dot planes during a photoluminescence experiment.

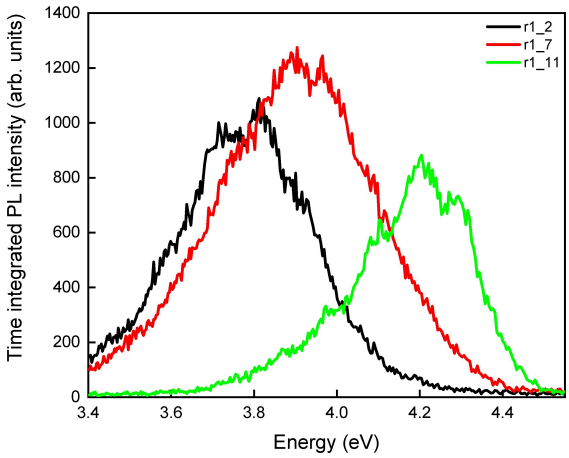

(a)

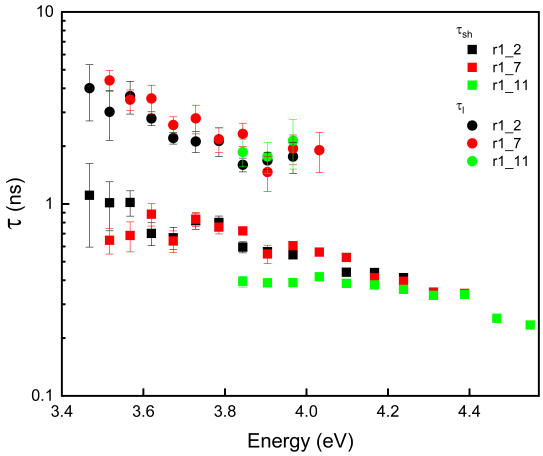

(b)

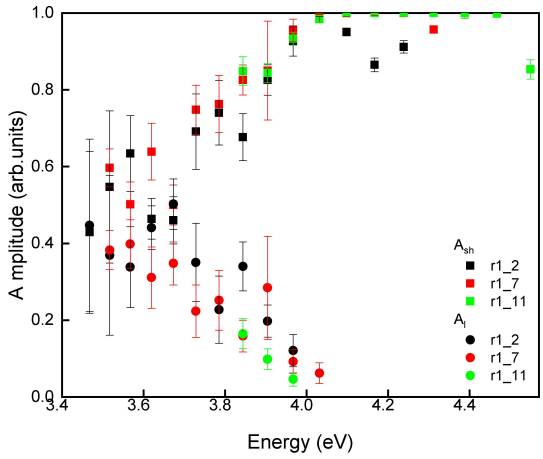

(c)

FIGURE 5.21: (a) Time integrated PL intensity, extracted parameters from normalized decay profiles fit, such as (b) time decay and (c) amplitude, as a function of emission energy measured at different position on the 10 planes sample; black, red and green colour correspond to $r1\_2$, $r1\_7$, $r1\_11$ position on the sample respectively.

5.3 Discussion

In sections 5.1 and 5.2, we highlighted two important points. On the one hand, the dynamics of PL is not systematically monoexponential and, on the other hand, even if the QCSE plays an important role in the dynamics, the morphology of the dots, i.e. the form factor, n is not to be neglected.

Regarding the first point, numerous studies, such as Bretagnon et al. [54, 95] and Stachursky et al. [96], explored the dynamic behavior of large QD, finding non-exponential dynamics and bi-exponential dynamics, respectively. The first study [54, 95] focused on large QDs that emit between 1.8 and 3.7 eV. In these systems with very long lifetimes, the dynamics is totally governed by the QCSE and it is completely non-exponential: as the carriers recombine, the probability of recombination decreases. Strictly speaking, therefore, there is no lifetime. However, over very long times, the screening of the electric field disappears and it is then possible to extract a lifetime.

Stachursky et al. [96] discovered a biexponential dynamics on a set of quantum dots synthesized in the group of N. Granjean like those we have studied. Their interpretations take into account the fine structure of the QD exciton. The first possibility is that the short time corresponds to an effective time resulting from the combination between the radiative lifetime of the $|\pm 1\rangle$ and the transfer time to the dark state $|\pm 2\rangle$ via a spin-flip. The long time would then be the repopulation of the bright-state from the dark-state. This type of process had previously been observed in CdSe quantum dots [93, 129]. However, this explanation is not compatible with the temperature-dependent experiments: repopulation from the dark-state should be thermally activated, which is not observed. The second proposition is that the two dynamics correspond to recombinations from the two bright-states $|+1\rangle$ and $|-1\rangle$ which are split by the exchange interaction. However, according to the authors themselves, this explanation is not entirely satisfactory.

Moreover, Kako et al. [57] have also observed bi-exponential photoluminescence decays, attributing the fast dynamics to the size-dependence radiative time of the QDs, and the long component to the transfer from the WL, independent of the emission energy. It should be noted that this transfer time is of the order of ten nanoseconds.

About the second point, size and morphology affects other physical properties of QDs. Research conducted by Ref. [88] has further examined the fine-structure splitting (FSS) in GaN/AlN QDs. Their study, which combined micro-photoluminescence (μPL) and theoretical calculation, concluded that even a minor fluctuation in QD size or shape can induce a change in FSS energy of several meV for different QDs that have the same emission energy. In other words, the structural elongation or aspect ratio in a QD can significantly impact the FSS. More importantly, they found that the FSS depends on QD size. Contrary to what is seen in InAs/GaAs QDs, the bright-state splitting in GaN/AlN QDs drastically increases with increasing emission energy. Therefore, for large QDs (emitting below 3.4 eV), it approaches zero meV, while for small QDs (emitting above 3.9 eV), it can reach up to 7 meV.

The delineation by size does not solely influence the basic excitonic properties but also extends to affect the intricacies of many-body interactions, most notably, the characteristics of biexcitons. The binding energy of biexcitons is another feature that exhibits size-dependent variations. This energy arises from the Coulomb interaction, involving both attractive (electron-hole) and repulsive (hole-hole, electron-electron) interactions. The lateral size of a QD significantly impacts the biexciton binding energy, which can vary from -6 meV to +6 meV [92]. This effect was further studied by the team of Simeonov [89], who discovered that biexciton binding energy exhibits two regimes, predominantly governed by the dot height through the QCSE. The binding energy varies from +3 meV for the smallest dots to -11 meV for the largest ones. There is also a secondary variation of binding energy of opposite sign for dots having the same height but different lateral size. Therefore, large QDs emitting around 3.9 eV have a negative biexciton binding energy, unlike small QDs emitting above 4 eV.

Furthermore, the work of Hönig [90] delves into the behavior of two electron-hole pairs in wurtzite QDs. Their study found that hybrid biexcitons are dominant for QDs larger than 6 nm in lateral size. These findings contribute to the understanding of the fundamental

differences and complexities introduced by the coexistence of small and large QDs in the GaN/AlN system.

5.4 Conclusion

We have performed low temperature TRPL experiments on a single plane of GaN/AlN QDs, whose emission energy mostly lies above the bulk GaN bandgap. The PL data show a three-component dynamics: a first exponential decay with a short time-constant (0.3 ns), independent of photon energy, a second one that follows the expected evolution for the radiative lifetime with increasing QD height, and finally a very long component with a plateau-like behavior.

We attribute the fast dynamics to a nonradiative relaxation process of e-h pairs toward a dark state and the concomitant existence of a very long component, which shows up as a constant background in the PL decays, that corresponds to the reverse process where the dots come back to their original state.

Concerning the dynamics of the radiative recombination process, we have established that, in the absence of any screening of the built-in electric field, the PL spectrum of QDs with a normal height distribution presents a Gaussian lineshape with a characteristic time evolution that is easily described by an analytical model: after a pulsed excitation the position of the line maximum undergoes a redshift that varies linearly with increasing delay time and is accompanied by a decrease in the FWHM. This behavior originates from the combined effect of the quantum confinement and the QCSE, and constitutes a criterion to conclude on the possible occurrence of screening and/or many-body effects in the population dynamics within GaN/AlN QDs. Moreover, our analysis enables an improved precision concerning the determination of the energy-dependence of the QD radiative lifetime when compared to a method that involves a systematic study of the decay-profiles corresponding to different narrow PL-energy windows.

By completing previous results from other groups, our data provide new evidence that the dependence of the effective PL lifetime with emission energy follows a global trend that is an intrinsic feature of the GaN/AlN QD system where the built-in electric field acts as the most dramatic parameter. Numerical simulations, which show a good qualitative agreement over an energy range of 1 eV and six orders of magnitude for the effective PL lifetime when assuming a built-in electric field value of 7 MV/cm, enable to estimate that the dot height in our sample is distributed around a mean value of 1.6 nm ($\sim$ 6 MLs). Remarkably, in small QDs emitting at high photon energies, around 3.5-4.1 eV, and hence for which the impact of QCSE is less pronounced, we can evidence the effects of lateral confinement on the carriers. The latter affects the wave function extent and the emission energy but only slightly the carrier overlap and the corresponding oscillator strength (equivalently the radiative lifetime).

In addition to these findings, our temperature-dependent measurements underscore the absence of an observable shift in PL energy with varying temperature and the static nature of recombination dynamics. This indicates the persistence of deep carrier localization within the quantum dots, even at room temperature, demonstrating the absence of a non-radiative recombination channel. These results strongly suggest that GaN/AlN quantum dots display resilient quantum confinement and efficient radiative recombination across the temperature spectrum studied. Consequently, we can confidently assert the robust nature of the quantum confinement exhibited by GaN/AlN quantum dots.

In the course of our investigations, we have also turned our focus towards a sample, which consists of 10 planes of GaN/AlN Quantum Dots (QDs) displaying two distinctive morphologies. In this sample, we have identified a smaller subset of QDs that emit predominantly around 4.2 eV and a larger group of QDs with emission centered around 3.8 eV. These subsets are principally associated with island heights of 4 and 6 monolayers (MLs), respectively.

In essence, the 10 plane GaN/AlN QD sample with its two distinct morphologies presents a fascinating platform for future research, providing both experimental advantages and a

broader spectrum of behaviors to investigate. Its compatibility with the single plane sample findings further underscores its value in advancing our understanding of quantum dot systems.

Chapter 6

Carrier relaxation mechanisms in GaN/AlN QDs

This chapter is dedicated to providing a deep dive into the intricate world of carrier relaxation mechanisms within GaN/AlN quantum dots (QDs). Our investigative journey is structured to offer a thorough understanding of these mechanisms, enabling further development in quantum dot technologies and their practical applications.

To start with, Section 6.1 provides an overview of the chapter, establishing the context and relevance of our work. The content is structured to progressively build upon our comprehension of carrier dynamics in GaN/AlN QDs.

In Section 6.2, we examine the relaxation dynamics in non-degenerate pump-probe experiments, with subsections dedicated to studying the initial dynamics and larger timescale behaviors in single plane and 10 planes GaN/AlN QDs. An integral part of our investigation in this section involves conducting pump power measurements. These measurements enable us to examine the dynamics under varying carrier injection rates. Understanding these dynamics is essential for revealing the influence of multi-carrier injection on the observed carrier relaxation processes.

As we progress to Section 6.3, it focuses on the results from degenerate pump-probe experiments on 10 planes GaN/AlN QDs, providing a complementary perspective on the carrier dynamics and further emphasizing the nuances of these nanostructures.

Section 6.4 digs deeper into the rise time dynamics in non-degenerate pump-probe experiments. The study draws together observations from both small and large QDs to form a detailed picture of how carriers populate energy states within GaN/AlN QDs under different experimental conditions.

In Section 8.6, we give an overview of all the characteristic times observed in our studies, tying together the various threads of investigation and providing a comprehensive understanding of the relaxation dynamics in these systems.

The chapter culminates with Section 6.6 where we present our conclusions drawn from these studies, summarizing the key findings and discussing their implications for future research and technological applications of GaN/AlN QDs.

Through this chapter, we aim to contribute to the broader understanding of carrier relaxation mechanisms in quantum dots, with particular emphasis on the behaviors unique to GaN/AlN QD systems.

6.1 Introduction

In the previous chapter we studied by TRPL the lifetime of electron-hole pairs trapped on the lowest energy states of the quantum dots. We will now focus on the above processes, i.e. the relaxation from the wetting layer and along the excited states. For this type of study, the PL is of no help since it only measures the dynamics of thermalized carriers. On the contrary, the pump-probe technique measures the dynamics of non-equilibrium carriers. The principle

is as follows: a first ultra-short and very intense laser pulse, called *pulse-pump*, creates a population of electron-hole pairs at a given energy. We then measure the deviation ΔT from the linear transmission T_0 of a second pulse, *the probe*, less intense and delayed with respect to the pump. If the intensity of the probe is sufficiently low with respect to the pump, the latter measures the linear transmission of the sample as it has been disturbed by the pump. The signal is caused by the partial population of the excited states under the effect of the pump which decreases the absorption from the ground state of the system leading to an increase in the transmission which lasts for the lifetime of the tested excited state. Sometimes, there is the possibility of absorption of a probe photon from an excited state populated by the pump pulse towards a state which was not directly accessible from the ground state. There is then an induced absorption which gives rise to a positive differential transmission. If pump and probe have the same photon energy, the experiment is said to be degenerate. The differential transmission is measured at the energy at which the photocarriers are created. The signal is instantaneous and we only have access to the depopulation dynamics of the tested state. If, on the contrary, pump and probe have different energies, the experiment is said to be non-degenerate. The signal only appears when the carriers relax from the energy at which they are created towards the level tested by the probe. We then have access to the population and depopulation dynamics of the tested state.

In what follows, we will report the results obtained with both variants of the experiment. In a first part, we will present non-denegerate pump-probe results obtained on the two samples. Additionally, we supplement our study with degenerate experiments conducted on the 10 plane of dots sample. The two series of experiments were carried out at room temperature and we studied the influence of the excitation power on the dynamics. Along with the differential transmission, we measure the PL spectrum. Thus, in the case of the sample with 10 dot planes, we know at what energy the photocarriers created by the pump pulse recombine.

6.2 Relaxation dynamics in non-degenerate PP experiment

The principle of the experiment is schematized in the energy diagram presented in figure 6.1a. The energy levels represented are the following: E_0 is the fundamental level of the quantum dot (unpopulated dot), E_1 is the radiative state (bright state $|\pm 1\rangle$ in the excitonic representation), and E_3 is the energy at the bottom of the continuum of state formed by the wetting layer. The energy E_3 of the pump is fixed for all the experiments. It is chosen so as to create the electron-hole pairs in the wetting layer. The energy of the probe is tunable between E_3 and E_1 which is the energy of the maximum of the PL peak.

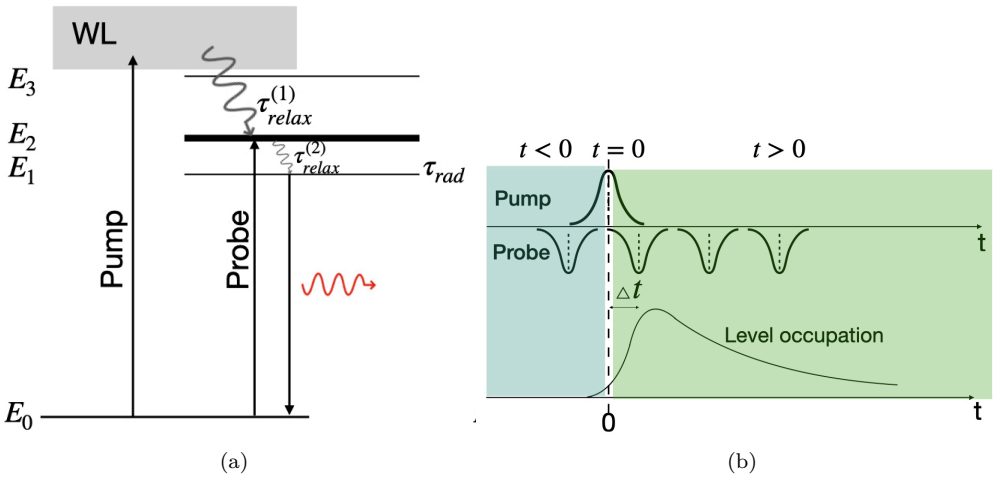

(a) (b)

FIGURE 6.1: Schematic representation of the non-degenerate pump-probe experiment on the energy level diagram of the QD.

The population at the tested level, with energy E_2, is not expected to increase instantaneously with the arrival of the pump but to build up gradually with a delay Δt related to the relaxation process from the wetting layer characterized by the time constant $\tau_{relax}^{(1)}$ (Fig 6.1b). Using the pulse excitation (pump), we can create an electronic population in the WL (energy E_3) that relaxes to the lowest excited state (energy E_1) and afterwords depopulates radiatively (see Fig. 6.1a). By changing the energy of the probe, we can access the population of any energy state. Adding the temporal delay between pump and probe allows exploring the relaxation process (see Fig. 6.1b). Using the non-degenerate pump-probe experiment, we can trace the carriers from the top to the bottom of excited energy band.

TABLE 6.1: Excitation parameters for non-degenerate pump-probe experiments. The first part of the table and the second one contain the excitation conditions for 1 plane GaN/AlN QDs and 10 planes GaN/AlN QDs samples experiments respectively.

Energy (eV)	**P** (mW)	**Energy per pulse** (nJ)	**Photon flux** (photons $\cdot$ cm^{-2})
Pump			
4.66	3±0.5	15	$2.5 \cdot 10^{14}$
Probe			
4.59			$7.2 \cdot 10^{13}$
4.51			$7.4 \cdot 10^{13}$
4.43			$7.5 \cdot 10^{13}$
4.35			$7.6 \cdot 10^{13}$
4.28	0.3±0.1	1.5	$7.8 \cdot 10^{13}$
4.20			$7.9 \cdot 10^{13}$
4.13			$8 \cdot 10^{13}$
4.07			$8.2 \cdot 10^{13}$
4			$8.3 \cdot 10^{13}$
3.94			$8.4 \cdot 10^{13}$
Pump			
4.66	6±0.5	30	$5.3 \cdot 10^{13}$
Probe			
4.59			$1.5 \cdot 10^{13}$
4.51			$1.5 \cdot 10^{13}$
4.43			$1.6 \cdot 10^{13}$
4.35			$1.6 \cdot 10^{13}$
4.28	0.6±0.1	3	$1.6 \cdot 10^{13}$
4.20			$1.6 \cdot 10^{13}$
4.13			$1.7 \cdot 10^{13}$
4.07			$1.7 \cdot 10^{13}$
4			$1.7 \cdot 10^{13}$
3.94			$1.8 \cdot 10^{13}$

In our experiment we used two-color femtosecond pulses: E_{pump} at 4.66 eV and E_{probe} in the range from 3.94 to 4.59 eV with a repetition rate of 200 kHz. We performed a series of non-degenerate pump-probe experiments at RT on two samples: 1 plane and 10 planes of GaN/AlN QDs.

In a non-degenerate pump-probe experiment, both the spatial profiles and the intensities of the pump and probe beams play critical roles in the accurate measurement and interpretation of the system dynamics. To ensure that the probe beam actually investigates the area of the sample excited by the pump, it is crucial that the pump spot diameter on the sample is larger than the one of the probe. In this way, the probe beam probes an area that is uniformly

excited by the pump, ensuring that the detected signals are representative of the pump-induced changes and not influenced by unexcited regions of the sample. In order to estimate the size of the excitation spot and to have a precise overlap, the beam profiles of the pump and the probe were measured. The sensitivity of the beam profiler camera being very low below 4.3 eV, only high energy probes were captured. The average waist diameter of the pump spot was about 0.1 mm while, for the probe the excitation spot varied around 0.06 mm (Fig. 6.2). Details of the excitation parameters are summarized in Tab. 6.1. Simultaneously, the probe's optical intensity should be lower than the pump's to avoid the probe beam causing nonlinear optical effects in the sample. If the probe beam's intensity is too high, it could induce its own changes in the sample, complicating the interpretation of the data by introducing additional signals not associated with the pump-induced dynamics.

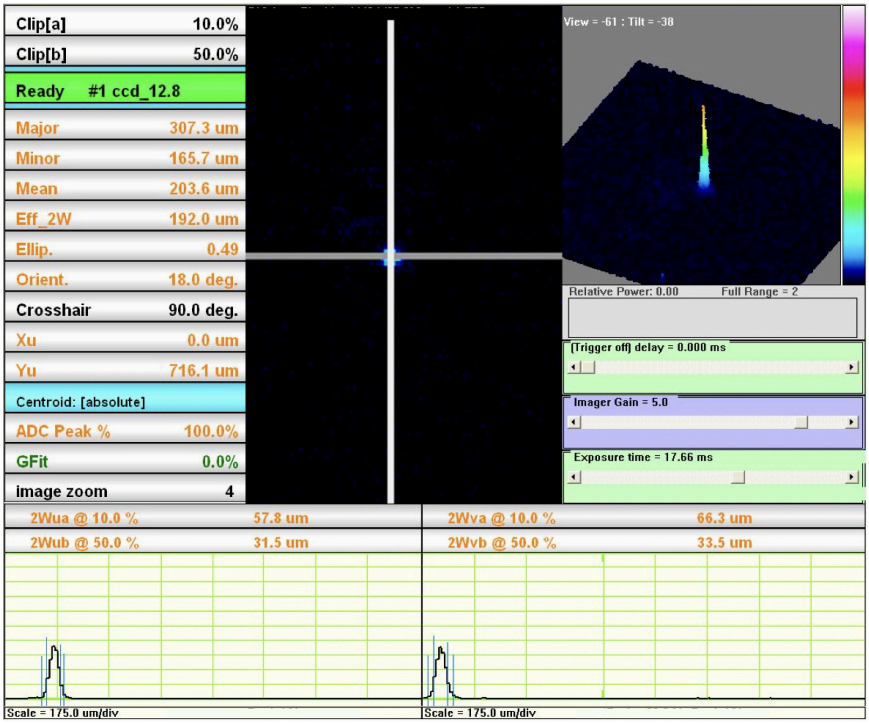

FIGURE 6.2: Capture of the beam profile of the probe signal tuned to 4.35 eV.

Regarding the description of the studied samples in Sec. 3.2.1 where the density of QDs was estimated to be in the range of 10^{10}-10^{11} cm^{-2} [49], the non-degenerate pump-probe experiment has been performed in a regime of much higher excitation. Unfortunately, this is necessary if we want to keep a high signal to noise ratio.

Fig. 6.3 presents a typical result of the differential transmission signal in the non-degenerate pump-probe experiment. The maximum of the signal corresponds to the moment when the probed level has the highest population resulting in a minimum of absorption. For convenience, this instant is chosen as zero-delay time since the population of the probe level a priori presents a delay with respect to the arrival of the pump. We performed the experiments on two different time scales with different temporal resolutions in order to study the rise and relaxation dynamics of the signals.

In all cases, a negative signal is recorded. It is present from the negative delays, i.e. when the probe precedes the pump, and persists after complete relaxation. We are not going to discuss this phenomenon for the moment, we will devote a specific paragraph to it later in this chapter. This negative background was subtracted from the decay profiles to make the analysis that we present now.

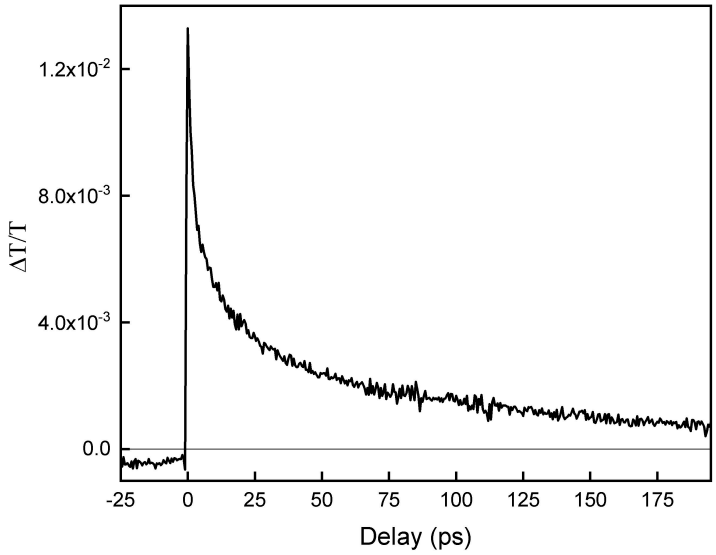

FIGURE 6.3: Typical transient differential transmission signal measured on the 10-plane sample in the two-color pump-probe experiment at room temperature. $E_{pump} = 4.66$ eV, $E_{probe} = 4.5$ eV.

6.2.1 1 plane GaN/AlN QDs

Initial investigation of immediate dynamics

We first present the immediate dynamics of the system by studying the rise times of the signals as a function of the probed energy. We will do this analysis by considering that the dynamics of appearance of the signals is relative to the relaxation process which starts from the wetting layer and extends to the probed energy states (see Fig. 6.1a). This assumption is not necessarily true. Indeed, if we consider a state supplied with carriers with a characteristic time $\tau^{(1)}_{relax}$ and which depopulates with a lifetime $\tau^{(2)}_{relax}$, the number of carriers $n(t)$ is given by an elementary equation

$$n(t) = \frac{e^{-t/\tau^{(1)}_{relax}} - e^{-t/\tau^{(2)}_{relax}}}{\tau^{(1)}_{relax} - \tau^{(2)}_{relax}} \tag{6.1}$$

which is invariant under a permutation of $\tau^{(1)}_{relax}$ and $\tau^{(2)}_{relax}$. The rise time observed experimentally can therefore correspond to the life time of the tested state if it is shorter than the feeding time. However, we will see later that this hypothesis will be confirmed by comparing the present results with the TRPL data obtained in the previous chapter. With this point clarified, to ensure a thorough examination of these short delay dynamics, we scale the experiments for delays ranging from -1 and 2 ps.

Figure 6.4 presents a detailed overview of our findings. This figure shows the differential transmission signals of GaN/AlN QDs as a function of delay between pump and probe pulses at different E_{probe}. The dashed line on the figure denotes zero picosecond delay, serving as a reference point to comprehend the changes in the signal over time. As we delve deeper into the generated signals, we take note of the following characteristics: the rise signal of the differential transmission ($\Delta T/T$) does not conform to a straightforward monotonic trend. Instead, we notice an unusual overlapping of what appears to be an oscillation or a negative signal with the onset of the primary signal. This peculiar overlap effectively blurs the rise of the signal, making it challenging to determine the precise rise time.

However, despite this intricate complication, it is safe to conclude that the rise time, irrespective of the probed energies, is always confined within a maximum limit of 1 picosecond. This

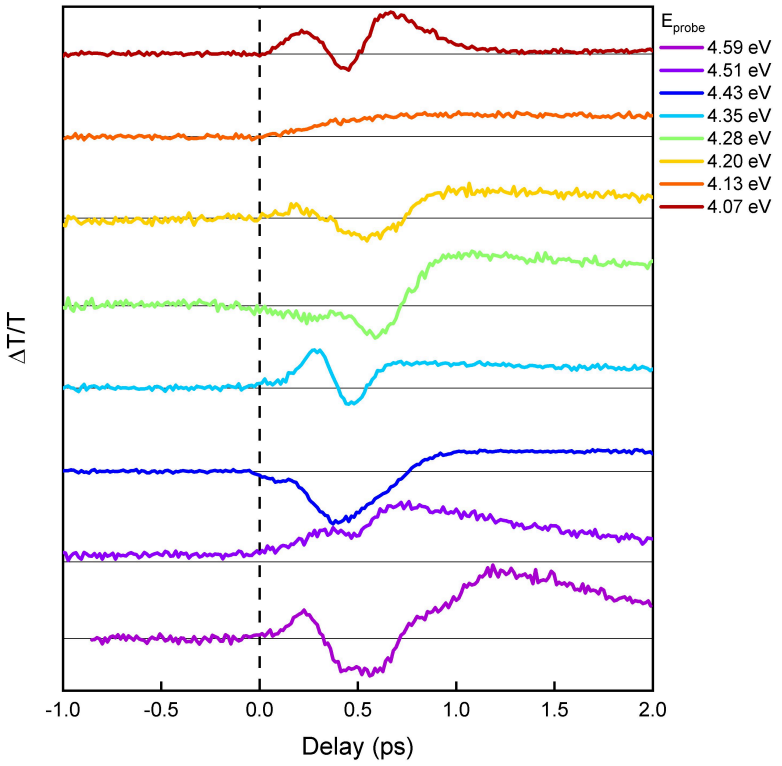

FIGURE 6.4: Differential transmission signal of 1 plane GaN/AlN QDs ensemble as a function of time delay between pump and probe pulses at different E_{probe}. The dashed line represents zero ps delay.

indicates a rapid dynamics that set the stage for the subsequent behavior of the carriers in the GaN/AlN quantum dots.

Relaxation dynamics over larger time scales

Futher, we investigate the relaxation dynamics of the $\Delta T/T$ - signal on a full time scale of about 200 ps. Fig. 6.5 presents the signal of differential transmission as a function of the time delay between pump and probe pulses for E_{probe} equal to 4.2, 4.28, 4.51 and 4.59 eV. We observe that for $E_{probe} > 4.5$ eV i.e. when it approaches the degeneracy with E_{pump}, the dynamic is monoexponential and extremely fast. For lower energies, the dynamics is very well reproduced by a double exponential function of which we have named τ^{l}_{relax}, τ^{sh}_{relax} the long time constant and short, respectively.

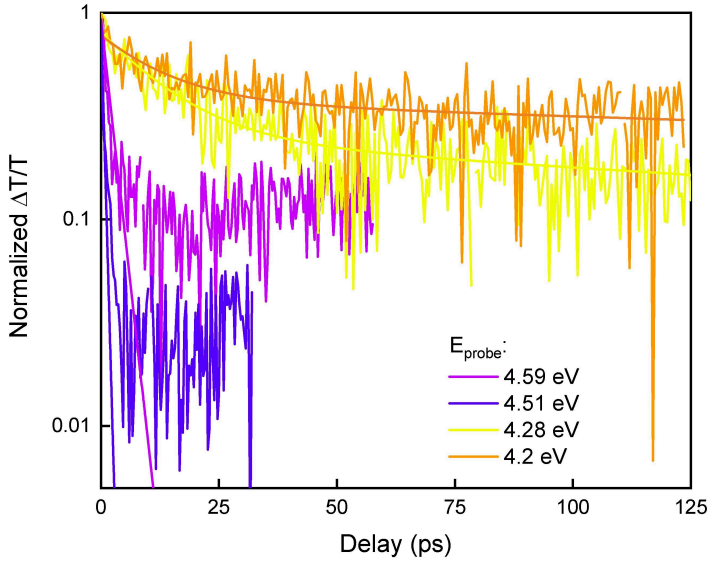

FIGURE 6.5: Normalized differential transmission signal decay of 1 plane GaN/AlN QDs ensemble as a function of time delay between pump and probe pulses at different E_{probe}.

All the characteristic time constants investigated for the 1-plane sample of QD GaN/AlN are shown in Fig. 6.6. It combines the results of TRPL (10 K) and non-degenerate PP (RT) experiments. The black dashes on the upper scale of the graph mark the energy of the pump, as well as the different values taken by the energy of the probe. It should be kept in mind that the two series of experiments were carried out at different temperatures (10 K for the TRPL and room temperature for the PP), even if the TRPL experiments in temperature (sec. 5.1.4) did not demonstrate any thermally activated non-radiative phenomena.

As previously stated, when $E_{probe} > 4.5$ eV, the dynamics is monoexponential with a characteristic time constant $\tau^{sh}_{relax} \simeq 1$ ps. When 4.1 eV $< E_{probe} <$ 4.5 eV, τ^{sh}_{relax} reaches a value $\simeq 20$ ps while the second time constant, τ^{l}_{relax}, is very close to the fast component τ_s associated with PL decay. Thus, when the probe is resonant with the photoluminescence, the relaxation dynamics of the pump-probe signal corresponds to the lifetime of the electron-hole pairs in the quantum dots. Below 4.1 eV, no signal could be detected. Note that the energy range for which a biexponential dynamics is observed corresponds to the structure that we have identified as a possible excited state of QDs also emitting at 3.8 eV, in the sample with 10 dot planes (Fig 5.15 and 5.16).

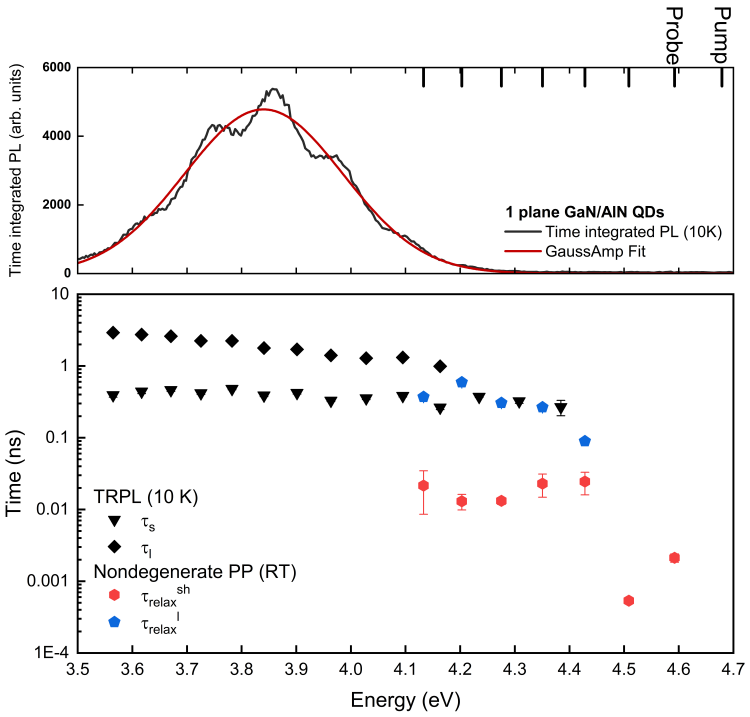

FIGURE 6.6: Top figure, time integrated TRPL spectrum of 1-plane GaN/AlN QDs ensemble measured at 10K (black curve) with a gaussian fit (red curve). Bottom figure, radiative lifetime τ_l (black diamonds) and fast time constant ascribed to a nonradiative process τ_s (black down triangles) as a function of emission energy. Blue pentagons and red circles correspond to the long τ^{l}_{relax} and the fast τ^{sh}_{relax} relaxation time constants, respectively, obtained from the non-degenerate pump-probe experiment at RT.

6.2.2 10 planes GaN/AlN QDs

On this sample, it is possible to carry out a detailed study according to the size of the QDs. However, the metallic mask deposited on the surface of the sample makes it possible to identify up to 14 different positions. If for each of these positions, we vary the wavelength of the probe over almost ten values, we see that it is not possible to carry out the complete study, especially since the wavelengths are modified manually by acting on the phase-matching angle and the delays inside the parametric amplifier.

As discussed previously, the sample of interest poses a significant degree of complexity due to the presence of two distinct morphologies and the size gradient of the quantum dots within the sample. To begin our analysis of this sample, we first focus on the ensemble of smaller dots, where the center of the PL line is situated around 4.3 eV. This specific group is found at the $r1\_11$ spot on the sample.

Subsequently, we will broaden our investigation to include the lower energy dots located at position $r1\_2$, which emit around 3.8 eV. An additional consideration leading us to begin our study with smaller dots is to rule out the potential influence of the screening effect, which could distort our findings. In these small quantum dots, the oscillator strength is high and the Stark effect is negligible, thus offering a cleaner platform for our exploratory efforts.

We make here the same assumption as for the 1-plane sample that the rise dynamics of the signal is related to the feeding by the wetting layer of the probed level while the decay relates to the thermalization towards the lower energy states. The consistency between the lifetimes obtained by the different experimental techniques that we used will support this interpretation in the paragraph 6.3.

Negative background

As mentioned earlier in this chapter, a signal is present for negative delays, i.e. before the pump arrives. We have systematically removed it from the results presented so far in order to focus on the relaxation dynamics. We propose to study it here in more detail in order to give some possible explanations for its presence. This signal is negative and remains present even when the repetition rate decreases to 50 kHz, which corresponds to a period of 20 µs.

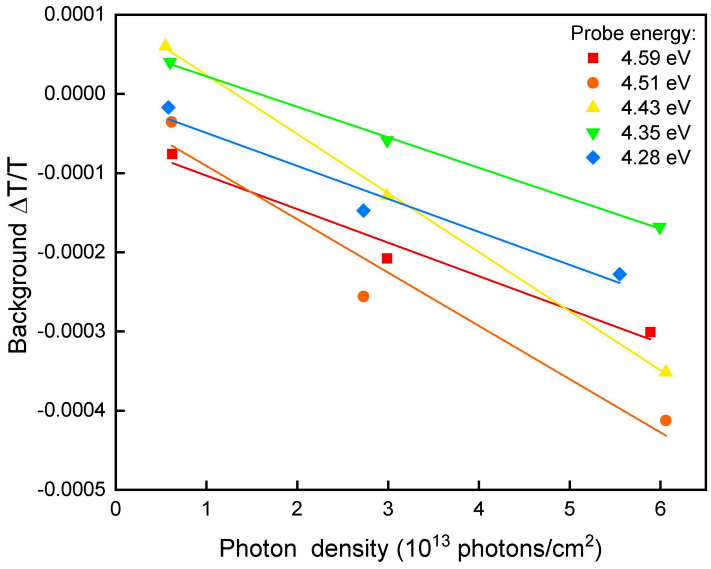

FIGURE 6.7: Negative background signal before zero time delay as a function of pump photon density measured at different E_{probe} at $r1\_11$ position on the sample.

We can see on the figure 6.7 that, for all probe energies, the background increases linearly in absolute value with the incident photon flux. This indicates that we are not dealing with an artifact but that the pump does populate long-lived states from which probe absorption becomes possible. Indeed, it is an induced absorption since the signal is negative. If this is the case, these states have a particularly long lifetime, of the order of magnitude of the 20 µs period mentioned above. The figure 6.8 shows the evolution of the background as a function of the energy of the probe for the different positions marked on the sample by the metal mask. First of all, we notice that the general trend is the same whatever the position and whatever the size of the dots. The observed behavior suggests that these long-lived states are most probably associated with specific energy levels within the QDs. The increasing absolute value of the background as the probe energy approaches 4.59 eV suggests that there are long-lived states around this energy that are efficiently populated by the pump pulse. The data show a maximum around $E_{probe} = 4.2\ eV$ and a decrease for higher energies. It could indicate that these long-lived states are associated with particular energy levels that are common across different QD sizes, which would be populated when the pump pulse has sufficient energy (around 4.2 eV in this case).

The observed irregularity at 4.2 eV could be due to several factors. If there is already significant absorption at this energy (as suggested by PLE spectrum see Fig. 5.15), the induced absorption signal could indeed be masked or reduced. This is because the probe pulse may already be significantly absorbed at this energy, leaving fewer photons available for additional absorption due to the pump-induced states. Another possibility is that there may be other energy states or processes becoming significant at this energy, which could interfere with the usual dynamics of the pump-probe system. This could include processes like multiphoton absorption or energy transfer processes that can alter the energy distribution of the excited states.

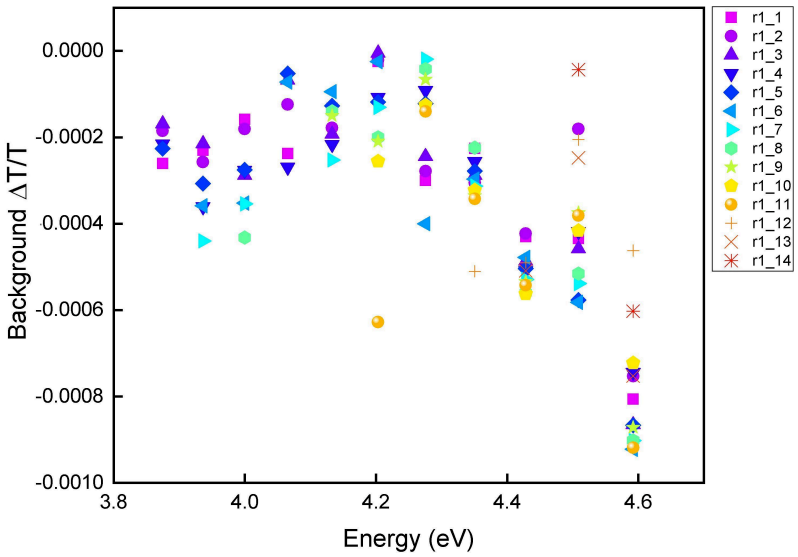

FIGURE 6.8: Background level of the differential transmission signal before zero time delay as a function of probe energy at different positions on the 10 planes GaN/AlN QDs sample.

A possible explanation is that some of the carriers photocreated by the pump are captured on deep defects in the aluminum nitride matrix, which would explain the particularly high lifetime. In our research, we have also considered the study of photochromism and the effects of point defect charge states on optical absorption in aluminum nitride (AlN) [130], specifically under UV excitation. This research has uncovered that the change in transmittance (or absorption) with increased power of UV excitation is both monotonically enhanced across the observed spectral range and gradually approaches saturation. Interestingly, these alterations are also observed to be metastable at room temperature, with absorption coefficients showing only minor changes on a daily basis. These findings confirm the potential for UV excitation to induce long-lasting absorption changes at the defect levels in AlN, which can persist for hours.

While this is a significant observation in the context of AlN studies, it holds minimal impact on our research with GaN/AlN Quantum Dots due to the drastically different timescales. Therefore, in our analysis, we have decided to subtract this background absorption related to UV-induced defects. This is due to the understanding that these prolonged changes would not interfere significantly with our quantum dot experiments, which occur over much shorter durations. As a result, this treatment allows for a more accurate interpretation of our experimental data, focusing on the immediate effects rather than long-term, metastable changes.

Unravelling the complexities of differential transmission signals in extended delays

Dependence of relaxation dynamics on pump power: Firstly, we have performed pump-probe experiments as a function of excitation power. The characteristics of the pump and probe pulses, in particular the photon fluxes as a function of the average powers used, are given in the table 6.2. It appears that the photon density is larger than the surface density of QDs. These measurements were performed on the position $r1\_11$ of the sample with 10 planes of dots, i.e. a region in which the high energy dots are predominant.

TABLE 6.2: Excitation parameters for power dependent non-degenerate pump-probe experiment.

Energy (eV)	**P** (mW)	**Energy per pulse** (nJ)	**Photon flux** (photons $\cdot$ cm^{-2})
Pump			
	7±0.5	35	$6 \cdot 10^{13}$
4.66	3.5±0.5	18	$3 \cdot 10^{13}$
	0.7±0.1	3.5	$6 \cdot 10^{12}$
Probe			
$4.59 - 3.94$	0.6±0.1	3	$1.5 - 1.8 \cdot 10^{13}$

In our investigations, we performed a set of non-degenerate pump-probe experiments varying both pump power and probe energy. From these experiments (see Fig. 6.9), we noted that the differential transmission decays did not follow an exponential pattern, which is typically associated with a lifetime relaxation process. Instead, the decay we saw seemed to be a mix of something like a power law and a longer decay, which might be exponential. This kind of decay did not match the typical lifetime models we would expect. In order to better understand which phenomena are responsible for the thermalization of the carriers towards the dots, we have modeled the differential transmission decays with a three-level model and compared these simulations with the experimental results. We have modeled the relaxation of electron-hole pairs by the following set of rate equations:

$$\begin{aligned} \frac{dn_2}{dt} &= -\alpha \frac{N_0 - n_1}{N_0}\, n_2^2, \\ \frac{dn_1}{dt} &= +\alpha \frac{N_0 - n_1}{N_0}\, n_2^2 - \frac{n_1}{\tau_{rad}}, \\ \frac{dn_0}{dt} &= \frac{n_1}{\tau_{rad}}, \end{aligned} \tag{6.2}$$

where n_2, n_1 and n_0 represent the number of photocarriers at the probe energy, thermalized inside the dots and in the ground state, respectively. N_0 is the number of available states inside the dots. τ_{rad} is the QD radiative lifetime and α is a probability per unit times per electron-hole pair that characterises the efficiency of the multi-carrier process involved in the thermalization.

This model is able to account for the dynamics evolution with the carrier density, *via* the term n_2^2, as well as the saturation of the dot levels, *via* the $\frac{N_0 - n_1}{N_0}$ term. The efficiency transfer of carriers from the probe energy towards the dots depends simultaneously on the number of unoccupied dots, on the carrier density and on a coefficient α which quantifies the intrinsic efficiency of the considered phenomenon but which is for the moment only an adjustable parameter. When the saturation of the dots is reached, the τ_{rad} lifetime governs the relaxation of the carriers that occupy higher energy states.

In our approach, we introduce both the discrete level population and carrier density as they offer two distinct but complementary perspectives on the same system. In our model, the discrete level population, labeled as n_2, n_1, and n_0, indicates the precise quantum states occupied by the carriers. This perspective is essential when we want to examine the processes

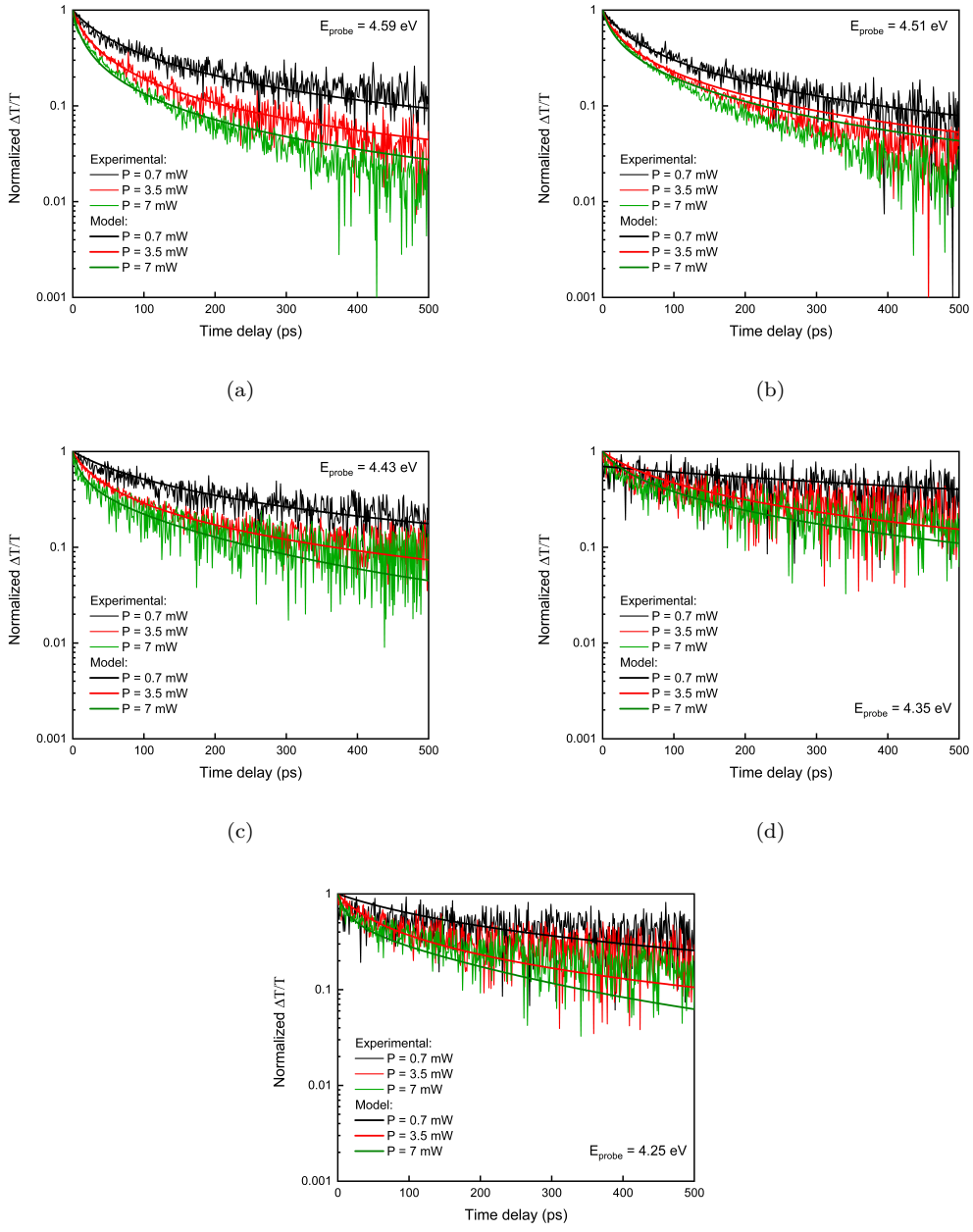

FIGURE 6.9: Comparison between the power dependence of the pump-probe dynamics and the three-level model for different probe photon-energy: *a*)4.59 eV, *b*)4.51 eV, *c*)4.43 eV, *d*)4.35 eV and *e*)4.28 eV.

at an individual level, such as how carriers are moving from one state to another, and the specific rates at which these transitions occur. Conversely, the carrier density informs us about the total number of carriers present in the system, regardless of their specific states. When dealing with an ensemble of QDs, we have to take into account the statistical distribution of carriers across the entire ensemble. Each QD is not identical, and the unique properties of individual QDs, such as their size and shape, can affect the behavior of carriers within them. Hence, the carrier density provides a more extensive, macroscopic view that averages across the entire ensemble. This measure becomes crucial when we are concerned with properties and behaviors on a wide scale system, like how the system as a whole responds to shifts in external conditions, including changes in pump power or probe energy. So, the combination

of the discrete level population (which illustrates the behavior within individual QDs) and the carrier density (which averages over the entire ensemble and acknowledges the role of the wetting layer) delivers a comprehensive representation of the system and its behavior.

Figure 6.9 shows attempts to fit the experimental decays with the three-level model. N_0 is fixed for all decays and the carrier densities are expressed as a fraction of $N_0 \cdot \alpha$ and n_0 are then varied to reproduce the shape of the decays. For a given probe energy, α is kept constant and only the initial carrier density n_0 is responsible for the change in dynamics. We see that the model reproduces quite well the experimental decays, especially at short times and for high probe energies, i.e. when we are close to the degeneracy between pump and probe. Figure 6.10 shows the evolution of the product $\alpha\ N_0$ with the photon energy of the probe. It can be seen that the efficiency of the quadratic relaxation process decreases as the probe energy decreases relatively to the pump energy. A linear fit allows to extract a quantitative evolution:

$$\alpha \cdot\ N_0(\mathrm{ps}^{-1}) = 0.54\ E_{probe} - 2.32 \tag{6.3}$$

This expression allows to extrapolate that $\alpha = 0$ when $E_{probe} = 4.28$ eV, i.e. when the probe is almost resonant with the PL peak maximum. Thus, the occurrence of multi-pair processes gradually decreases until they disappear when the carriers are thermalized in the dots.

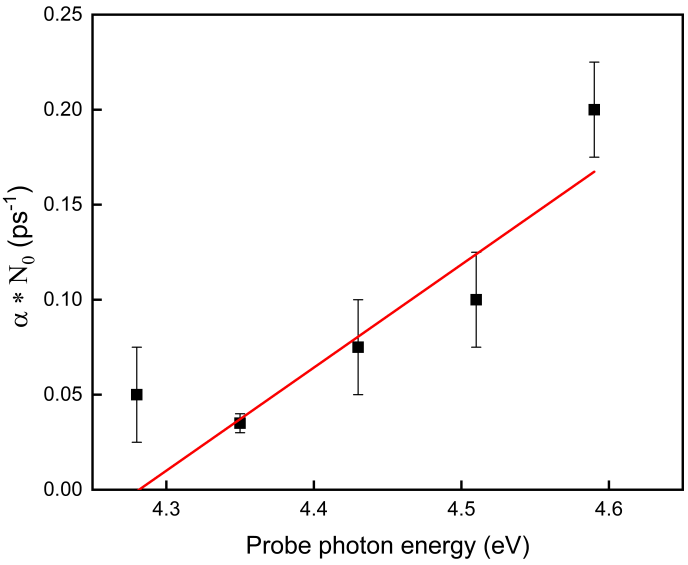

FIGURE 6.10: Evolution of the product $\alpha \cdot N_0$ with the probe photon-energy.

Figure 6.11 shows the evolution, as a function of probe photon energy, of the ratio $n_0/n_{0\ max}$ where n_0 is the initial population of carriers at a given E_{probe} while $n_{0\ max}$ is the initial population when the probe power reaches its largest value (7 mW). It reflects the efficiency of the conversion of probe photons to electron-hole pairs and their subsequent transfer to the energy states being probed. The two horizontal lines are the ideal values expected for these ratios if the photon electron-hole pair conversion efficiency as well as the transfer to the state tested by the probe were both 100 %. If we take into account the error bars, except for the data at 4.51 eV, the ratios of the initial populations are indeed in the power ratio. This analysis shows that we can therefore explain the variation in dynamics as a function of the power with a model which includes a quadratic recombination term and this, by varying the population in proportions compatible with the experimental conditions. However, the fact that sometimes the ratios are quite different from the ideal value is an indication that the conversion and transfer processes are not fully efficient and that their efficiency can vary depending on the conditions of the experiment, such as the power of the pump and the photon energy of the probe. It can also indicate other potential factors impacting the system, such

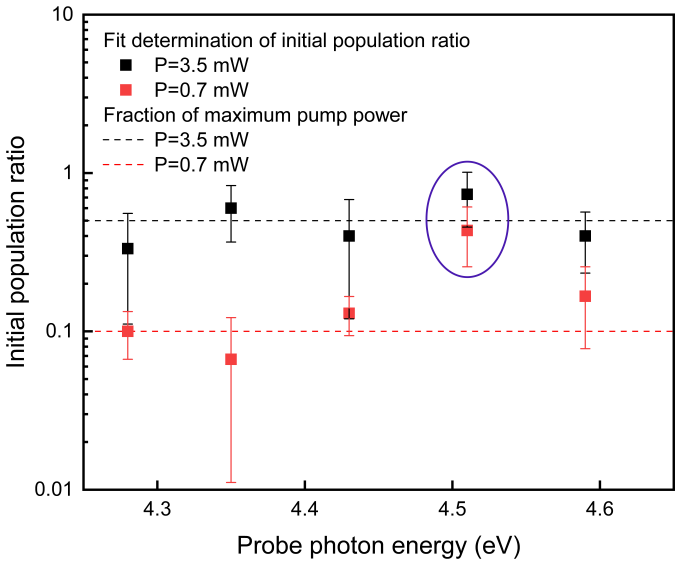

FIGURE 6.11: Model extracted values of the initial population of electron-hole, expressed as a fraction of the maximum population related to the maximum value of the pump power, as a fonction of the probe photon-energy.

as variable quantum dot properties, carrier recombination processes, saturation effects, and external influences like temperature or impurities.

Thus, we found that this system of equations (Eq. 6.2) aligns well with our experimental decays. However, because the dynamic of these equations depends on the number of carriers and requires a numerical solution rather than an analytical one, we cannot derive a relaxation lifetime from it. This underscores the complexity of the processes at play within the GaN/AlN QDs and the challenges inherent in extracting straightforward metrics such as relaxation lifetimes.

To acquire a quantitative average lifetime $\langle\tau\rangle$, we have chosen to adjust the decays with a stretched exponential:

$$y(t) = y(0)e^{-(\frac{t}{\tau_0})^{\delta}}, \tag{6.4}$$

where τ_0 is the decay time and δ the dispersion factor with $0 < \delta < 1$. When δ is equal to 1, $y(t)$ is a simple exponential function with time constant τ_0 while, for $\delta = 0$, it is a constant fonction. The behavior of $y(t)$ for intermediate values of δ is shown in figure 6.13. All curves have an intersection point for $t = \tau_0$. For $t < \tau$, the stretched exponential has a faster dynamic than the exponential, while for $t > \tau_0$ this dynamic is slowed down. The use of the stretched exponential makes it possible to define an average relaxation time $\langle\tau\rangle$ which is equal to the area contained under the curve $y(t)$ and which is expressed as:

$$\langle\tau\rangle \equiv \int_0^{\infty} e^{-\left(\frac{t}{\tau_0}\right)^{\delta}} dt = \frac{\tau_0}{\delta}\,\Gamma\left(\frac{1}{\delta}\right), \tag{6.5}$$

where Γ is the *gamma function*.

As shown in Fig 6.12, in the majority of cases, the dynamics that we encounter have complex shapes that are not exponential and that evolve according to the energy of the pump. This is an additional argument for the use of this model, that is able to reproduce these different dynamics with a limited number of adjustable parameters. Indeed, the study of the 10-plane

sample leads to the manipulation of a large number of data which depend on the position on the sample and the energy of the probe. Thus, it is convenient to compare different dynamics based on a single average lifetime as a function of parameters such as photon density, probe energy, and so forth.

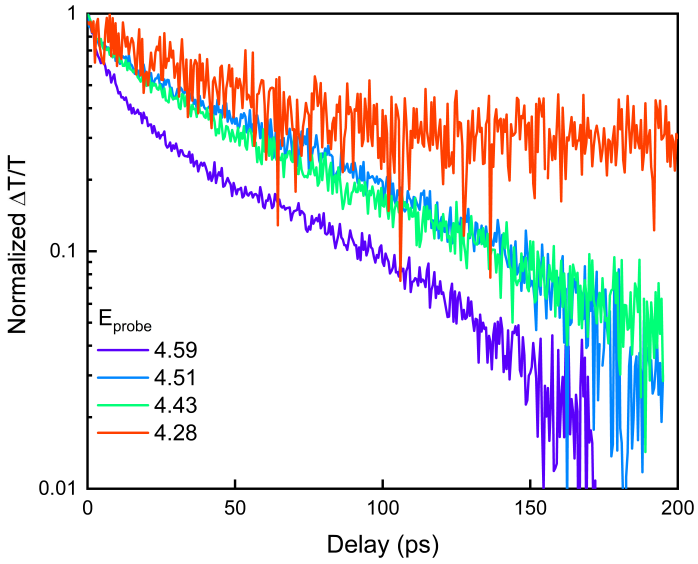

(a)

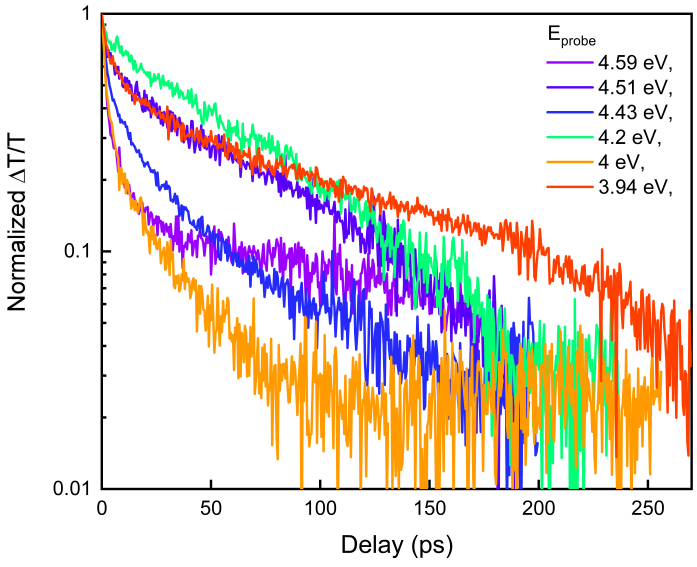

(b)

FIGURE 6.12: Normalized differential transmission signal decays measured at $r1\_11$ (small QDs) (a) and $r1\_2$ (large QDs) (b) positions on the 10 planes of GaN/AlN QDs sample excited with the E_{pump} at 4.66 eV and tested with different E_{probe}.

Next is presented the comparison between a two-exponential fit and a stretched exponential fit, since the two-exponential decay was used in the single-plane experiment. Examples of fit with a double-exponential and a stretched exponential are shown in figure 6.14. This is the differential transmission measured at position $r1\_6$ for a probe energy of 4.51 eV. The blue

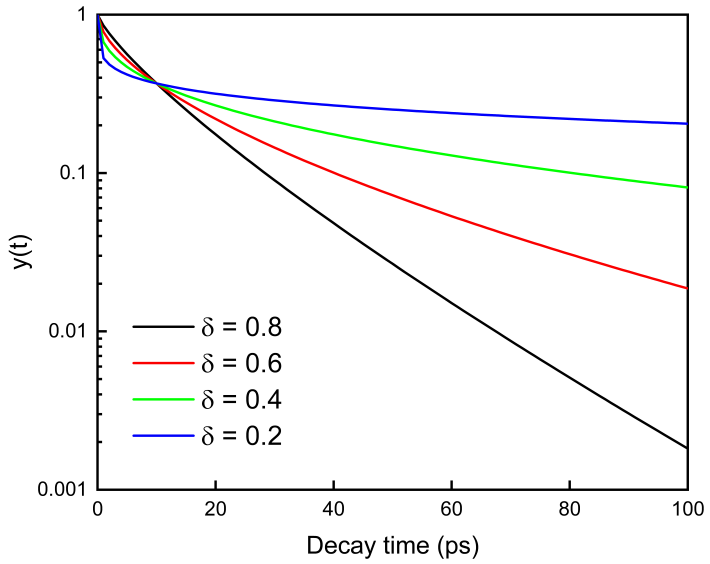

FIGURE 6.13: A plot of the differential exponential function $y(t) = y(0)\ e^{-(\frac{t}{\tau})^{\delta}}$ with $\tau = 10$ ps and $\delta = 0.2,\ 0.4,\ 0.6,\ 0.8$.

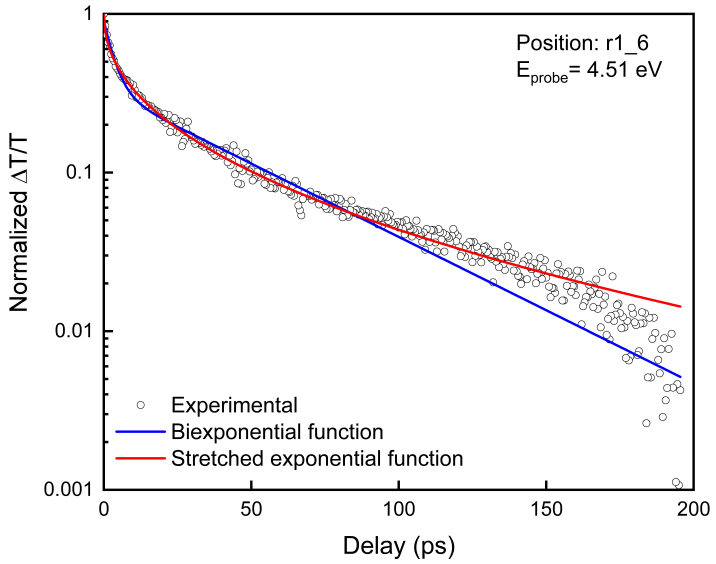

FIGURE 6.14: Example of adjustment of the pump-probe dynamics (circles) with a bi-exponential function (blue line) and a stretched exponential (red line).

solid curve is a fit with a sum of two exponentials:

$$I(t) = A_1\ e^{-\frac{t}{\tau_1}} + A_2\ e^{-\frac{t}{\tau_2}},$$

where $A_1 = 0.58$, $A_2 = 0.33$, $\tau_1 = 3.54$ ps and $\tau_1 = 47$ ps. The red continuous curve is a fit with the stretched exponential function

$$I(t) = I(0)\ e^{-\left(\frac{t}{\tau_0}\right)^{\delta}},$$

with $\tau_0 = 7.74$ ps and $\delta = 0.45$. We find that if, at first glance, the experimental dynamics suggests a bi-exponential behavior, the stretched exponential function better reproduces the experimental curve over two orders of magnitude. Considering all the reasoning for using the stretched exponential fit, we choose to continue with it for consistency and comprehensive understanding.

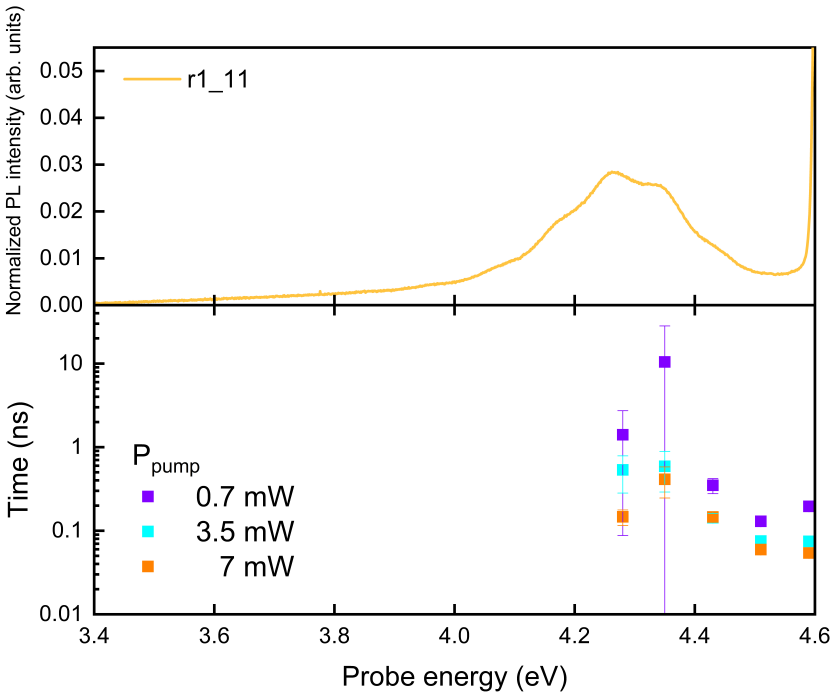

FIGURE 6.15: On the top there is the PL spectrum of the QDs ensembles measured at $r1\_11$ position on the sample, on the bottom presented the relaxation mean time constants $\langle \tau_{relax} \rangle$ extracted from the differential transmission decay signal measured at different power of the pump.

Hence, having established an effective methodology for analyzing our findings, let us now proceed to examine the actual results obtained from our study. Figure 6.15 shows the PL spectrum at the $r1\_11$ position and the evolution of the average relaxation time, $\langle \tau_{relax} \rangle$ with the probe energy for three different pump pulse powers (7, 3.5 and 0.7 mW). We first notice that the global behavior is preserved when the incident photon density is modified, namely a slowing down of the dynamics when the probe tends to be resonant with the luminescence. From the other side, the characteristic times decrease with the pump power. This behavior is summarized in Fig. 6.16 which presents the time constants as a function of the incident photon flux for the different probe energies used. On one hand, the acceleration of the dynamics with increasing pump power suggests that multi-carrier scattering mechanisms, such as Auger effect [131, 132, 110], exciton-exciton annihilation [133] or bimolecular recombination [134] could play a key role in the energy relaxation process. On the other hand, if the dynamics is also conditioned by the radiative lifetime inside the dots, a strong injection of photocreated carriers will be likely to provoke a transient screening of the internal electric field, resulting in a decrease of the lifetime and, consequently, an acceleration of the relaxation dynamics. Multi-carrier annihilation processes should present a n^2 dependence of the dynamics where n is the density of considered carriers. However, the fact that we have only three measurement

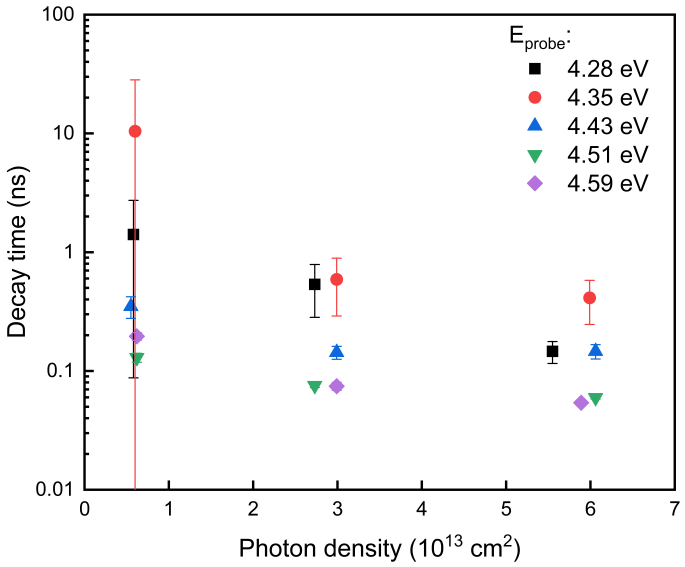

FIGURE 6.16: Average relaxation time constants $\langle \tau_{relax} \rangle$ as a function of excitation photon density of the pump.

points for each curve prevents us from determining precisely the mathematical form of this evolution.

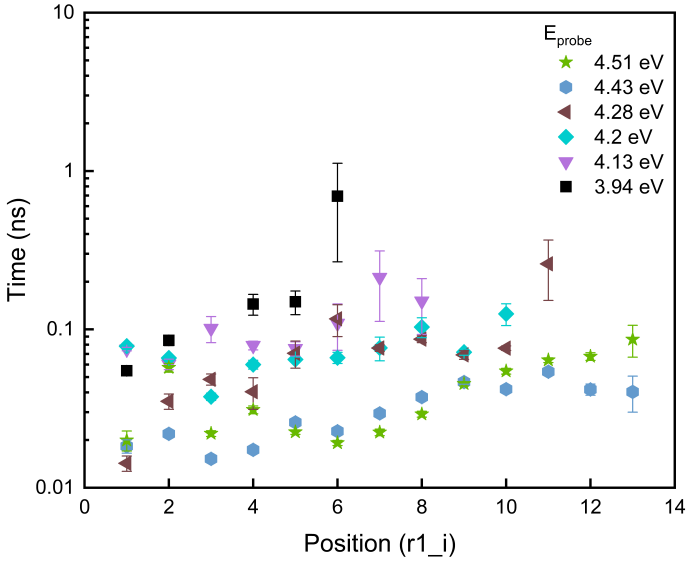

FIGURE 6.17: Time $\langle \tau_{relax} \rangle$ decay as a function of position on the sample extracted by means of stretched exponential fit of differential transmission signals $\Delta T/T$ decays at different E_{probe}.

Evolution of decay times as a function of position on the sample: As we explained earlier, there are 14 accessible positions on the surface of the sample which correspond to different quantum dot heights. Position $r1\_1$ is relative to the largest dots while position $r1\_14$ is related to smallest dots. The figure 6.17 presents the average relaxation time $\langle \tau_{relax} \rangle$

as a function of the position on the sample for different values of the probe energy. Two major trends appear on this graph. On the one hand, $\langle \tau_{relax} \rangle$ is decreasing when E_{probe} increases. On the other hand, at fixed E_{probe}, $\langle \tau_{relax} \rangle$ increases when the index i identifying the position increases, i.e. when the energy of the PL tends to come in resonance with the probe. One explanation is that carrier relaxation is rapid if one probes within the continuum of excited states. This is due to the vast number of available states for the carriers to transition to, which allows for rapid relaxation. On the other hand, when the probe is resonant with a discrete state inside the dot, the dynamic is slowed down because the lifetime of this discrete state, essentially the radiative lifetime, which will govern the relaxation.

Evolution of decay times as a function the probe energy: Another way to synthesize the data is to plot $\langle \tau_{relax} \rangle$ as a function of the energy of the probe E_{probe} for different positions on the sample (Fig. 6.18). For each specific position, which corresponds to a fixed photoluminescence (PL) energy, we observe that the relaxation time $\langle \tau_{relax} \rangle$ increases as the E_{probe} gets closer to the PL energy. This trend further substantiates the notion that the resonance between the probe and the discrete energy levels of quantum dots significantly affects the relaxation dynamics of the system. When the E_{probe} closely matches the energy of the PL, it suggests that the probe beam is resonating with the discrete energy levels of the QDs. As previously explained, this resonance condition slows down the relaxation dynamics as carriers in the resonating energy levels might take longer to be transfered to other states. This prolongation of carrier residency within the specific energy levels subsequently increases the overall relaxation time $\langle \tau_{relax} \rangle$.

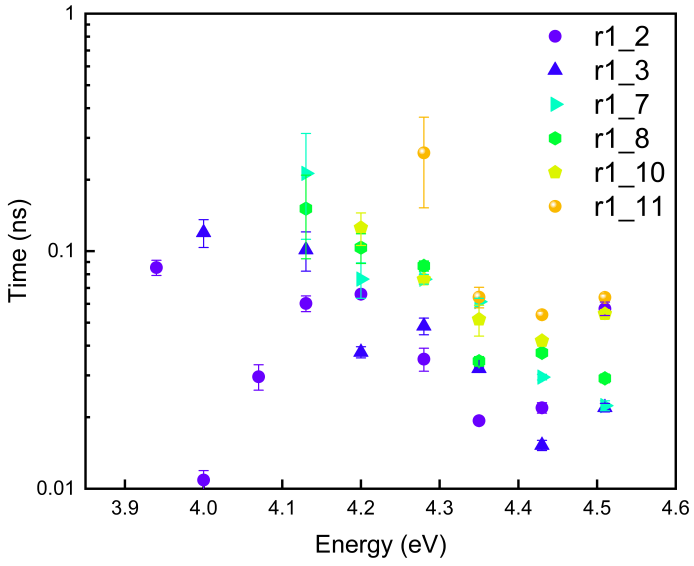

FIGURE 6.18: Time decay $\langle \tau_{relax} \rangle$ as a function of E_{probe} extracted by means of stretched exponential fit of differential transmission signals $\Delta T/T$ decays at different positions.

A comparative analysis of relaxation dynamics on the large delays: small dots versus large dots

Now, we will juxtapose the results obtained from the examination of small and large dots, which were identified on opposite regions of the sample. On the top of figure 8.4, we can see the PL and PLE spectra for position $r1\_11$ (small dots). On the bottom of the figure are reported the different time constants: lifetime of the PL (τ_l and τ_{sh}), depending on the emission energy as well as the mean relaxation time $\langle \tau_{relax} \rangle$ of the non-degenerate pump-probe signal as a function of the probe energy. Recall that, in pump-probe experiments, carriers are always created at an energy of 4.59 eV. This energy corresponds to the maximum

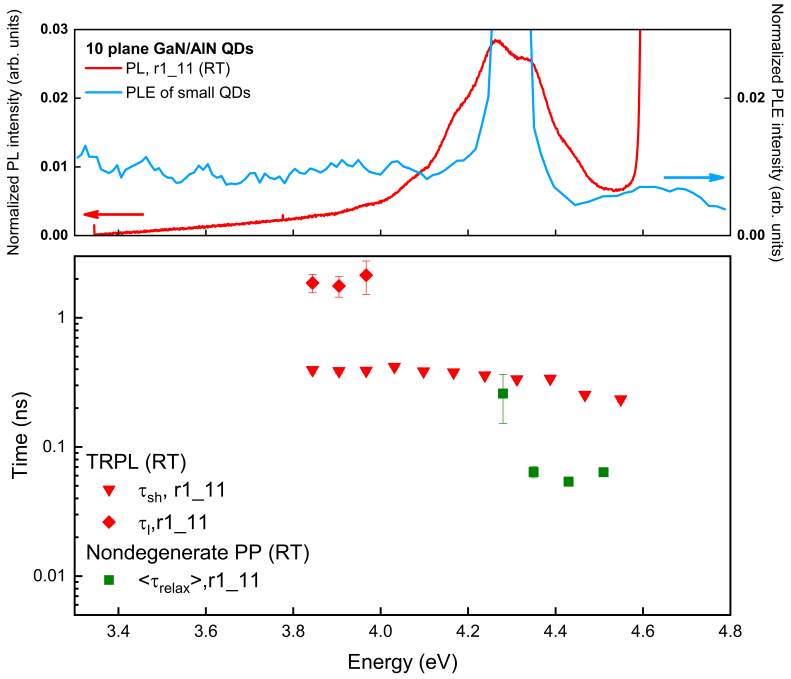

FIGURE 6.19: Top graph, PL spectrum of 10-plane GaN/AlN QDs ensemble measured at $r1\_11$ position on the sample at RT (red curve) and PLE spectrum for small QDs ensemble, which PL peak is close to 4.3 eV(blue curve). Bottom graph, time decays constants extracted from TRPL experiment: τ_l (red diamonds) and τ_{sh} (red down triangles). The time constants $<\tau_{relax}>$ (green squares) correspond to the average relaxation times of the differential transmission signal.

of a structure in the PLE spectrum that we can attribute to the wetting layer. We find that when E_{probe} is between 4.3 and 4.6 eV, $\langle\tau_{relax}\rangle$ is about 60 ps then it increases to equal the fast component τ_{sh} of the PL when E_{probe} approaches the maximum of the PL line.

We drew the same graph for the large dots (position $r1\_2$ of the metal mask). The same general trend is observed (Fig.8.5). However, the amount of energy the carriers have to relax to reach the quantum dots is higher ($\simeq$ 0.9 eV). If we still observe the structure of PLE at 4.6 eV, it is here accompanied by a partner centered around 4.1 eV which could be the first excited level of the quantum dot. If we are interested in the evolution of $\langle\tau_{relax}\rangle$, associated with the pump-probe dynamics, we find out that the its evolution surprisingly follows the shape of the PLE spectrum while its values are distributed around a mean of $\simeq$ 30 ps. In particular, a marked slowing down of the relaxation dynamics coincides with the structure that we have associated with the first excited level of the dot. In these large dots, the signal is no longer measurable below an energy of 3.9 eV because of the drastic reduction of the oscillator strength by the quantum confined Stark effect. However, the measurement performed at 3.9 eV seems to indicate the same trend as in the small dots. Namely, an increase of $\langle\tau_{relax}\rangle$ which tends asymptotically towards the fast component of the PL.

In the case of small dots, whose emission energy is above 4.2 eV, the relaxation takes place in a quasi-continuum of energy states between the creation of carriers in the wetting layer and their capture in the dots. The relaxation time of the pump-probe signal corresponds to this leakage time which is slowed down when the probe becomes resonant with the discrete state of the dots since there is then no other possible way out than radiative recombination which takes place on much larger time scales. If we now look at the large dots, which emit around 3.7 eV, the evolution of the relaxation time with the probe energy is no longer monotonic. Indeed, when the energy of the probe is between 4.59 eV and $\simeq$ 4.2 eV, the relaxation is done in a continuum of state. Around 4.2 eV, the probe is resonant with the first excited state of

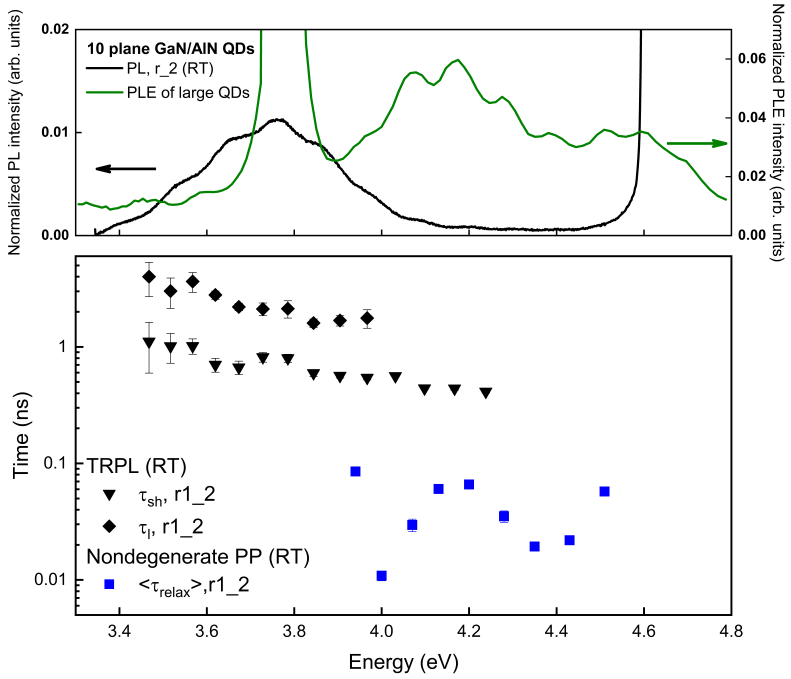

FIGURE 6.20: Top graph, PL spectrum of 10-plane GaN/AlN QDs ensemble measured at $r1\_2$ position on the sample at RT (black curve) and PLE spectrum for large QDs ensemble, which PL peak is around 3.8 eV(green curve). Bottom graph, time decay constants extracted from TRPL experiment: τ_l (black diamonds) and τ_{sh} (black down triangles). The time constants $<\tau_{relax}>$ (blue squares) correspond to the average relaxation times of the differential transmission signal.

the dot. The decay time then increases due to the reduction of the available final states, the relaxation occurring between two discrete states of the dot. From the PLE and pump-probe data, we deduce that there is only one optically active state in the small dots and two states in the large dots.

Having analyzed the non-degenerate pump-probe experimental results and observed interesting trends in both small and large quantum dots, it is time to delve deeper into our investigation. The degenerate pump-probe experiments present a natural progression, enabling us to explore in greater detail the resonant processes and intricate carrier interactions within the quantum dots.

This next phase of our exploration will not only serve to validate the observations from the non-degenerate experiments but also aims to enrich our understanding of the system behavior. By turning our attention to the degenerate pump-probe results, we hope to shine a light on these complex processes and further unravel the intriguing dynamics at play in GaN/AlN QDs. Let us delve into these results now, keeping in mind that we will further analyze our findings on immediate delays from non-degenerate results at a subsequent stage.

6.3 Degenerate PP on 10 planes GaN/AlN QDs

The principle of the experiment is schematized in Fig 6.21. As explained above, the pump and the probe have the same energy E_2 which is varied continuously between E_1 and E_3. At $t = 0$, the pump populates the level E_2. The electron-hole pairs relax towards lower energy levels with a characteristic time τ_{relax}. When the delay between the pump and the probe increases, the probe tests a less and less populated level E_2 see Fig. 6.21b.

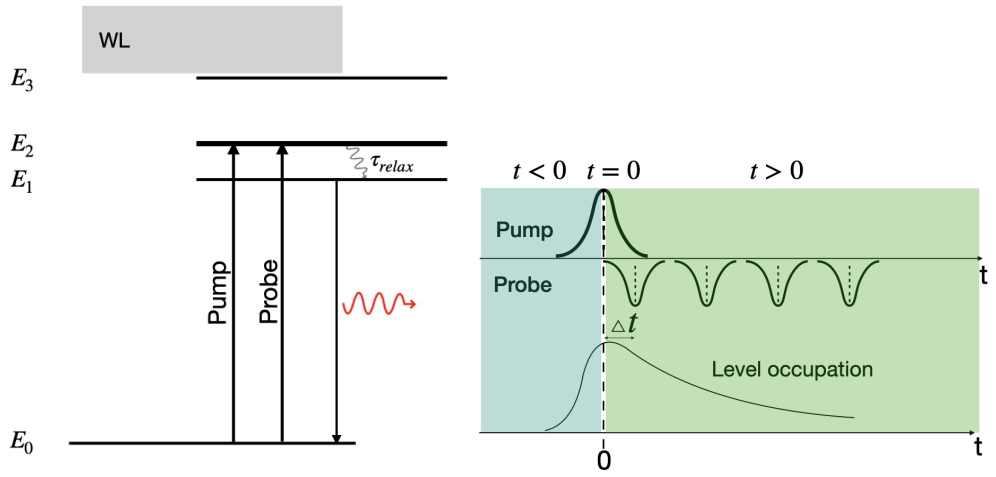

FIGURE 6.21: Schematic representation of the degenerate pump-probe experiment on the energy level diagram of the QD.

TABLE 6.3: Excitation parameters for degenerate pump-probe experiments.

$Energy$ (eV)	P_{pump} (mW)	P_{probe} (mW)	$Photonflux_{pump}$ (photons $\cdot$ cm^{-2})	$Photonflux_{probe}$ (photons $\cdot$ cm^{-2})
4.59	0.35	0.3	$1.2 \cdot 10^{13}$	$1 \cdot 10^{13}$
4.51	0.45	0.45	$1.6 \cdot 10^{13}$	$1.6 \cdot 10^{13}$
4.43	0.65	0.5	$2.3 \cdot 10^{13}$	$1.8 \cdot 10^{13}$
4.35	0.9	0.6	$3.3 \cdot 10^{13}$	$2.2 \cdot 10^{13}$
4.28	0.9	0.8	$3.4 \cdot 10^{13}$	$3 \cdot 10^{13}$
4.20	1	1	$3.8 \cdot 10^{13}$	$3.8 \cdot 10^{13}$
4.13	1.2	1	$4.6 \cdot 10^{13}$	$3.9 \cdot 10^{13}$
4.07	1.8	1.1	$7 \cdot 10^{13}$	$4.3 \cdot 10^{13}$
3.94	1.8	1.3	$7.3 \cdot 10^{13}$	$5.3 \cdot 10^{13}$
3.87	1.4	1.3	$5.8 \cdot 10^{13}$	$5.3 \cdot 10^{13}$

The degenerate pump-probe experiment has been performed on the 10-plane GaN/AlN QDs sample at RT. To cover a large spectral range, the pulse energy was varied from 3.87 up to 4.59 eV (320-270 nm), and the repetition rate was 200 kHz. The spot diameter of both pump and probe focused beams was about 0.05 mm. The excitation conditions are presented in Tab. 6.3. As far as possible, we have kept the photon flux of the probe $Photonflux_{probe}$ at values lower than that of the photon flux of the pump $Photonflux_{pump}$. It is two orders of magnitude higher here than in the PL experiments of chapter 5. However, overall, it remained difficult to detect a signal for values of $Photonflux_{probe}$ that were too low.

Fig. 6.22 presents two examples of the characteristic dynamics of the normalized transmission signal T of the probe as a function of the delay between the pump and the probe pulses. They were measured at 4.59 (purple line) and 4.13 eV (green line). We chose to show these two specific profiles because the relaxation dynamics switches from a biexponential decay to a monoexponential one for $E_{probe} \leq 4.5$ eV. The rise time of the signal does not provide any information on the dynamics of the carriers: it is only limited by the duration of the pulses since pump and probe have the same energy.

The extracted decay times are presented in Fig. 6.23a (blue and green symbols) along with the PL lifetimes measured at the same energy (red symbols). As we mentioned in the introduction, we recorded the PL spectra simultaneously with the PP experiment (Fig. 6.23b). Unfortunately, the current run of experiments was performed before the deposition of the

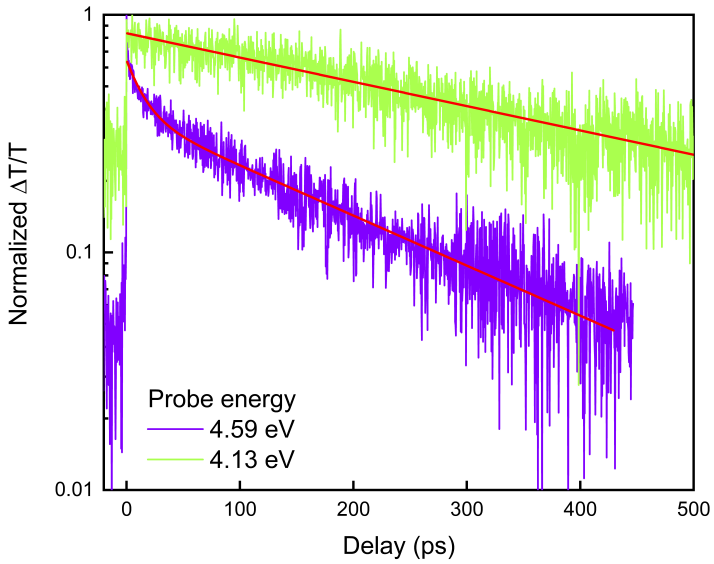

FIGURE 6.22: Normalized decay of transmission signal off the probe as a function of the delay between the pump and the probe pulses measured at different E_{probe}. The red lines is the fit lines of the decay profiles.

metallic mask on the sample surface. However, a comparison of Fig. 6.23b with Fig. 5.14 of chapter 5 reveals that we are close to the $r1\_8$ position, i.e. a region where the two different morphologies of QDs coexist. Indeed, depending on the excitation energy, we can observe the two photoluminescence peaks centered at 4.2 and 3.8 eV, respectively. The peak centered at 4.2 eV dominates the spectrum when the pump energy is between 4.4 and 4.6 eV, while the one centered at 3.8 eV becomes intense when the excitation is between 4.1 and 4.3 eV. This is in agreement with the PLE results presented in chapter 5. For an energy lower than 4.1 eV, the PP signal is reduced to an instantaneous dynamic corresponding to the temporal overlap of the two pulses. This energy corresponds approximately to the boundary between the emission spectra relating to the two dot morphologies.

The points corresponding to the slow component t_l of the signal of ΔT align remarkably with the short time constant τ_{sh} of the PL. We can think that, for QDs which emit at an energy larger than 4.1 eV, the oscillator strength is still large enough to create electron-hole pairs in resonance with the radiative level of the QDs. The degenerate PP experience then presents the same dynamics as the PL. On the other hand, for lower energies, the absorption is too weak to observe a signal of differential transmission.

Overall, our investigations into the relaxation dynamics in GaN/AlN quantum dots through both non-degenerate and degenerate pump-probe experiments have led to notable insights. These complementary methods, probing the system under different conditions, allowed us to confirm and extend our understanding of the relaxation processes.

In the non-degenerate pump-probe experiment (see Subsec. 6.2.2), our observations revealed that the mean relaxation time, $\langle\tau_{relax}\rangle$, exhibited a dependence on the probe pulse energy, E_{probe}. As E_{probe} neared the peak of the photoluminescence line, an increase in $\langle\tau_{relax}\rangle$ was observed for both small and large quantum dots. This suggested that the relaxation dynamics were increasingly governed by radiative recombination as the probe energy approached resonance with the radiative transitions of the quantum dots.

These findings were further confirmed and enriched by the results from the degenerate pump-probe experiment. We observed a similar increase in the relaxation time, specifically for quantum dots with emission energy greater than 4.1 eV. In this regime, the oscillator strength was found to be sufficient to create electron-hole pairs in resonance with the radiative level

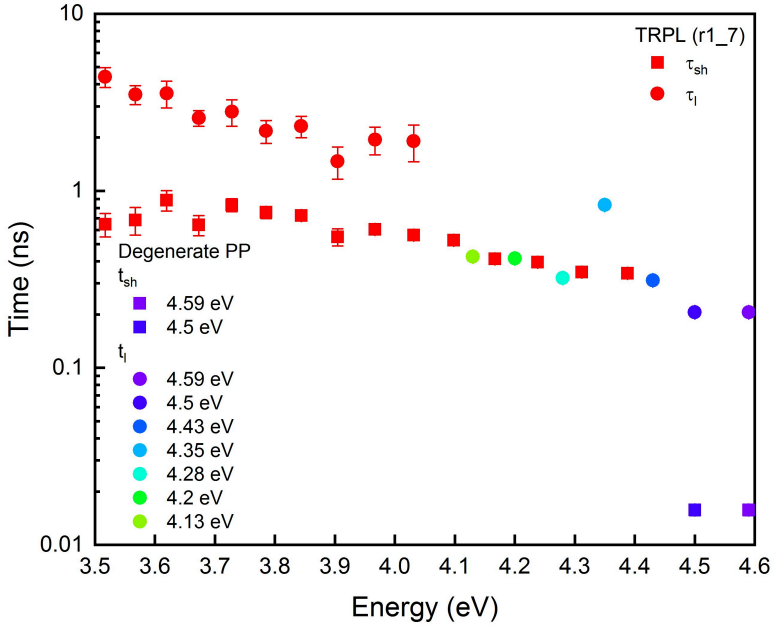

(a)

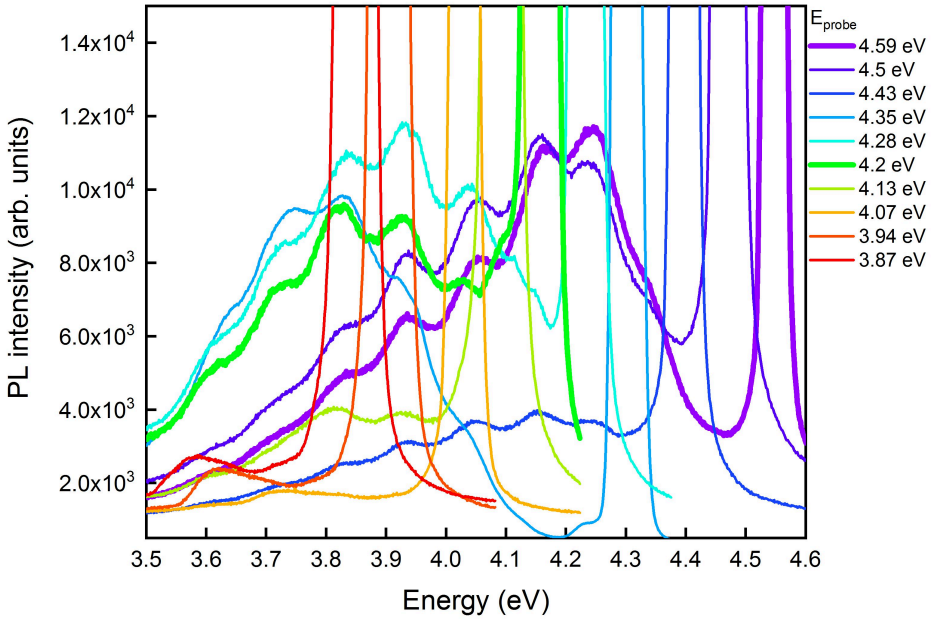

(b)

FIGURE 6.23: Relaxation time of ΔT as a function of the energy of the pulses E_{pump} and E_{probe}, and lifetime of the PL at the corresponding detection energy (a). PL spectra measured during the degenerate PP experiments for different pulse energies between 3.87 and 4.59 eV (b).

of the quantum dots, aligning the degenerate pump-probe dynamics with those observed in photoluminescence. This provided additional evidence of resonance phenomena in these structures.

These observations, while consistent across both sets of experiments, illustrate the value of employing diverse experimental approaches when exploring complex systems. Each experimental setup offered unique perspectives, allowing us to probe different aspects of the system and construct a more comprehensive understanding of the relaxation dynamics in GaN/AlN quantum dots. As we continue our investigations, these findings provide a solid foundation for further analysis and experimental work.

6.4 Exploring the rise time dynamics in non-degenerate pump-probe experiments

Having thoroughly analyzed the behavior of relaxation dynamics and oscillator strength in the context of both non-degenerate and degenerate pump-probe experiments, we are now well-equipped to revisit our non-degenerate pump-probe results. This time, however, we will shift our focus to the rise time of the signal, which, up to now, has remained unexplored in our study. This paragraph is both the most original and, as we will see, the most difficult to interpret. Contrary to a degenerate experiment which would only provide the relaxation time of the carriers towards states located at a lower energy than the probe, the non-degenerate pump-probe allows in theory to access the populating times from states located at higher energy than the probe. It gives us the possibility to reconstruct all the dynamics of the carriers from their creation, following an excitation pulse, in the wetting layer to their recombination from the discrete states of the QDs (see Fig. 6.1).

With our enhanced understanding from the previous analyses, we now delve into the examination of rise times. As we venture into this, let us remain conscious of the fact that our interpretation of the results is an interconnected narrative. The observations from studying the rise time should supplement, confirm, or challenge our existing understanding, helping to create a holistic portrayal of our system's behavior.

6.4.1 Small QDs

As with our prior analysis, we will start with the exploration of small QDs, examining how the rise time depends on the power of the pump. This analysis is crucial in understanding the initial carrier processes, and how the excitation conditions can influence these processes.

Dependence of rise dynamics on pump power The figures 6.24a, 6.24b and 6.24c present the differential transmission signals measured at the position $r1\_11$ on the sample, from which the background has been subtracted, for three different energies of the probe (a) 4.59 eV (b), 4.43 eV and (c) 4.28 eV, respectively. For each probe energy, three decays are presented which were obtained with different pump powers. Two phenomena are observed.

The first is the appearance of a negative signal around a zero time frame for E_{probe} approaches $E_{PL_{max}}$. Such behavior was confirmed at different positions on the sample. The amplitude of this signal increases with the power of the pump (see Fig.6.24c) and when the probe energy tends to the PL energy. The negative sign of this signal indicates that we are dealing with an induced absorption. There are two competing phenomena that give rise to signals of opposite signs.

It could be a two-photon absorption to higher energy states. The signal in question would then be instantaneous on the scale of our experiment, i.e. proportional to the cross convolution between the pump and the probe. If from a theoretical point of view, this interpretation is rather satisfactory, one can however wonder why this two-photon absorption would appear precisely when the energy of the probe reaches 4.28 eV. Indeed, given the fact that the pump is at an energy of 4.59 eV, the process would concern a transition of 8.87 eV. It would be curious that the final state is at such a high energy, and only this, when we would rather expect a transition to the AlN matrix, for example, whose band gap is $\simeq 6$ eV. The impossibility of identifying a credible final state for this two-photon absorption invites us to leave this interpretation aside.

This negative signal can also be explained by the existence of an instantaneous redshift, i.e. which occurs even before the carriers created at high energy have relaxed inside the dots. This immediate shift arises from the Coulomb interaction between the carriers which are photocreated in the system at high energy. When more than one e-h pair are created in the system at high energy, they interact with each other due to their electric charges. This interaction is instantaneous and can impact the overall energy landscape of the quantum dot, including the resonance energy. It is in other words probing the biexciton state. This can cause an immediate shift in the resonance energy, meaning the energy decreases. This type of behavior has already been observed in pump-probe experiments on colloidal CdSe

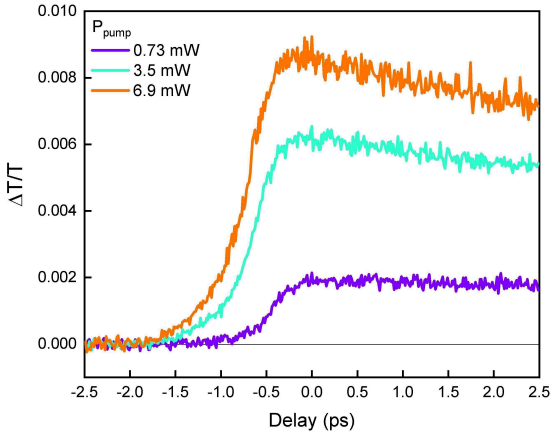

(a)

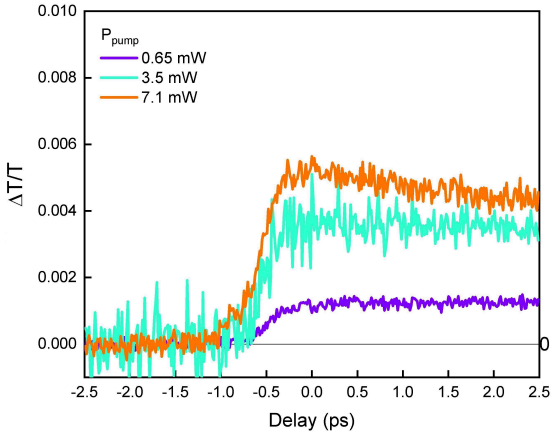

(b)

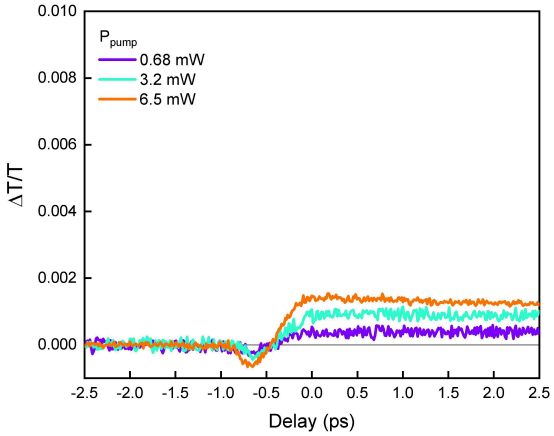

(c)

FIGURE 6.24: Differential transmission signal with extracted background measured at $r1\_11$ position on the sample at different probe energies (a) 4.59 eV (b) 4.43 eV (c) 4.28 eV and variable power of the pump.

nanocrystals [135]. In this type of samples, whose exciton energies correspond to visible wavelengths, it was possible for the authors to benefit from the spectral resolution by using a continuum as the probe-pulse. The photocarriers are created, as in our experiment at higher energy (3 eV).

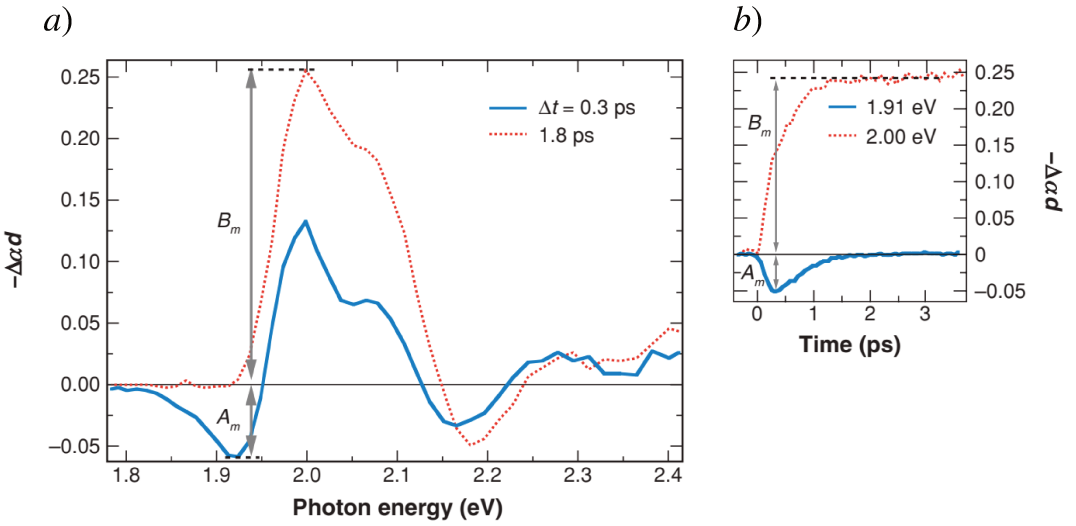

FIGURE 6.25: *a*) Transient absorption spectra of CdSe nanocrystals measured at 0.3 ps (blue solid line) and 1.8 ps (red dotted line) after excitation by a 100-fs, 3 eV pump-pulse. *b*) Signal dynamics at the positions of the bleaching peak (2.00 eV) and the photoinduced absorption (1.91 eV). From reference [135].

To further elucidate this phenomenon and gain a comprehensive understanding, it would be beneficial to consider the results from previous studies described above[135], which have demonstrated similar interactions and energy shifts as illustrated in figure 6.25. On the left part of the figure, we can see the spectrum of $-\Delta\alpha d$ (where α is the absorption coefficient and d the thickness of the sample) for delays $\Delta t = 0.3$ ps (blue solid line) and $\Delta t = 1.8$ ps (red dotted line). We observe a negative signal at 1.91 eV which quickly relaxes as the positive signal, whose maximum is at 2.0 eV, builds up. The fact that this feature is redshifted with respect to the energy of the quantum dots is explained by the existence of an attractive exciton-exciton interaction (bound excitons). This is also the case in our experiments since the photoinduced signal appears in the low energy part of the PL. A repulsive exciton-exciton interaction would have given rise to a photoinduced signal at an energy higher than the energy of the nanocrystals. The right part of the figure shows the temporal profiles of the two signals of opposite sign. It can be seen that the very rapid relaxation of the negative signal takes place during the time necessary for the positive signal to reach its maximum. The explanation is as follows: the negative signal is instantaneous because it is caused by the Coulomb interaction with the created photocarriers. As these relax towards the nanocrystals, the negative signal disappears in favor of the positive signal due to the filling of the states of the dots. Back to figure 6.25 *a*), by spanning all the photon energies between 1.9 eV and 2.0 eV, we go from a signal which remains negative between the two delays to a signal which remains positive with all the possible intermediate situations. So, if the authors of [135] had plotted the temporal evolution of $-\Delta\alpha d$ at an energy of $\simeq 1.93$ eV for example, the shape of the function would have been the one that we observe in figure 6.24c, namely, a early negative signal followed by the growth of a positive signal.

If this interpretation is correct, it must be concluded that the exciton-exciton interaction in the present dots which emit at 4.28 eV is attractive. Earlier investigations into biexcitons in GaN/AlN quantum dots have demonstrated that the sign of their binding energy, E^b_{XX}, which originates from the exchange interaction, varies based on the quantum dot height

and lateral extension [89, 92, 90]. For a given dot height, the spatial separation between electrons and holes by the QCSE along the growth axis remains constant and so does the attractive interaction within the exciton. Decreasing the lateral extension reinforces the repulsive electron-electron and hole-hole interactions, which has the effect of decreasing the biexciton binding energy and the confinement energy as well. It results in a negative slope of E^b_{XX} versus the exciton energy (part *b*) of figure 6.26. On the contrary, E^b_{XX} decreases with the dot height: the repulsive interaction between carriers of the same sign remains now approximately constant, however, increasing the dot height reduces the overlap of the envelope functions of electrons and holes along the polar axis, thus decreasing the attractive Coulomb interaction between carriers of opposite charges in favor of the repulsive component. As a consequence, the evolution of E^b_{XX} with the exciton energy displays a positive slope (see part *a*) of figure 6.26).

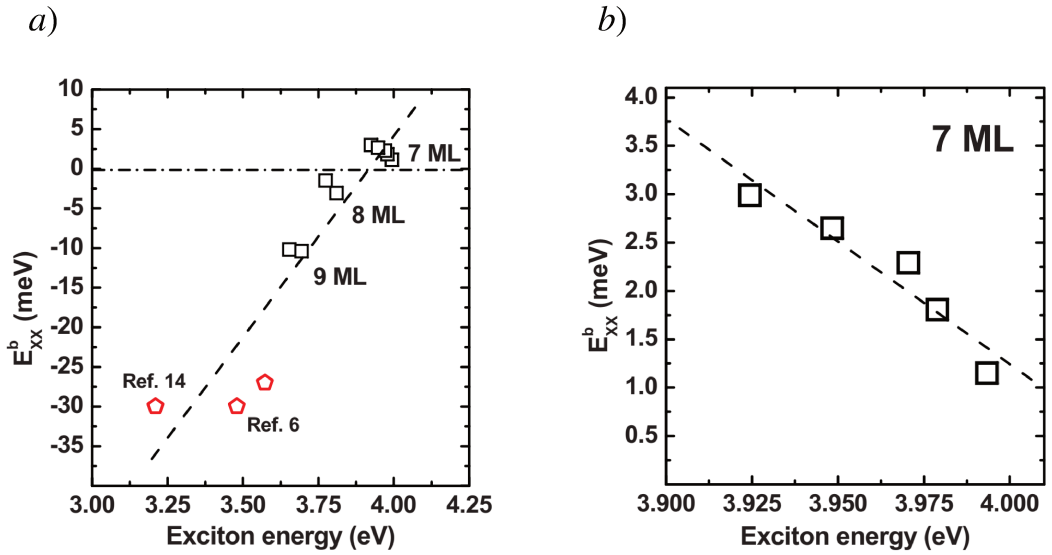

FIGURE 6.26: *a*) Dependence of E^b_{XX} on the exciton emission energy for the QDs of different vertical sizes. *b*) Dependence of E^b_{XX} on the exciton emission energy for the QDs with the same vertical size (7 ML). From reference [89].

Following this exploration of the first observed behavior, we can proceed to delve into the second distinctive phenomenon that manifested in our experimental observations. It is the decrease of the signal approaching the energy of the maximum of the PL of the QDs (Fig. 6.24), that can be explained by the state filling effect. QDs have a distinct and quantized energy state structure that can only hold a limited number of carriers (due to the Pauli exclusion principle). When we use an external pump to introduce additional energy into the system, these energy states can be excited. This means that once an energy state is occupied or "filled," no further carriers can be excited into that same state. As we tune the probe energy close to the PL peak, we are essentially trying to excite carriers into states that are already filled. This state filling effect manifests itself in a pump-probe measurement as a decrease in the differential transmission signal. Since filled states cannot absorb additional probe photons, the overall transmission through the sample increases, resulting in a lower differential transmission signal. This effect is more pronounced as the probe energy approaches the PL peak, which is when we would expect the QD states to be maximally filled due to the pump excitation.

When the onset of the signal was not altered by the presence of the negative dip, we fited the risetime as a function of the pump fluence. The negative background mentioned above has been subtracted from the experimental data and the fitting function has the expression:

$$y(t) = \frac{A}{2}\left[1 + \mathrm{erf}\left(\frac{t - t_0}{\sqrt{2}\sigma}\right)\right] e^{-\frac{t}{\tau}}, \tag{6.6}$$

where A is an amplitude, τ is the relaxation time of the signal while t_0 and σ are the origin and the amplitude, respectively, of the *Gauss error function* defined as:

$$\mathrm{erf}\left(\frac{t-t_0}{\sqrt{2}\sigma}\right) = \frac{1}{\sigma\sqrt{2\pi}}\int_0^{t-t_0} e^{-\frac{1}{2}\left(\frac{t'}{\sigma}\right)^2} dt'. \tag{6.7}$$

Moving forward in our discussion, we will adapt a slight change in notation: hereafter, σ will be referred to as the τ_{rise}.

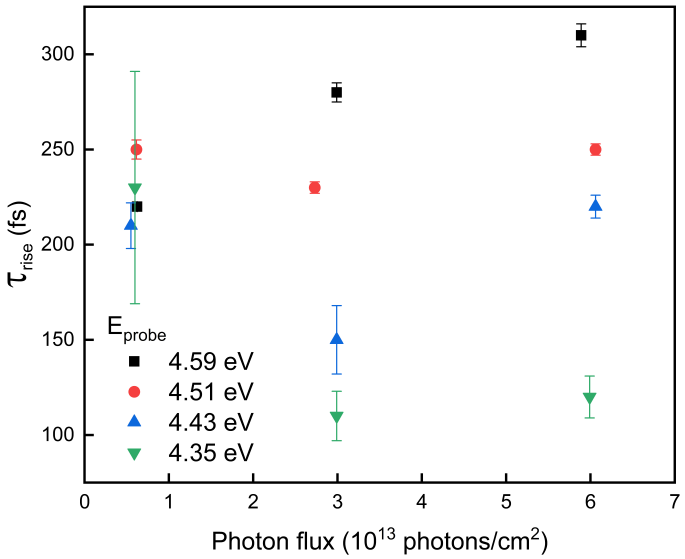

FIGURE 6.27: Rise time τ_{rise} of the differential transmission signal measured at $r1\_11$ position as a function of the excitation density of the pump.

The results are displayed in Fig. 6.27 for different probe energies. It is difficult to draw a clear trend from these data. First of all, we are dealing with very short times, around 200 fs, whose variations are at the limit of the temporal resolution of our experiment and which present important error bars. Moreoverer, τ_{rise} is significantly shorter than in the QD systems studied so far. It is in the range of a few hundred femtoseconds while in other III-V QDs the capture times vary between a few picoseconds and a few tens of picoseconds depending on the system morphology and the excitation conditions [131, 136, 137, 138].

Let consider the evolution of the rise time as a function of probe energy. To examine this aspect, we selected the highest power available in our experimental setup. The corresponding rise time values, τ_{rise}, are plotted against the probe energy in Fig. 6.28. Simultaneously, we present the photoluminescence (PL) and photoluminescence excitation (PLE) spectra associated with the position labeled as $r1\_11$. Following an assumption where we attribute the rise time of the ΔT signal to the population time of the probe level from the pumped one (see Subsec. 6.2.2), we would expect an increase of the rise time when the amount of energy to relax is larger, ie when the photon energy of the probe decreases. On the contrary, we notice that, as the probe energy approaches the peak of the photoluminescence (PL) line, the rise time becomes shorter.

A possible interpretation would be that the maximum of the differential transmission signal is reached when a substantial fraction of the states at an energy lower than E_{probe} are populated. In this hypothesis, the carrier relaxation immediately after the arrival of the pump would be extremely efficient and the carriers would not stay long enough at the energy of the probe to observe a signal until state filling at lower energy has begun. In essence, an intense pump

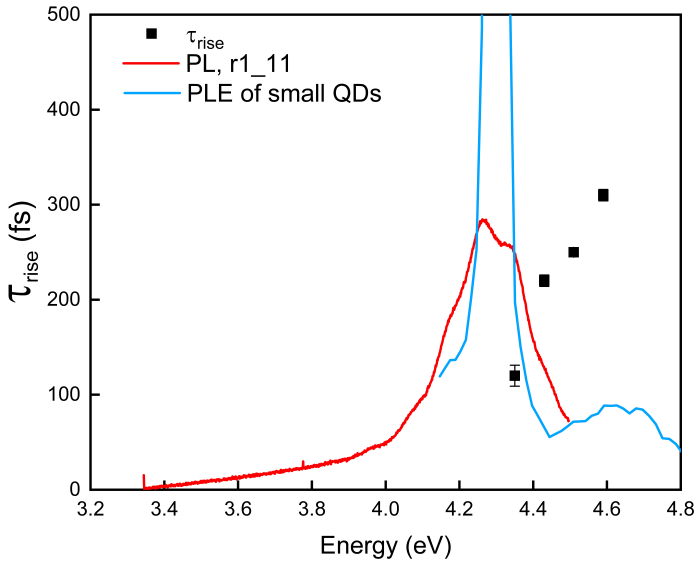

FIGURE 6.28: Rise time as a function of the E_{probe} tested at $r1\_11$ position on the 10 planes GaNAlN QDs sample extracted from fit function (Eq. (6.6)) of short delay pump-probe measurements.

causes carriers to populate energy states so rapidly that the standard dynamics, relaxing from the pump to the probed level, happen too quickly to be distinctly captured in the ΔT rise.

Basically, the physics of relaxation is not the same during the rise of the signal and during its relaxation. At the early beginning, the pump pulse populates a system empty of carriers whose lifetime on each of the states is extremely short, leading to an efficient thermalization in a few hundred fs which fills all the available states up to the energy of the probe. The decay of the signal corresponds to the disappearance of a thermalized population either by radiative recombination, or by relaxation towards lower energy states when these are again vacant. It therefore takes place over much longer time scales than its appearance.

Concerning the dependence with the density of injected carriers, while the long-time dynamics accelerates when the carrier density increases, we see here that it is not systematic. Indeed, it is only when the probe is at an energy of 4.35 eV that τ_{rise} decreases for an increase in the photon flux. For the three other energies tested, the rise time remains more or less constant, and even tends to increase slightly with this one when $E_{probe} = 4.59$ eV. However, if we look at the figure 6.24, we see that the maximum value reached by the signal also increases with the power of the pump. In other words, a larger number of states are populated leading to an increase of the rise time.

6.4.2 Large QDs

As previously discussed, probing the ground state of such dots is infeasible due to the overwhelming influence of the QCSE. This poses a challenge, as we would expect to observe effects related to the transient shielding of the electric field [139]. The normalized differential transmission signals $\Delta T/T$, measured at position $r1\_2$ (large QDs) for different probe energies E_{probe}, are plotted in Fig 6.29 for pump-probe delays between -0.5 and 1.5 ps. The corresponding fits (Eq. (6.6)) are plotted as well. We will not discuss a possible evolution of the rise times with the flux of incident photons, the measurements having been made only for the highest pump power.

The corresponding values of τ_{rise} are plotted against the energy of the probe in Fig. 6.30. In the same figure we have plotted the PL and PLE spectra relative to the position $r1\_2$. As in the case of small dots when E_{probe} is decreased, here from 4.5 to 3.8 eV, the rise times are of the

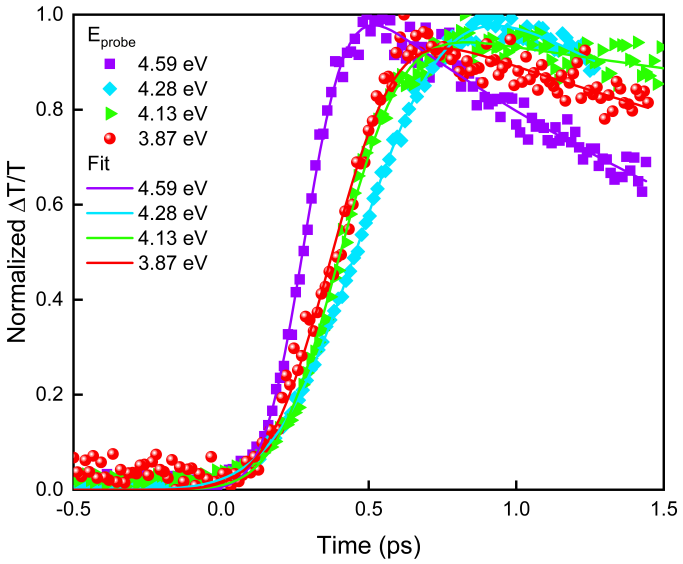

FIGURE 6.29: Normalized $\Delta T/T$ signal at different E_{probe} measured at $r1\_2$ position on the 10 planes GaN/AlN QDs sample at RT.

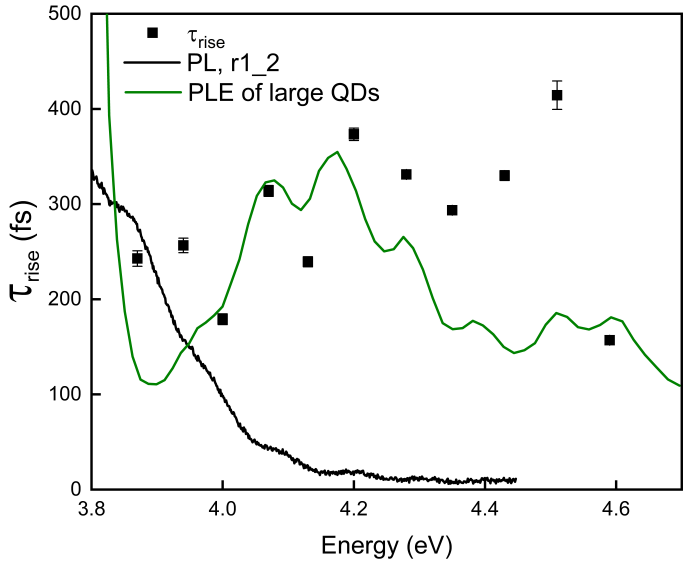

FIGURE 6.30: Rise time as a function of the E_{probe} tested at $r1\_2$ position on the 10 planes GaNAlN QDs sample extracted from fit function (Eq. (6.6)) of short delay pump-probe measurements.

order of several hundreds of fs and generally show a decrease with, however, fairly significant fluctuations. However, in contrast to small dot situtation, the point at 4.59 eV presents the lowest value of τ_{rise} equal to 150 fs. We lack elements to explain why the behaviors of small and large dots are so different when pump and probe are degenerated while on all the energies tested the evolution of the rise times is very similar.

There are a number of published works concerning the carrier capture and intraband relaxation times in III-V semiconductor quantum dots. Morris et al.[131] measured the capture

times in InAs/GaAs dots at 77 K by studying the rise time of the non-resonant TRPL. The dot density is $5 \cdot 10^9$ cm^{-2} and the photon flux is varied between $5 \cdot 10^{10}$ cm^{-2} and $5 \cdot 10^{13}$ cm^{-2}. The Auger effect is responsible for a decrease in capture time from 32 to 12 ps. Müller et al.[110] measured in the same type of dots, at $T = 5$ K, a capture times of 4.7 ps under weak excitation. The phenomena invoked to explain the relaxation are multi-phonon emission and electron-hole scattering. Sauvage et al.[136] determined the intra-band relaxation time of the electron in InAs/GaAs finding a value of 3 ps at room temperature. Ohnesorge et al.[132] as well as Sosnowski et al.[140] have studied InGaAs/GaAs quantum dots. Ohnesorge concludes that if the Auger effect dominates at high injection, it is the multiphonon emission which is dominant at low injection, whereas Sosnowski rather invokes electron-hole scattering. The orders of magnitude of the capture times are quite different since if the reference [132] never gives times shorter than 40 ps the reference [140] announces relaxation times of 5.2 and 0.6 ps for the electron and the hole, respectively. It emerges from these studies that the Auger effect becomes preponderant when the injected carrier density is approximately two orders of magnitude greater than the surface density of quantum dots. For lower carrier densities relaxation would be ensured by multi-phonon emission and electron-hole scattering. Overall, the rise times we observe, shorter than one ps, are at least one order of magnitude lower than those published in the aforementioned studies. There may be several explanations for this. GaN is a polar material which has a strong carrier-phonon coupling that should enhance multi-phonons emission, and that the large hole effective mass should facilitate the energy relaxation through electron-hole scattering. Moreover, our studies are carried out at room temperature and under very high pump-powers probably beyond the threshold necessary for the Auger effect to play an important role in thermalization.

6.5 Overview of all the characteristic times

To provide a comprehensive overview of all the characteristic times, let incorporate the rise time results from the non-degenerate pump-probe differential transmission signal into Fig.8.4 and Fig.8.5. This will offer a complete visualization of all the significant temporal aspects that we've investigated.

In our GaN/AlN quantum dot samples, we observe a complex series of carrier dynamics following excitation by a high-energy light source. The process initiates with the generation of photocarriers within the wetting layer upon absorption of incident light. Given the high photon flux in our experimental conditions, a large number of carriers (both electrons and holes) are created, leading to a multi-carrier environment. Here, several carrier-carrier interactions occur, including Coulomb interactions, scattering events, and exciton formation. Due to these interactions and the high energy imparted by the incident light, carriers are initially in a non-equilibrium state. Once thermalized within the wetting layer, carriers start to transition into the quantum dots. By means of non-degenerate pump-probe experiments, we have traced these carriers during relaxation towards the radiative state. The rise time, describing the initial response as carriers are photo-created and start interacting, and the relaxation time, illustrating the decay of the response as carriers recombine, are interconnected through shared contributing mechanisms.

The carriers redistribute across the available energy states, initiating population of the available energy states inside the QDs. Consistent with the Boltzmann distribution, higher energy states are less populated than lower ones initially. The time taken for the signal to rise from its baseline to its peak is the rise time τ_{rise}. Our experiments show that this rise time is subpicosecond and initially faster at lower probe energies, indicating quick filling of the lower energy states. This trend is maintained for both ensembles of the QDs (Fig 8.4 and Fig. 8.5). The capture of the carriers in the dots is extremely efficient with a characteristic time at least one order of magnitude lower than in InAs/GaAs quantum dots for example. This is probably explained by the intrinsic characteristics of GaN but also by the particular conditions of our experiments.

However, the behavior of this rise time as a function of the carrier density is difficult to interpret. In particular, the existence of an inflection point appears as we cross the 4.5 eV threshold, beyond which the rise time begins to lengthen, as we increase the pump power (see

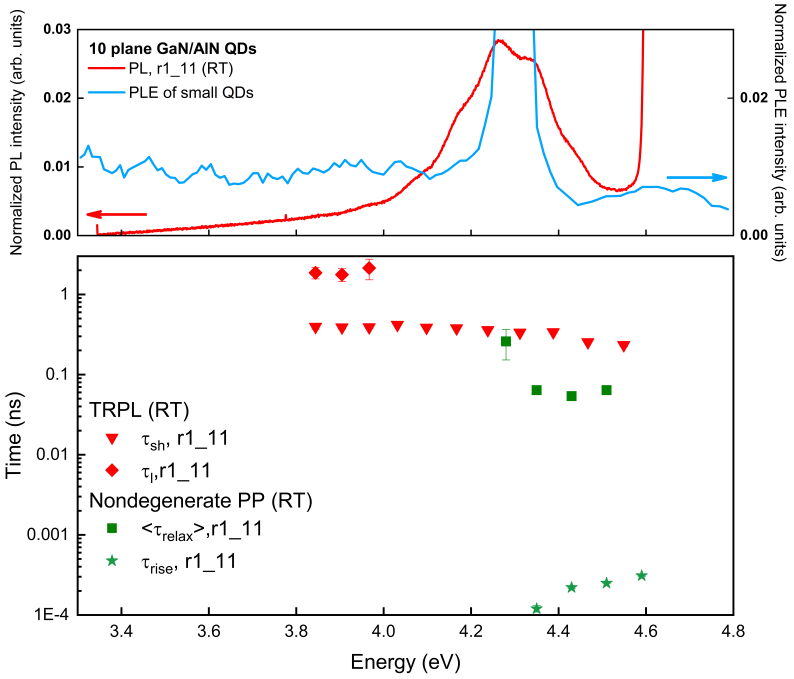

FIGURE 6.31: Top graph, PL spectrum of 10-plane GaN/AlN QDs ensemble measured at $r1\_11$ position on the sample at RT (red curve) and PLE spectrum for small QDs ensemble, which PL peak is close to 4.3 eV(blue curve). Bottom graph, time decays constants extracted from TRPL experiment: τ_l (red diamonds) and τ_{sh} (red down triangles). The time constants $<\tau_{relax}>$ (green squares) correspond to the relaxation times of the differential transmission signal, while τ_{rise} (green stars) is the corresponding rise time.

Sec. 6.4). This lengthening of the rise time is accompanied by an increase in the maximum value taken by the signal. In other words, by exciting more strongly, one gives the possibility to the charge carriers to explore more states. The time it takes to reach the maximum is longer because there are more states to fill. We cannot give a deeper justification without a thorough knowledge of the electronic density of state of our system.

However, the processes at work during the rise time lead to the creation of a quasi-thermalized population whose lifetime is conditioned by the filling of the lower energy states. This dynamic is responsible for the relaxation of the pump-probe signal at long times. Our results indicate that the relaxation process to the lower energy ground state is influenced by several factors, including carrier-carrier interactions, probe energy and pump power. When the probe is resonant with the ground state of the dots, we essentially observe a behavior which approaches an exponential characteristic of the radiative recombination of the electron-hole pairs. When the pump power increases, the number of carriers in the system also increases and the states within the QDs start to get more densely populated, causing a saturation effect. But paradoxically, this also leads to a faster relaxation process in terms of the time scale of the overall system response. We suggest that these multi-carrier processes, together with transient screening of the internal electric field due to strong carrier injection, may play a key role in the observed power-dependence of the relaxation dynamics (see Subsec. 6.2.2). soon as the energy of the probe exceeds that of the ground state, we have the appearance of Auger-type processes which tend to accelerate the dynamics and complicate the shape of the decay.

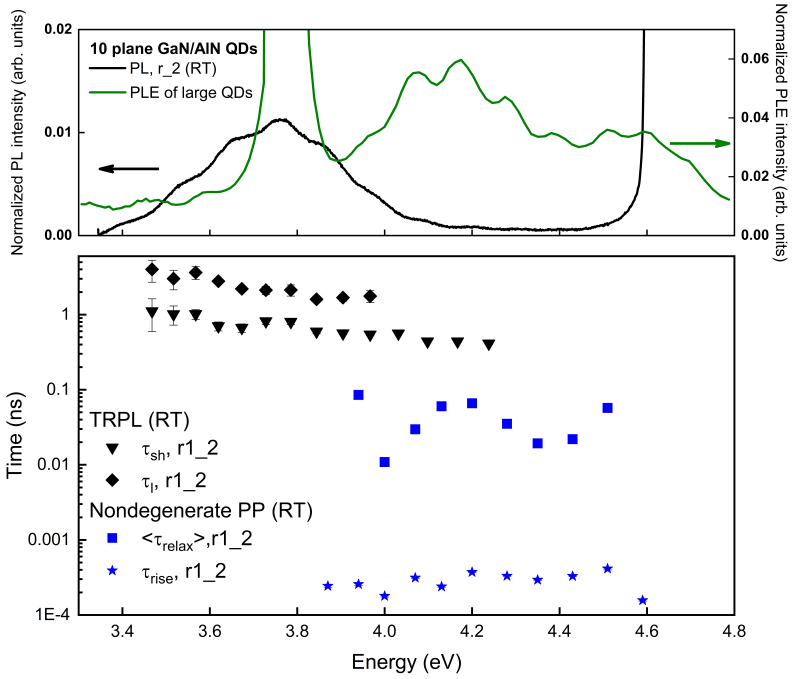

FIGURE 6.32: Top graph, PL spectrum of 10-plane GaN/AlN QDs ensemble measured at $r1\_2$ position on the sample at RT (black curve) and PLE spectrum for large QDs ensemble, which PL peak is around 3.8 eV(green curve). Bottom graph, time decay constants extracted from TRPL experiment: τ_l (black diamonds) and τ_{sh} (black down triangles). The time constants $<\tau_{relax}>$ (blue squares) correspond to the relaxation times of the differential transmission signal, while τ_{rise} (blue stars) is the corresponding rise time.

6.6 Conclusion

In this chapter, we have delved into the study of carrier relaxation mechanisms in GaN/AlN QDs, using both non-degenerate and degenerate pump-probe techniques. Through these experiments, we have gained insights into the dynamics of non-equilibrium carriers, which cannot be adequately explored through TRPL alone.

In our non-degenerate pump-probe experiments, we observed a negative differential transmission signal in a form of background, suggesting the presence of induced absorption phenomena. This was likely due to the population of long-lived states by the pump, possibly from carrier capture on deep defects in the AlN matrix. However, these phenomena occur on a significantly larger timescale than our primary focus in this study, which is the immediate relaxation dynamics following photoexcitation. As such, the detailed analysis of these effects has been left beyond the scope of this research.

The study of the relaxation dynamics of 1 plane GaN/AlN quantum dots (QDs) through non-degenerate pump-probe experiments has shed light on the relaxation process from the wetting layer to the probed energy states. However, the analysis of rise time dynamics was obscured by the superposition of a negative signal and oscillations. The rise time for all tested energies was found to be less than or equal to 1 ps, and the decay dynamics at higher energies ($>$ 4.5 eV) was fast and monoexponential. For lower energies, the differential transmission signal decay was represented by a double-exponential function, with long and short time constants noted as τ^{sh}_{relax} and τ^{l}_{relax}, respectively. The latter one aproaches the τ_s of the TRPL decay. The energy range where the biexponential dynamics has been observed corresponds to what was identified as a possible excited state of QDs.

Our investigation further extended to a 10-plane sample, where a metallic mask deposited on the surface created 14 distinct positions, each with unique quantum dot heights. Each of these positions represents a "sample" of its own, with varying quantum dot sizes and intricate depth profiles. The breadth of information attainable from each position is so extensive that it could potentially form the basis of a separate PhD thesis. However, for the scope of this study, we focused our attention on two extreme ensembles of QDs: small and large ones, with PL centered around 4.3 eV and 3.8 eV, respectively.

Given the number of variables and the extensive data accumulated, it is not unexpected that the relaxation dynamics of the 10-plane sample appear more complex when compared to the 1-plane sample.

Our research study adopted a three-level model, a critical tool that confirms the presence of multi-carrier processes at play in GaN/AlN quantum dots under our experimental conditions. It illuminated the gradual fading of multi-pair processes as the carriers thermalize within the dots. We found that the quadratic relaxation process efficiency decreases as the probe energy reduces relative to the pump energy. Given the complex dynamics within the quantum dots, we opted for a measurement of average relaxation dynamics, $<\tau_{relax}>$, which represents dynamic variations effectively, but not the actual relaxation lifetimes.

Our experimental results demonstrated significant changes in the dynamics as a function of the pump power. We observed an acceleration of dynamics with increasing pump power, suggesting that multi-carrier scattering mechanisms, such as Auger effect, exciton-exciton annihilation or bimolecular recombination, play a key role in the energy relaxation process. These findings have important implications for applications that rely on efficient energy transfer and ultrafast dynamics, such as optoelectronic devices and quantum information processing. We found that the relaxation time, $<\tau_{relax}>$, is dependent on the E_{probe}. The average relaxation time evolves from few tens of ps to a few ns, as the E_{probe} descends from wetting layer to radiative levels. The relaxation time remarkably aligns with the short time constant τ_{sh} of the TRPL at the resonance with the QDs. The degenerate pump-probe experiments, confirms for quantum dots emitting at an energy larger than 4.1 eV the oscillator strength was sufficient to create electron-hole pairs resonating with the quantum dots' radiative level, which led to dynamics similar to TRPL.

In the case of larger quantum dots with PL at 3.8 eV, the reduced oscillator strength by the quantum confined Stark effect conceals the resonance phenomenon. Despite this, a noticeable slowing down in the relaxation dynamics, $<\tau_{relax}>$, is observed which aligns with the trend seen in the PLE spectrum. This suggests that the resonance between the probe and the discrete energy levels of quantum dots significantly affects the relaxation dynamics of the system. This resonance condition appears to decelerate the relaxation dynamics, potentially due to carriers in the resonant energy states requiring more time for transitioning to other states.

Our examination of the rise time at immediate delays has revealed the presence of a negative dip around zero delay for the probe energy approaching the photoluminescence (PL) peak. This phenomenon can be understood in terms of the immediate effect of pump-induced carrier injection on the quantum dot system. Upon the pump's arrival, carriers are introduced, leading to a range of exchange interactions among them. Such interactions, whether attractive or repulsive, prompt an immediate modification of the quantum dot energy levels. This dynamic results in a transient shift in resonance, causing a momentary decrease in the probe pulse absorption near zero delay. This suggests an attractive exciton-exciton interaction within the QDs under study, which emit at 4.28 eV. This interpretation aligns with previous research into biexcitons in GaN/AlN QDs [135]. It has been shown that the sign of the biexciton binding energy varies depending on the quantum dot's size and spatial dimensions. Hence, the quantum dot's physical properties directly influence the nature of multi-particle interactions within, manifesting as observable effects on carrier dynamics and energy absorption.

Apart from the transient decrease in absorption caused by the sudden shift in resonance, we further identified a distinctive characteristic of the system's response to our probe energy: a swift rise time (τ_{rise}) of roughly 200 femtoseconds. The rise times observed in our GaN/AlN

quantum dot system are exceptionally rapid, compared to other similar systems, such as InAs/GaAs quantum dots, where the rise times were observed to be relatively slower.

In addition, we observe a unique relationship between the probe energy and rise time. As the probe energy approaches the PL peak, we observe a distinct reduction in rise time based on energy dependency. This pattern suggests a mechanism closely linked to the rapid and effective filling of available states post-excitation. In this context, the built-up of the ΔT signal represents the time taken to fill available states below the probed level, differing from the traditional interpretation of relaxation from the wetting level towards it. The rapid filling of these lower energy states emphasizes the system's impressive efficiency, evident in the sub-picosecond rise times. Furthermore, the connection between rise time and carrier density, especially around the 4.5 eV threshold, is of interest. Beyond a certain point, rise time starts to expand with increased pump power, indicating that with higher excitation, carriers fill more states, resulting in a protracted rise time due to greater state availability.

Ultimately, the intricacies and specifics of our experimental conditions posed occasional challenges in data interpretation. This was particularly true as we worked under ultimate high-density excitation conditions, especially when compared to the density of the QDs. However, it's undeniable that these very conditions provided invaluable insights. They enabled a deeper understanding of multi-carrier interaction mechanisms. Furthermore, they highlighted their significance in the relaxation process within the GaN/AlN quantum dots.

Chapter 7

Conclusion and future directions

7.1 Conclusion

Thanks to the combined use of different techniques of ultrafast optics, we have studied the relaxation of electron-hole pairs in samples of state-of-the-art GaN/AlN quantum dots. The dynamics of the carriers has been analyzed from their photo-creation in the wetting layer to their recombination from the discrete states of the dots on time scales ranging from a few hundred femtoseconds to a few nanoseconds. Two samples were investigated. The first one contained a single plane of dots emitting at 3.8 eV, the second one 10 planes of dots with a height gradient of these, which emitted between 3.5 and 4.4 eV depending on the excited region.

Time-resolved photoluminescence experiments showed that while the evolution of radiative lifetimes with the dot size is qualitatively explained by the quantum confined Stark effect, the deviation of the experimental decays from the simple exponential function allowed to draw valuable conclusions on the structure of the samples. In particular, we have demonstrated the reversible capture of carriers from the dots towards a dark state or the joint presence within the same sample of two different dot morphologies recombining over two different time ranges. We have also developed an analytical model allowing us to conclude on the presence of a screening of the internal electric field by the photo-injected carriers during the recombination.

The degenerate and non-degenerate differential-transmission experiments performed on the two samples have shown that the thermalization and capture of carriers into the dots is extremely efficient and takes place on sub-picosecond scales. The efficiency of these processes, superior to those at work in other III-V semiconductor systems, is most certainly due to the particular properties of GaN (strong electron-phonon coupling, high effective hole mass) as well as to the particular conditions of our experiments (room temperature, need to inject a high density of carriers to generate detectable signals). It results in the very rapid creation of a thermalized population. The evolution of the rise times with the photon energy of the corresponding pump-probe signals suggests that these are built by the saturation of the states available at energies lower than that of the probe pulse used to measure the dynamics. At long times, relaxation is governed by the final lifetimes and density of available states. It is in particular slowed down when the energy tested is resonant with the ground state of the dot or one of its excited states. On the other hand, it is accelerated by the Auger effect and, probably, by a transient screening of the internal electric field when the density of injected carriers increases.

While considerable insights have been gained, the complexity of these systems and their potential for a wide range of applications underscore the need for further research.

7.2 Future Directions

All the results summarized in the previous paragraph are original and present considerable advances in the knowledge of the structural and optical properties of GaN/AlN quantum dots. However, here are some ideas to go further.

Beyond the TRPL and the PLE, often used to study GaN/AlN, it is the joint use of degenerate and non-degenerate pump-probe experiments that constitutes the heart of this work. They are, however, only a first attempt and certain limitations did not enable us to go as far as we would have liked given the limited time.

In particular, no experiment depending on the temperature of the samples could be performed. These could have helped us identifying the physical processes responsible for thermalization[132]. In addition, the obligation to work at room temperature probably limited the temporal resolution of our set-up by bringing the relaxation times to their lowest values. The experiments as a function of the carrier density showed that we had often worked at powers for which the multi-carrier processes (Auger like) masked all the other possible relaxation processes. Working at very low injection as we did in our TRPL experiments does not seem realistic to us. However, with the experience acquired on the study of these systems, we could aim at working under a wider range of excitation levels. There may also exist intermediate regimes where a complex interplay between single-particle quantum effects, exciton-exciton interactions, and many-body effects takes place. Unveiling the behavior in these transitional regimes could reveal.

The strategy used in non-degenerate experiments, keeping the pump at a fixed energy and varying the energy of the probe, does not appear to us to be the right one. Taking a step back, it seems obvious to us that, on the contrary, it would have been necessary to keep the probe energy fixed and to change the energy of the pump. However, for technical reasons, this alternative was not possible. We are currently working on the possibility of generating a super-continuum which would serve as a probe and which could go far enough into the UV. The study of Coulomb interactions observed at very short times would benefit from this type of improvement. The extent of the continuum obtained will set constraints in terms of the absorption spectrum of the samples.

Since we are talking about samples, It appeared that working on a sample containing several planes of dots undoubtedly improves the yield of the experiments. Working on a height-gradient sample is useful for exploring, as we have done, the relationship between emission energy and lifetime, all other structural characteristics remaining equal. On the other hand, this greatly complicated the interpretation of the relaxation processes. Especially since low-height dots, in which confinement prevails over the quantum confined Stark effect, give the most exploitable results. However, this particular sample did allow some conclusions to be drawn regarding dependence of transition energies according to the lateral extension of the dots as well as the probable presence of two different morphologies of dots. This is a point that could be further explored through a deeper knowledge of the structure and morphology of the samples. Scanning Transmission Electron Microscopy (STEM) would be a highly beneficial complementary method to further elucidate the physical properties of these quantum dots. Since our samples are covered with a capping layer, STEM can provide valuable structural information that is not directly accessible via optical techniques. It would allow us to precisely determine the size, shape, and distribution of the quantum dots and to identify any structural defects or variations in the quantum dots or the surrounding matrix.

Chapter 8

Synthèse de la thèse en français

8.1 Introduction

Les hétérostructures de semi-conducteurs constituent un domaine de recherche actif depuis plusieurs décennies. La première publication sur les boîtes quantiques (QD) est généralement attribuée à Alexei Ekimov et ses collègues, qui ont rendu compte de la synthèse de nanocristaux semi-conducteurs en 1981. Ces travaux représentent une avancée majeure dans le domaine des nanotechnologies. Il a démontré qu'il était possible de synthétiser des cristaux semi-conducteurs de chlorure de cuivre (CuCl) [1] à l'échelle nanométrique avec des tailles et des formes bien définies. Depuis les premières caractérisations optiques dans les années 80 [2, 3, 4, 5], les boîtes QD présentent un énorme intérêt en raison de leur optique unique dépendant de la aille [6, 7, 8, 9], propriétés électroniques [10]. Les nanoparticules constituées de matériaux métalliques ou semi-conducteurs ont trouvé leur place dans de nombreux domaines, notamment la chimie, la physique et les sciences biomédicales. En conséquence, les QD ont été intégrés avec succès dans notre vie quotidienne dans le cadre des applications disponibles, telles que :

- Technologie d'affichage, y compris les téléviseurs, les moniteurs et les smartphones [11]
- Imagerie médicale et diagnostic [12, 13, 14]
- Éclairage et ampoules à diodes électroluminescentes (DEL) économes en énergie [15, 16]
- Cellules solaires et photovoltaïque [17, 18]
- Imagerie et détection biologiques [19, 20]
- Étiquetage de sécurité et mesures anti-contrefaçon [21, 22]
- Informatique quantique et traitement de l'information [23, 24, 25]

Ces dernières technologies utilisent les principes de la mécanique quantique pour effectuer des tâches informatiques et informationnelles. Contrairement aux ordinateurs classiques qui utilisent des chiffres ou des bits binaires pour représenter des informations et effectuer des calculs, les ordinateurs quantiques utilisent des bits ou qubits quantiques, qui peuvent exister simultanément dans plusieurs états.

Après le développement de la mécanique quantique, qui a fourni une compréhension fondamentale du comportement de la matière et de l'énergie aux niveaux atomique et subatomique au début du 20e siècle, la deuxième révolution quantique [26] a développé des applications pratiques basées sur les principes de mécanique quantique. A ce stade, les QD occupaient une place importante en raison de leur utilisation potentielle dans les technologies quantiques.

Leur synthèse, leur caractérisation et leur application restent donc un domaine de recherche très actif. Au-delà des aspects fondamentaux, l'intérêt constant porté aux QD à semi-conducteurs est motivé par leur potentiel pour un large éventail d'applications.

Voici quelques exemples de la manière dont les QD sont utilisés dans les appareils quantiques :

- Appareils Qubit : les QD sont utilisés comme qubits potentiels dans les appareils d'informatique quantique et de communication. En contrôlant les états électroniques des QD, les chercheurs peuvent créer un système de qubits pouvant être utilisé pour effectuer des opérations quantiques [27, 28].
- Émetteurs de photons uniques : les QD peuvent également être utilisés comme émetteurs de photons uniques, qui sont des composants essentiels dans les systèmes de communication quantique. En excitant un QD avec un laser, les chercheurs peuvent générer des photons uniques, qui peuvent être utilisés pour transmettre des informations de manière sécurisée [29, 30, 31].
- Capteurs quantiques : les QD sont utilisés comme détecteurs hautement sensibles dans les capteurs quantiques. En surveillant les états électroniques des QD, les chercheurs peuvent détecter des changements dans les grandeurs physiques, telles que les champs magnétiques ou la température, avec une grande précision [32, 33].
- Mémoire quantique : les QD sont explorés en tant que dispositifs de mémoire quantique potentiels. En utilisant les états électroniques des QD pour stocker des informations quantiques, les chercheurs espèrent créer un dispositif de mémoire quantique stable et efficace [34].
- Cryptographie quantique : les QD sont utilisés dans le développement de systèmes de cryptographie quantique. En utilisant les propriétés électroniques uniques des QD, les chercheurs espèrent créer des canaux de communication sécurisés, impossibles à pirater ou à intercepter [35, 36].

Pour une revue voir par exemple [37, 38].

Il existe plusieurs catégories populaires de QD à semi-conducteurs qui font actuellement l'objet de recherches et de développements pour les technologies quantiques, chacune ayant ses propres propriétés et avantages. La première catégorie est celle des QD colloïdaux. Ils sont généralement fabriqués à partir de matériaux tels que le séléniure de cadmium, le sulfure de plomb ou l'arséniure d'indium. Les QD colloïdaux sont plus adaptés aux applications qui nécessitent une efficacité élevée, une adaptabilité et une large gamme de tailles et de formes. Le deuxième type est celui des QD auto-assemblés, qui sont formés par auto-assemblage au cours du processus de croissance épitaxiale. Parmi eux, le système le mieux maîtrisé et le plus étudié consiste en des QD d'arséniure d'indium dans une matrice d'arséniure de gallium (InAs/GaAs). Les QD auto-assemblés sont connus pour leur haute qualité optique, ce qui signifie qu'ils peuvent émettre des photons de haute pureté et cohérence. C'est l'exigence pour les éléments constitutifs potentiels des dispositifs quantiques (produire un seul photon par demande, car l'émission de plusieurs photons peut compromettre la sécurité de la cryptographie quantique et réduire les performances des ordinateurs quantiques).

Les QD semi-conducteurs de la famille des arséniures, tels que In(Ga)As/(Al)GaAs, ont été largement étudiés en tant qu'émetteurs de photons uniques (SPE) [39, 40]. Le principal inconvénient des systèmes à base d'arséniure est leur température de fonctionnement cryogénique, ce qui complique leur intégration dans des dispositifs réels. D'autre part, parmi la large gamme de systèmes QD disponibles, les QD GaN/Al(Ga)N offrent des fonctionnalités intéressantes en raison des larges décalages de bande à l'interface AlN/GaN, permettant un confinement tridimensionnel des électrons-trous (eh) s'associe jusqu'à température ambiante [41]. Une autre différence entre les arséniures et les nitrures est la plage spectrale de fonctionnement. Les premiers ont une bande interdite relativement petite, ce qui signifie qu'ils peuvent absorber et émettre des photons dans les régions proche infrarouge et visible du spectre. Les nitrures ont une bande interdite relativement grande, ce qui signifie qu'ils peuvent absorber et émettre des photons dans les régions ultraviolettes et visibles du spectre. Cependant, la plage d'émission des nitrures pourrait être ajustée en fonction de la composition du matériau.

Contrairement aux arséniures, les progrès dans les méthodes de synthèse des nitrures QD sont lents en raison d'une mauvaise cristallinité. Les premières croissances de QD GaN/AlN ont été réalisées à la fin des années 1990 [42, 43]. Depuis lors, la croissance des cristaux de nitrure III a été l'un des principaux problèmes liés au développement de dispositifs au

nitrure III. Isamu Akasaki, Hiroshi Amano et Shuji Nakamura ont beaucoup contribué au développement des méthodes de croissance des matériaux en nitrure de gallium et, par conséquent, la première LED bleue à haut rendement a été présentée en 1994. Les travaux ultérieurs de ces scientifiques ont été récompensés par un prix Nobel de physique décerné par l'Académie royale des sciences de Suède en 2014 pour l'invention de diodes électroluminescentes bleues efficaces qui ont permis d'obtenir des sources de lumière blanche brillantes et économes en énergie. Ainsi, relativement récemment, les nitrures III se sont révélés être les deuxièmes semi-conducteurs les plus importants après le silicium. Cela était principalement dû à l'amélioration de la qualité des matériaux. L'utilisation de QD de nitrures III dans des dispositifs quantiques fonctionnels nécessite une structure cristalline de haute qualité et l'absence de défauts structurels tels que des dislocations. Cela signifie que le domaine de la fabrication de substrats en nitrure III et le développement de méthodes de croissance restent l'un des principaux domaines de recherche.

Les avantages d'une qualité cristalline accrue et d'une réduction des impuretés dans les nanostructures de nitrure de gallium ont été exploités pour obtenir une émission de photons UV uniques à 300 K [44, 45] et même au-dessus [46]. Une orientation optique de longue durée a également été observée expérimentalement [47]. De telles réalisations expérimentales vont de pair avec de gros efforts concernant la croissance de QD de nitrure auto-assemblés afin de contrôler leurs paramètres structurels, notamment leur taille et leur densité superficielle [48, 49].

Parmi la large gamme de nanostructures III-V, les propriétés structurelles et donc optiques des nitrures III ont suscité un grand intérêt. Sous forme cristalline de wurtzite, ces matériaux présentent une polarisation spontanée sans présence de champ électrique externe [50]. Les premières études théoriques sur la polarisation spontanée et les constantes piézoélectriques des nitrures III-V (AlN, GaN et InN) [51] ont mis en évidence que les constantes piézoélectriques sont jusqu'à dix fois plus grandes que dans les composés semi-conducteurs III-V et II-VI conventionnels et comparable aux composés ZnO. En développant des QD GaN de wurtzite encapsulés dans une matrice d'AlN, la différence de polarisations spontanées et piézoélectriques entre les deux matériaux provoque la présence d'un fort champ électrique intégré le long de la direction $[000\bar{1}]$. L'étude théorique de Williams et al. [52] a rapporté que les simulations des QD au nitrure étaient significativement différentes de celles des QD à base de GaAs. La combinaison d'un champ électrique intrinsèque avec un confinement quantique dans les QD donne naissance à l'effet Stark confiné quantique (QCSE). Ce dernier a été responsable d'une émission optique fortement décalée vers le rouge dans les grands QD rapportés dans [53, 54]. Le champ électrique intrinsèque peut atteindre des valeurs allant jusqu'à 10 MV/cm [55].

Le champ électrique diminue la force de l'oscillateur en induisant une séparation spatiale des fonctions d'onde des électrons et des trous (formation d'un dipôle), conduisant ainsi à une forte dépendance de la durée de vie radiative de la hauteur de la boîte [56, 57, 54] qui s'étend sur plusieurs ordres de grandeur, de la picoseconde à la microseconde. Les conséquences sont dramatiques pour les plus grandes QD. Premièrement, à mesure que leur probabilité de recombinaison radiative diminue, d'autres mécanismes de déphasage deviennent dominants et la durée de vie radiative de ces QD dépassera les valeurs les plus optimistes du temps de déphasage que l'on pourrait attendre pour ce type de système. De plus, leur faible force d'oscillateur gênera toute excitation résonante et le contrôle de phénomènes cohérents. Enfin, l'éventuel écrantage transitoire du champ électrique est responsable d'une dynamique de recombinaison complexe, non exponentielle et fortement dépendante du nombre de paires eh injectées [54]. Ce sont des inconvénients majeurs si l'on considère par exemple la possibilité de générer et de manipuler des états intriqués. C'est ce qui motive les présents travaux sur les petits QD GaN/AlN dont l'énergie d'émission se situe au-dessus de la bande interdite massive du GaN et pour lesquels une valeur significative de la force de l'oscillateur est préservée. En raison de leur courte durée de vie radiative - de l'ordre de la nanoseconde - ces QD devraient également être moins sensibles à tout éventuel écran du champ électrique intégré, que ce soit en raison du régime d'injection de porteurs (faible à élevé) ou de charges environnantes.

Les conditions clés pour utiliser les QD pour les applications nanophotoniques reposent sur la compréhension complète et, si possible, le contrôle des différentes dynamiques associées

aux excitations électroniques, à savoir la relaxation de population, de spin et de phase. Par exemple, générer des photons indiscernables à partir de QD uniques nécessite que la durée de vie radiative de l'exciton T_1 soit plus courte que son temps de cohérence T_2, ce qui est favorisé dans le régime de Purcell [58, 59].

Bien qu'il y ait eu de nombreuses études sur la relaxation des porteurs dans les QD GaN, une compréhension complète du mécanisme complet n'a pas encore été atteinte. Certaines études se sont concentrées sur le rôle des interactions porteur-phonon dans le processus de relaxation [60], où l'énergie des porteurs est transférée aux vibrations du réseau. D'autres études ont étudié l'influence des états de surface et des processus de recombinaison de surface sur la relaxation des porteurs [61]. De plus, l'influence des effets de confinement quantique sur la dynamique des porteurs dans les QD GaN a été largement étudiée. Malgré ces études, il manque encore une compréhension complète du mécanisme complet de relaxation des porteurs dans les QD GaN. Après l'excitation, les porteurs se détendent de manière non radiative jusqu'à l'état radiatif dans la plage ps. Cela nécessite donc des méthodes de spectroscopie optique ultra-rapides fonctionnant dans la gamme spectrale UV profonde. Ces exigences rendent l'enquête assez difficile. Il existe également des défis liés à la modélisation théorique de ces systèmes complexes.

Dans ce travail, nous nous intéressons à la dynamique de relaxation des paires e-h dans des QD de nitrure de gallium encapsulés dans une matrice de nitrure d'aluminium (GaN/AlN) au moyen de techniques de spectroscopie optique ultra-rapide. Nous profiterons de l'utilisation conjointe d'expériences de photoluminescence résolues en temps et de transmission différentielle pour suivre la dynamique de relaxation des paires e-h depuis leur injection dans la couche mouillante ou dans les états excités des QD jusqu'à leur piégeage et recombinaison dans les boîtes. Nous extrairons les temps caractéristiques à chaque étape de relaxation et tenterons de faire la lumière sur les processus physiques à l'œuvre lors de la thermalisation du porteur.

8.2 Introduction aux boîtes quantiques wurtzite GaN/AlN

Dans le premier chapitre, nous introduisons les notions nécessaires pour que le lecteur non spécialiste puisse comprendre sereinement la physique des boîtes quantiques AlN/GaN.

Dans la section 2.1, nous présenterons de manière concise les semi-conducteurs nitrures, leur structure cristalline responsable des champs de polarisation interne rencontrés dans les nanostructures, leur structure de bande ainsi qu'un aperçu rapide de leurs propriétés optiques.

La section 2.2 présentera les concepts de base des boîtes quantiques semi-conducteurs, quel que soit le matériau à partir duquel ils sont fabriqués. Nous passerons en revue les effets du confinement sur les états électroniques, leur structure fine et leurs complexes excitoniques.

Enfin, nous exposerons dans la section 2.2 les spécificités des boîtes quantiques GaN/AlN : nous détaillerons les conséquences du champ de polarisation interne sur leurs états électroniques et leurs propriétés optiques.

8.3 Échantillons QD GaN/AlN

Dans ce chapitre, nous nous concentrons sur la croissance et la caractérisation structurelle des échantillons GaN/AlN QD.

Dans la section 3.1, nous discutons de la croissance des QD GaN/AlN par auto-assemblage, qui est une technique courante utilisée pour former des QD. Nous discutons également des paramètres de contrôle utilisés pour optimiser la croissance des QD, notamment la température du substrat, le taux de croissance et la composition du matériau.

Dans la section 3.2 nous présentons les détails des échantillons étudiés. Plus précisément, nous étudions deux échantillons différents : les QD GaN/AlN à 1 plan et les QD GaN/AlN à 10 plans. Ces échantillons ont des distributions de taille QD et un nombre de couches empilées différentes, ce qui a des effets significatifs sur leurs propriétés électroniques et optiques.

8.4 Installations expérimentales

Le chapitre 4 propose une présentation complète des techniques expérimentales utilisées dans ce travail de recherche pour explorer les propriétés optiques des QD GaN/AlN développés par MBE.

Premièrement, la section 4.1 présente la photoluminescence en onde continue, une méthode fondamentale mais puissante pour étudier les états électroniques intrinsèques et extrinsèques des semi-conducteurs.

Le principe et le dispositif expérimental de la photoluminescence résolue dans le temps (TRPL) sont présentés dans la section 4.2. Cette technique, avec une résolution de l'ordre de quelques picosecondes, sonde la durée de vie des paires eh après leur thermalisation et capture dans les QD. Les techniques cryogéniques sont également présentées dans cette section.

À l'avenir, la section 4.3 décrit la configuration de l'expérience pompe-sonde non dégénérée et dégénérée, qui a été utilisée pour l'étude de la dynamique des porteurs dans les QD GaN/AlN. Une partie importante de la discussion est consacrée à la description de la source laser d'excitation, y compris l'oscillateur Ti: saphir et l'amplificateur régénérateur. La technique de génération de sonde, qui utilise un amplificateur paramétrique optique (OPA) et la génération de deuxième harmonique, est également discutée. De plus, la technique de génération de pompe est décrite.

Enfin, la section 4.4 revisite la photoluminescence dans un contexte plus large, fournissant des informations supplémentaires sur la manière dont cet outil puissant peut être utilisé pour contrôler l'étude des boîtes quantiques.

Dans l'ensemble, ce chapitre présente une description détaillée de la configuration expérimentale utilisée pour étudier les propriétés optiques des QD GaN/ALN. Les techniques et équipements décrits dans ce chapitre ont été essentiels à la réussite de cette étude.

8.5 Dynamique de recombinaison dans l'ensemble de QDs GaN/AlN

Ce chapitre est consacré à l'étude par photoluminescence résolue en temps (TRPL) de la dynamique de recombinaison de paires e-h dans des ensembles QD GaN/AlN qui ont la particularité d'émettre à une énergie de photons supérieure à la bande interdite du GaN. Sur les deux échantillons concernés, nous effectuons une étude détaillée des durées de vie en fonction de l'énergie d'émission.

Les résultats liés à l'échantillon à 1 plan sont exposés dans la section 5.1. Ils sont interprétés avec des modèles analytiques et numériques. Bien que le QCSE régisse la dépendance entre la durée de vie et l'énergie sur une plage de 3 eV, l'écart par rapport à cette tendance s'explique par la prise en compte de l'effet de l'extension latérale des boîtes sur l'énergie de confinement.

Puis, dans la section 5.2, l'étude de l'échantillon à 10-plan de boîtes, qui présente également un gradient de hauteur des boîtes, permet de mettre en évidence l'existence de deux morphologies différentes de QD qui ont des durées de vie moyennes différentes pour une énergie photonique donnée, mais qui sont modulées en fonction de la hauteur des boîtes par le QCSE.

Dépendance de la durée de vie radiative sur la hauteur de la boîte

Les constantes de temps extraites au moyen de la procédure d'ajustement sont résumées dans la Fig. 8.1 avec les données de la littérature relatives aux échantillons contenant différentes hauteurs de QD GaN/AlN. Nos données expérimentales complètent bien l'ensemble des données des références [54, 57]. Afin d'estimer l'énergie d'émission et la durée de vie radiative des paires e-h dans les QD GaN/AlN, l'équation de la fonction d'enveloppe a été résolue numériquement pour les électrons et les trous, en utilisant une méthode des différences finies au moyen d'un SCILAB FAIT MAISON. code. Le confinement dans le plan de la couche, c'est-à-dire perpendiculairement à la direction de croissance, est, dans un premier temps, négligé car

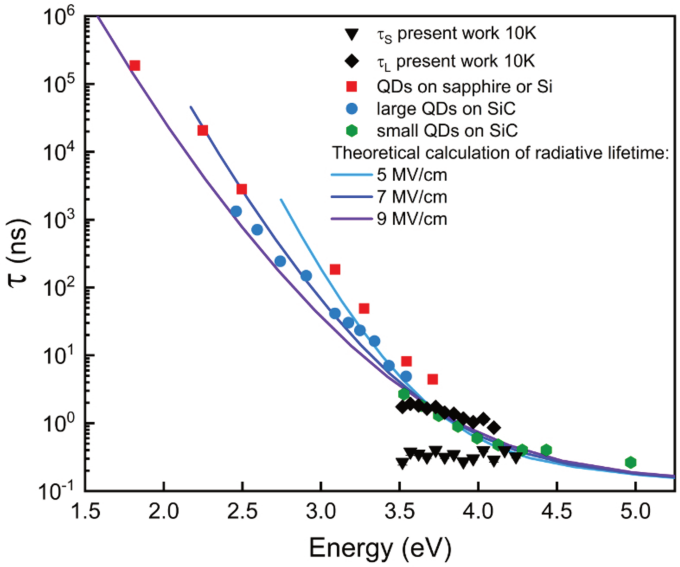

FIGURE 8.1: Durée de vie radiative τ_l des QD GaN/AlN en fonction de l'énergie d'émission : diamants noirs (travaux actuels), carrés rouges (Réf. [54]), cercles bleus et hexagones verts (Réf. [57]). Les triangles noirs vers le bas correspondent à la constante de temps rapide τ_s (travail actuel) attribuée à un processus de relaxation non radiative. Les lignes continues sont les résultats de calculs de τ_{rad} basés sur une modélisation de fonction d'enveloppe 2D pour différentes valeurs du champ électrique intégré.

le champ électrique intégré a l'impact le plus important sur les propriétés optiques des nanostructures à base de nitrure III développées le long de la c-axe. Ainsi, les QD sont d'abord modélisés sous forme de QW bidimensionnels (2D) soumis à un champ électrique statique dans la direction de croissance, les porteurs étant libres de se propager dans le plan du puits. Nous avons pris en compte le décalage vers le bleu de la bande interdite de GaN à 3,71 eV à basse température ($T = 10$ K) dû à la déformation provenant de la croissance pseudomorphique sur la couche d'AlN. La durée de vie radiative τ_{rad} est alors donnée par l'expression : $A \cdot (\hbar\omega)^{-3} |J_{eh}|^{-2}$ [118] où $\hbar\omega$ est le photon énergie, J_{eh} est l'intégrale de chevauchement des fonctions d'enveloppe d'électrons et de trous et A est un paramètre réglable. La fonction résultante $\tau_{rad}(\hbar\omega)$ est tracée sous forme de ligne continue sur la Fig. 8.1 pour différentes valeurs du champ électrique F et $A = 20$ ns·eV^{-1}. Un calcul aussi simple fournit des courbes qui reproduisent qualitativement la variation expérimentale de la durée de vie radiative sur six ordres de grandeur pour des valeurs de champ électrique comprises entre $F = 5$ MV/cm et $F = 9$ MV. /cm, le meilleur accord étant obtenu pour une valeur moyenne de champ électrique incorporé $F = 7$ MV/cm. La valeur moyenne de nos données expérimentales est en bon accord avec les données compilées de la littérature montrant la variation de la durée de vie radiative pour une large gamme de hauteurs de boîtes.

Afin d'être plus quantitatif, notons que l'ensemble QD de notre échantillon présente un large élargissement inhomogène. Pour illustrer cet aspect, nous considérons la Fig. 8.2, qui montre que la variation de la durée de vie radiative ne correspond pas exactement aux courbes (traits continus) qui ne prennent en compte que la variation du QCSE due aux changements de hauteur des boîtes. En fait, les fluctuations se produisant au sein de l'ensemble de boîtes sont susceptibles de provenir également du confinement latéral avec un poids croissant de ce dernier lorsque la taille latérale du QD devient comparable au rayon de Bohr de l'exciton. En effet, le modèle 2D QW fonctionne mieux pour les boîtes les plus grands pour lesquels les variations de la force de l'oscillateur sont essentiellement dues aux changements du chevauchement e-h le long de l'axe de croissance. Pour les petites boîtes, la localisation dans le plan des fonctions enveloppes n'est plus négligeable. Pour estimer cet effet sur l'énergie et la durée de

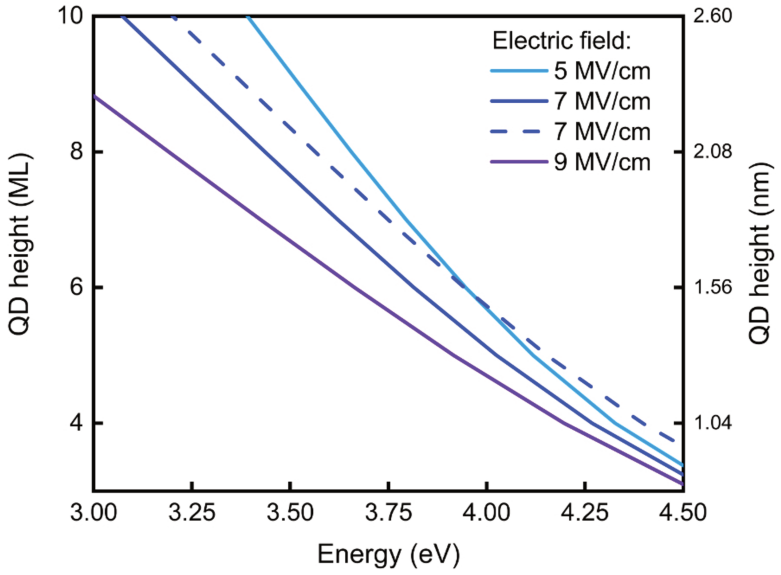

FIGURE 8.2: Durée de vie radiative τ_L des QD GaN/AlN en fonction de l'énergie d'émission. Les lignes continues sont issues de calculs 2D-QW de τ_{rad} pour différentes valeurs du champ électrique intégré en supposant une variation continue de la hauteur de la boîte. Les lignes pointillées montrent l'effet de la taille latérale du QD avec des rayons compris entre 3 et 20 nm. Chaque courbe correspond à une hauteur QD différente exprimée en ML. La taille des diamants noirs est proportionnelle à l'intensité PL, qui reflète le poids de la hauteur de la boîte correspondant dans la distribution QD.

vie d'une paire e-h, nous avons effectué un calcul simple basé sur la méthode variationnelle (voir Annexe C) : le potentiel de confinement dans le plan est supposé être en escalier avec une symétrie cylindrique. La fonction d'enveloppe dans le plan des porteurs est considérée comme une gaussienne centrée dans la boîte cylindrique et pour laquelle l'étendue spatiale est le paramètre variationnel. Cette méthode est connue pour donner des résultats qualitatifs raisonnables malgré sa simplicité [119]. Pour une hauteur QD donnée, une variation du rayon de localisation a peu d'influence sur le recouvrement latéral alors qu'elle affecte fortement l'énergie de confinement. En conséquence, la variation de la durée de vie en fonctipetites boîteson de l'énergie devient moins prononcée. Ceci est illustré sur la figure 8.2 qui montre sous forme de lignes pointillées l'effet de la variation de la taille de la boîte latéral sur l'énergie de transition et la durée de vie radiative pour différentes hauteurs de boîte. On voit ainsi que la pente des lignes pointillées correspond bien à la variation relativement plate de la durée de vie radiative en fonction de l'énergie d'émission des photons observée expérimentalement. Évidemment, des calculs plus réalistes prendraient en compte les différents confinements latéraux subis par les électrons et les trous. Premièrement, ces porteurs ont des masses effectives différentes et la fonction d'onde de la particule la plus légère, l'électron, devrait s'infiltrer dans la barrière. Deuxièmement, si la forme de la boîte ressemble à une pyramide tronquée, comme le confirment des mesures de microscopie électronique à transmission à haute résolution [120], le potentiel de confinement agirait différemment sur les deux particules qui sont repoussées vers des côtés opposés, l'électron vers le côté opposé. sommet de la pyramide et le trou dans la couche mouillante. Par conséquent, les deux effets modifieront le chevauchement latéral des fonctions d'onde des électrons et des trous [121]. Cependant, notre approche montre qu'une description aussi détaillée des fonctions d'onde QD n'est pas obligatoire. Le confinement latéral joue un rôle majeur en décalant vers le bleu l'énergie d'émission sans modifier le chevauchement eh et donc la durée de vie radiative.

Enfin, on peut interpréter ces données de la manière suivante : d'une boîte à l'autre toute variation de la durée de vie radiative moyenne est principalement régie par un changement de

la hauteur de la boîte qui fait intervenir le QCSE comme déjà démontré dans de nombreuses publications (voir par ex. Fig. 8.1 qui affiche les données de la littérature). Cependant, la présente analyse montre que, au sein d'un échantillon QD donné, des changements dans l'énergie d'émission QD de plusieurs centaines de meV accompagnés de légers changements dans la durée de vie radiative peuvent être compris grâce aux fluctuations des dimensions latérales des boîtes au sein d'un sous-ensemble QD donné correspondant. à une hauteur bien définie. À cet égard, nous rappelons que l'identification de sous-ensembles GaN/AlN QD avec une hauteur bien définie au sein du même échantillon a déjà été rapportée pour des boîtes présentant une variation de l'énergie de liaison du biexciton corrélée à l'énergie de l'exciton et au rayon de la boîte dans un sous-ensemble QD avec une hauteur donnée [89]. Notons que pour les QD émettant autour de 3,5-4,1 eV, comme ceux étudiés ici, l'effet du champ électrique intégré est moins important que dans les boîtes plus élevés où le QCSE a des effets plus dramatiques sur l'énergie d'émission et la force de l'oscillateur. et pour lequel seul un rayon moyen doit être considéré. Ainsi, dans les boîtes émettant dans le domaine UV, qui sont d'un intérêt primordial pour l'émission de photons uniques [44, 45], le poids plus faible du QCSE permet de révéler des effets autrement cachés provenant de changements dans le confinement latéral e-h, soit c'est ce qui régit les variations de l'énergie de liaison du biexciton [89] ou une relative insensibilité de la durée de vie radiative tout en couvrant une large gamme spectrale de l'énergie d'émission QD (ici, jusqu'à 600 $\sim$ meV).

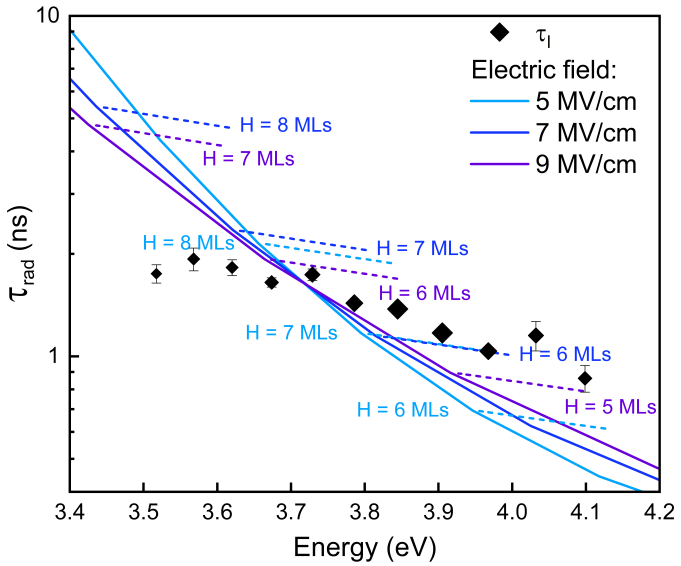

FIGURE 8.3: Corrélation entre l'énergie de transition calculée et la hauteur QD pour différentes valeurs du champ électrique intégré. Les lignes droites correspondent à des calculs basés sur un modèle QW 2D (pas de confinement latéral), tandis que celles en pointillés correspondent à des calculs basés sur la méthode variationnelle pour des petites boîtes de rayon latéral de 3 nm.

Le comportement rapporté confirme que le principal mécanisme à l'origine de la relaxation de la population de paires eh est le processus de recombinaison radiative et que la durée de vie radiative suit l'évolution attendue pour les QD soumis au QCSE. De plus, nos résultats renforcent le fait que, si l'on prend soin d'éviter tout écran du champ électrique intégré, la relation entre la durée de vie radiative et l'énergie d'émission tend vers une tendance universelle (Fig. **??**). Cela peut être bien compris dans un modèle simple incluant une valeur moyenne du champ électrique intégré qui est la même pour tous les échantillons GaN/AlN QD. D'un point de vue pratique, les calculs présentés sur la Fig. 8.3 permettent d'estimer que la hauteur QD se situe entre 5 et 8 MLs (1,3 et 2,08 nm).

Discussion

Dans les sections 5.1 et 5.2, nous avons souligné deux points importants. D'une part, la dynamique des PL n'est pas systématiquement monoexponentielle et, d'autre part, même si le QCSE joue un rôle important dans la dynamique, la morphologie des boîtes, c'est à dire le facteur de forme, n n'est pas à négliger.

Concernant le premier point, de nombreuses études, telles que Bretagnon et al. [54, 95] et Stachursky et al. [96], ont exploré le comportement dynamique des grands QD, trouvant des dynamiques non exponentielles et bi- dynamique exponentielle, respectivement. La première étude [54, 95] s'est concentrée sur les grands QD émettant entre 1,8 et 3,7 eV. Dans ces systèmes aux durées de vie très longues, la dynamique est totalement gouvernée par le QCSE et elle est totalement non exponentielle : à mesure que les porteurs se recombinent, la probabilité de recombinaison diminue. Il n'y a donc pas de vie à proprement parler. Cependant, sur des temps très longs, l'écran du champ électrique disparaît et il est alors possible d'en extraire une durée de vie.

Stachursky et al. [96] ont découvert une dynamique biexponentielle sur un ensemble de boîtes quantiques synthétisés dans le groupe de N. Granjean comme ceux que nous avons étudiés. Leurs interprétations tiennent compte de la structure fine de l'exciton QD. La première possibilité est que le temps court correspond à un temps effectif résultant de la combinaison entre la durée de vie radiative du $|\pm 1\rangle$ et le temps de transfert vers l'état sombre $|\pm 2\rangle$ via un spin-flip. Le temps long serait alors le repeuplement de l'état lumineux à partir de l'état sombre. Ce type de processus avait déjà été observé dans les boîtes quantiques CdSe [93, 129]. Cependant, cette explication n'est pas compatible avec les expériences dépendant de la température : le repeuplement à partir de l'état sombre devrait être activé thermiquement, ce qui n'est pas observé. La deuxième proposition est que les deux dynamiques correspondent à des recombinaisons des deux états brillants $|+1\rangle$ et $|-1\rangle$ qui sont séparés par l'interaction d'échange. Cependant, selon les auteurs eux-mêmes, cette explication n'est pas entièrement satisfaisante.

De plus, Kako et al. [57] ont également observé des désintégrations bi-exponentielles de photoluminescence, attribuant la dynamique rapide au temps de rayonnement dépendant de la taille des QD, et la composante longue au transfert depuis le WL, indépendant du temps de rayonnement des QD. énergie d'émission. Il est à noter que ce temps de transfert est de l'ordre d'une dizaine de nanosecondes.

Concernant le deuxième point, la taille et la morphologie affectent d'autres propriétés physiques des QD. Les recherches menées par Ref. [88] ont examiné plus en détail la division en structure fine (FSS) dans les QD GaN/AlN. Leur étude, qui combinait micro-photoluminescence (μPL) et calcul théorique, a conclu que même une fluctuation mineure de la taille ou de la forme du QD peut induire une modification de l'énergie FSS de plusieurs meV pour différents QD ayant la même énergie d'émission. En d'autres termes, l'allongement structurel ou le rapport d'aspect d'un QD peut avoir un impact significatif sur le FSS. Plus important encore, ils ont constaté que le FSS dépend de la taille du QD. Contrairement à ce qui est observé dans les QD InAs/GaAs, la division à l'état brillant dans les QD GaN/AlN augmente considérablement avec l'augmentation de l'énergie d'émission. Par conséquent, pour les grands QD (émettant en dessous de 3,4 eV), il s'approche de zéro meV, tandis que pour les petits QD (émettant au-dessus de 3,9 eV), il peut atteindre jusqu'à 7 meV.

La délimitation par taille n'influence pas uniquement les propriétés excitoniques de base, mais s'étend également à la complexité des interactions à plusieurs corps, notamment les caractéristiques des biexcitons. L'énergie de liaison des biexcitons est une autre caractéristique qui présente des variations en fonction de la taille. Cette énergie provient de l'interaction coulombienne, impliquant à la fois des interactions attractives (électron-trou) et répulsives (trou-trou, électron-électron). La taille latérale d'un QD a un impact significatif sur l'énergie de liaison du biexciton, qui peut varier de -6 meV à +6 meV [92]. Cet effet a été étudié plus en détail par l'équipe de Simeonov [89], qui a découvert que l'énergie de liaison des biexcitons présente deux régimes, principalement régis par la hauteur de la boîte via le QCSE. L'énergie de liaison varie de +3 meV pour les plus petites boîtes à -11 meV pour les plus grands. Il existe également une variation secondaire de l'énergie de liaison de signe opposé pour des

boîtes ayant la même hauteur mais une taille latérale différente. Par conséquent, les grands QD émettant autour de 3,9 eV ont une énergie de liaison biexciton négative, contrairement aux petits QD émettant au-dessus de 4 eV.

De plus, les travaux de Hönig [90] se penchent sur le comportement de deux paires électron-trou dans les QD de wurtzite. Leur étude a révélé que les biexcitons hybrides sont dominants pour les QD de plus de 6 nm de taille latérale. Ces résultats contribuent à la compréhension des différences et complexités fondamentales introduites par la coexistence de petits et grands QD dans le système GaN/AlN.

Conclusion

Nous avons réalisé des expériences TRPL à basse température sur un seul plan de QD GaN/AlN, dont l'énergie d'émission se situe principalement au-dessus de la bande interdite globale du GaN. Les données PL montrent une dynamique à trois composantes : une première décroissance exponentielle avec une constante de temps courte (0,3 ns), indépendante de l'énergie des photons, une seconde qui suit l'évolution attendue de la durée de vie radiative avec l'augmentation de la hauteur QD, et enfin un composant très long avec un comportement de type plateau.

Nous attribuons la dynamique rapide à un processus de relaxation non radiative des paires e-h vers un état sombre et à l'existence concomitante d'une très longue composante, qui apparaît comme un fond constant dans les désintégrations PL, qui correspond au processus inverse où les boîtes reviennent à leur état d'origine.

Concernant la dynamique du processus de recombinaison radiative, nous avons établi qu'en l'absence de tout écran du champ électrique intégré, le spectre PL des QD avec une distribution de hauteur normale présente une forme de raie gaussienne avec une évolution temporelle caractéristique qui est facilement décrit par un modèle analytique : après une excitation pulsée, la position du maximum de la ligne subit un redshift qui varie linéairement avec l'augmentation du temps de retard et s'accompagne d'une diminution du FWHM. Ce comportement provient de l'effet combiné du confinement quantique et du QCSE, et constitue un critère pour conclure sur l'apparition possible d'effets de criblage et/ou d'effets à N corps dans la dynamique de population au sein des QD GaN/AlN. De plus, notre analyse permet une précision améliorée concernant la détermination de la dépendance énergétique de la durée de vie radiative du QD par rapport à une méthode qui implique une étude systématique des profils de désintégration correspondant à différentes fenêtres étroites d'énergie PL.

En complétant les résultats précédents d'autres groupes, nos données fournissent de nouvelles preuves que la dépendance de la durée de vie effective du PL avec l'énergie d'émission suit une tendance globale qui est une caractéristique intrinsèque du système GaN/AlN QD où le champ électrique intégré agit comme le paramètre le plus dramatique. Les simulations numériques, qui montrent un bon accord qualitatif sur une plage d'énergie de 1 eV et six ordres de grandeur pour la durée de vie effective du PL en supposant une valeur de champ électrique intégré de 7 MV/cm, permettent d'estimer que la hauteur de la boîte dans notre échantillon est distribué autour d'une valeur moyenne de 1,6 nm ($\sim$ 6 MLs). Remarquablement, dans les petits QD émettant à des énergies photoniques élevées, autour de 3,5-4,1 eV, et donc pour lesquels l'impact du QCSE est moins prononcé, nous pouvons mettre en évidence les effets du confinement latéral sur les porteurs. Ce dernier affecte l'étendue de la fonction d'onde et l'énergie d'émission, mais seulement légèrement le chevauchement des porteurs et la force de l'oscillateur correspondante (de manière équivalente à la durée de vie radiative).

En plus de ces résultats, nos mesures dépendantes de la température soulignent l'absence de changement observable de l'énergie PL avec des variations de température et la nature statique de la dynamique de recombinaison. Cela indique la persistance d'une localisation profonde des porteurs au sein des boîtes quantiques, même à température ambiante, démontrant l'absence de canal de recombinaison non radiatif. Ces résultats suggèrent fortement que les boîtes quantiques GaN/AlN présentent un confinement quantique résilient et une recombinaison radiative efficace sur tout le spectre de température étudié. Par conséquent, nous pouvons affirmer avec confiance la nature robuste du confinement quantique présenté par les boîtes quantiques GaN/AlN.

Au cours de nos investigations, nous nous sommes également tournés vers un échantillon constitué de 10 plans de boîtes quantiques (QD) GaN/AlN présentant deux morphologies distinctes. Dans cet échantillon, nous avons identifié un sous-ensemble plus petit de QD qui émettent principalement autour de 4,2 eV et un groupe plus large de QD dont l'émission est centrée autour de 3,8 eV. Ces sous-ensembles sont principalement associés à des hauteurs d'îlots de 4 et 6 monocouches (ML), respectivement.

Essentiellement, l'échantillon GaN/AlN QD à 10 plans, avec ses deux morphologies distinctes, présente une plate-forme fascinante pour les recherches futures, offrant à la fois des avantages expérimentaux et un spectre plus large de comportements à étudier. Sa compatibilité avec les résultats des échantillons à plan unique souligne encore sa valeur pour faire progresser notre compréhension des systèmes de boîtes quantiques.

8.6 Mécanismes de relaxation des porteurs dans les QDs GaN/AlN

Ce chapitre est consacré à une plongée approfondie dans le monde complexe des mécanismes de relaxation des porteurs au sein des boîtes quantiques (QD) GaN/AlN. Notre parcours d'enquête est structuré pour offrir une compréhension approfondie de ces mécanismes, permettant un développement ultérieur des technologies de boîtes quantiques et de leurs applications pratiques.

Pour commencer, la section 6.1 donne un aperçu du chapitre, établissant le contexte et la pertinence de notre travail. Le contenu est structuré pour s'appuyer progressivement sur notre compréhension de la dynamique des porteurs dans les QD GaN/AlN.

Dans la section 6.2, nous examinons la dynamique de relaxation dans des expériences pompe-sonde non dégénérées, avec des sous-sections dédiées à l'étude de la dynamique initiale et des comportements à plus grande échelle de temps dans les QD GaN/AlN à un seul plan et à 10 plans. Une partie intégrante de notre enquête dans cette section consiste à effectuer des mesures de puissance de pompe. Ces mesures nous permettent d'examiner la dynamique sous différents taux d'injection de porteurs. Comprendre ces dynamiques est essentiel pour révéler l'influence de l'injection multi-porteurs sur les processus de relaxation des porteurs observés.

Au fur et à mesure que nous progressons vers la section 6.3, elle se concentre sur les résultats d'expériences pompe-sonde dégénérées sur des QD GaN/AlN à 10 plans, offrant une perspective complémentaire sur la dynamique des porteurs et soulignant davantage les nuances de ces nanostructures.

La section 6.4 approfondit la dynamique du temps de montée dans les expériences pompe-sonde non dégénérées. L'étude rassemble des observations de petits et de grands QD pour former une image détaillée de la façon dont les porteurs peuplent les états énergétiques au sein des QD GaN/AlN dans différentes conditions expérimentales.

Dans la section 8.6, nous donnons un aperçu de tous les temps caractéristiques observés dans nos études, reliant les différents fils d'investigation et fournissant une compréhension globale de la dynamique de relaxation dans ces systèmes.

Le chapitre se termine par la section 6.6 où nous présentons nos conclusions tirées de ces études, résumant les principaux résultats et discutant de leurs implications pour les recherches futures et les applications technologiques des QD GaN/AlN.

À travers ce chapitre, nous visons à contribuer à une compréhension plus large des mécanismes de relaxation des porteurs dans les boîtes quantiques, avec un accent particulier sur les comportements propres aux systèmes GaN/AlN QD.

Synthèse de tous les temps caractéristiques

Pour fournir un synthèse complet de tous les temps caractéristiques, incorporons les résultats du temps de montée du signal de transmission différentiel pompe-sonde non dégénéré dans

les Fig.8.4 et Fig.8.5 . Cela offrira une visualisation complète de tous les aspects temporels importants que nous avons étudiés.

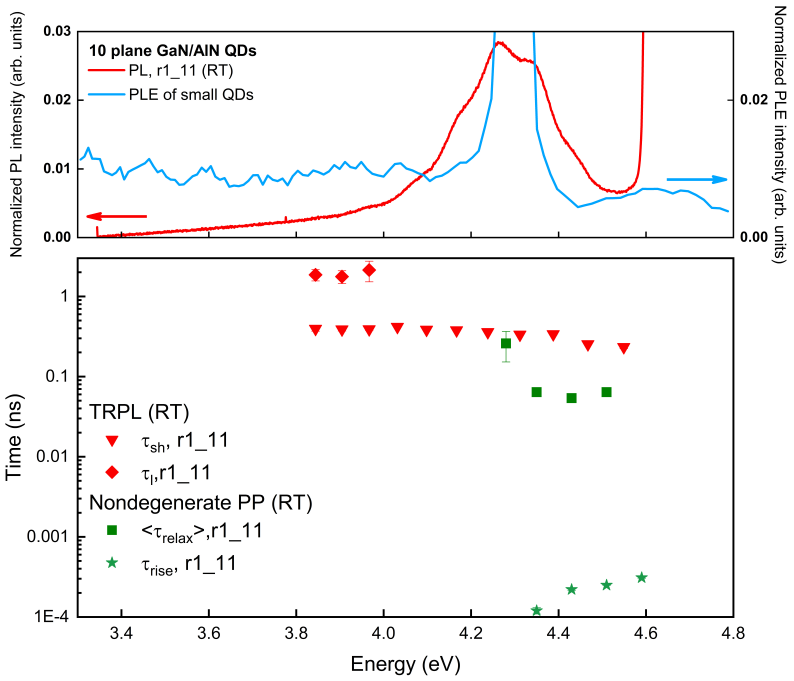

FIGURE 8.4: Graphique du haut, spectre PL de l'ensemble de QD GaN/AlN à 10 plans mesuré à la position $r1\_11$ sur l'échantillon à température ambiante (courbe rouge) et spectre PLE pour un petit ensemble de QD, dont le pic PL est proche de 4,3 eV (bleu courbe). Graphique du bas, constantes de désintégration du temps extraites de l'expérience TRPL : τ_l (losanges rouges) et τ_{sh} (triangles rouges vers le bas). Les constantes de temps $<\tau_{relax}>$ (carrés verts) correspondent aux temps de relaxation du signal de transmission différentielle, tandis que τ_{rise} (étoiles vertes) est le temps de montée correspondant.

Dans nos échantillons de boîtes quantiques GaN/AlN, nous observons une série complexe de dynamiques de porteurs suite à une excitation par une source de lumière à haute énergie. Le processus démarre par la génération de photoporteurs au sein de la couche mouillante lors de l'absorption de la lumière incidente. Étant donné le flux élevé de photons dans nos conditions expérimentales, un grand nombre de porteurs (électrons et trous) sont créés, conduisant à un environnement multi-porteurs. Ici, plusieurs interactions porteur-porteur se produisent, notamment les interactions coulombiennes, les événements de diffusion et la formation d'excitons. En raison de ces interactions et de la haute énergie conférée par la lumière incidente, les porteurs sont initialement dans un état de non-équilibre. Une fois thermalisés dans la couche mouillante, les porteurs commencent à passer aux boîtes quantiques. Grâce à des expériences pompe-sonde non dégénérées, nous avons suivi ces porteurs lors de la relaxation vers l'état radiatif. Le temps de montée, décrivant la réponse initiale lorsque les porteurs sont photo-créés et commencent à interagir, et le temps de relaxation, illustrant la décroissance de la réponse lorsque les porteurs se recombinent, sont interconnectés via des mécanismes de contribution partagés.

Les porteurs se redistribuent entre les états d'énergie disponibles, initiant ainsi le peuplement des états d'énergie disponibles à l'intérieur des QD. Conformément à la distribution de Boltzmann, les états d'énergie supérieure sont initialement moins peuplés que les états d'énergie inférieure. Le temps nécessaire au signal pour passer de sa ligne de base à son pic est le temps de montée τ_{rise}. Nos expériences montrent que ce temps de montée est inférieur à la picoseconde et initialement plus rapide aux énergies de sonde inférieures, indiquant un remplissage rapide des états d'énergie inférieurs. Cette tendance est maintenue pour les deux ensembles

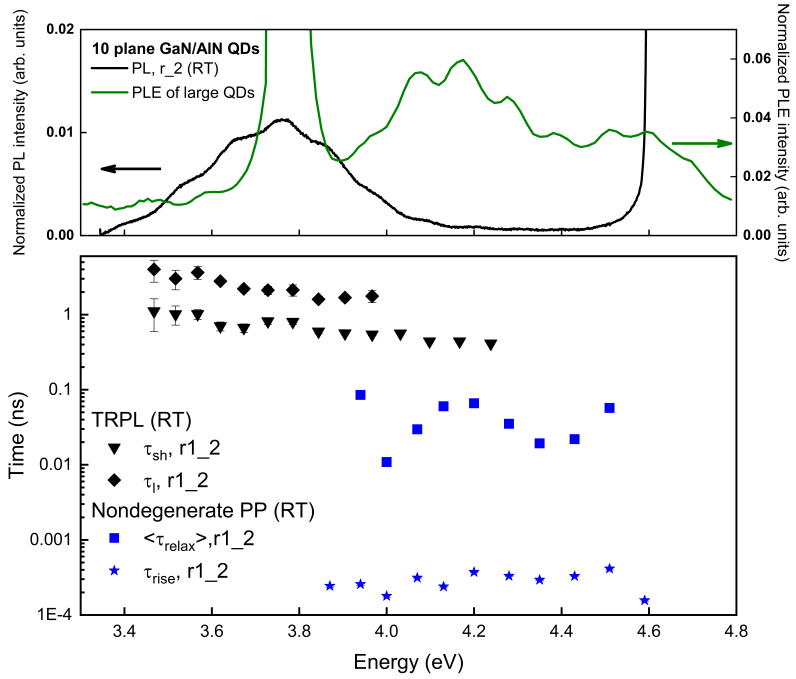

FIGURE 8.5: Graphique du haut, spectre PL de l'ensemble de QD GaN/AlN à 10 plans mesuré à la position $r1\_2$ sur l'échantillon à température ambiante (courbe noire) et spectre PLE pour un grand ensemble de QD, dont le pic PL est d'environ 3,8 eV (courbe verte). Graphique du bas, constantes de décroissance temporelle extraites de l'expérience TRPL : τ_l (losanges noirs) et τ_{sh} (triangles noirs vers le bas). Les constantes de temps $<\tau_{relax}>$ (carrés bleus) correspondent aux temps de relaxation du signal de transmission différentielle, tandis que τ_{rise} (étoiles bleues) est le temps de montée correspondant.

de QD (Fig 8.4 et Fig. 8.5). La capture des porteurs dans les boîtes est extrêmement efficace avec un temps caractéristique au moins un ordre de grandeur inférieur à celui des boîtes quantiques InAs/GaAs par exemple. Ceci s'explique probablement par les caractéristiques intrinsèques du GaN mais aussi par les conditions particulières de nos expériences.

Cependant, l'évolution de ce temps de montée en fonction de la densité de porteurs est difficile à interpréter. En particulier, l'existence d'un point d'inflexion apparaît lorsqu'on franchit le seuil de 4,5 eV, au-delà duquel le temps de montée commence à s'allonger, à mesure qu'on augmente la puissance de la pompe (voir Sec. 6.4). Cet allongement du temps de montée s'accompagne d'une augmentation de la valeur maximale prise par le signal. En d'autres termes, en excitant plus fortement, on donne la possibilité aux porteurs de charge d'explorer plus d'états. Le temps nécessaire pour atteindre le maximum est plus long car il y a plus d'états à remplir. Nous ne pouvons pas donner une justification plus approfondie sans une connaissance approfondie de la densité d'état électronique de notre système.

Cependant, les processus à l'œuvre pendant le temps de montée conduisent à la création d'une population quasi thermalisée dont la durée de vie est conditionnée par le remplissage des états d'énergie inférieurs. Cette dynamique est responsable de la relaxation du signal pompe-sonde sur des temps longs. Nos résultats indiquent que le processus de relaxation vers l'état fondamental de plus basse énergie est influencé par plusieurs facteurs, notamment les interactions porteur-porteur, l'énergie de la sonde et la puissance de la pompe. Lorsque la sonde entre en résonance avec l'état fondamental des boîtes, on observe essentiellement un comportement qui se rapproche d'une caractéristique exponentielle de la recombinaison radiative des paires électron-trou. Lorsque la puissance de la pompe augmente, le nombre de porteurs dans le système augmente également et les États au sein des QD commencent à

devenir plus densément peuplés, provoquant un effet de saturation. Mais paradoxalement, cela conduit également à un processus de relaxation plus rapide en termes de temps de réponse global du système. Nous suggérons que ces processus multiporteurs, ainsi que le filtrage transitoire du champ électrique interne dû à une forte injection de porteurs, pourraient jouer un rôle clé dans la dépendance en puissance observée de la dynamique de relaxation (voir Subsec. **??**). dès que l'énergie de la sonde dépasse celle de l'état fondamental, on assiste à l'apparition de processus de type Auger qui tendent à accélérer la dynamique et à compliquer la forme de la désintégration.

Conclusion

Dans ce chapitre, nous avons approfondi l'étude des mécanismes de relaxation des porteurs dans les QD GaN/AlN, en utilisant à la fois des techniques pompe-sonde non dégénérées et dégénérées. Grâce à ces expériences, nous avons acquis des connaissances sur la dynamique des porteurs hors équilibre, qui ne peuvent pas être explorées de manière adéquate par le seul TRPL.

Dans nos expériences pompe-sonde non dégénérées, nous avons observé un signal de transmission différentiel négatif sous forme de fond, suggérant la présence de phénomènes d'absorption induits. Cela était probablement dû à la population d'états à longue durée de vie par la pompe, peut-être à cause de la capture de porteurs sur des défauts profonds dans la matrice AlN. Cependant, ces phénomènes se produisent sur une échelle de temps nettement plus longue que celle qui nous intéresse principalement dans cette étude, à savoir la dynamique de relaxation immédiate suivant la photoexcitation. En tant que telle, l'analyse détaillée de ces effets a été laissée au-delà de la portée de cette recherche.

L'étude de la dynamique de relaxation de boîtes quantiques (QD) GaN/AlN à 1 plan à travers des expériences pompe-sonde non dégénérées a mis en lumière le processus de relaxation depuis la couche mouillante jusqu'aux états énergétiques sondés. Cependant, l'analyse de la dynamique du temps de montée a été obscurcie par la superposition d'un signal négatif et d'oscillations. Le temps de montée pour toutes les énergies testées s'est avéré inférieur ou égal à 1 ps, et la dynamique de désintégration aux énergies plus élevées ($>$ 4,5 eV) était rapide et monoexponentielle. Pour les énergies inférieures, la décroissance du signal de transmission différentiel était représentée par une fonction double exponentielle, avec des constantes de temps longues et courtes notées τ^{sh}_{relax} et τ^{l}_{relax}, respectivement. Ce dernier se rapproche du τ_s de la désintégration TRPL. La plage d'énergie dans laquelle la dynamique biexponentielle a été observée correspond à ce qui a été identifié comme un possible état excité des QD.

Notre enquête s'est ensuite étendue à un échantillon à 10 plans, dans lequel un masque métallique déposé sur la surface a créé 14 positions distinctes, chacune avec des hauteurs de boîtes quantiques uniques. Chacune de ces positions représente un « échantillon » en soi, avec différentes tailles de boîtes quantiques et des profils de profondeur complexes. L'étendue des informations accessibles à partir de chaque poste est si vaste qu'elle pourrait potentiellement constituer la base d'une thèse de doctorat distincte. Cependant, dans le cadre de cette étude, nous avons concentré notre attention sur deux ensembles extrêmes de QD : les petits et les grands, avec des PL centrés respectivement autour de 4,3 eV et 3,8 eV.

Compte tenu du nombre de variables et des nombreuses données accumulées, il n'est pas surprenant que la dynamique de relaxation de l'échantillon à 10 plans semble plus complexe que celle de l'échantillon à 1 plan.

Notre étude de recherche a adopté un modèle à trois niveaux, un outil essentiel qui confirme la présence de processus multi-porteurs en jeu dans les boîtes quantiques GaN/AlN dans nos conditions expérimentales. Il a mis en lumière la disparition progressive des processus multi-paires à mesure que les porteurs se thermalisent dans les boîtes. Nous avons constaté que l'efficacité du processus de relaxation quadratique diminue à mesure que l'énergie de la sonde diminue par rapport à l'énergie de la pompe. Compte tenu de la dynamique complexe au sein des boîtes quantiques, nous avons opté pour une mesure de la dynamique de relaxation moyenne, $<\tau_{relax}>$, qui représente efficacement les variations dynamiques, mais pas les durées de vie réelles de relaxation.

Nos résultats expérimentaux ont démontré des changements significatifs dans la dynamique en fonction de la puissance de la pompe. Nous avons observé une accélération de la dynamique avec l'augmentation de la puissance de la pompe, ce qui suggère que les mécanismes de diffusion multi-porteuses, tels que l'effet Auger, l'annihilation exciton-exciton ou la recombinaison bimoléculaire, jouent un rôle clé dans le processus de relaxation énergétique. Ces découvertes ont des implications importantes pour les applications qui reposent sur un transfert d'énergie efficace et une dynamique ultrarapide, telles que les dispositifs optoélectroniques et le traitement de l'information quantique. Nous avons constaté que le temps de relaxation, $<\tau_{relax}>$, dépend du E_{probe}. Le temps de relaxation moyen évolue de quelques dizaines de ps à quelques ns, au fur et à mesure que la E_{probe} descend de la couche mouillante jusqu'aux niveaux radiatifs. Le temps de relaxation s'aligne remarquablement sur la constante de temps courte τ_{sh} du TRPL à la résonance avec les QD. Les expériences pompe-sonde dégénérées confirment que pour les boîtes quantiques émettant à une énergie supérieure à 4,1 eV, la force de l'oscillateur était suffisante pour créer des paires électron-trou résonnant avec le niveau radiatif des boîtes quantiques, ce qui a conduit à une dynamique similaire à TRPL.

Dans le cas de boîtes quantiques plus grandes avec PL à 3,8 eV, la force réduite de l'oscillateur due à l'effet Stark confiné quantique masque le phénomène de résonance. Malgré cela, un ralentissement notable de la dynamique de relaxation, $<\tau_{relax}>$, est observé, ce qui correspond à la tendance observée dans le spectre PLE. Ceci suggère que la résonance entre la sonde et les niveaux d'énergie discrets des boîtes quantiques affecte de manière significative la dynamique de relaxation du système. Cette condition de résonance semble ralentir la dynamique de relaxation, potentiellement due au fait que les porteurs dans les états d'énergie de résonance nécessitent plus de temps pour passer à d'autres états.

Notre examen du temps de montée avec des retards immédiats a révélé la présence d'un creux négatif autour du retard zéro pour l'énergie de la sonde approchant du pic de photoluminescence (PL). Ce phénomène peut être compris en termes d'effet immédiat de l'injection de porteur induite par une pompe sur le système de boîtes quantiques. À l'arrivée de la pompe, des porteurs sont introduits, conduisant à toute une gamme d'interactions d'échange entre eux. De telles interactions, qu'elles soient attractives ou répulsives, provoquent une modification immédiate des niveaux d'énergie des boîtes quantiques. Cette dynamique se traduit par un décalage transitoire de la résonance, provoquant une diminution momentanée de l'absorption de l'impulsion de la sonde proche du délai zéro. Cela suggère une interaction exciton-exciton intéressante au sein des QD étudiés, qui émettent à 4,28 eV. Cette interprétation s'aligne sur les recherches antérieures sur les biexcitons dans les QD GaN/AlN [135]. Il a été démontré que le signe de l'énergie de liaison du biexciton varie en fonction de la taille et des dimensions spatiales de la boîte quantique. Par conséquent, les propriétés physiques de la boîte quantique influencent directement la nature des interactions multiparticulaires, se manifestant par des effets observables sur la dynamique des porteurs et l'absorption d'énergie.

Outre la diminution transitoire de l'absorption provoquée par le changement soudain de résonance, nous avons en outre identifié une caractéristique distinctive de la réponse du système à l'énergie de notre sonde : un temps de montée rapide (τ_{rise}) d'environ 200 femtosecondes. Les temps de montée observés dans notre système de boîtes quantiques GaN/AlN sont exceptionnellement rapides, comparés à d'autres systèmes similaires, tels que les boîtes quantiques InAs/GaAs, où les temps de montée ont été observés comme étant relativement plus lents.

De plus, nous observons une relation unique entre l'énergie de la sonde et le temps de montée. À mesure que l'énergie de la sonde se rapproche du pic PL, nous observons une nette réduction du temps de montée basée sur la dépendance énergétique. Ce schéma suggère un mécanisme étroitement lié au remplissage rapide et efficace des états disponibles après excitation. Dans ce contexte, l'accumulation du signal ΔT représente le temps nécessaire pour remplir les états disponibles en dessous du niveau sondé, différant de l'interprétation traditionnelle de la relaxation du niveau de mouillage vers celui-ci. Le remplissage rapide de ces états d'énergie inférieurs souligne l'efficacité impressionnante du système, évidente dans les temps de montée inférieurs à la picoseconde. De plus, le lien entre le temps de montée et la densité de porteurs, notamment autour du seuil de 4,5 eV, est intéressant. Au-delà d'un certain point, le temps de montée commence à augmenter avec l'augmentation de la puissance de la pompe, ce qui

indique qu'avec une excitation plus élevée, les porteurs remplissent plus d'états, ce qui entraîne un temps de montée plus long en raison d'une plus grande disponibilité des états.

En fin de compte, les subtilités et les spécificités de nos conditions expérimentales ont posé des défis occasionnels dans l'interprétation des données. Cela était particulièrement vrai lorsque nous travaillions dans des conditions d'excitation ultimes à haute densité, surtout par rapport à la densité des QD. Cependant, il est indéniable que ces conditions ont fourni des informations inestimables. Ils ont permis de mieux comprendre les mécanismes d'interaction multi-porteurs. De plus, ils ont souligné leur importance dans le processus de relaxation au sein des boîtes quantiques GaN/AlN.

8.7 Conclusion et directions futures

Conclusion

Grâce à l'utilisation combinée de différentes techniques d'optique ultrarapide, nous avons étudié la relaxation de paires électron-trou dans des échantillons de boîtes quantiques GaN/AlN de boîte. La dynamique des porteurs a été analysée depuis leur photo-création dans la couche mouillante jusqu'à leur recombinaison à partir des états discrets des boîtes sur des échelles de temps allant de quelques centaines de femtosecondes à quelques nanosecondes. Deux échantillons ont été étudiés. Le premier contenait un seul plan de boîtes émettant à 3,8 eV, le second 10 plans de boîtes avec un gradient de hauteur de ceux-ci, qui émettaient entre 3,5 et 4,4 eV selon la région excitée.

Des expériences de photoluminescence résolues dans le temps ont montré que, même si l'évolution des durées de vie radiatives avec la taille de la boîte est expliquée qualitativement par l'effet Stark confiné quantique, l'écart des désintégrations expérimentales par rapport à la simple fonction exponentielle a permis de tirer des conclusions précieuses sur la structure des échantillons. En particulier, nous avons démontré la capture réversible des porteurs depuis les boîtes vers un état sombre ou la présence conjointe au sein d'un même échantillon de deux morphologies de boîtes différentes se recombinant sur deux plages de temps différentes. Nous avons également développé un modèle analytique permettant de conclure à la présence d'un écrantage du champ électrique interne par les porteurs photo-injectés lors de la recombinaison.

Les expériences de transmission différentielle dégénérées et non dégénérées réalisées sur les deux échantillons ont montré que la thermalisation et la capture des porteurs dans les boîtes sont extrêmement efficaces et se déroulent à des échelles inférieures à la picoseconde. L'efficacité de ces procédés, supérieure à ceux à l'œuvre dans d'autres systèmes semiconducteurs III-V, est très certainement due aux propriétés particulières du GaN (fort couplage électron-phonon, masse effective élevée des trous) ainsi qu'aux conditions particulières de notre expériences (température ambiante, nécessité d'injecter une forte densité de porteurs pour générer des signaux détectables). Il en résulte la création très rapide d'une population thermalisée. L'évolution des temps de montée avec l'énergie photonique des signaux pompe-sonde correspondants suggère que ceux-ci sont construits par la saturation des états disponibles à des énergies inférieures à celle de l'impulsion sonde utilisée pour mesurer la dynamique. Aux temps longs, la relaxation est régie par les durées de vie finales et la densité des états disponibles. Elle est notamment ralentie lorsque l'énergie testée est en résonance avec l'état fondamental de la boîte ou l'un de ses états excités. En revanche, elle est accélérée par l'effet Auger et, probablement, par un écrantage transitoire du champ électrique interne lorsque la densité de porteurs injectés augmente.

Même si des connaissances considérables ont été acquises, la complexité de ces systèmes et leur potentiel pour un large éventail d'applications soulignent la nécessité de poursuivre les recherches.

Directions futures

Tous les résultats résumés dans le paragraphe précédent sont originaux et présentent des avancées considérables dans la connaissance des propriétés structurales et optiques des boîtes quantiques GaN/AlN. Voici cependant quelques idées pour aller plus loin.

Au-delà du TRPL et du PLE, souvent utilisés pour étudier GaN/AlN, c'est l'utilisation conjointe d'expériences pompe-sonde dégénérées et non dégénérées qui constitue le cœur de ces travaux. Il ne s'agit cependant que d'une première tentative et certaines limitations ne nous ont pas permis d'aller aussi loin que nous l'aurions souhaité compte tenu du temps limité.

En particulier, aucune expérience dépendant de la température des échantillons n'a pu être réalisée. Ceux-ci auraient pu nous aider à identifier les processus physiques responsables de la thermalisation[132]. De plus, l'obligation de travailler à température ambiante a probablement limité la résolution temporelle de notre dispositif en ramenant les temps de relaxation à leurs valeurs les plus basses. Les expériences en fonction de la densité de porteurs ont montré que l'on avait souvent travaillé à des puissances pour lesquelles les processus multi-porteurs (type Auger) masquaient tous les autres processus de relaxation possibles. Travailler à très faible injection comme nous l'avons fait dans nos expériences TRPL ne nous semble pas réaliste. Cependant, avec l'expérience acquise sur l'étude de ces systèmes, nous pourrions viser à travailler sous une gamme plus large de niveaux d'excitation. Il peut également exister des régimes intermédiaires dans lesquels se produit une interaction complexe entre les effets quantiques d'une seule particule, les interactions exciton-exciton et les effets à plusieurs corps. Dévoiler le comportement de ces régimes de transition pourrait être révélateur.

La stratégie utilisée dans les expériences non dégénérées, consistant à maintenir la pompe à une énergie fixe et à faire varier l'énergie de la sonde, ne nous paraît pas la bonne. Avec du recul, il nous paraît évident qu'il aurait fallu au contraire maintenir l'énergie de la sonde fixe et changer l'énergie de la pompe. Toutefois, pour des raisons techniques, cette alternative n'était pas possible. Nous travaillons actuellement sur la possibilité de générer un super-continuum qui servirait de sonde et qui pourrait aller assez loin dans l'UV. L'étude des interactions coulombiennes observées à des temps très courts bénéficierait de ce type d'amélioration. L'étendue du continuum obtenu imposera des contraintes en termes de spectre d'absorption des échantillons.

Puisqu'il s'agit d'échantillons, il est apparu que travailler sur un échantillon contenant plusieurs plans de boîtes améliore sans aucun doute le rendement des expériences. Travailler sur un échantillon à gradient de hauteur est utile pour explorer, comme nous l'avons fait, la relation entre l'énergie d'émission et la durée de vie, toutes autres caractéristiques structurelles restant égales. En revanche, cela complique grandement l'interprétation des processus de relaxation. D'autant plus que les boîtes de faible hauteur, dans lesquels le confinement prévaut sur l'effet Stark confiné quantique, donnent les résultats les plus exploitables. Cependant, cet échantillon particulier a permis de tirer certaines conclusions concernant la dépendance des énergies de transition en fonction de l'extension latérale des boîtes ainsi que la présence probable de deux morphologies différentes de boîtes. C'est un point qui pourrait être approfondi grâce à une connaissance plus approfondie de la structure et de la morphologie des échantillons. La microscopie électronique à transmission par balayage (STEM) serait une méthode complémentaire très bénéfique pour élucider davantage les propriétés physiques de ces boîtes quantiques. Étant donné que nos échantillons sont recouverts d'une couche de recouvrement, STEM peut fournir des informations structurelles précieuses qui ne sont pas directement accessibles via les techniques optiques. Cela nous permettrait de déterminer avec précision la taille, la forme et la distribution des boîtes quantiques et d'identifier tout défaut structurel ou variation des boîtes quantiques ou de la matrice environnante.

Appendix A

Removing the oscillations from PL spectra

As shown in Fig. A.1, PL spectra are modulated by fringes due to Fabry-Perot interferences occurring in the epilayer stack. We remove these oscillations by applying a Gaussian fit to time-sliced PL spectra in order to get access to the time evolution of the fitting parameters: the energy position of the PL maximum E_{max}, its width and its intensity.

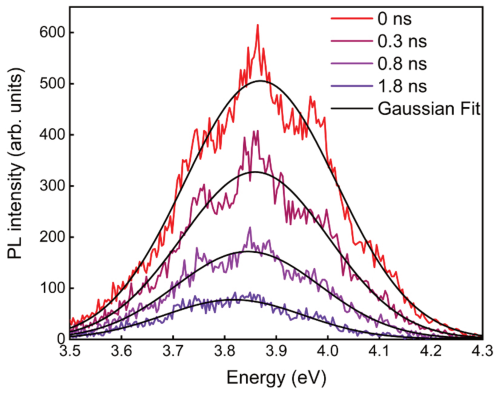

FIGURE A.1: Low temperature ($T = 10$ K) PL spectra of a GaN/AlN QD ensemble at different delay times after the laser pulse excitation.

Appendix B

Modeling of the spectro-temporal evolution of the PL spectra

In order to obtain an analytical expression of the spectro-temporal evolution of the PL spectrum emitted by an ensemble of GaN/AlN QDs, we first make the assumption that the height distribution is normal, resulting in a Gaussian lineshape. If the density of injected e-h pairs is small enough, the recombination probability is time-independent and it exists a function $\tau(E)$ describing the variation of the radiative lifetime as a function of emission energy. The consequence is that the dynamics of each spectral component is exponential with a decay time $\tau(E)$.

The PL intensity can then be written:

$$I_{PL}(E,t) \propto \exp\left\{\left[-\frac{(E-E_0)^2}{\Gamma_{inh}^2}\right]\right\} \exp\{(-\gamma(E)\,t),\} \tag{B.1}$$

where we have introduced the radiative relaxation rate:

$$\gamma(E) = \frac{1}{\tau(E)}. \tag{B.2}$$

When γ only depends linearly and quadratically on E, i.e., when its Taylor expansion is stopped at the second order, the shape of I_{PL} as a function of photon energy E remains a Gaussian at any time. The energy position of the PL maximum $E_{max}(t)$ and the FWHM $\Delta E(t)$ versus time are obtained by canceling the first and the second derivatives of Eq.(5.7) relative to the photon energy E, respectively. The calculation of these derivatives is straightforward and gives:

$$\frac{\partial}{\partial E} I_{PL}(E,t) = \left(-\frac{d\gamma}{dE}\cdot t - \frac{2(E-E_0)}{\Gamma_{inh}^2}\right)\cdot I_{PL}(E,t), \tag{B.3}$$

and

$$\frac{\partial^2}{\partial E^2} I_{PL}(E,t) = \left(-t\cdot\frac{d^2\gamma}{dE^2} + t^2\cdot\left(\frac{d\gamma}{dE}\right)^2 + \frac{4t}{\Gamma_{inh}^2}\left(\frac{d\gamma}{dE}\right)(E-E_0) - \right.$$
$$\left. - \frac{2}{\Gamma_{inh}^2} + \frac{4}{\Gamma_{inh}^4}(E-E_0)^2\right)\cdot I_{PL}(E,t). \tag{B.4}$$

B.1 γ is independent of E

If $\gamma = \gamma_0$ is independent of E, the first derivative cancels for:

$$E_{max} = E_0, \tag{B.5}$$

and the second derivative for:

$$E_{\pm} = E_0 \pm \frac{\Gamma_{inh}}{\sqrt{2}}. \tag{B.6}$$

Hence, the FWHM is given by:

$$\Delta E = E_+ - E_- = \sqrt{2}\Gamma_{inh}. \tag{B.7}$$

We recover the simple case of a Gaussian lineshape whose spectral position is independent of time and whose intensity decays with a lifetime $\tau_0 = \gamma_0^{-1}$.

B.2 General case: γ is a function of E

If now γ is a quadratic function of E that we can expand around E_0:

$$\gamma(E) = \gamma_0 + \gamma_1 \cdot (E - E_0) + \frac{1}{2}\gamma_2 \cdot (E - E_0)^2. \tag{B.8}$$

The first derivative of I_{PL} cancels for:

$$\begin{aligned} E_{max}(t) &= E_0 - \frac{\Gamma_{inh}^2}{2}\frac{d\gamma}{dE} \cdot t \\ &= E_0 - \frac{\Gamma_{inh}^2}{2}\left(\gamma_1 + \gamma_2 \cdot (E_{max}(t) - E_0)\right) \cdot t, \\ E_{max}(t) &= E_0 - \frac{\Gamma_{inh}^2 \gamma_1 \cdot t}{2 + \Gamma_{inh}^2 \gamma_2 \cdot t}. \end{aligned} \tag{B.9}$$

The time evolution of the FWHM is obtained by canceling the second derivative, which gives:

$$\begin{aligned} E_{\pm}(t) &= E_{max}(t) \pm \frac{\Gamma_{inh}}{\sqrt{2}}\sqrt{1 + \frac{\Gamma_{inh}^2}{2}\frac{d^2\gamma}{dE^2} \cdot t} \\ &= E_0 - \frac{\Gamma_{inh}^2 \gamma_1 . t \mp \Gamma_{inh}\sqrt{2 + \Gamma_{inh}^2 \gamma_2 . t}}{2 + \Gamma_{inh}^2 \gamma_2 \cdot t}. \end{aligned} \tag{B.10}$$

$$\Delta E(t) = E_+(t) - E_-(t) = \frac{2\,\Gamma_{inh}}{\sqrt{2 + \Gamma_{inh}^2 \gamma_2 \cdot t}}. \tag{B.11}$$

The intensity is then given by the PL emission maximum at $E_{max}(t)$:

$$I_{PL}\left(E_{max}, t\right) \propto \exp\left\{\left(-\gamma_0 \cdot t + \frac{1}{2}\left(\frac{\Gamma_{inh}^2 \gamma_1^2}{2 + \Gamma_{inh}^2 \gamma_2 t}\right) \cdot t^2\right)\right\}. \tag{B.12}$$

Appendix C

Variational calculation of in-plane wave-functions

A variational calculation enables to estimate the influence of an in-plane confinement potential on the energies and radiative lifetimes of QDs. We consider as a first approximation that the potential is separable in the z and (x, y) directions. The built-in electric field is taken into account along the vertical direction and does not play any role on the lateral confinement. The Hamiltonian of a particle with effective mass m^* trapped in an abrupt potential V_0 with a cylindrical symmetry is given by:

$$H = -\frac{\hbar^2}{2m^*}\frac{1}{\rho}\frac{\partial}{\partial\rho}\left(\rho\frac{\partial}{\partial\rho}\right) + V_0\Theta\left(\rho - \rho_0\right), \tag{C.1}$$

where ρ is the radial coordinate, Θ is the Heaviside step function and ρ_0 is the spatial extension of the lateral potential. The confinement energy can be found using the variational method by minimizing:

$$E\left(\rho_0, \sigma\right) = \langle\phi\left(\sigma\right)|H|\phi\left(\sigma\right)\rangle. \tag{C.2}$$

as a function of the extension parameter σ, where ϕ is a normalized Gaussian envelope-function:

$$\phi\left(\rho\right) = \frac{1}{\sigma\sqrt{\pi}} exp\left[-\left(\frac{\rho}{\sigma}\right)^2\right]. \tag{C.3}$$

The problem is solved analytically and gives:

$$\sigma = \rho_0\sqrt{2}\left[\ln\left(\frac{2m^*\rho_0^2 V_0}{\hbar^2}\right)\right]^{-1/2}, \tag{C.4}$$

and

$$E\left(\rho_0\right) = \frac{\hbar^2}{2m^*\rho_0^2}\left[1 + \ln\left(\frac{2m^*\rho_0^2}{\hbar^2}V_0\right)\right]. \tag{C.5}$$

The procedure is realized for electrons and holes with effective masses $m_e^* = 0.2m_0$ and $m_h^* = 0.81m_0$ [**Rinke2008**],respectively, with m_0 the free electron mass, giving the confinement

energies E_e and E_h, as well as the in-plane extensions σ_e and σ_h of the corresponding envelope-functions. The overlap integral can also be evaluated analytically:

$$\int_0^{+\infty} \phi_e(\rho)\,\phi_h(\rho)\,2\pi\rho d\rho = 2\frac{\sigma_e\sigma_h}{\sigma_e^2+\sigma_h^2}. \tag{C.6}$$

Bibliography

[1] A.I. Ekimov, A.A. Onuschenko, and V.A. Tsekhomskii. "Exciton light absorption by CuCl microcrystals in glass matrix". In: *Sov. Glass Phys. Chem* 6 (1980), pp. 511–512.

[2] R. Rossetti and L. Brus. "Electron-hole recombination emission as a probe of surface chemistry in aqueous cadmium sulfide colloids". In: *The Journal of Physical Chemistry* 86.23 (1982), pp. 4470–4472. DOI: 10.1021/j100220a003.

[3] A.I. Ekimov and A.A. Onushchenko. "Size quantization of the electron energy spectrum in a microscopic semiconductor crystal". In: *ZhETF Pisma Redaktsiiu* 40 (1984), p. 337.

[4] L. Goldstein et al. "Growth by molecular beam epitaxy and characterization of InAs/GaAs strained-layer superlattices". In: *Applied Physics Letters* 47.10 (1985), pp. 1099–1101. DOI: 10.1063/1.96342.

[5] J. Cibert et al. "Optically detected carrier confinement to one and zero dimension in GaAs quantum well wires and boxes". In: *Applied Physics Letters* 49.19 (1986), pp. 1275–1277. DOI: 10.1063/1.97384.

[6] P. Gilliot et al. "Nonlinearities of CuCl Microcrystals". In: *physica status solidi (b)* 159.1 (1990), pp. 259–265. DOI: https://doi.org/10.1002/pssb.2221590130. URL: https://onlinelibrary.wiley.com/doi/abs/10.1002/pssb.2221590130.

[7] R. Levy et al. "Biexciton luminescence in CuCl microcrystallites". In: *Phys. Rev. B* 44 (20 1991), pp. 11286–11292. DOI: 10.1103/PhysRevB.44.11286. URL: https://link.aps.org/doi/10.1103/PhysRevB.44.11286.

[8] B. Kippelen et al. "Picosecond excite and probe nonlinear absorption measurements in CuCl quantum dots". In: *Applied Physics Letters* 59.26 (Dec. 1991), pp. 3378–3380. ISSN: 0003-6951. DOI: 10.1063/1.105680. eprint: https://pubs.aip.org/aip/apl/article-pdf/59/26/3378/7783969/3378_1_online.pdf. URL: https://doi.org/10.1063/1.105680.

[9] J. Valenta et al. "Hole-filling of persistent spectral holes in the excitonic absorption band of CuBr quantum dots". In: *Applied Physics Letters* 70.6 (Feb. 1997), pp. 680–682. ISSN: 0003-6951. DOI: 10.1063/1.118273. eprint: https://pubs.aip.org/aip/apl/article-pdf/70/6/680/10171032/680_1_online.pdf. URL: https://doi.org/10.1063/1.118273.

[10] R. C. Ashoori. "Electrons in artificial atoms". In: *Nature* 379 (6564 1996), pp. 413–419. DOI: 10.1038/379413a0.

[11] Haiguang Zhao et al. "Efficient and stable tandem luminescent solar concentrators based on carbon dots and perovskite quantum dots". In: *Nano Energy* 50 (2018), pp. 756–765. ISSN: 2211-2855. DOI: https://doi.org/10.1016/j.nanoen.2018.06.025.

[12] Shan Jin et al. "Application of Quantum Dots in Biological Imaging". In: *J. Nanomaterials* 2011 (2011). ISSN: 1687-4110. DOI: 10.1155/2011/834139.

[13] Xiaohu Gao et al. "In vivo cancer targeting and imaging with semiconductor quantum dots". In: *Nature biotechnology* 22 (2004), pp. 969–976. DOI: 10.1038/nbt994.

[14] Hyojung Choi et al. "Renal clearance of quantum dots". In: *Nature biotechnology* 25 (2007), pp. 1165–1170. DOI: 10.1038/nbt1340.

[15] Neda Heydari et al. "Quantum Dot-Based Light Emitting Diodes (QDLEDs): New Progress". In: *Quantum-dot Based Light-emitting Diodes*. Ed. by Morteza Sasani Ghamsari. Rijeka: IntechOpen, 2017. Chap. 3. DOI: 10.5772/intechopen.69014.

[16] Geun Woo Baek et al. "Progress in the Development of Active-Matrix Quantum-Dot Light-Emitting Diodes Driven by Non-Si Thin-Film Transistors". In: *Materials* 15.23 (2022). DOI: 10.3390/ma15238511.

[17] A. J. Nozik et al. “Semiconductor Quantum Dots and Quantum Dot Arrays and Applications of Multiple Exciton Generation to Third-Generation Photovoltaic Solar Cells”. In: *Chemical Reviews* 110.11 (2010), pp. 6873–6890. DOI: 10.1021/cr900289f.

[18] Octavi E. Semonin, Joseph M. Luther, and Matthew C. Beard. “Quantum dots for next-generation photovoltaics”. In: *Materials Today* 15.11 (2012), pp. 508–515. ISSN: 1369-7021. DOI: https://doi.org/10.1016/S1369-7021(12)70220-1.

[19] X. Michalet et al. “Quantum Dots for Live Cells, in Vivo Imaging, and Diagnostics”. In: *Science* 307.5709 (2005), pp. 538–544. DOI: 10.1126/science.1104274.

[20] Mohammad Ehtisham Khan, Akbar Mohammad, and Taeho Yoon. “State-of-the-art developments in carbon quantum dots (CQDs): Photo-catalysis, bio-imaging, and biosensing applications”. In: *Chemosphere* 302 (2022), p. 134815. ISSN: 0045-6535. DOI: https://doi.org/10.1016/j.chemosphere.2022.134815.

[21] Jing Jia et al. “Recent advances in synthesis and applications of room temperature phosphorescence carbon dots”. In: *Talanta* 231 (2021), p. 122350. ISSN: 0039-9140. DOI: https://doi.org/10.1016/j.talanta.2021.122350.

[22] Hao Suo et al. “High-security anti-counterfeiting through upconversion luminescence”. In: *Materials Today Physics* 21 (2021), p. 100520. ISSN: 2542-5293. DOI: https://doi.org/10.1016/j.mtphys.2021.100520.

[23] Christoph Kloeffel and Daniel Loss. “Prospects for Spin-Based Quantum Computing in Quantum Dots”. In: *Annual Review of Condensed Matter Physics* 4.1 (2013), pp. 51–81. DOI: 10.1146/annurev-conmatphys-030212-184248.

[24] Peter Lodahl. “Quantum-dot based photonic quantum networks”. In: *Quantum Science and Technology* 3.1 (2017), p. 013001. DOI: 10.1088/2058-9565/aa91bb.

[25] Fulvio Flamini, Nicolò Spagnolo, and Fabio Sciarrino. “Photonic quantum information processing: a review”. In: *Reports on Progress in Physics* 82.1 (2018), p. 016001. DOI: 10.1088/1361-6633/aad5b2.

[26] Jonathan P. Dowling and Gerard J. Milburn. “Quantum Technology: The Second Quantum Revolution”. In: *Philosophical Transactions: Mathematical, Physical and Engineering Sciences* 361.1809 (2002), pp. 1655–1674. DOI: 10.1098/rsta.2003.1227.

[27] Anasua Chatterjee et al. “Semiconductor qubits in practice”. In: *Nature Reviews Physics* 3.3 (2021), pp. 157–177. DOI: 10.1038/s42254-021-00283-9.

[28] AMJ Zwerver et al. “Qubits made by advanced semiconductor manufacturing”. In: *Nature Electronics* 5.3 (2022), pp. 184–190. DOI: 10.1038/s41928-022-00727-9.

[29] C. L. Salter et al. “An Electrically Driven Entangled Light Source”. In: *Conference on Lasers and Electro-Optics 2010*. Optica Publishing Group, 2010, QWH5. DOI: 10.1364/QELS.2010.QWH5.

[30] Igor Aharonovich, Dirk Englund, and Milos Toth. “Solid-state single-photon emitters”. In: *Nature photonics* 10.10 (2016), pp. 631–641. DOI: 10.1038/nphoton.2016.186.

[31] Y. Arakawa and M. J. Holmes. “Progress in quantum-dot single photon sources for quantum information technologies: A broad spectrum overview”. In: *Applied Physics Reviews* 7.2 (2020), p. 021309. DOI: 10.1063/5.0010193.

[32] Catherine J Murphy. “Peer reviewed: optical sensing with quantum dots”. In: *Analytical Chemistry* 74.19 (2002), 520–A. DOI: 10.1021/ac022124v.

[33] C. L. Degen, F. Reinhard, and P. Cappellaro. “Quantum sensing”. In: *Rev. Mod. Phys.* 89 (3 2017), p. 035002. DOI: 10.1103/RevModPhys.89.035002.

[34] Khabat Heshami et al. “Quantum memories: emerging applications and recent advances”. In: *Journal of Modern Optics* 63.20 (2016), pp. 2005–2028. DOI: 10.1080/09500340.2016.1148212.

[35] T. Heindel et al. “Quantum key distribution using quantum dot single-photon emitting diodes in the red and near infrared spectral range”. In: *New Journal of Physics* 14.8 (2012), p. 083001. DOI: 10.1088/1367-2630/14/8/083001.

[36] Daniel A. Vajner et al. “Quantum Communication Using Semiconductor Quantum Dots”. In: *Advanced Quantum Technologies* 5.7 (2022), p. 2100116. DOI: https://doi.org/10.1002/qute.202100116.

[37] W. Zhou and J. J. Coleman. “Semiconductor quantum dots”. In: *Current Opinion in Solid State and Materials Science* 20.6 (2016), pp. 352–360. ISSN: 1359-0286. DOI: https://doi.org/10.1016/j.cossms.2016.06.006.

[38] F. Pelayo García de Arquer et al. “Semiconductor quantum dots: Technological progress and future challenges”. In: *Science* 373.6555 (2021), eaaz8541. DOI: 10.1126/science.aaz8541.

[39] L. Cavigli et al. “High temperature single photon emitter monolithically integrated on silicon”. In: *Applied Physics Letters* 100.23 (2012), p. 231112. DOI: 10.1063/1.4726189.

[40] Ł. Dusanowski et al. “Single photon emission up to liquid nitrogen temperature from charged excitons confined in GaAs-based epitaxial nanostructures”. In: *Applied Physics Letters* 106.23 (2015), p. 233107. DOI: 10.1063/1.4922455.

[41] B. Damilano et al. “Violet to Orange Room Temperature Luminescence from GaN Quantum Dots on Si(111) Substrates”. In: *physica status solidi (b)* 216.1 (1999), pp. 451–455.

[42] B. Damilano et al. “From visible to white light emission by GaN quantum dots on Si(111) substrate”. In: *Applied Physics Letters* 75.7 (1999), pp. 962–964. DOI: 10.1063/1.124567.

[43] F. Widmann et al. “Blue-light emission from GaN self-assembled quantum dots due to giant piezoelectric effect”. In: *Phys. Rev. B* 58 (24 1998), R15989–R15992. DOI: 10.1103/PhysRevB.58.R15989.

[44] M. J. Holmes et al. “Room-temperature triggered single photon emission from a III-nitride site-controlled nanowire quantum dot”. In: *Nano letters* 14 (2014), pp. 982–6. DOI: 10.1021/nl404400d.

[45] S. Tamariz et al. “Toward Bright and Pure Single Photon Emitters at 300 K Based on GaN Quantum Dots on Silicon”. In: *ACS Photonics* 7.6 (2020), pp. 1515–1522. DOI: 10.1021/acsphotonics.0c00310.

[46] Mark J. Holmes et al. “Single Photons from a Hot Solid-State Emitter at 350 K”. In: *ACS Photonics* 3.4 (2016), pp. 543–546. DOI: 10.1021/acsphotonics.6b00112.

[47] D. Lagarde et al. “Room-temperature optical orientation of the exciton spin in cubic GaN/AlN quantum dots”. In: *Phys. Rev. B* 77 (4 2008), p. 041304. DOI: 10.1103/PhysRevB.77.041304.

[48] B. Damilano, J. Brault, and J. Massies. “Formation of GaN quantum dots by molecular beam epitaxy using NH3 as nitrogen source”. In: *Journal of Applied Physics* 118.2 (2015), p. 024304. DOI: 10.1063/1.4923425.

[49] S. Tamariz, G. Callsen, and N. Grandjean. “Density control of GaN quantum dots on AlN single crystal”. In: *Applied Physics Letters* 114.8 (2019), p. 082101. DOI: 10.1063/1.5083018.

[50] O. Ambacher et al. “Pyroelectric properties of Al(In)GaN/GaN hetero- and quantum well structures”. In: *Journal of Physics: Condensed Matter* 14.13 (2002), pp. 3399–3434. DOI: 10.1088/0953-8984/14/13/302. URL: https://doi.org/10.1088/0953-8984/14/13/302.

[51] F. Bernardini, V. Fiorentini, and D. Vanderbilt. “Spontaneous polarization and piezoelectric constants of III-V nitrides”. In: *Phys. Rev. B* 56 (16 1997), R10024–R10027. DOI: 10.1103/PhysRevB.56.R10024.

[52] D. P. Williams et al. “Theory of GaN Quantum Dots for Optical Applications”. In: *IEEE Journal of Selected Topics in Quantum Electronics* 15.4 (2009), pp. 1092–1103. DOI: 10.1109/JSTQE.2009.2018828.

[53] J. Simon et al. “Direct comparison of recombination dynamics in cubic and hexagonal GaN/AlN quantum dots”. In: *Phys. Rev. B* 68 (3 2003), p. 035312. DOI: 10.1103/PhysRevB.68.035312.

[54] T. Bretagnon et al. “Radiative lifetime of a single electron-hole pair in GaN/AlN quantum dots”. In: *Phys. Rev. B* 73 (11 2006), p. 113304. DOI: 10.1103/PhysRevB.73.113304.

[55] L. Zhou et al. “Measurement of electric field across individual wurtzite GaN quantum dots using electron holography”. In: *Applied Physics Letters* 99.10 (2011), p. 101905. DOI: 10.1063/1.3636109.

[56] A. D. Andreev and E. P. O’Reilly. “Optical transitions and radiative lifetime in GaN/AlN self-organized quantum dots”. In: *Applied Physics Letters* 79.4 (2001), pp. 521–523. DOI: 10.1063/1.1386405.

[57] S. Kako et al. “Size-dependent radiative decay time of excitons in GaN/AlN self-assembled quantum dots”. In: *Applied Physics Letters* 83.5 (2003), pp. 984–986. DOI: 10.1063/1.1596382.

[58] I. Robert-Philip et al. “Generation of non-classical light by single quantum dots”. In: *Journal of Luminescence* 102-103 (2003), pp. 67–71. ISSN: 0022-2313. DOI: https://doi.org/10.1016/S0022-2313(02)00515-X.

[59] J. Bylander, I. Robert-Philip, and I. Abram. In: *The European Physical Journal D* 22 (2003), pp. 295–301. DOI: 10.1140/epjd/e2002-00236-6.

[60] X. B. Zhang et al. “Influence of electron-phonon interaction on the optical properties of III nitride semiconductors”. In: *Journal of Physics: Condensed Matter* 13.32 (2001), p. 7053. DOI: 10.1088/0953-8984/13/32/312.

[61] Jun Deng et al. “Studies on Carrier Recombination in GaN/AlN Quantum Dots in Nanowires with a Core–Shell Structure”. In: *Nanomaterials* 10.11 (2020). ISSN: 2079-4991. DOI: 10.3390/nano10112299.

[62] M. Henini. “Properties of Group III nitrides”. In: *Microelectronics Journal* 26.2 (1995). ISSN: 0026-2692. DOI: https://doi.org/10.1016/0026-2692(95)90023-3.

[63] I. Vurgaftman and J. R. Meyer. “Band parameters for nitrogen-containing semiconductors”. In: *Journal of Applied Physics* 94.6 (2003), pp. 3675–3696. DOI: 10.1063/1.1600519. URL: https://doi.org/10.1063/1.1600519.

[64] J.F. Nye and P.P.L.J.F. Nye. *Physical Properties of Crystals: Their Representation by Tensors and Matrices*. Oxford science publications. Clarendon Press, 1985. ISBN: 9780198511656. URL: https://books.google.fr/books?id=ugwql-uVB44C.

[65] Lu Yan-Wu, Cai Lin, and Liang Shuang. “Strained and Piezoelectric Characteristics of Nitride Quantum Dots”. In: *Chinese Physics Letters* 23.4 (2006), pp. 956–959. DOI: 10.1088/0256-307x/23/4/054.

[66] K. Kim, W. R. L. Lambrecht, and B. Segall. “Elastic constants and related properties of tetrahedrally bonded BN, AlN, GaN, and InN”. In: *Phys. Rev. B* 53 (24 1996), pp. 16310–16326. DOI: 10.1103/PhysRevB.53.16310. URL: https://link.aps.org/doi/10.1103/PhysRevB.53.16310.

[67] D. Fritsch, H. Schmidt, and M. Grundmann. “Band-structure pseudopotential calculation of zinc-blende and wurtzite AlN, GaN, and InN”. In: *Phys. Rev. B* 67 (23 2003), p. 235205. DOI: 10.1103/PhysRevB.67.235205. URL: https://link.aps.org/doi/10.1103/PhysRevB.67.235205.

[68] M. Suzuki, T. Uenoyama, and A. Yanase. “First-principles calculations of effective-mass parameters of AlN and GaN”. In: *Phys. Rev. B* 52 (11 1995), pp. 8132–8139. DOI: 10.1103/PhysRevB.52.8132. URL: https://link.aps.org/doi/10.1103/PhysRevB.52.8132.

[69] G. D. Chen et al. “Fundamental optical transitions in GaN”. In: *Applied Physics Letters* 68.20 (1996), pp. 2784–2786. DOI: 10.1063/1.116606. URL: https://doi.org/10.1063/1.116606.

[70] F. Litimein et al. “The electronic structure of wurtzite and zincblende AlN: an ab initio comparative study”. In: *New Journal of Physics* 4.1 (2002), p. 64. DOI: 10.1088/1367-2630/4/1/364.

[71] Magloire Tchounkeu et al. “Optical properties of GaN epilayers on sapphire”. In: *Journal of Applied Physics* 80.9 (1996), pp. 5352–5360. DOI: 10.1063/1.363475. URL: https://doi.org/10.1063/1.363475.

[72] L. Claudio de Carvalho et al. “Valence-band splittings in cubic and hexagonal AlN, GaN, and InN”. In: *Applied Physics Letters* 97.23 (2010), p. 232101. DOI: 10.1063/1.3524234. URL: https://doi.org/10.1063/1.3524234.

[73] Y.P. Varshni. “Temperature dependence of the energy gap in semiconductors”. In: *Physica* 34.1 (1967), pp. 149–154. ISSN: 0031-8914. DOI: https://doi.org/10.1016/0031-8914(67)90062-6. URL: https://www.sciencedirect.com/science/article/pii/0031891467900626.

[74] Qimin Yan et al. “Effects of strain on the band structure of group-III nitrides”. In: *Phys. Rev. B* 90 (12 2014), p. 125118. DOI: 10.1103/PhysRevB.90.125118. URL: https://link.aps.org/doi/10.1103/PhysRevB.90.125118.

[75] K. Kornitzer et al. “Photoluminescence and reflectance spectroscopy of excitonic transitions in high-quality homoepitaxial GaN films”. In: *Phys. Rev. B* 60 (3 1999), pp. 1471–

1473. DOI: 10.1103/PhysRevB.60.1471. URL: https://link.aps.org/doi/10.1103/PhysRevB.60.1471.

[76] Robert Seguin. "Electronic fine structure and recombination dynamics in single InAs quantum dots". PhD thesis. Fakultät II - Mathematik und Naturwissenschaften der Technischen Universität Berlin, 2008.

[77] M. Reischle et al. "Influence of the Dark Exciton State on the Optical and Quantum Optical Properties of Single Quantum Dots". In: *Phys. Rev. Lett.* 101 (14 2008), p. 146402. DOI: 10.1103/PhysRevLett.101.146402. URL: https://link.aps.org/doi/10.1103/PhysRevLett.101.146402.

[78] H. Mäntynen et al. "Single-photon sources with quantum dots in III–V nanowires". In: *Nanophotonics* 8.5 (2019), pp. 747–769. DOI: doi:10.1515/nanoph-2019-0007. URL: https://doi.org/10.1515/nanoph-2019-0007.

[79] Y. Z. Hu et al. "Biexcitons in semiconductor quantum dots". In: *Phys. Rev. Lett.* 64 (15 1990), pp. 1805–1807. DOI: 10.1103/PhysRevLett.64.1805. URL: https://link.aps.org/doi/10.1103/PhysRevLett.64.1805.

[80] P. Roussignol et al. "Time-resolved direct observation of Auger recombination in semiconductor-doped glasses". In: *Applied Physics Letters* 51.23 (1987), pp. 1882–1884. DOI: 10.1063/1.98499. URL: https://doi.org/10.1063/1.98499.

[81] Annika Kurzmann et al. "Auger Recombination in Self-Assembled Quantum Dots: Quenching and Broadening of the Charged Exciton Transition". In: *Nano Letters* 16.5 (2016). PMID: 27087053, pp. 3367–3372. DOI: 10.1021/acs.nanolett.6b01082. URL: https://doi.org/10.1021/acs.nanolett.6b01082.

[82] Christopher Melnychuk and Philippe Guyot-Sionnest. "Multicarrier Dynamics in Quantum Dots". In: *Chemical Reviews* 121.4 (2021). PMID: 33428388, pp. 2325–2372. DOI: 10.1021/acs.chemrev.0c00931. URL: https://doi.org/10.1021/acs.chemrev.0c00931.

[83] F. Widmann et al. "Blue-light emission from GaN self-assembled quantum dots due to giant piezoelectric effect". In: *Phys. Rev. B* 58 (24 1998), R15989–R15992. DOI: 10.1103/PhysRevB.58.R15989. URL: https://link.aps.org/doi/10.1103/PhysRevB.58.R15989.

[84] T. Nakaoka, S. Kako, and Y. Arakawa. "Quantum confined Stark effect in single self-assembled GaN/AlN quantum dots". In: *Physica E: Low-dimensional Systems and Nanostructures* 32.1 (2006). Proceedings of the 12th International Conference on Modulated Semiconductor Structures, pp. 148–151. ISSN: 1386-9477. DOI: https://doi.org/10.1016/j.physe.2005.12.028.

[85] A. D. Andreev and E. P. O'Reilly. "Theory of the electronic structure of GaN/AlN hexagonal quantum dots". In: *Phys. Rev. B* 62 (23 2000), pp. 15851–15870. DOI: 10.1103/PhysRevB.62.15851. URL: https://link.aps.org/doi/10.1103/PhysRevB.62.15851.

[86] V. Ranjan et al. "Self-consistent calculations of the optical properties of GaN quantum dots". In: *Phys. Rev. B* 68 (11 2003), p. 115305. DOI: 10.1103/PhysRevB.68.115305. URL: https://link.aps.org/doi/10.1103/PhysRevB.68.115305.

[87] R. Bardoux et al. "Photoluminescence of single GaN/AlN hexagonal quantum dots on Si (111): spectral diffusion effects". In: *Phys. Rev. B* 74 (19 2006), p. 195319. DOI: 10.1103/PhysRevB.74.195319. URL: https://link.aps.org/doi/10.1103/PhysRevB.74.195319.

[88] C. Kindel et al. "Exciton fine-structure splitting in GaN/AlN quantum dots". In: *Phys. Rev. B* 81 (24 2010), p. 241309. DOI: 10.1103/PhysRevB.81.241309. URL: https://link.aps.org/doi/10.1103/PhysRevB.81.241309.

[89] D. Simeonov et al. "Complex behavior of biexcitons in GaN quantum dots due to a giant built-in polarization field". In: *Phys. Rev. B* 77 (7 2008), p. 075306. DOI: 10.1103/PhysRevB.77.075306.

[90] G. Hönig et al. "Manifestation of unconventional biexciton states in quantum dots". In: *Nature Communications* 5 (1 2014), p. 5721. DOI: 10.1038/ncomms6721. URL: https://doi.org/10.1038/ncomms6721.

[91] Mark J. Holmes et al. "Probing the Excitonic States of Site-Controlled GaN Nanowire Quantum Dots". In: *Nano Letters* 15.2 (2015), pp. 1047–1051. DOI: 10.1021/nl503949u.

[92] S. Amloy et al. “Size dependent biexciton binding energies in GaN quantum dots”. In: *Applied Physics Letters* 99.25 (2011), p. 251903. DOI: 10.1063/1.3670040. URL: https://doi.org/10.1063/1.3670040.

[93] Olivier Labeau, Philippe Tamarat, and Brahim Lounis. “Temperature Dependence of the Luminescence Lifetime of Single CdSe/ZnS Quantum Dots”. In: *Phys. Rev. Lett.* 90 (25 2003), p. 257404. DOI: 10.1103/PhysRevLett.90.257404. URL: https://link.aps.org/doi/10.1103/PhysRevLett.90.257404.

[94] J. Simon et al. “Time-Resolved Photoluminescence Studies of Cubic and Hexagonal GaN Quantum Dots”. In: *Physica status solidi (b)* 224.1 (2001), pp. 13–16. DOI: https://doi.org/10.1002/1521-3951(200103)224:1<13::AID-PSSB13>3.0.CO;2-M.

[95] T. Bretagnon et al. “Time dependence of the photoluminescence of GaN/AlN quantum dots under high photoexcitation”. In: *Phys. Rev. B* 68 (20 2003), p. 205301. DOI: 10.1103/PhysRevB.68.205301. URL: https://link.aps.org/doi/10.1103/PhysRevB.68.205301.

[96] J. Stachurski et al. “Single photon emission and recombination dynamics in self-assembled GaN/AlN quantum dots”. In: *Light: Science and Applications* 11.114 (2022). DOI: 10.1038/s41377-022-00799-4. URL: https://doi.org/10.1038/s41377-022-00799-4.

[97] Takashi Matsuoka. “Progress in nitride semiconductors from GaN to InN—MOVPE growth and characteristics”. In: *Superlattices and Microstructures* 37.1 (2005), pp. 19–32. ISSN: 0749-6036. DOI: https://doi.org/10.1016/j.spmi.2004.06.003. URL: https://www.sciencedirect.com/science/article/pii/S0749603604001739.

[98] R. Oliver. “Growth and characterisation of nitride nanostructures”. In: *Materials Science and Technology* 18.11 (2002), pp. 1257–1271. DOI: 10.1179/026708302225007358.

[99] Y. Arakawa. “Progress in GaN-based quantum dots for optoelectronics applications”. In: *IEEE Journal of Selected Topics in Quantum Electronics* 8.4 (2002), pp. 823–832. DOI: 10.1109/JSTQE.2002.801675.

[100] R. Ferrando. “Surface Diffusion: Simulations”. In: *Encyclopedia of Materials: Science and Technology*. Ed. by K.H. Jürgen Buschow et al. Oxford: Elsevier, 2006, pp. 1–6. ISBN: 978-0-08-043152-9. DOI: https://doi.org/10.1016/B0-08-043152-6/02105-7. URL: https://www.sciencedirect.com/science/article/pii/B0080431526021057.

[101] Chun-Yuan Huang et al. “Self-ordered InGaAs quantum dots grown at low growth rates”. In: *Journal of Applied Physics* 103.4 (2008), p. 044301. DOI: 10.1063/1.2841216.

[102] Yangfeng Li et al. “Surface morphology and optical properties of InGaN quantum dots with varying growth interruption time”. In: *Materials Research Express* 7.1 (2019), p. 015903. DOI: 10.1088/2053-1591/ab5be0. URL: https://dx.doi.org/10.1088/2053-1591/ab5be0.

[103] Bruno Daudin. “Polar and nonpolar GaN quantum dots”. In: *Journal of Physics: Condensed Matter* 20.47 (2008), p. 473201. DOI: 10.1088/0953-8984/20/47/473201. URL: https://dx.doi.org/10.1088/0953-8984/20/47/473201.

[104] P. Sohi, D. Martin, and N. Grandjean. “Critical thickness of GaN on AlN: impact of growth temperature and dislocation density”. In: *Semiconductor Science and Technology* 32.7 (2017), p. 075010. DOI: 10.1088/1361-6641/aa7248.

[105] D. Simeonov et al. “Stanski-Krastanov GaN/AlN quantum dots grown by metal organic vapor phase epitaxy”. In: *Journal of Applied Physics* 99.8 (2006), p. 083509. DOI: 10.1063/1.2189975.

[106] C. B. Murray, D. J. Norris, and M. G. Bawendi. “Photoluminescence Spectroscopy of Semiconductor Quantum Dots and Wires”. In: *Annual Review of Materials Science* 30.1 (2000), pp. 545–610. DOI: 10.1146/annurev.matsci.30.1.545.

[107] D. Gammon et al. “Photoluminescence Excitation Spectroscopy of Semiconductor Quantum Dots”. In: *Physical Review Letters* 76.16 (1996), pp. 3005–3008. DOI: 10.1103/PhysRevLett.76.3005.

[108] K. Kyhm et al. “Gain dynamics and excitonic transition in CdSe colloidal quantum dots”. In: *Optical Materials* 30.1 (2007). Selected papers from the 4th International Symposium on Laser, Scintillator and Nonlinear Optical Matetials: ISLNOM-4, pp. 158–160. ISSN: 0925-3467. DOI: https://doi.org/10.1016/j.optmat.

2006.11.036. URL: https://www.sciencedirect.com/science/article/pii/S0925346706004137.

[109] Ma Hong et al. "Size-dependent optical properties and carriers dynamics in CdSe/ZnS quantum dots". In: *Chinese Physics B* 17.4 (2008), p. 1280. DOI: 10.1088/1674-1056/17/4/022. URL: https://dx.doi.org/10.1088/1674-1056/17/4/022.

[110] Thomas Müller et al. "Ultrafast intraband spectroscopy of electron capture and relaxation in InAs/GaAs quantum dots". In: *Applied Physics Letters* 83.17 (2003), pp. 3572–3574.

[111] H. Kurtze et al. "Carrier relaxation dynamics in self-assembled semiconductor quantum dots". In: *Phys. Rev. B* 80 (23 2009), p. 235319. DOI: 10.1103/PhysRevB.80.235319. URL: https://link.aps.org/doi/10.1103/PhysRevB.80.235319.

[112] R. P. Prasankumar et al. "Ultrafast carrier dynamics in an InAs/InGaAs quantum dots-in-a-well heterostructure". In: *Opt. Express* 16.2 (2008), pp. 1165–1173. DOI: 10.1364/OE.16.001165. URL: https://opg.optica.org/oe/abstract.cfm?URI=oe-16-2-1165.

[113] Clemens Burda et al. "The relaxation pathways of CdSe nanoparticles monitored with femtosecond time-resolution from the visible to the IR: Assignment of the transient features by carrier quenching". In: *The Journal of Physical Chemistry B* 105.49 (2001), pp. 12286–12292.

[114] D. P. Williams, A. D. Andreev, and E. P. O'Reilly. "Dependence of exciton energy on dot size in GaN/AlN quantum dots". In: *Phys. Rev. B* 73 (24 2006), p. 241301. DOI: 10.1103/PhysRevB.73.241301.

[115] M. Henini. "Handbook of Self Assembled Semiconductor Nanostructures for Novel Devices in Photonics and Electronics". In: London: Elsevier, Amsterdam, 2008, pp. 236–260.

[116] F. Stokker-Cheregi et al. "Quantum confinement dependence of the energy splitting and recombination dynamics of A and B excitons in a GaN/AlGaN quantum well". In: *Phys. Rev. B* 79.5 (24 2009), p. 245316. DOI: 10.1103/PhysRevB.79.245316.

[117] Francisco M. Gómez-Campos and Marco Califano. In: *Nano Letters* 12.9 (2012), pp. 4508–4517. DOI: 10.1021/nl3016279.

[118] A. Thränhardt et al. In: *Phys. Rev. B* 65.6 (3 2002), p. 035327. DOI: 10.1103/PhysRevB.65.035327.

[119] J.-Y. Marzin and G. Bastard. In: *Solid State Communications* 92 (5 1994), pp. 437–442. DOI: 10.1016/0038-1098(94)90524-X.

[120] M. Arlery et al. "Quantitative characterization of GaN quantum-dot structures in AlN by high-resolution transmission electron microscopy". In: *Applied Physics Letters* 74.22 (1999), pp. 3287–3289. DOI: 10.1063/1.123321.

[121] Raphaël Butté and Nicolas Grandjean. "Effects of Polarization in Optoelectronic Quantum Structures". In: *Polarization Effects in Semiconductors: From Ab InitioTheory to Device Applications*. Ed. by Colin Wood and Debdeep Jena. Boston, MA: Springer US, New York, 2008, pp. 467–511. ISBN: 978-0-387-68319-5. DOI: 10.1007/978-0-387-68319-5_9.

[122] I. A. Aleksandrov, V. G. Mansurov, and K. S. Zhuravlev. "Recombination processes in structures with GaN/ALN quantum dots". In: *Physica E: Low-dimensional Systems and Nanostructures* 75 (2016), pp. 309–316. ISSN: 1386-9477. DOI: https://doi.org/10.1016/j.physe.2015.10.004. URL: https://www.sciencedirect.com/science/article/pii/S1386947715302332.

[123] G. Zegrya and D. Samosvat. "Mechanisms of Auger recombination in semiconducting quantum dots". In: *Journal of Experimental and Theoretical Physics* 104 (2007), pp. 951–965. DOI: 10.1134/S1063776107060131.

[124] J. Renard et al. "Suppression of nonradiative processes in long-lived polar GaN/AlN quantum dots". In: *Applied Physics Letters* 95.13 (2009), p. 131903. DOI: 10.1063/1.3238311. URL: https://doi.org/10.1063/1.3238311.

[125] M. Ohmori, P. Vitushinskiy, and H. Sakaki. "Diffusion process of excitons in the wetting layer and their trapping by quantum dots in sparsely spaced InAs quantum dot systems". In: *Applied Physics Letters* 98.13 (2011), p. 133109. DOI: 10.1063/1.3574080. URL: https://doi.org/10.1063/1.3574080.

[126] C. Adelmann et al. In: *Phys. Rev. B* 70 (12 2004), p. 125427. DOI: 10.1103/PhysRevB.70.125427.

[127] F. Widmann et al. "Growth kinetics and optical properties of self-organized GaN quantum dots". In: *Journal of Applied Physics* 83.12 (1998), pp. 7618–7624. DOI: 10.1063/1.367878.

[128] K. Hoshino, S. Kako, and Y. Arakawa. "Formation and optical properties of stacked GaN self-assembled quantum dots grown by metalorganic chemical vapor deposition". In: *Applied Physics Letters* 85.7 (2004), pp. 1262–1264. DOI: 10.1063/1.1784524.

[129] G. Sallen et al. "Exciton dynamics of a single quantum dot embedded in a nanowire". In: *Phys. Rev. B* 80 (8 2009), p. 085310. DOI: 10.1103/PhysRevB.80.085310. URL: https://link.aps.org/doi/10.1103/PhysRevB.80.085310.

[130] Ivan Gamov et al. "Photochromism and influence of point defect charge states on optical absorption in aluminum nitride (AlN)". In: *Journal of Applied Physics* 129.11 (Mar. 2021), p. 113103. ISSN: 0021-8979. DOI: 10.1063/5.0044519. URL: https://doi.org/10.1063/5.0044519.

[131] D Morris, N Perret, and S Fafard. "Carrier energy relaxation by means of Auger processes in InAs/GaAs self-assembled quantum dots". In: *Applied Physics Letters* 75.23 (1999), pp. 3593–3595.

[132] B. Ohnesorge et al. "Rapid carrier relaxation in self-assembled $In_xGa_{1-x}As$/GaAs quantum dots". In: *Phys. Rev. B* 54 (16 1996), pp. 11532–11538. DOI: 10.1103/PhysRevB.54.11532. URL: https://link.aps.org/doi/10.1103/PhysRevB.54.11532.

[133] Ke Wei et al. "Observation of Ultrafast Exciton–Exciton Annihilation in CsPbBr3 Quantum Dots". In: *Advanced Optical Materials* 4.12 (2016), pp. 1993–1997. DOI: https://doi.org/10.1002/adom.201600352. URL: https://onlinelibrary.wiley.com/doi/abs/10.1002/adom.201600352.

[134] H. Htoon et al. "Effect of Zero- to One-Dimensional Transformation on Multiparticle Auger Recombination in Semiconductor Quantum Rods". In: *Phys. Rev. Lett.* 91 (22 2003), p. 227401. DOI: 10.1103/PhysRevLett.91.227401. URL: https://link.aps.org/doi/10.1103/PhysRevLett.91.227401.

[135] Victor I. Klimov. "Spectral and Dynamical Properties of Multiexcitons in Semiconductor Nanocrystals". In: *Annual Review of Physical Chemistry* 58.1 (2007). PMID: 17163837, pp. 635–673. DOI: 10.1146/annurev.physchem.58.032806.104537.

[136] S Sauvage et al. "Saturation of intraband absorption and electron relaxation time in n-doped InAs/GaAs self-assembled quantum dots". In: *Applied physics letters* 73.26 (1998), pp. 3818–3821.

[137] S. Sanguinetti et al. "Role of the wetting layer in the carrier relaxation in quantum dots". In: *Applied Physics Letters* 81.4 (2002), pp. 613–615. DOI: 10.1063/1.1495525. URL: https://doi.org/10.1063/1.1495525.

[138] S. Hinooda et al. "Wetting layer carrier dynamics in InAs/InP quantum dots". In: *Applied Physics Letters* 78.20 (2001), pp. 3052–3054. DOI: 10.1063/1.1338953.

[139] S. Kalliakos, P. Lefebvre, and T. Taliercio. "Nonlinear behavior of photoabsorption in hexagonal nitride quantum wells due to free carrier screening of the internal fields". In: *Phys. Rev. B* 67 (20 2003), p. 205307. DOI: 10.1103/PhysRevB.67.205307. URL: https://link.aps.org/doi/10.1103/PhysRevB.67.205307.

[140] T. S. Sosnowski et al. "Rapid carrier relaxation in $In_{0.4}Ga_{0.6}As$/GaAs quantum dots characterized by differential transmission spectroscopy". In: *Phys. Rev. B* 57 (16 1998), R9423–R9426. DOI: 10.1103/PhysRevB.57.R9423. URL: https://link.aps.org/doi/10.1103/PhysRevB.57.R9423.

Maryna HRYTSAIENKO

Dynamique de relaxation dans des boîtes quantiques GaN/AlN: étude par photoluminescence et transmission différentielle pompe-sonde résolues en temps

Résumé

Dans cette étude, nous avons approfondi la dynamique complexe de relaxation des paires électron-trou au sein de boîtes quantiques GaN/AlN à l'état de l'art. Grâce à l'utilisation combinée de différentes techniques d'optique ultra-rapide, nous avons étudié la dynamique des paires électron-trou depuis leur photocréation dans la couche de mouillage jusqu'à leur recombinaison à partir des états discrets des boîtes, sur des échelles de temps allant de quelques centaines de femtosecondes à quelques nanosecondes. La photoluminescence résolue en temps a montré que l'effet Stark quantique confiné est le principal facteur responsable de la dépendance des durées de vie radiatives en fonction de la taille de la boîte. Á partir de la forme des déclins, qui s'écartait de la simple fonction exponentielle attendue, nous avons extrait des informations pertinentes sur la structure de l'échantillon comme, par exemple, la présence d'un état sombre influençant la dynamique via une capture réversible des porteurs. De plus, différentes morphologies de boîtes ont été identifiées dans un autre échantillon, chacune présentant de temps de recombinaison spécifique. Notre modèle analytique a également confirmé l'absence d'écrantage du champ électrique interne par les porteurs photo-injectés pendant la recombinaison. Les expériences de pompe-sonde dégénérées et non-dégénérées ont révélé une efficacité des processus de thermalisation et de capture dans les boîtes rarement observée dans d'autres systèmes semi-conducteurs III-V. Ces découvertes soulignent les propriétés uniques du GaN et des conditions expérimentales spécifiques employées. L'évolution du temps de montée du signal de transmission différentielle avec l'énergie des photons indique une saturation des états en dessous de l'énergie de l'impulsion de sonde. Parallèlement, la dynamique de relaxation est régie à la fois par les durées de vie radiatives et la densité des états accessibles à plus basse énergie. Plus précisément, cette dynamique ralentit lorsque l'énergie de sonde est résonnante avec l'état fondamental de la boîte ou l'un de ses états excités. En revanche, des processus tels que l'effet Auger, et potentiellement un écrantage du champ électrique interne, accélèrent cette dynamique, en particulier à des densités de porteurs élevées.

UNIVERSITÉ DE STRASBOURG

Maryna HRYTSAIENKO

Relaxation dynamics in GaN/AlN quantum dots: study by time-resolved photoluminescence and pump-probe differential transmission

IPCMS

Abstrasct

In this study, we investigated the complex relaxation dynamics of electron-hole pairs within state-of-the-art GaN/AlN quantum dots. Thanks to the combined use of different ultrafast optics techniques, we have studied the dynamics of electron-hole pairs from their photocreation in the wetting layer to their recombination from the discrete states of the dots, on timescales ranging from a few hundred femtoseconds to a few nanoseconds. Time-resolved photoluminescence showed that the quantum confined Stark effect is the main factor responsible for the dependence of radiative lifetimes on dot size. From the shape of the decays, which deviated from the expected simple exponential function, we extracted relevant information about the structure of the sample, highlighting the reversible capture of carriers in a dark state. Additionally, different dot morphologies were identified in another sample, each exhibiting specific recombination times. Our analytical model also confirmed the absence of screening of the internal electric field by the photo-injected carriers during recombination. Degenerate and non-degenerate pump-probe experiments have revealed an efficiency of thermalization and capture processes in dots rarely seen in other III-V semiconductor systems. These findings highlight the unique properties of GaN and the specific experimental conditions employed. The evolution of the rise time of the differential transmission signal with the energy of the photons indicates a saturation of the states below the energy of the probe pulse. At the same time, the relaxation dynamics is governed by both the radiative lifetimes and the density of accessible states at lower energies. More precisely, this dynamic slows down when the probe energy is resonant with the ground state of the dot or one of its excited states. On the other hand, processes such as the Auger effect, and potentially screening of the internal electric field, accelerate this dynamics, especially at high carrier densities.